Synthesis of new nanomaterials based on porphyrins and graphene for elaboration of sensitive and selective DNA biosensors

Yaqiong Wang

université PARIS-SACLAY

NNT : 2017SACLS338

Thèse de doctorat

UNIVERSITÉ PARIS SUD
Comprendre le monde, construire l'avenir

Synthesis of new nanomaterials based on porphyrins and graphene for elaboration of sensitive and selective DNA biosensors

Thèse de doctorat de l'Université Paris-Saclay
préparée à l'Université Paris-Sud

École doctorale n°571 Sciences chimiques : molécules, matériaux, instrumentation et biosystèmes (2MIB)
Spécialité de doctorat : chimie

Thèse présentée et soutenue à Orsay, le 9 Octobre 2017, par

Yaqiong WANG

Composition du Jury :

Hynd REMITA
Directrice de Recherche
Laboratoire de Chime Physique (–Université Paris-Sud) — Présidente

Jean-Louis MARTY
Professeur
IMAgES Institute of Modelling and Analysis (– Université de Perpignan) — Rapporteur

Florence LAGARDE
Chargée de Recherche
Institut des Sciences Analytiques (– Université Lyon 1) — Rapporteur

Bernd SCHÖLLHORN
Professeur
Laboratoire d'Electrochimie Moléculaire (– Université Paris Diderot Paris 7) — Examinateur

Abdelkader ZEBDA
Chargé de Recherche
Laboratoire TIMC-IMAG (–Université Grenoble Alpes) — Examinateur

Helene SAURIAT-DORIZON
Maître de Conférences
Institut de Chimie Moléculaire et des Matériaux d'Orsay (– Université Paris-Sud) — Examinateur

Hafsa KORRI-YOUSSOUFI
Directrice de recherche
Institut de Chimie Moléculaire et des Matériaux d'Orsay (–Université Paris-Sud) — Directrice de thèse

Table of contents

PART B: RESULTS AND DISCUSSION

RESUMÉ

Les biocapteurs électrochimiques sont une classe de capteurs très prometteurs pour l'identification et la quantification de biomolécules en solution. En effet, cet outil d'analyse présente un certain nombre de propriétés intrinsèques qui en font d'eux des outils très attractifs et prometteurs dans des domaines aussi variés que le médical, l'agroalimentaire, l'environnement…. Ils possèdent une grande sensibilité dans leur réponse (jusqu'à l'attomole détecté) en temps réel et directe, une facilité de mise en œuvre, à faible coût et la possibilité de les miniaturiser et les intégrer dans des équipements transportables. Les biocapteurs sont classés en trois catégories selon la nature des biomolécules immobilisées à la surface ou des réactions étudiées. On peut citer les immunocapteurs, les capteurs enzymatiques et les capteurs d'ADN. Dans le cadre de ma thèse, je me suis intéressée à développer des capteurs d'ADN capables de détecter deux maladies infectieuses, l'hépatite C et la tuberculose, en ciblant des échantillons d'ADN synthétiques et PCR

L'infection par le virus de l'hépatite C (VHC) est un problème de santé mondial qui a touché environ 170 millions de personnes dans le monde et constitue l'une des principales causes de décès liés à une cirrhose hépatique et à un carcinome hépatocellulaire. L'importance des tests de diagnostic moléculaire à faible coût est particulièrement importante pour les pays en développement car ils sont déjà accablés par un nombre croissant de patients atteints d'hépatite C qui sont généralement économiquement en arrière. L'avènement des approches diagnostics moléculaires a permis de développer des analyses d'acide nucléique plus sensibles et spécifiques que les technologies à base d'anticorps.

La tuberculose (TB) est causée par le bacille à l'acide *Mycobacterium tuberculosis* (Mtb) et présente l'un des taux d'infection les plus élevés au monde touchant 1 personne sur 3 et 1,5 million de décès en 2013. Dans les pays les plus pauvres, le plus grand obstacle qui subsiste est la difficulté à détecter le bacille en dehors des lieux hospitaliers. Par conséquent, il est nécessaire de disposer d'un nouvel outil de diagnostic qui puisse être déployé rapidement et facilement dans des zones éloignées à forte charge de TB, et à faible coût en comparaison des

méthodes de diagnostic conventionnelles.

La mise au point d'outils performants pour détecter rapidement et à des états précoces ces deux pathologies est un défi auquel je me suis attachée durant ma thèse. De tels exemples ont été utilisés pour démontrer que par la suite ces capteurs d'ADN pourraient être généralisés et étendues à toutes autres maladies infectieuses.

La particularité des capteurs électrochimiques que j'ai développés durant ma thèse, repose sur le développement de nouveaux nanomatériaux associant des porphyrines fonctionnalisées à des feuilles de graphène, sur lesquels sont immobilisés les brins d'ADN d'intérêts. Cet assemblage moléculaire constitue la base du transducteur électrochimique, qui comme nous l'avons démontré, offre des propriétés très intéressantes aux capteurs en termes de gamme dynamique de détection, de limite de détection, de sensibilité et de sélectivité. La plus grande partie de mon travail de thèse a été de mettre au point et d'optimiser la synthèse de ces matériaux hybrides pour offrir les meilleures performances aux capteurs d'ADN à visés thérapeutiques.

Ce manuscrit est constitué de deux parties. Une première partie bibliographique introduit les capteurs d'ADN électrochimiques en général (avec ou sans marquage) ainsi que les différents transducteurs électrochimiques utilisés dans ce type de capteurs : les polymères organiques conducteurs (notamment le polypyrrole), les nanoparticules et associées et les matériaux à base de carbone (le fullerène et les nanotubes de carbone). Cette partie présente également l'état de l'art sur le graphène incluant les différents types de graphène et leurs approches de synthèse. J'expose ensuite les applications du graphène dans les capteurs d'ADN, les différentes approches d'immobilisation des brins d'ADN sur la surface du graphène et quelques exemples d'applications associant le graphène réduit à différents matériaux (comme les nanoparticules, les polymères conducteurs et des composés aromatiques). Enfin, un dernier chapitre est consacré à la présentation des porphyrines, leur propriété électrochimique, leur synthèse suivi de quelques exemples d'application dans les capteurs associés au graphène.

La deuxième partie du manuscrit présente mes résultats, divisés en quatre chapitres qui

décrivent les différents matériaux hybrides élaborés durant ma thèse et leur intégration au sein de capteurs d'ADN. Ces chapitres sont 1) la synthèse et la caractérisation, par plusieurs techniques physico-chimiques des différents nanomatériaux élaborés à base de graphène réduit (RGO) et de porphyrines fonctionnalisées, 2) le développement d'un capteur d'ADN à base de RGO et d'une porphyrine de manganèse, 3) étude de l'effet du nombre des fonctions acides carboxyliques de la porphyrine sur les performances du capteur à base de RGO et 4) élaboration d'un capteur auto-assemblé.

1. Synthèse et propriétés des nanomatériaux.

Dans cette partie, je présente tout d'abord, la synthèse de différentes porphyrines utilisées : la tétraphénylporphyrine portant une fonction carboxylique en para d'un groupement phényl, la H_2TPP-1CP et une tétraphénylporphyrine substituée par quatre fonctions carboxyliques, H_2TPP-4CP. Les fonctions COOH sont utilisées comme point d'ancrage de l'ADN selon un couplage peptidique entre une fonction amine de l'ADN en position terminale et cette fonction COOH de la porphyrine. La tétraphénylporphyrine H_2TPP-1CP est métallée par un métal électroactif, le manganèse, (MnTPP-1CP) pour des études complémentaires. En effet, l'intérêt de préparer un tel complexe a permis la caractérisation du matériau formé sur la surface en suivant le signal redox intense et réversible du complexe de manganèse (III). Une stratégie de synthèse pour chaque molécule est développée et les molécules sont correctement caractérisées selon les techniques d'analyses usuelles (RMN, SM, UV). Le graphène a été ensuite préparé selon différents protocoles opératoires et caractérisé par XPS et Raman. Les différentes qualités de graphène obtenues sont comparées et des études électrochimiques ont démontré que le graphène oxydé réduit chimiquement (CRGO) offrait les meilleurs propriétés en terme de conductivité et donc de transfert de charge, nécessaires pour la bonne mise en œuvre du capteur électrochimique d'ADN.

Par la suite, les matériaux hybrides sont préparés et déposés sur l'électrode de carbone soit en formant successivement une couche de graphène puis de porphyrines soit en préformant le matériau en solution. Chaque matériau a été caractérisé par microscopie électronique à balayage (MEB), spectroscopie de photoélectrons aux rayons X (XPS), par

spectrophotométrie infrarouge à Transformée de Fourier (FT-IR) et par électrochimie. Ces études ont fait ressortir plusieurs avantages sur les nano hybrides. La quantité de porphyrine immobilisée sur la surface de l'électrode est accrue en raison de la grande surface d'adsorption du graphène. La structure conjuguée du graphène CRGO permet une interaction forte et stable avec les tétraphénylporphyrines par des interactions de type π-π. Ce mode d'interaction ne perturbe pas la structure électronique intrinsèque du CRGO et lui permet ainsi de conserver toutes ses propriétés de conductivité et de transfert de charge. L'augmentation des charges négatives sur la porphyrine permet une meilleure dispersion des feuilles de nano-hybrides sur la surface de l'électrode.

Une étude approfondie a été menée pour comprendre le mode d'association entre les porphyrines mono/ tetra carboxyliques avec le graphène. J'ai réalisé des expériences de microscopie à force atomique (AFM), spectroscopie UV-visibles et Raman. Ces études ont fait ressortir que la tétraphénylporphyrine portant un groupement carboxylique viendrait interagir sur toute la surface du graphène et formerait plusieurs couches d'empilement. Dans le cas des porphyrines portant quatre fonctions acides carboxyliques, la présence des fonctions alcools et acides en périphéries des feuilles de graphène privilégierait des interactions aux extrémités plutôt qu'en surface du graphène.

2. Capteurs d'ADN à base de RGO et de porphyrine de manganèse.

L'objectif du chapitre II est une preuve de concept de notre approche par l'élaboration du premier capteur d'ADN basé sur un nanomatériau associant du graphène (CRGO) à une porphyrine de manganèse mono fonctionnalisée par une fonction carboxylique, comme point d'ancrage de l'ADN. Nous démontrerons que cette association entre le complexe et le graphène améliore les propriétés électriques et conductrices du matériau lors de la détection électrochimique du brin d'ADN complémentaire. Le manganèse (Mn) a été choisi comme cation métallique, car le complexe formé possède un signal électrochimique réversible et intense qui a permis la caractérisation par voie électrochimique. La stratégie suivie pour la construction du capteur d'ADN repose sur un greffage covalent entre le brin d'ADN en solution et la fonction acide de la métalloporphyrine, préalablement immobilisée sur

l'électrode de carbone et le graphène.

Les conditions de greffage ont été optimisées par divers tests électrochimiques en faisant varier le rapport de concentration de MnTPP-1CP et CRGO, la concentration en réactifs activés (EDC et NHS), et le temps de greffage. Finalement, l'étape de couplage a été caractérisée par différentes techniques d'analyses telles que les mesures FT-IR, MEB, voltammétrie cyclique (VC) et impédancemétrie (EIS). L'hybridation en présence de l'ADN complémentaire a été suivie par EIS dans une solution de $[Fe(CN)_6]^{3-/4-}$ à 5 mM et a permis de déterminer une gamme dynamique de [100 aM-10 pM] et une limite de détection de 2×10^{-16} M. Ce premier résultat s'est montré très encourageant et prometteur pour le développement de nouveaux outils à base de porphyrine et de graphène pour le diagnostic médical. Cependant, une étude de la sélectivité du capteur d'ADN par impédancemétrie (EIS) a montré une variation du signal de 9% du capteur en présence d'une séquence non complémentaire contre 27% en présence d'une séquence modifiée au niveau d'une seule base de l'ADN. Ce résultat montre que ce nanomatériau hybride présente une surface d'adsorption non-spécifique non négligeable. C'est pourquoi, nous avons cherché à améliorer cette propriété du capteur en diminuant ces interactions non souhaitées lors de la détection. Une des solutions proposée a été d'augmenter le nombre de charges négatives sur la surface de l'électrode modifiée afin de limiter par répulsion de charges, les adsorptions des brins d'ADN, également chargés négativement.

Ce travail d'optimisation du matériau a fait l'objet de la deuxième partie de ma thèse, par une étude comparative entre deux porphyrines fonctionnalisées.

3. Capteurs d'ADN à base de CRGO et de porphyrines polyfonctionnalisées- Effet du nombre de fonctions acides carboxyliques sur les performances du capteur.

L'objectif du chapitre III, s'inscrit dans la continuité du chapitre II, par une étude comparative entre deux nanomatériaux associant le graphène CRGO et une tétraphénylporphyrine fonctionnalisée par un et quatre fonctions carboxyliques nommés H_2TPP-1CP/CRGO et H_2TPP-4CP/CRGO respectivement. Le capteur d'ADN a été obtenu, dans chaque cas, en suivant les mêmes conditions que dans le chapitre II, en immergeant

l'électrode, modifiée par le nanohybride, dans une solution de 1 µM contenant le brin d'ADN à greffer en présence d'agents activant (EDC et NHS). Les deux capteurs obtenus ssDNA/H_2TPP-1CP/CRGO et ssDNA/H_2TPP-4CP/CRGO respectivement, sont caractérisés par voltammétrie par vague carrée (SWV) et impédancemétrie (EIS). Les études par impédance dans le PBS ont bien montré, dans les deux cas, l'immobilisation de l'ADN sur la surface, grâce à l'augmentation de la résistance du transfert d'électron (R_{ct}). Cette augmentation s'explique par la présence de l'ADN sur la surface qui encombre la surface et rend le transfert d'électrons entre la surface et la solution plus difficile. L'épaisseur de la biocouche nanohybride (ssDNA/H_2TPP-nCP/CRGO) a été déterminée par impédance et vaut 30 nm et 6 nm pour le capteur n=1 et n=4 respectivement. Ce résultat est en accord avec l'hypothèse émise précédemment, dans laquelle les porphyrines mono fonctionnalisées (n=1) interagiraient plutôt sur la surface du graphène, contrairement aux porphyrines tétrasubstituées (n=4) qui se lieraient aux feuilles de graphène par leurs extrémités. Ce résultat a été conforté par des études d'AFM. La réaction d'hybridation en présence du brin complémentaire a été suivie par voltammétrie à vague carrée (SWV) en présence d'une sonde redox neutre, la benzoquinone. Une gamme dynamique a été obtenue pour les deux capteurs sur une gamme de concentration d'ADN du même ordre de grandeur et une limite de détection de l'ordre du femtomolaire. Par contre, il a été observé une différence lors de l'étude de la sélectivité de chacun de ces capteurs, en présence d'une concentration de 1 fmole du brin d'ADN non complémentaire. En effet, une variation de l'ordre de 30% de l'intensité du courant de réduction de la benzoquinone a été mesurée par SWV pour le capteur ADN/H_2TPP-1CP/CRGO contre seulement 15% pour le capteur chargé négativement sur sa surface ADN/H_2TPP-4CP/CRGO. Cette différence peut s'expliquer par la présence plus importante de charges négatives sur la surface de l'électrode à pH 7, pour le capteur ADN/H_2TPP-4CP/CRGO, réduisant ainsi par répulsions électroniques les adsorptions de l'ADN sur la surface.

Le capteur ADN/H_2TPP-4CP/CRGO a été ensuite utilisé pour détecter l'ADN du gène rpoB de *Mycobacterium tuberculosis* dans des échantillons réels de PCR. La séquence d'ADN immobilisée est une séquence complémentaire du gène rpoB. Les résultats de

détection et de sélectivité sont de la même qualité que ceux obtenus lors de la détection du gène de l'hépatite B, avec une variation seulement de 10% du courant en présence du brin non complémentaire. Ce résultat montre l'énorme potentiel de la plateforme H_2TPP-4CP/CRGO pour la détection électrochimique d'agents pathogènes pour des applications de type diagnostique et thérapeutique.

Par ailleurs, nous avons essayé de comprendre l'origine de ces adsorptions non spécifiques de l'ADN sur l'électrode. Nous avons émis l'hypothèse que ces interactions venaient de l'adsorption de l'ADN directement sur l'électrode de carbone. En effet, les feuilles de graphène ne recouvrant pas la totalité de l'électrode, des surfaces de carbone seraient ainsi disponibles pour l'adsorption des protéines ou de l'ADN. Cet aspect du travail est abordé dans le chapitre IV.

4. Capteurs d'ADN auto-assemblés

Les protéines ou l'ADN sont connues pour s'adsorber sur de nombreuses surfaces dont le carbone. Plusieurs approches sont décrites dans la littérature pour limiter ou bloquer ces interactions (utilisations de protéines, de polyéthylène glycol..). L'une d'entre elles consiste à recouvrir la surface de carbone par une monocouche auto-assemblée (SAM) de phénylethylamine (β-PEA), couche qui présente des groupements phényles orientés et perpendiculaires à la surface rendant celle-ci plus hydrophobe. Cette organisation devrait aussi améliorer l'immobilisation du matériau nanohybride par des interactions de type π-π entre le graphène et les groupes aromatiques terminaux de la couche SAM. Dans un premier temps, la formation de la couche de β-PEA a été préparée et optimisée par électrodéposition du monomère à différentes concentrations (1mM, 2 mM et 4mM). Ces différentes couches ont été étudiées et caractérisées par des mesures de SWV, EIS et AFM. Puis nous avons immobilisé le matériau hybride H_2TPP-4CP/CRGO, qui s'est avéré être le plus performant dans le chapitre III. Ces études ont montré que quelque soit la concentration en β-PEA, l'incorporation d'une telle monocouche entre l'électrode et le nanomatériau, H_2TPP-4CP/CRGO, améliore la conductivité de la couche en augmentant la réversibilité du signal redox de la sonde électrochimique en solution (benzoquinone). Par ailleurs, une couche SAM

obtenue par électrodéposition de 2 mM de β-PEA conduit à une couche plus organisée et une meilleure orientation des groupements phényles sur la surface de l'électrode. Cette organisation a permis ainsi une meilleure interaction du nanomatériau H_2TPP-4CP/CRGO avec la monocouche, rendant certainement plus accessible les fonctions carboxyliques à la surface. En effet, avec cette surface modifiée, nous avons obtenu un meilleur taux de recouvrement de l'ADN sur la couche (11 nmol.cm^{-2}). La réaction d'hybridation a été ensuite étudiée, par la technique SWV pour chacun des capteurs présentant des couches mono-assemblées différentes (ADN/H_2TPP-4CP/CRGO/1β-PEA, ADN/H_2TPP-4CP/CRGO/2β-PEA et ADN/H_2TPP-4CP/CRGO/4β-PEA). Nous avons observé lors de l'ajout croissant de concentration de l'ADN complémentaire de 1aM à 1 nM, une augmentation de l'intensité du courant de réduction de la benzoquinone en hydroquinone pour les capteurs ADN/H_2TPP-4CP/CRGO/2β-PEA et ADN/H_2TPP-4CP/CRGO/4β-PEA. Cette réponse du signal est caractéristique d'un signal on. De plus, le capteur ADN/H_2TPP-4CP/CRGO/2β-PEA a présenté une plus large gamme dynamique de [10^{-16} M- 10^{-9} M] et une limite de détection de 10^{-19} M. Une étude de la sensibilité des capteurs en présence du brin d'ADN non-complémentaire a montré une très faible, voire absence de réponse électrochimique des capteurs ADN/H_2TPP-4CP/CRGO/2β-PEA et ADN/H_2TPP-4CP/CRGO/4β-PEA, même pour des concentrations élevées de l'ADN non complémentaires. Ainsi l'incorporation d'une couche auto assemblée sur la surface, avec une concentration supérieur à 2mM, a permis l'absence de toutes adsorptions non spécifiques de l'ADN sur la surface du capteur. Il reste néanmoins à réaliser des études de détection du capteur ADN/H_2TPP-4CP/CRGO/2β-PEA en milieu biologique pour évaluer sa performance.

Ainsi au travers de mes travaux de thèse, j'ai pu élaborer un capteur d'ADN, à base de graphène et de porphyrine, qui présente un énorme potentiel pour la détection électrochimique d'agents pathogènes pour des applications de type diagnostique et thérapeutique.

GENERAL

INTRODUCTION

GENERAL INTRODUCTION

The project of my thesis consisted on the development of nanomaterials that are able to act as molecular transducers for the construction of DNA sensors, based on electrochemical response. Electrochemical DNA sensors become an attractive technique for the identification of biomolecules due to miniaturization possibilities, low cost and direct lecture of electric signals. However the choice of a transducer, which affords an electrochemical signal, is crucial in biosensor construction. Performance of DNA sensor is characterized by some important parameters such as dynamic and linear range of detection, limit of detection (LOD), sensitivity, and selectivity.

During my thesis, developing efficient conducting transducers combining the porphyrins functionalized with various groups and graphene for high sensitive and selective electrochemical detection was a main objective of my research. I worked on DNA detection and in the development of DNA sensors for two infectious diseases like hepatitis C with synthetic DNA targets and *tuberculosis* DNA from real PCR samples. Such examples were used to demonstrate that DNA sensor could be generalised to all infectious diseases and used in point of care system. These DNA sensors are especially attractive in the biological field and public health. I divided my thesis into two Parts, Part A, of which describe generally about electrochemical DNA sensor and transduces developed and explored in DNA sensors and Part B is related to the results and discussion of my work, which will be composed of four chapters.

Firstly, the hybrid nanomaterials which combined the features of both graphene (high conductivity and large specific surface area) and porphyrins (physical and chemical properties and electron transfer ability), such as tetraphenylporphyrin bearing one and four carboxylic groups named H_2TPP-nCP$_{(n=1,\ 4)}$ and tetraphenylporphyrin incorporating manganese (III) (MnTPP-1CP) were successfully synthesized. The interaction between H_2TPP-nCP$_{(n=1,\ 4)}$ and chemically reduced graphene oxide (CRGO) was studied in my thesis work. To investigate the characteristic properties of as-prepared nanomaterials, scanning electron microscopy

(SEM), atomic force microscopy (AFM), UV-visible spectra, Fourier Transform infrared spectra (FT-IR), X-ray photoelectron spectra (XPS) and Raman spectroscopy were utilized. The restored π-network of CRGO was expected to provide a good substrate for anchoring π-conjugated molecules through π–π stacking interactions as non-covalent approach which does not disrupt the intrinsic electronic structure of the CRGO and retains the total conductivity of graphene. The porphyrins are able to incorporate many different metal ions for redox activities that can improve the ability of electron transfer and provide catalytic activity. The electrochemical properties was explored by electrochemical impedance spectroscopy (EIS) and cyclic voltammetry (CV), which was expected to confirm that both the tight interaction exists between H_2TPP-n$CP_{(n=1,4)}$ and CRGO, and the hybrid nanomaterial H_2TPP-4CP/CRGO possesses more negative charge due to the presence of carboxylic groups on the surface introduced by attached porphyrins. The electrochemical process and reversibility monitored in neutral redox marker p-benzoquinone without charge ligands was to be tested to demonstrate that the hybrid nanomaterials possess high electroactivity with enhanced k_s calculated by Nicolson model, compared to CRGO. In order to further investigate the characteristics and electrochemical properties of hybrid nanomaterial H_2TPP-nCP/CRGO, a porphyrin of manganese (Mn) was to be utilized through the electrochemical test of the signal response of the Mn^{3+}/Mn^{2+} redox complex.

The purpose in chapter II is to exploit a DNA sensor based on the hybrid nanomaterial MnTPP-1CP/CRGO which could improve the electrical properties and lead to a sensing layer for electrochemical DNA detection. The functionalization of phenyl ring with a carboxylic group allows the attachment of single-stranded amino DNA (ssDNA) on the complex through covalent interactions. The manganese (Mn) has been chosen as metallic cation, due to its reversible and electrochemical signal response that will allow the electrochemical characterization. The strategy followed for the construction of DNA sensor was to be characterized through different analytical techniques such as FT-IR, UV and electrochemical measurements. The immobilization of ssDNA and hybridization with complementary sequences (cDNA) lead to the change of electrochemical properties for MnTPP-1CP/CRGO. The conditions for the constructive process of DNA sensor, including the concentration ratio

of MnTPP-1CP and CRGO, the concentration of activated reactants (EDC and NHS), and the hybridization time was also to be optimized by various electrochemical tests. Selectivity of the DNA sensor was investigated in presence of non-complementary and one-mismatched DNA sequence. A detection limit was estimated and could be improved by introducing more negative charge function on the porphyrins, thanks to their chemical modification. The selectivity was expected to be improved by adding more negative charges on the electrode surface due to the charge repulsions.

Thus, the purpose in chapter III was to focus on DNA sensor based on the H_2TPP-nCP/CRGO hybrid nanomaterials (with n=1 or 4) covalently attached with single-strand DNA to afford ssDNA/H_2TPP-nCP/CRGO. The layer was characterized by Atomic Force Microscopy (AFM) and electrochemical methods. I wanted to present novel electrochemical DNA sensor based on self-assembled nanomaterial of a π-electron-rich conjugated structure of CRGO associated with two types of π-conjugated H_2TPP-1CP and H_2TPP-4CP, respectively. Porphyrin molecules are versatile compounds that are easily functionalized with numerous designed carboxylic groups that could covalently interact with a 5'-amino single-strand DNA (ssDNA) through stable amide link. The electronic properties of such nanomaterials was studied through square wave voltammetry (SWV), electrochemical impendence spectra (EIS), and cyclic voltammetry (CV). On respectively employing a negatively charged redox marker, $[Fe(CN)_6]^{3-/4-}$ and a neutral one, *p*-benzoquinone, the pattern of interaction between H_2TPP-nCP/CRGO and ssDNA could be envisaged by means of the calculated relative change of diffusion coefficient (D_0) and homogenous electron constant (k_s). The DNA immobilization and hybridization with complementary sequences were to be monitored by following the variation of the reduced current of redox couple *p*-benzoquinone/hydroquinone. On the basis of previously developed and optimized conditions, the electrochemical DNA sensor based on H_2TPP-4CP/CRGO was expected to prepare and exhibite a broader linear range with a lower detection limit compared to ssDNA/H_2TPP-1CP/CRGO platform. Furthermore, the DNA sensor was expected to be applied for sensing DNA of rpoB gene of *Mycobacterium tuberculosis* in real PCR samples. The elaborated DNA sensor was suitable for detection of sequences with wild-type samples, discriminating them

from a single nucleotide polymorphism (SNP) T (TCG/TTG) with mutation. This shows enormous potential on this platform for further applications in pathogens diagnostic and therapeutic purpose.

According to some results before mentioned, the variation of the non-specific absorption value was still high and should be improved such as blocking the glassy carbon electrode with aromatic compounds to avoid any self-assembled adsorptions on the electrode. The Chapter IV will devote to eliminate non-specific absorptions.

The purpose of incorporating β-PEA layer in such DNA sensor was to underline homogeneous surface coverage of H_2TPP-4CP/CRGO with preformed monolayers (M) with phenyl in end position. Such function could improve the immobilization of composite as followed, thus can be obtained by π-π staking interactions of composite formed with graphene and the terminal functional groups of SAM layer. In addition, such modification demonstrates its ability to prevent non-specific adsorptions of DNA on the electrode surface during the hybridization reaction. The formation of β-PEA layer was optimized by electrodeposition of monomer in different concentrations, followed by the immobilization of hybrid complex moieties H_2TPP-4CP/CRGO and the grafting of ssDNA. All the steps of construction were to be studied and characterized by SWV, EIS measurements and AFM experiments. Via varying the concentration of β-PEA modified on the GCE surface, I expected to successfully obtain a homogeneous surface and allow to have a uniform covering of H_2TPP-4CP/CRGO onto the surface of electrode with β-PEA, which was to make an electrochemical detection directly with an increase in redox marker signal called “signal on”, which has many advantages compared to biosensors with decrease in signal “signal off”. Detection of cDNA was investigated for each sensing layer. The superior performance of DNA sensor was expected to exhibit an excellent sensitivity with low limit detection and broad linear range for H_2TPP-4CP/CRGO/β-PEA platform. Moreover, the selectivity with less non-specific DNA adsorption was also expected and could be expected to be successfully applied for real samples detection demonstrating a potential application.

PART A:

BIBLIOGRAPHY

CHAPTER I:

Electrochemical DNA sensor

CHAPTER I: Electrochemical DNA sensor

1. Definition

The first and the most widespread used commercial biosensor is the blood glucose biosensor which was developed by Leland C. Clark in 1962[1] reputed as the father of the biosensor (Fig. 1).

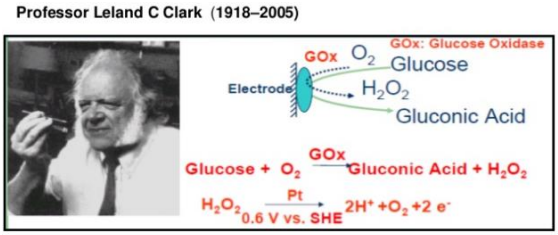

Fig. 1. *The first commercial biosensor developed by Professor Leland C Clark*

Biosensor are analytical tools for the analysis of biomaterial samples to gain an understanding of their biocomposition, structure and function by converting a biological response into a measurable response.

In terms of the conceptual and fundamental mode of operation, three main compounds compose a biosensor including the bio-receptor, the transducer, and the amplifier. The sample analytes including antigen, protein or viral DNA, can be detected by bio-receptor (antibody, enzyme, DNA, aptamer, respectively) immobilized on the transducer, which transforms the effect of the recognition process into an observable and measurable signal. The variation of the signal is proportional to the concentration of the target in the solution and can be measured by different techniques such as optical[2], thermal[3], piezoelectric[4] and electrochemical[5] methods (Fig. 2).

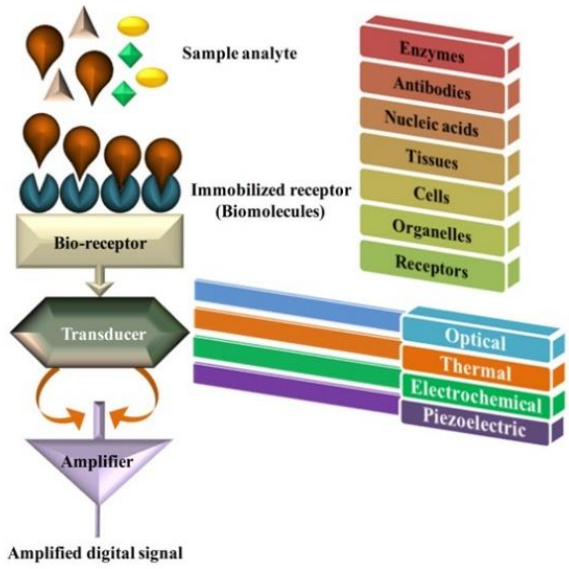

Fig. 2. *Schematic presentation of biosensors*

Although numerous methods have been used for the detection and identification of biomolecules, these biosensors suffer from certain drawbacks. For instance, optical biosensors, though very sensitive, however, cannot be used in turbid media[6]. Thermal biosensors cannot be utilized with systems with very little heat change. Moreover, they are difficult to handle, necessary to use large equipment. Typically electrochemical method, due to the possibility of miniaturization, low cost, and direct electric signals[7], has emerged as the most commonly used biosensors and becomes an attractive technique for identification of biomolecules. They have been found to overcome most of the disadvantages, which inhibit the use of other types of biosensors.

Electrochemical biosensors, due to their rapidement, easy to handle and low cost, become the most commonly used class of biosensors[8]. Depending upon the electrochemical property to be measured by a detector system, electrochemical biosensors may further be divided into conductometric, potentiometric and amperometric biosensors[4]. References are also made to other types of electrochemical detection techniques, such as impedimetric, which measures impedance (both resistance and capacitance), and field-effect, which uses transistor technology to measure current as a result of a potentiometric effect at a gate electrode[3].

According to the nature of the biomolecules immobilized on the surface or the reactions, biosensors are classified in three categories immunosensors, enzyme sensors and DNA

sensors. A basic DNA sensor is designed by the immobilization of a single strand oligonucleotide (ssDNA) on a transducer surface to recognize its complementary single strand DNA (cDNA) sequence via hybridization. Due to the specific and robust interaction between complementary sequences, DNA sensor is especially suited for biosensor applications.

Therefore, combing electrochemical technology with nucleic acid layers, the new concept of the electrochemical DNA hybridization biosensor was first introduced by Millan and Mikkelsen back in 1993[9], this exciting research area has received intense attention from several groups around the world, an impressive number of inventive designs for electrochemical DNA sensors have appeared and promised to provide a simple, accurate and inexpensive platform for patient diagnosis.[7] In my thesis, I will focus on electrochemical DNA sensor where the different technologies and principles will be described.

Performance of biosensor is characterized by some important parameters such as dynamic and linear range of detection, limit of detection (LOD), sensitivity, and selectivity (Fig. 3). Dynamic range represents concentration of analyte where a variation of the electrochemical signal is observed. The slope of the curve plotted in the linear range corresponds to the sensitivity of the biosensor. The lower value measured corresponds to the limit of quantification (LOD) and by extrapolation of this curve the detection limit (DL) could be calculated according to various methods described in analytical techniques. The most commonly used in biosensors devices concerns those taking into account signal to noise ratio, where DL is obtained by the equation:

$$x_{DL} = \frac{\alpha_0 + 3s_{bl}}{\alpha_1}$$

Where s_{bl} is the standard deviation, α_o is the measurement obtained with blank test and α_1 is the sensitivity obtained by the slope of the linear part of the calibration curve.

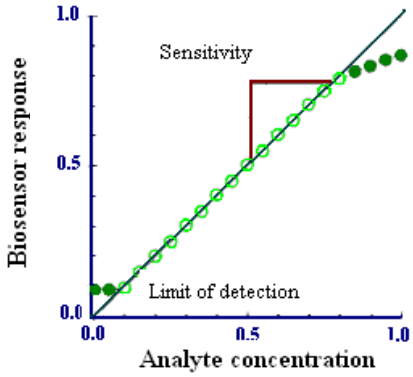

Fig. 3. *Presentation of parameters which characterize biosensors*

The key issues in the development of all biosensors include design of the transducers so that the analyte selectively interacts with the sensing surface[10,11] for achievements of efficient transduction of the bio-recognition event[12,13,14]. For example, various materials such as nanoparticles, polymers, carbon materials or complex of both are developed as transducers of electrochemical biosensor. Meanwhile, in order to meet the higher requirement of DNA analysis in different fields, the choice of detection technologies are also important for increasing the sensitivity and selectivity of the biosensor[15–18], and the response times in very sensitive systems[19].

Thus, the detection technologies and the property of transducer have a significant impact on the performance of the biosensor.

2. DNA detection technologies

The pivotal detection of electrochemical DNA sensor is based on the hybridization reaction between ssDNA and complementary cDNA, which results in changes of the electric properties of the surface. Different transductions are developed and can be subdivided into two main categories, label-based and label-free approaches[20,21].

2.1 Label-based electrochemical detection of DNA hybridization

2.1.1 DNA labelled with enzymes

Single strain DNA can be labelled by some enzymes such as horseradish peroxidase[22,23],

alkaline phosphatase[24] and glucose oxidase[25]. The basic principle is to label the DNA target with redox enzymes.

When the hybridization occurs with immobilized ssDNA probe on the surface, DNA labelled with enzyme remains on the electrode. Hybridization reaction could be followed through the catalytic properties of the enzymes in presence of their substrates where the obtained products are electroactive. In this case immobilized enzymes lead to production of electroactive species near the electrode surface, which gives a current related to the amount of hybridized DNA target (Fig. 4). For association of DNA with enzyme, some assays use affinity biotin/avidin system[23,24]

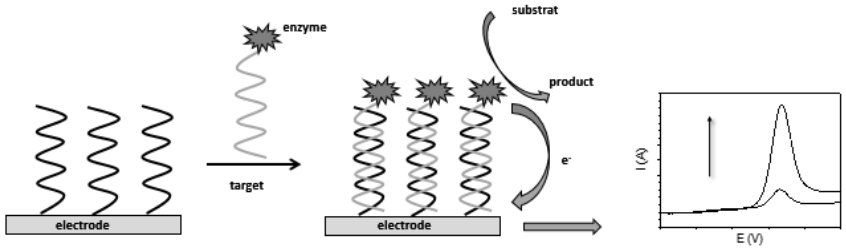

Fig. 4. *Schematic representation of detection by enzyme labelled DNA target*

As example, Spain. *et al* [26] developed an electrochemical horseradish peroxidase labelled DNA sensor based on polymer polyaniline nanofibers (PANI-NF) for the detection of *Staphylococcus aureus (S. aureus)*. The hybridization of target is detected by monitoring the reduction of a hydroquinone into quinone in presence of hydrogen peroxide in solution. The sensors have a wide dynamic range from 150×10^{-12} to 1×10^{-6} M with detection as low as 150 pM and excellent ability to discriminate DNA mismatches and a high sensitivity. The schematic representation is shown in Fig. 5.

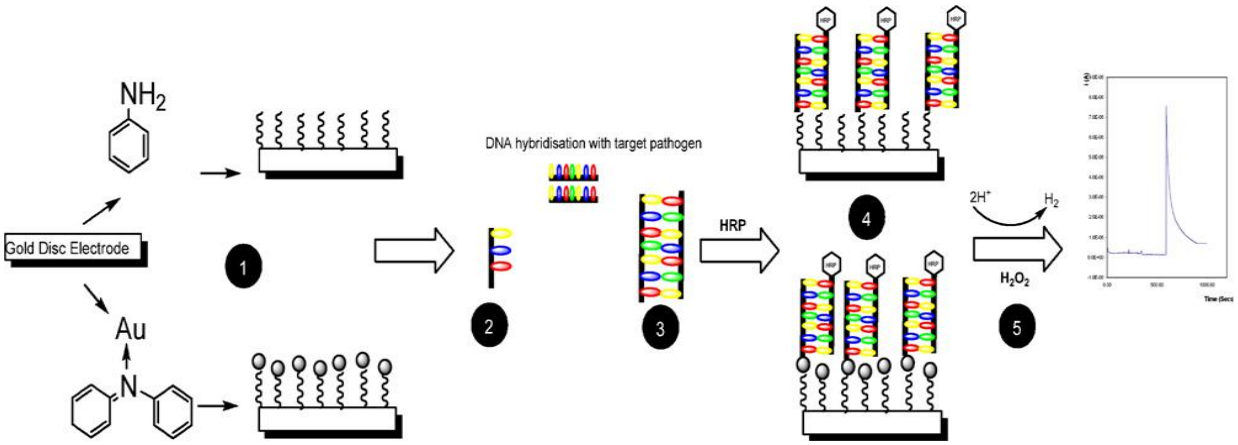

Fig. 5. *Schematic illustration of the hybridization detection protocol.*

2.1.2 DNA labelled with redox marker

The monitoring of hybridization between two complementary DNA strands could be performed by labelling of ssDNA probe with a redox marker, such as methylene blue (MB)[27–29] or ferrocene (Fc)[30]. The electroactive molecules on the surface were detected directly by straightforward transduction. Ricci et al. [28] developed an electrochemical DNA sensor, with which the DNA sensing platform is based on DNA probe terminally labelled with redox marker MB. Because the DNA sensor performance is dependent on the nature of the self-assembled monolayer on the electrode surface, the signal changes reflected the dynamics of the probe before and after hybridization. (Fig. 6).

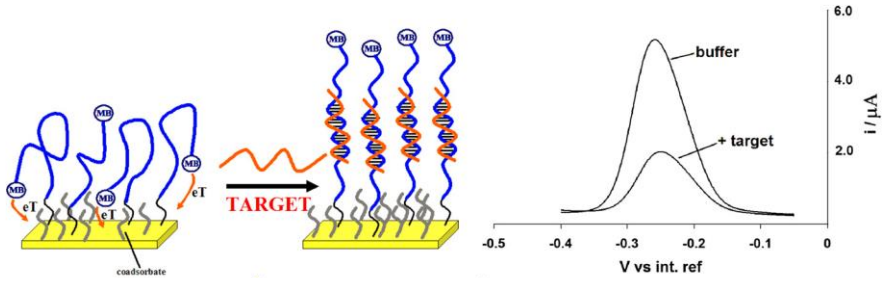

Fig.6. *Schematic representation of DNA sensors based on MB as redox marker modified ssDNA probe*

Moiroux et al.[31] has developed a DNA sensor, where ssDNA oligonucleotides, labelled with a small redox marker, an alkylferrocene unit (Fc), was attached by the 5'-end to a gold electrode surface (Fig.7). The authors follow the variation of current of Fc during the hybridization reaction. The disappearance of redox signal of Fc was observed after

hybridization. Authors explained that the Fc, which was close to the surface (curve a), was sequestered after hybridization due to the formation of a rigid dsDNA chain that could not allowed it to be reduced and oxidized on the surface (curve b). After de-hybridization, the redox signal was recovered again, (curve c)

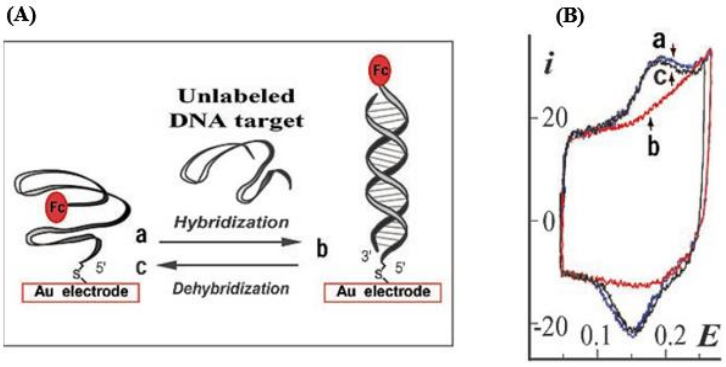

Fig.7. *Schematic representation of DNA sensors based on DNA labelled with Fc*

2.1.3 DNA labelled with nanomaterials

Nanomaterial can be used as an electrochemical label. Gao et al. designed for the first time an electrochemical DNA sensing strategy[32], Rasheed and Sandhyarani[33] explored an electrochemical probe which is formed by self-assembled ssDNA stabilized gold nanoparticles (AuNP) for the sensitive detection of the BRCA 1 gene (Fig. 8). The detection of the analytical signal was by the electrochemical oxidation of the gold nanoparticles in the presence of $HClO_4$ which was monitored using cyclic voltammetry/chronoamperometry to detect the concentration of BRCA1 gene. The sensitivity is in the attomolar range towards target DNA, offering orders of magnitude lower detection limit.

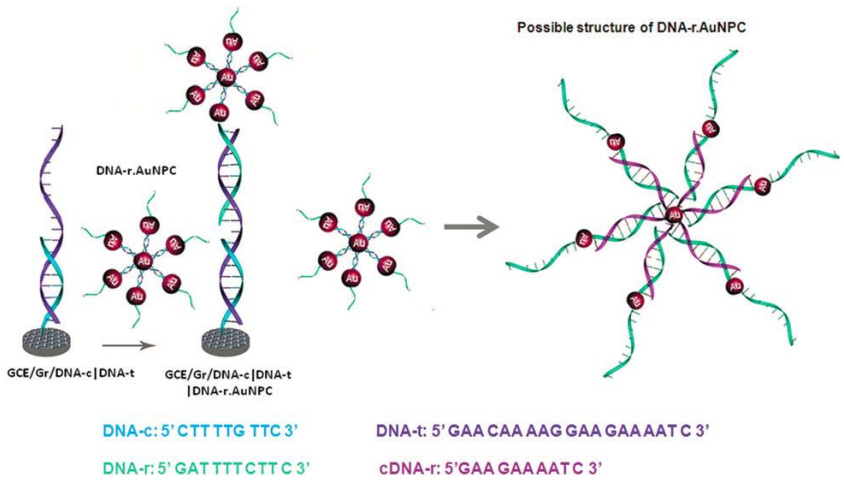

Fig. 8. *Schematic diagram for fabrication process hybridization application of DNA biosensor.*

2.2 Label-free electrochemical detection of DNA hybridization

One of the key obstacles of the label-based DNA sensor concepts discussed above is the requirement for an indicator to transduce the hybridization. A number of researchers, however, have begun developing label-free methods of determining hybridization involving electrochemical methods. Attractive attention has been given recently to direct label-free electrochemical detection schemes, in which the hybridization triggers a change in an electrical signal. Such protocols greatly simplify the sensing platform protocol because they eliminate the need for the indicator addition, association and detection steps and offer an instantaneous detection of the duplex formation. Such direct, *in situ* detection can be accomplished by monitoring changes in the intrinsic redox activity of the nucleic acid target or probe or changes in the electrochemical properties of the interface.

2.2.1 Direct detection based on redox properties of DNA bases

Observation of redox peaks of DNA bases, due to reduction and oxidation reactions, leads to monitoring of DNA hybridization. The most electroactive bases of DNA are guanine and adenine. Direct detection was reported for the first time by Palecek[34],[35]. The author monitored DNA hybridization through reduction of DNA nucleotidic bases (Fig. 9).

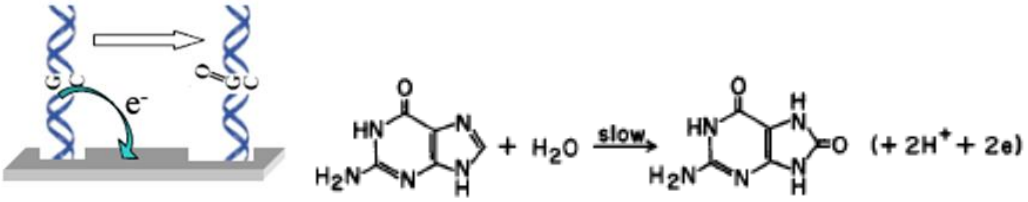

Fig. 9.*. Schematic presentation of biosensor based on redox properties of DNA and reaction of oxydation of guanine*

This strategy can serve for DNA detection and quantification. For example, Bollo et al., studied the oxidation peak of guanine at about 1 V after accumulation of DNA at open circuit potential on the electrode surface[36]. Additionally for signal amplification, the surface was modified with carbon nanotubes entrapped in chitosan. They obtained a linear relationship between amount of DNA and current corresponding to oxidation signal of guanine with 90.0 ppm dsDNA. However compulsory application of high potential for DNA oxidation is a drawback of this method.

2.2.2 Direct detection based on redox properties of redox markers in solution

In recent years, the sensitively label-free sensing technique of electrochemical impedance (EIS) is a useful tool for analyzing changes in interfacial properties of modified electrodes induced by binding of charged biomolecules on the surfaces. The changes in signal of different types of redox markers in solution near the electrode were detected by EIS. According to the charge properties of transduces, the choice of the redox markers possessing different charges, negatively, neutrally or positively, has large effect on the performance of biosensors.

Cui et al[37] developed a highly sensitive and selective electrochemical DNA hybridization sensor (Fig. 10) for breast cancer marker BRCA1 by using the sensitively label-free sensing technique of electrochemical impedance spectroscopy (EIS). Capacitance and electrical resistance of the electrode surface are the sensitive indicators and their modulations are related to the surface property variations. It is commonly known that the reasons for EIS response change are mainly owing to the charge effect and the steric hindrance impact. In order to verify the main reason for the EIS change after the hybridization, two redox markers were applied in these EIS tests, a positively charged complex $[Ru(NH_3)_6]^{3+}$ and a negatively

one $[Fe(CN)_6]^{3-/4-}$. The increased R_{ct} in negatively charged and decreased R_{ct} in positively charged demonstrated that the charge effect due to the strong negative charge of the DNA target played a key role in the measured electrochemical EIS signal with redox markers. Significantly, this developed biosensor strategy achieved a linear detection range from 1.0 FM to 10.0 pM with a limit of detection of 0.3 fM, when negatively charged $[Fe(CN)_6]^{3-/4-}$ as indicator[36] are applied.

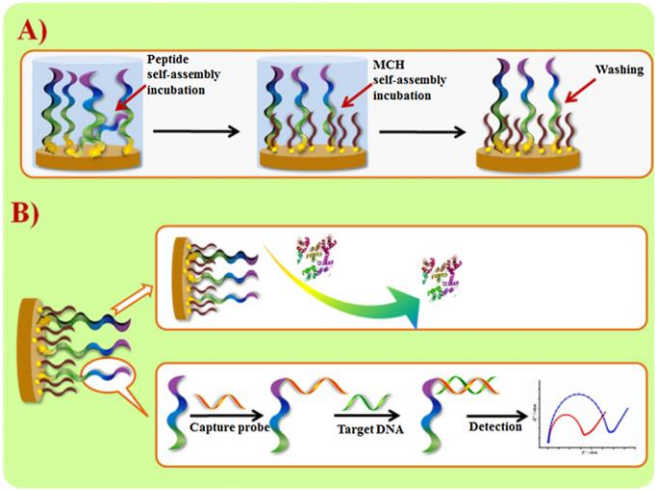

Fig. 10.*. (A) Schematic illustration of Peptide SAM formation on Au electrode surface. (B) DNA sensor fabrication and sensing procedures*

Zhu et al. has developed a novel protocol for development of electrochemical DNA sensor based on thionine-graphene (Th-G) nanocomposite modified gold electrode[38]. An amino-substituted ssDNA probe was covalently grafted onto the surface of the thionine-graphene nanocomposite by the cross-linker glutaraldehyde (GA). The hybridization reaction on the modified electrode was monitored by differential pulse voltammetry analysis (DPV) using an electroactive daunomycin, in solution, as the redox indicator (Fig. 8). Under optimum conditions, the proposed biosensor achieved a wide range of $1.0x10^{-12}$ to $1.0x10^{-7}$ M with a good linearity (R_2 = 0.9976) exhibiting high sensitivity and low detection limit of $1.26x10^{-13}$ M (S/N = 3). In addition, the biosensor was highly selective to discriminate one-base or two-base mismatched sequences (Fig. 11).

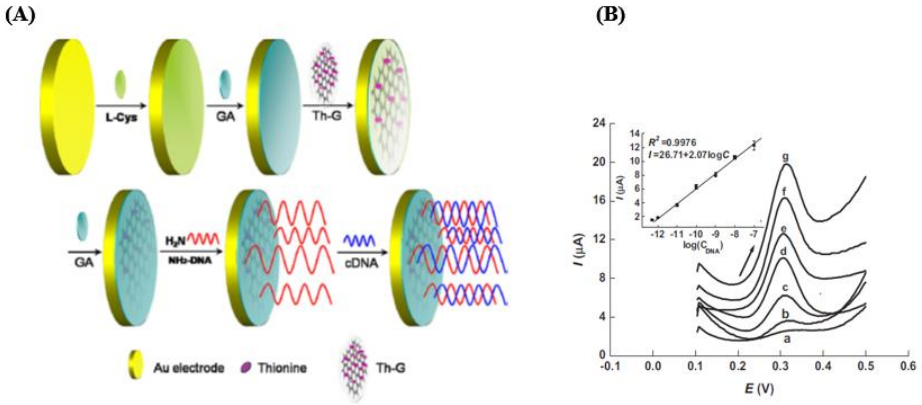

Fig. 11. *Schematic diagram of covalent immobilization of ssDNA probe on Th-G nanocomposite*

Li et al.[39]s elaborated the working mechanism of label-free electrochemical DNA sensor to detect DNase I activity (Fig. 12) by monitoring the redox signal of the methylene blue (MB) which well known to bind the guanine bases of DNA via intercalation process[44], before and after specific hydrolysis of DNA sequence. The SWV signals were linearly related to the different concentrations of DNase I

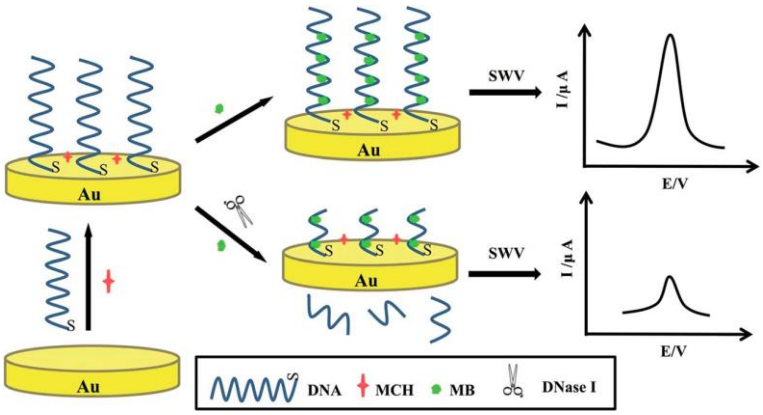

Fig. 12. *Schematic diagrams of the detection of DNase I activity based on electrochemical method.*

Regarding literature different redox indicators or DNA-binding intercalators were used for the development of label-free DNA sensors which are resumed in the Table 1.

Table 1 *DNA sensors developed with different indicators or intercalations*

Indicators /intercalators	**Method**	**Range**	**Sensitivity**	**Reference**
$[Fe(CN)_6]^{3-/4-}$	EIS	1.0 fM to 10.0 pM	0.3 fM	Bollo et al.[36]
$[Fe(CN)_6]^{3-/4-}$	EIS	2×10^{-12} to 2×10^{-6} M	3.2×10^{-13}M	Bo et al.[40]
$[Fe(CN)_6]^{3-/4-}$	EIS	1×10^{-11} to 1×10^{-14} M	5.4×10^{-15}M	Radhakrishnan et al.[41]
daunomycin	DPV	1.0×10^{-12} to 1.0×10^{-7} M	1.3×10^{-13}M	Zhu et al.[38]
MB	DPV	1.0×10^{-13} to 1.0×10^{-8} M	3.2×10^{-15}M	Huang et al.[42]
$[Ru(NH_3)_6]^{3+}$	DPV	1×10^{-10} to 1.0×10^{-7}M	3.5×10^{-11}M	Wang et al.[43]
$[Ru(bpy)_3]^{2+}$	CV	180 pM to 90 nM	90 pM	Yan et al. [44]
$[Co(phen)_3]^{3+}$	DPV	5.0×10^{-12} to 1.0×10^{-9}M	4.3×10^{-13} M	Liu et al.[45]

Thus label-free monitoring of bio recognition events provides a promising platform, which is simple, cost-effective, and requires no external modification of the biomolecules. The other essential role of the sensor is the choice of the transducer which provides a suitable platform that facilitates the immobilization of the DNA probe and provided a significant signal for electronic readout when hybridized DNA complex are formed. Recent researches are focus on the combination of different nanomaterials, with which endow additional properties as well as analytical performance of biosensors

3. Transducers for DNA sensor

Nowadays, in order to develop the higher requirement of DNA analysis, numerous nanomaterials have been employed significantly to construct electrochemical biosensors with the novel sensing platforms to improve the recognition property of the sensing layer and the signal output intensity of the sensing event for enhanced performance[29,51]. Some of them will be described in this document including polymers, nanoparticles or nanomaterials based on carbon materials. In each case, different and original approaches for immobilization of

ssDNA probes on the transducer surface have been employed such as adsorption[52], self-assembly [53,54], covalent binding[55,56], biotin -avidin interactions[57] and entrapment in a polymer matrix[58] .

3.1 Polymers

A class of organic polymers, known as conducting polymers (CPs), has become increasingly popular due to its unique electrical and optical properties. Several CPs are known to interact with biological samples while maintaining good biocompatibility and hence, CPs are applied for use in a numerous biological and medical applications[46].

For example, Li et al. prepared a new type of conjugated CP, poly(indole-5-carboxylic acid) (PICA), on GCE by means of anodic oxidation (Fig. 13)[47]. PICA exhibited optimal electrochemical behavior and thermal stability, with a conductivity of 10^{-2} S/cm and high redox activity compatible with the concept of molecular-wire transduction. The PICA-modified sensor showed comparable sensitivity and its detection limit was 1.0 nM, which can be further improved by increasing the side chain length because longer side chains permit greater freedom of movement and more enhanced hybridization[48].

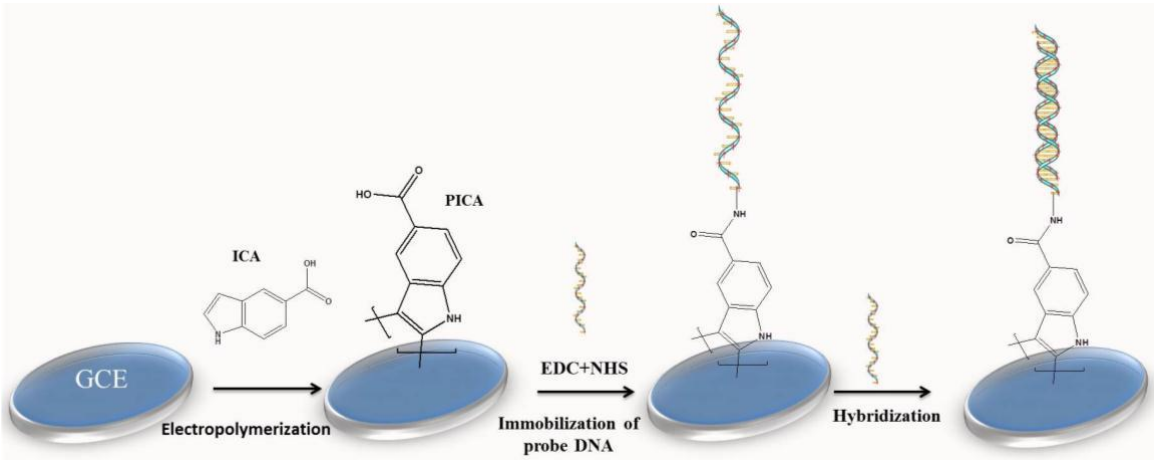

Fig. 13. *Schematic representation of the preparation of an electrochemical DNA sensor based on a poly(indole-5-carboxylic acid) (PICA) conducting polymer*

The summary of DNA sensors based on CP or CPC* were shown in Table 2.

***Table 2** DNA sensors based on CP or CPC**

No	Matrix	Range	Sensitivity	Reference
1	Polypyrrole	3.7 to 370 nM	1 nM	Peng et al.[49]
2	polyaniline	100 fg.mL^{-1} and 1 ng.mL^{-1}	100 fg.mL^{-1}	Davis et al.[50]
3	Boron doped diamond modified polyethylimine	10^{-19} g.L^{-1} to 1 ng.L^{-1}	10^{-19} g.L-1	Weng et al.[51]
4	Poly 5-carboxyindole	1.0×10^{-8} to 1.0×10^{-18}M	1.0×10^{-17} M	Mohan et al.[52]
5	Polyaniline/polyacylate modified Boron doped diamond	2.0×10^{-7} to 5.0×10^{-8}M	2.0×10^{-8}M	Gu et al.[53]

*CPC: conducting polymer composites consist of one or more non-conducting polymers and conductive-filler materials distributed throughout the polymer matrix.

3.2 Nanoparticles

Nanoparticles have numerous possible applications in biosensors. For example, functional nanoparticles bound to biological molecules (e.g. peptides, proteins, nucleic acids) have been developed for use in biosensors to detect and amplify various signals.

Electrochemical detection of DNA target immobilized on gold nanoparticles self-assembly modified electrode has been reported by Wang et al. (Fig. 14)[54] Self-assembly of colloidal Au onto a cystamine modified gold electrode can enlarge the electrode surface area and enhance greatly the amount of immobilized ssDNA. The electron transfer process of $[Fe(CN)_6]^{4-/3-}$ on the gold surface was investigated by EIS and evaluated in the range of 10-800 pM with a detection level as low as 5 pM.

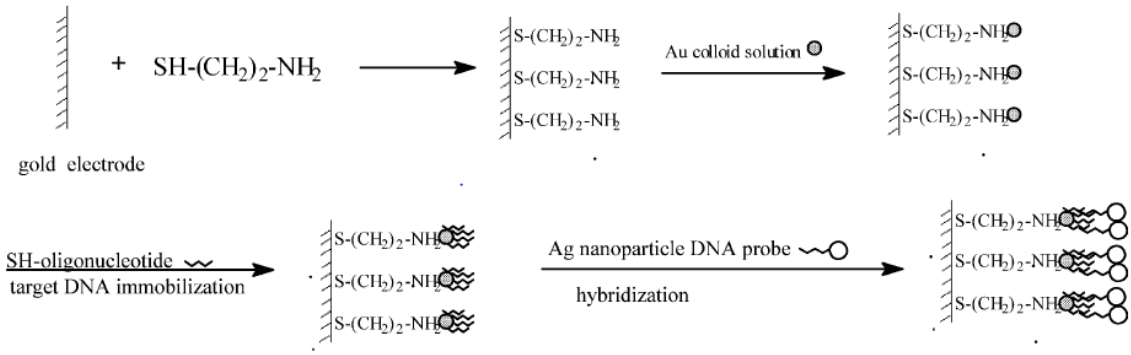

Fig. 14. *Schematic illustration of the process of the immobilization of DNA onto the gold electrode*

The electrochemical oxidation signal of Au nanoparticles anchored on a probe enabled the detection of factor V Leiden mutation in PCR samples[55]. Kerman et al. has reported that the unique binding event between *Escherichia coli* ssDNA binding protein (SSB) and single-stranded oligonucleotides conjugated to gold (Au) nanoparticles was utilized for the electrochemical detection of DNA hybridization (Fig. 15).[56]

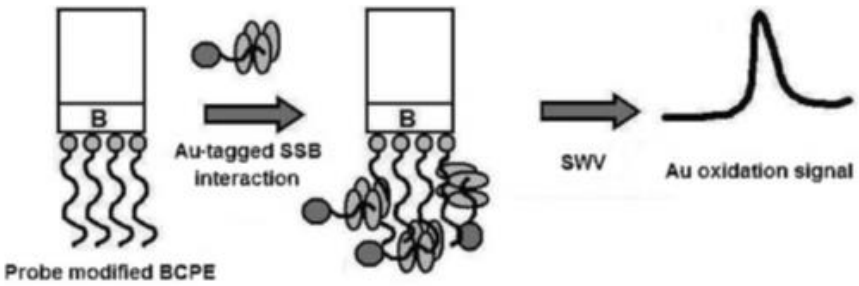

Fig. 15. *Schematic illustration of the hybridization detection protocol*

3.3 Association of nanoparticles and polymers

To further improve the performance of sensors combining various properties of materials, nanocomposites have attracted more attention in recent years.

Nanoparticles could embedded into porous over polymer film [68] that increase the electron transfer between the solution and the electrode, increase the immobilization surface of biomolecules on polymer. Feng et al.[57] reported the fabrication of a nano-porous

CeO_2/chitosan composite film as the immobilization matrix for colorectal cancer DNA sequence. Such matrix combined the excellent film forming ability of chitosan as a natural cationic polymer and the affinity of nano-CeO_2 towards the oxygen of DNA in addition to its good biocompatibility, nontoxicity and electronic conductivity. After hybridization, differential pulse voltammetry (DPV) was used to record the signal response of methylene blue (MB) which demonstrates different affinity for ssDNA and dsDNA. The established electrochemical DNA sensor has a relatively wide detection range from 1.59×10^{-11} to 1.16×10^{-7} M and the ability to discriminate completely complementary target sequence and four-base-mismatch sequence.

Nanoparticles of silver were combined with nanotubes of polypyrrole and poly(3,4-ethylenedioxythiophene) (PPy-PEDOT) and have been investigated by Radhakrishnan[38] for the sensing of DNA hybridization using EIS as the detection method. The dynamic detection range was observed from 1×10^{-11} to 1×10^{-14} M with a detection as low as 5.4×10^{-15} M (Fig. 16).

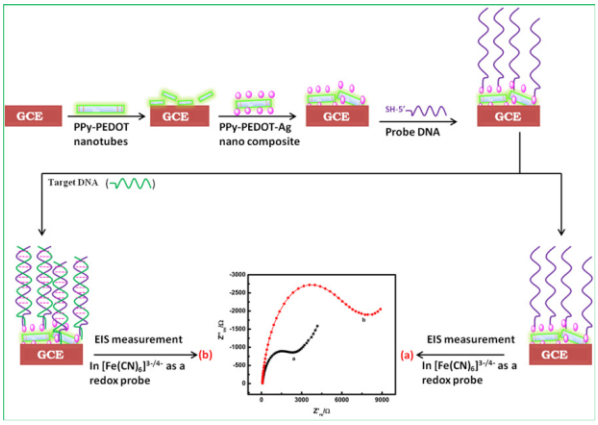

Fig. 16. *Schematic illustration of PPy–PEDOT–Ag nanocomposite*

Many others examples of association of nanoparticles with polymers, were described in the literature, and integrated into DNA sensors for the detection of different analytes. These biosensors demonstrated good performance. Some examples are presented in the table below (Table 3).

Table 3 *DNA sensors based on Polymer-nanocomposites (PNCs) modified electrode*

polymer combined with nanoparticles	**Analyte**	**LOD**	**Reference**
PANI-chitosan	Hydroquinone	9.7×10^{-7}M	Tang et al.[58]
PANI-AuNPs	DNA sequence associated with *S. aureus*	150 pM to 1 µM	Spain et al.[26]
PEDOT-AuNP	DNA sequence associated with *S. aureus*	150 pM to 1 µM	Spain et al.[59]
PPy-PANI-AuNPs	15 - mer DNA oligonucleotides	1.0×10^{-13} M	Wilson et al.[60]
PPy-PEDOT-AgNPs	27 - mer DNA oligonucleotides	5.4×10^{-15} M	Radhakrishnan et al.[41]
PPy-AuNPs	Designed target DNA from *Lactococcus* gene	8.4×10^{-13} M	Nowicka et al.[61]
PPy-MWCNT-AuNPs	*Avian influenza* virus H_5N_1	4.3×10^{-13}M	Liu et al.[45]

Among different nanomaterials, carbon nanomaterials hold potential promise as a material for designing a new generation of biosensors due to their unique characteristics.

3.4 Carbon materials

Carbon is an abundant element playing a major role in the chemistry life[70]. Various carbon allotropes exist including diamond (the carbon atoms are bonded together in a tetrahedral lattice arrangement, 3D), graphite (the carbon atoms are bonded together in sheets of a hexagonal lattice, 3D), graphene (2D), carbon nanotubes (single-walled carbon nanotubes (SWCNT) and multi-walled carbon nanotubes (MWCNT), 1D), and fullerenes (the carbon atoms are bonded together in spherical, tubular, or ellipsoidal formations, 0D) (Fig. 17). They all possess the capacity to hybridize into sp, sp^2 and sp^3 configurations with narrow gaps between their 2s and 2p electron shells and have very different physical and electrochemical properties such as wide potential windows, good electrocatalytic activity for many redox reactions [58,62,63].

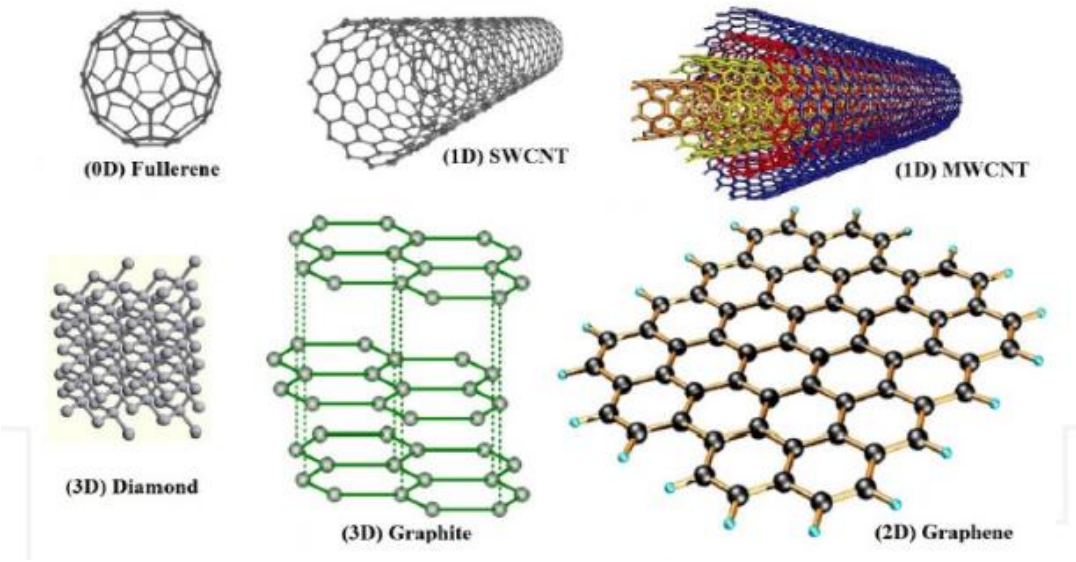

Fig. 17. *Different allotropes of carbon*[63]

These unique properties are responsible for enabling the design of versatile carbon-based nanomaterials for the sensitive detection of biological compounds and paving their way to many areas of biomedical research, including drug delivery systems, tissue scaffold reinforcements, and electrochemical sensors.

3.4.1 C_{60}

Fullerenes (C_{60}) due to its unique and favorable characteristics of easy chemical modification, conductivity, and electrochemical properties, has tremendously used in biosensor applications. Hang et al. fabricated a novel DNA sensor based on polyhydroxylated fullerenol (FLN) as the probe DNA immobilization platform which could be stabilized with thioglycolic acid (TGA) via covalent interaction (Fig. 18). Due to 3D FLN spherical structure with plenty of grafting sites (-OH), the amount of probe DNA was greatly amplified and remained flexible. This promotes the sensing interface and the hybridization with the DNA target. Authors observed with a such DNA sensor a wide linear range from 1.0 fM to 1.0 nM with a detection limit down to 0.17 fM in target DNA detection.[64]

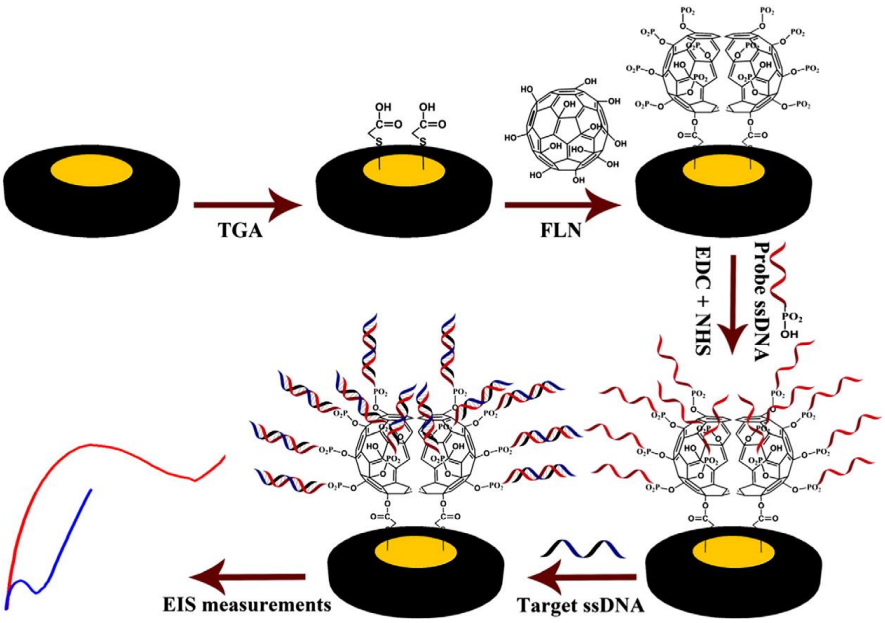

Fig. 18. *Illustration for the construction and detection strategy of the FLN-based DNA sensor*

3.4.2 CNTs-based materials

Carbon nanotubes (CNTs) due to their apparent electrical conductivity, large surface area, and low cost have been attracted more attention in recent years.

DNA oligonucleotides can be immobilized onto the CNT-based electrode through physical absorption or ionic adsorption through a composite of polymer and CNT [65]. However, covalent attachment plays more important role in CNT-based DNA electrochemical sensors as it lead to stable immobilization of DNA on CNT. Cai et al. [66] first reported the use of CNTs to fabricate an electrochemical DNA sensor for the specific DNA detection. A DNA probe with amino group at its 5'-phosphate end (NH_2-ssDNA) was covalently bonded onto the CNTs-COOH-modified glassy carbon electrode (GCE) surface. CNT-modified electrode allows fast electron transfer between electrode and the redox intercalator daunomycin (Fig. 19). The detection limit achieved is 1.0×10^{-10}M for complementary DNA.

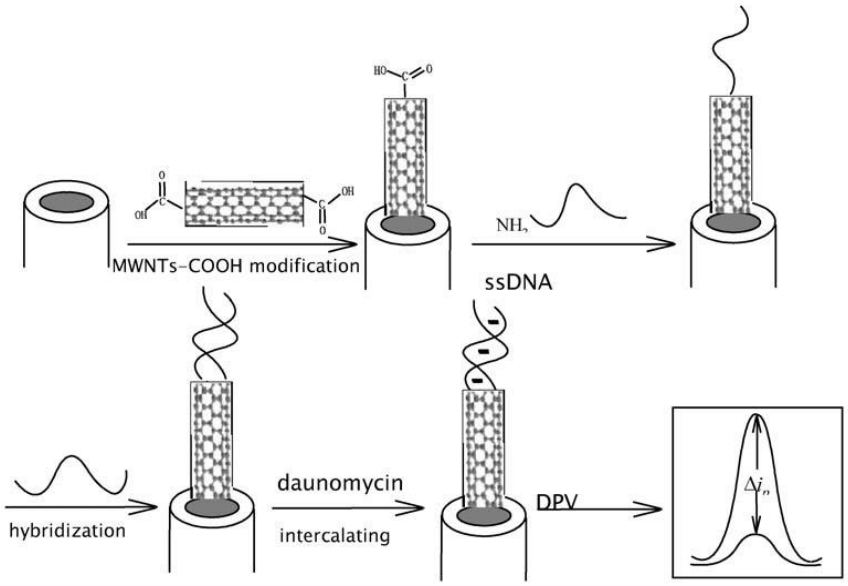

Fig. 19. *Schematic representation of the enhanced electrochemical detection of DNA hybridization based on the MWNTs–COOH constructed DNA biosensor*

A DNA biosensor based on composite of CNT and other materials are also studied by various groups for development of E-DNA biosensors. CNT natube could be used to improve the stability of the biosensors or to improve the electron transfer ability. For example PANI-Fe_3O_4-CNT nanocomposite has been fabricated for the detection of DNA probe of *Neisseria gonorrhoeae* (Fig.20). This modified sensor then treated with avidin and biotinylated oligonucleotides related to the gene of *N. gonorrhoeae* with methylene blue (MB) as electroactive indicator. Using differential pulse voltammetry, the developed sensor showed high sensitivity with wide concentration range from 1×10^{-19} M to 1×10^{-6} M. Author reported that the aggregation of Fe_3O_4 nanoparticles due to its high surface area and magnetic dipole interaction between nanoparticles limite their application in biosensors field. They overcome this drawback by dispersing Fe_3O_4 nanoparticles in PANI-CNT composite and CNT worked as templates for the coating of Fe_3O_4 and PANI with minimum aggregation [67].

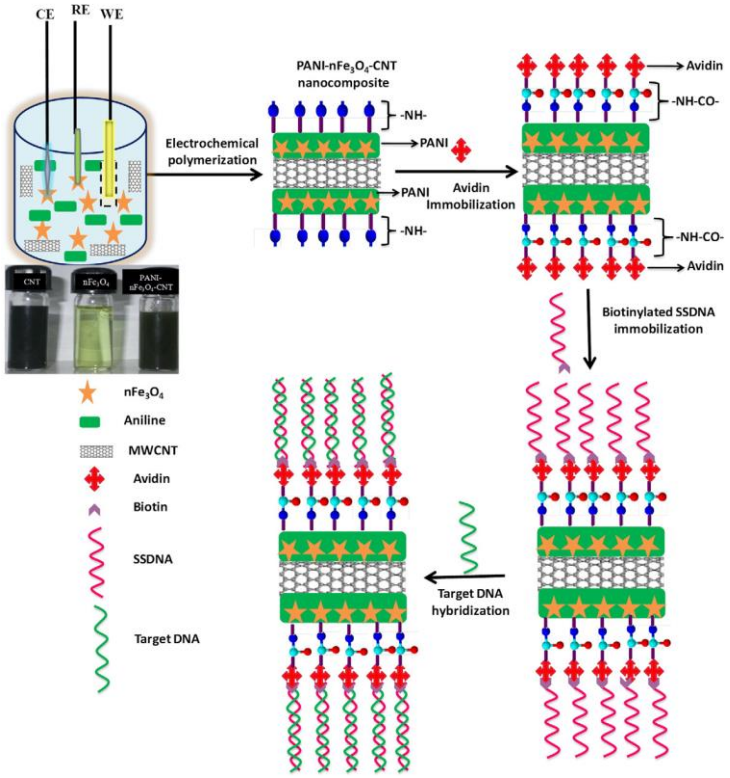

Fig. 20. *A schematic diagram depicting the preparation of PANI–nFe_3O_4–CNT nanocomposite*

Another example use MWCNTs to improve electron transfer ability in amperometric biosensors. Thus nanomaterial composed of MWCNTs coated with PPy acting as a transducer and redox dendrimers amplifying the electrochemical signal were reported a novel approach for highly sensitive amperometric detection of DNA. The biosensor was able of discrimination of DNA extracted from M. tuberculosis with single nucleotide polymorphism mutation which affair a drug resistance.[68] Improved electron transfer has been demonstrated compared to chemically modified surfaces, due to a homogeneous distribution of redox-active ferrocene bounded on the surface. The schematic represent of biosensor based on MWCNTs coated with PPy was shown in Fig. 21.

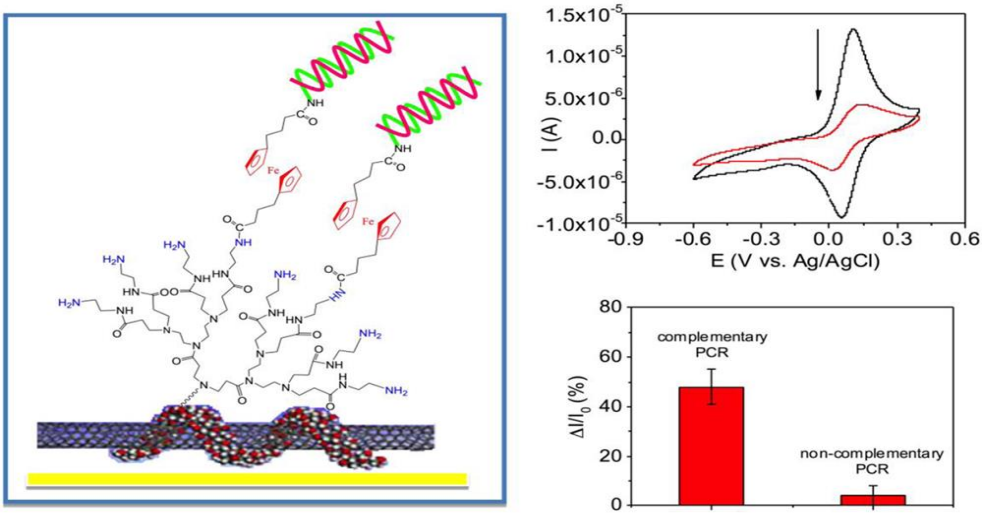

Fig.21. *Schematic represent of biosensor based on* MWCNTs coated with PPy

Despite many advantages and successful applications in biomedical engineering, there is a growing concern for safety with CNTs. Some recent studies have reported that the increased cytotoxicity of CNTs has been attributed to their agglomeration, induced oxidative stress, and incomplete removal of metal catalysts used to prepare CNTs[69–71]. In comparison with carbon nanotubes (CNTs), graphene is an ideal nanomaterial for various applications due to two obvious advantages superior to CNTs are shown as follows: 1. Graphene does not contain metallic impurities as CNTs do. In many cases, such impurities dominate the electrochemistry of CNTs and lead to misleading conclusions. 2. the production of graphene can be achieved using graphite that is cheap and accessible[72]. The properties of graphene are present in details in CHAPTER II.

CHAPTER II: Graphene

1. Introduction- history

Graphene was discovered in 2004 by Geim and Novoselov[73] and was isolated by mechanically cleaving of a graphite crystal. Graphene is a two-dimensional single layer of sp^2 hybridized carbon atoms arranged in a honeycomb lattice. It is also the base structure of all graphitic materials including graphite, carbon nanotubes and fullerenes (Fig.22).

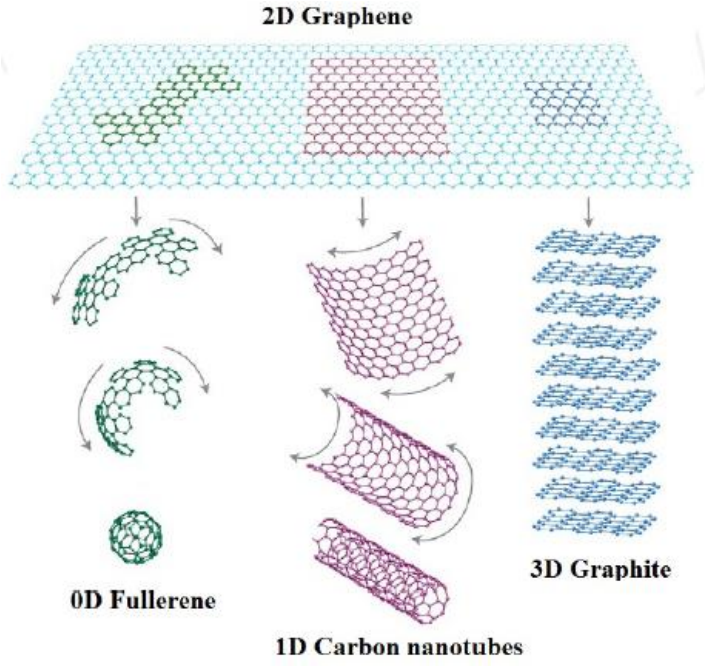

Fig. 22. *Basis of all graphitic forms. Reprinted form* ref [74]

Graphene has numerous electronic, mechanical, thermal, optical and chemical properties that make it a promising nanomaterial for use in energy-storage materials[75], drug delivery system[75], biosensors [76], polymer composites [62], liquid crystal devices[77], super-capacitors[78], nanoelectronics[79] and others. The Table 4 below lists some main

characteristics and properties of graphene compared to fullerene and carbon nanotubes one dimension [74].

Table 4 *Important parameters of carbon materials of different dimensionalities*[74].

Isomer	Graphene	Fullerene	Carbon nanotube
Dimension	2D	0D	1D
Hybridization	sp^2	sp^2	sp^2
Density (g/cm^3)	2.26	1.72	1.2-2.0
Bond length (Å)	1.42 (C=C)	1.40 (C=C) 1.46 (C-C)	1.44 (C=C)
Electronic properties	Zero-gap Semiconductor (~ 7200 S.m^{-1})	Semiconductor Eg=1.9 eV	Meta/semiconductor Eg=~0.3-1.1eV
theoretical specific surface area	(~ 2630 m^2 g^{-1})		
thickness of graphene	0.35 to 1.00 nm		

2. Graphene synthesis and its derivatives

A variety of methods have been developed to synthesize single or few-layer graphene sheets[80]. It is recently known that graphene can be grown via several different methods, which can be divided into two categories including epithaxial technique and the exfoliation methods. For each synthesis, the challenge remains to achieve complete and homogeneous dispersion of individual graphene sheets in various solvents[81]. Indeed, graphene sheets tend to form irreversible agglomerates through Van der Waals interactions due to their conjugated and planar structure. So, the prevention of aggregation is essential for graphene sheets because most of their unique properties are only associated with individual sheets.

2.1 Epithaxial technique

According to the different application of substrates, epithaxial technique was classified into two groups: metallic substrate and non-metallic substrate. Fig. 23 illustrates typical epithaxial processes. The hydrocarbon molecules (called E) are

deposited on the surface, undergo decomposition via a series of dehydrogenation reactions giving rise to various C_xH_y species shown as E_d, and H atoms. The new species are all able to diffuse across the surface. Smaller carbon species M and D form and diffuse on the surface, aggregating into larger clusters C. H atoms of the original molecule migrate on the surface, and form H_2 molecules which evaporate from the surface. Finally, some of the species like M and D, or even their bigger clusters C, may attach to the island G at its edge.

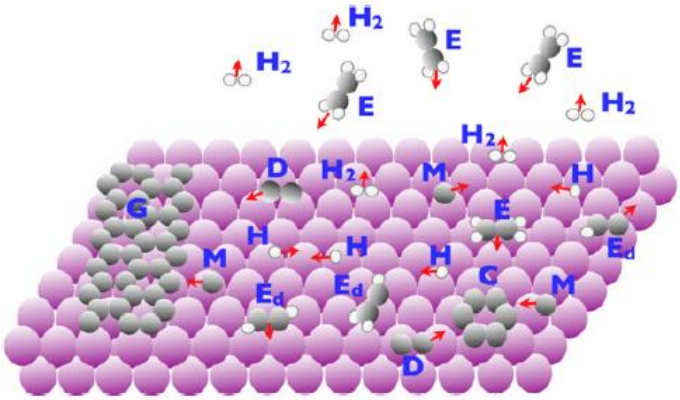

Fig. 23. *Schematic representation of typical epithaxial processes*

Chemical vapor deposition (CVD) is a thermal method based on growth of graphene by dissolving carbon atoms onto a catalytic metallic substrate, such as Ni, Cu, Co, Pt, Ir and followed by precipitating out after cooling to form large-scale graphene films[82]. The carbon atoms comes from a carbon-containing gas such as methane, ethane, or propane, decomposed at high-temperature. For example, the schematic representation of CVD process on Ni substrate was shown in Fig. 24. This technique was used to fabricate multilayer graphene nanoflake films[83,84], but the films are actually composed of 2-3 nm thick graphite nanoflakes rather than a single sheet. Meanwhile, it requires additional transfer steps to fabricate the devices, since the CVD graphene is produced on certain metallic substrates, leading to contaminations and destruction of graphene sheets.

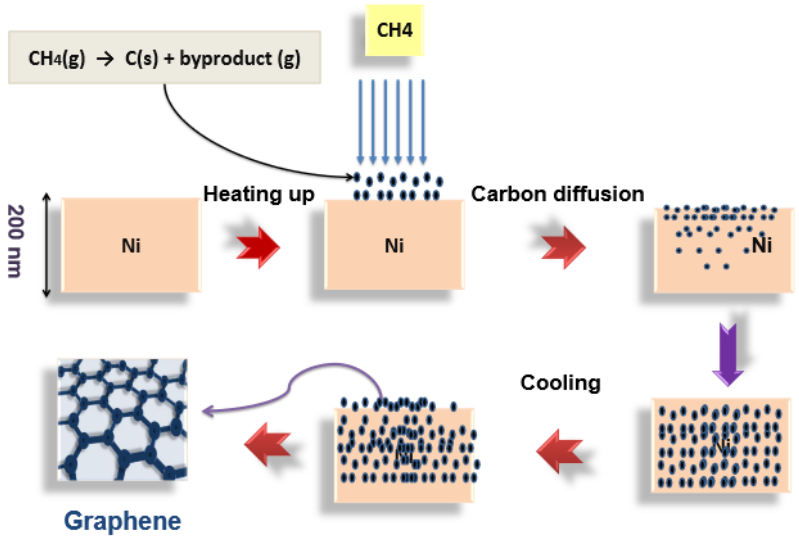

Fig. 24. *Schematic representation of CVD processes on Ni substrate*

Efforts are also made to grow graphene on silicon carbide (SiC) wafers via sublimation of silicon atoms[85], which allows the production of a large area of single layer of graphene with a high yield up to 95%, a high conductivity and high-quality (Fig. 25A). The thermal decomposition of SiC appears the most promising from the perspective of electronic device fabrication, thanks to its direct-growth process on a semiconductor surface, and the extent of control on number of layers, quality, and uniformity obtained. However, bulk SiC substrates present limitations in terms of costs, sizes, and difficulty in micromachining.

Direct growth of graphene on hetero-epitaxial cubic silicon carbide (3C-SiC) on silicon (Si) substrate would overcome above-mentioned limitations[86,87](Fig. 25B). Two major advantages by associating with Si are first, 3C-SiC on Si substrate wafers are at the moment less expensive than 3C-SiC by orders of magnitude, large size up to 12 inches could be obtained and finally, the Si-based substrate provides easy access to integrated circuit technology and infrastructure. However, in the case of silicon carbide on silicon, the quality of the graphene film produced in high/ultra-high vacuum is limited due to the difficulty in controlling sublimation rates at relatively low temperature. In compared to the exfoliated graphene, a considerably higher I_D/I_G ratio about ~1 was indicated by Raman[88,89].

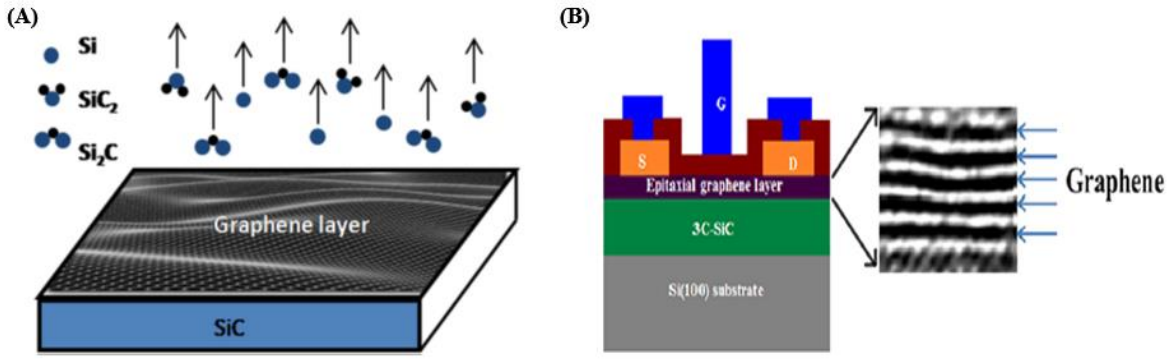

Fig. 25. *(A) Growth of epitaxial graphene on silicon carbide wafer (B) 3C-SiC on Si substrate wafer via sublimation of silicon atoms*

2.2 Exfoliation methods

2.2.1 Physical mechanical exfoliation

Mechanical exfoliation is a simple peeling process from a commercially highly oriented pyrolytic graphite (HOPG) sheet (Fig. 26A). This technique, also called "scotch-tape" method was first employed by Novoselov et al.[90,91]. For fundamental research, this kind of graphene is incontrollable in shape, size and location. Hence the yield of devices is extremely low, and such pristine graphene is more suitable only for theoretical study and proof-of-concept demonstration. Graphite can also be exfoliated in presence of small molecules (*N*-methyl-pyrrolidone[92] or surfactant sodium dodecylbenzene sulfonate, SDBS)[93] that intercalate between the layers of graphite to produce monolayer graphene. (Fig. 26B) However, the disadvantage of this process is the high cost of the solvent.

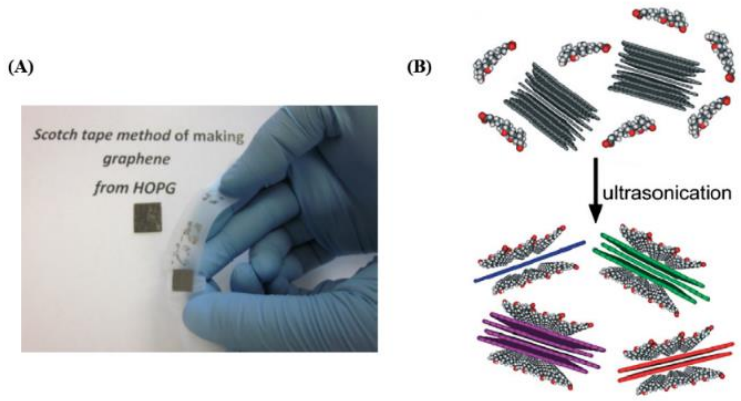

Fig. 26. *Schematic illustration of the graphene exfoliation process*

2.2.2 Electrochemical exfoliation of graphite

Electrochemical techniques are alternatively used to produce graphene flakes because they are simple, economic, non-destructive, environmentally friend, operates at ambient temperature and pressure, and the thickness which could be controlled by adjusting the electrode potential. In recent years, some researchers have attempted to produce graphene sheets by using electrochemical exfoliation of graphite anode, which was first reported by Lotya et al. in 2008[93]. Liu et al.[94] used a mixed solution containing ionic liquid 1-octyl-3-methyl-imidazolium hexafluorophosphate and water as electrolyte. Through intercalation of PF_6- ions into the graphite anode assisted by oxidation of graphite edges by hydroxyl radicals, a dispersion containing graphene was obtained (Fig. 27). Alanyalıoğlu et al. controlled the thickness and order of graphene by using surfactant-assisted electrochemical processes at different intercalation potentials of 1.3, 1.4, 1.6, and 1.8 V vs. Pt[95].

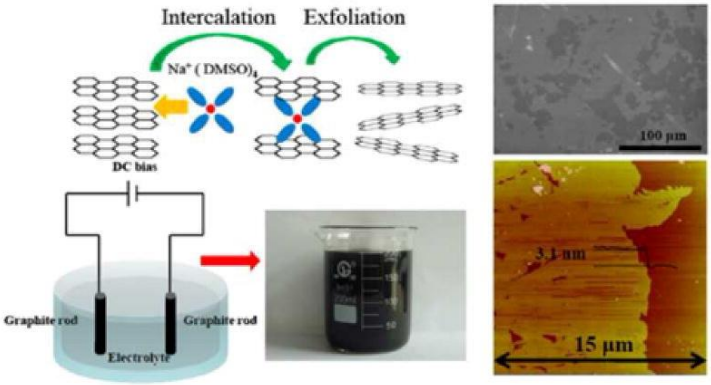

Fig. 27. *Schematic illustration of the graphene exfoliation process by electrohemical techniques*

2.2.3 Chemically oxidized to GO and then reduced to RGO

The pristine graphite sheet is atomically flat with the Van der Waals thickness of ~0.34 nm. Graphene oxide sheets obtained from graphite are thicker due to the displacement of sp^3 hybridized carbon atoms slightly above and below the original graphene plane and presence of covalently bound oxygen atoms. This method is based on the oxidative exfoliation of natural graphite to graphene oxide (GO) followed by its reduction. Thus, this method is expected to obtain single layer. The reduction of GO sheets to RGO can be reduced via electrochemical, chemical or thermal reduction to restore the π-conjugated structure and conductivity. This is one of the most efficient methods for low-cost and large-scale production of single layer graphene [96] [97,94]. In this case, Graphite oxide is usually synthesized through the oxidation of graphite in the presence of strong oxidants including concentrated sulfuric acid, nitric acid and potassium permanganate based on Hummers method [88] or modified Hummers' method [96,98,99]. The graphite oxide is decorated by hydroxyl and epoxy functional groups on the hexagonal network of carbon atoms with carbonyl and carboxyl groups at the edges. Graphite oxide is highly hydrophilic and forms stable aqueous suspensions due to the large number of oxygen-containing functional groups as well as the repulsive electrostatic interactions at the edges of the platelets[100,101].

Zhang et al. has reduced graphene oxide film electrochemically by cyclic

voltammetry technique in 6 M KOH aqueous solution. The ratio of oxygen/carbon content was significantly decreased after electrochemical reduction[102]. The drawback of this reduction is the intensive alkaline solution, which is adhesive and difficult to remove. More recently, many researches have been reported the conversion of graphene oxide (GO) into chemically reduced graphene oxide (CRGO) by chemical treatments[103,104,105]

Chemical reduction of GO sheets has been performed with several reducing solvents including hydrazine[106,107,108] and sodium borohydrate[109,110]. The re-establishment of the conjugated graphene network could be attributed to the reaction pathway proposed by Stankovich et al[100,111] (Fig. 28) However, the carboxylic acid group were unlikely reduced by hydrazine. Another possible route GO was preformed using sodium borohydrate ($NaBH_4$) in aqueous solution, where sodium borohydrate is more effective than hydrazine as a reductant although it can be hydrolyzed by water slowly. The C/O ratio was as high as 13.4:1 compared to 6.2:1 for hydrazine.

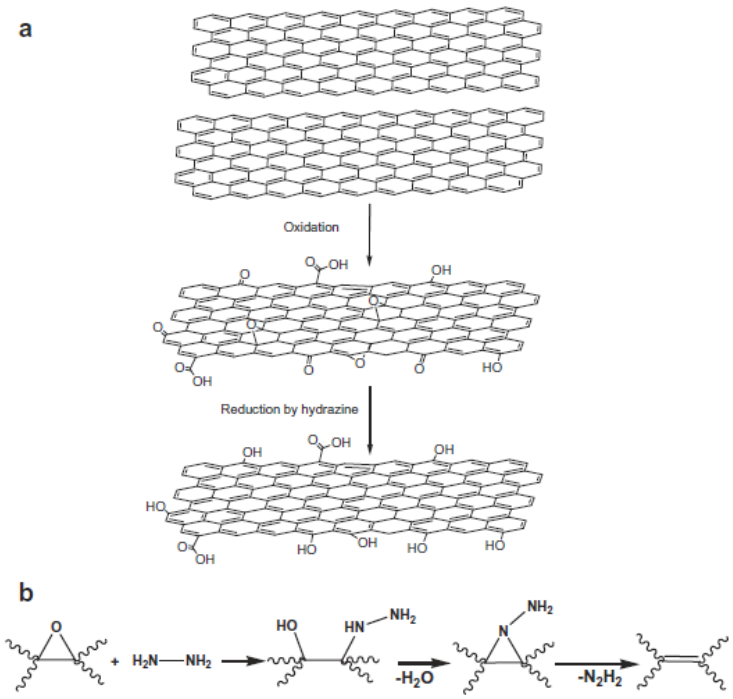

Fig. 28. *(a) Oxidation of graphite to graphene oxide and reduction to reduced graphene oxide. (b) A proposed reaction pathway for epoxy reduction by hydrazine.*

Thermal reduction is another approach to reduce GO to reduced graphene oxide.

It utilizes the heat treatment to remove the oxide functional groups from graphene oxide surfaces. Aksay's group have exfoliated and reduced stacked GO by heating GO to 1050 ℃, where oxide functional groups were eliminated as carbon dioxide[85,112]. It was calculated that high pressure as high as 2.5 MPa was required to separate GO sheets by numerically evaluating the Hamaker constant while the pressure generated during the exfoliation was 1-2 orders of magnitude higher. Although the thermal reduction can produce 80% single layer RGO, the left vacancies and structural defects may affect the electrical and mechanical properties of RGO. However, the conductivity was measured to be 1000-2300 S/m, suggesting the effective reduction and restoration of electronic structures from GO.

Recently, Dubin et al. elaborated a simple one-step solvothermal reduction method to produce reduced graphene oxide by thermal deoxygenation of GO at 200 ℃ refluxing in N-methyl-2-pyrrolidinone (NMP) as reductant agent. The RGO layers remained in a stable dispersion after the reaction. This approach provides a simple, low-temperature method to produce reduced graphene oxide, which is considered as an excellent way to synthesize RGO, in spite of structural defects inevitably as indicated by Raman spectroscopic studies[104].

One of the challenge in the development of graphene-based sensor devices is that graphene or reduced graphene oxide (RGO) are hydrophobic and tend to agglomerate in water, and even restack to form graphite owing to van-der Waals interactions and strong π-π stacking[113,114]. As a result, considerable effort has been expended in improving the compatibility and dispersion of graphene. Recently, a vast majority of researches on the enhancement of dispersion and self-assembly properties of RGO was focus on the modification and entrapment of functional moieties tuning graphene's dispersion and performance to achieve the best performance of DNA sensors, which will be elaborated in next section. In this respect, a majority of work to make RGO a viable option for applications through both covalent interactions and noncovalent bonds. In contrast, the noncovalent functionalization is largely preferred as it does not alter the π-conjugated structure and the electronic properties of graphene,

while it simultaneously introduces new chemical groups on the surface[115]. In addition, the mild and nonpermanent character of noncovalent interactions offers high flexibility with regards to the treatment of the afforded products.

3. Electrochemical DNA sensors based on graphene

The graphene surface has been selected as the excellent substrate for DNA detection because its surface and structure is independent of pH, salt concentration and so on.[116]. Different approaches are described in the literature, to attach single-stranded DNA strand (ssDNA), on the graphene. These techniques include direct adsorption of DNA onto graphene through weak interactions, covalent attachment by different functional groups (amide, ester) or by using materials (nanoparticules, polymers) or aromatics compounds. The way to fix DNA onto the surface is crucial in the construction of sensor, in term of orientation, stability and accessibility.

3.1 Different approaches to immobilize DNA onto reduced graphene oxide

3.1.1 Through physical adsorption

DNA adsorption on graphene surface is well known and because of its high specific surface area, the carbon familly possesses potentially larger DNA adsorption capacities than other nanomaterials[117]. Due to the nature of the nucleobases of DNA (aromatic skeleton, polar), nucleotides interact with reduced graphene oxide through several interaction forces like, hydrogen bonding, base staking, electrostatics, van der Waals and hydrophobic interactions. Besides, Song et al.[118] has demonstrated that numerical simulations and experimental had confirmed that the ssDNA sequence could adsorb on graphene sheet surface with all nucleobases as unexpected. Indeed, the Fig. 29 illustrates the two modes of interaction of single-stranded DNA strand on two different surfaces: graphene -Au(111) surface (in green and yellow sphere respectively) and on a typical Au(111) surface (the figure inset).

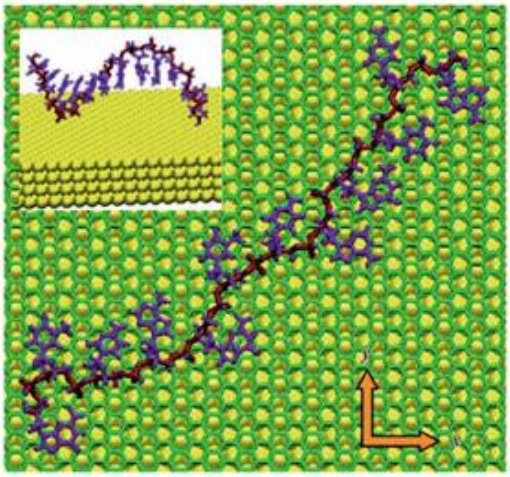

Fig. 29. *Schematic representation of an ssDNA nucleobase on the surface of the graphene-on-Au(111) material.*

3.1.2 Through covalent attachment

The presence of carboxylic acid and hydroxyl groups at the edges and on the basal plane of reduced graphene oxide are used to fix ssDNA sequence. Bonanni et al[119] could successfully functionalize graphene with ssDNA oligomers with carbodiimide chemistry (Fig 30). They showed that such DNA–graphene hybrid structures exhibit strong biorecognition ability.

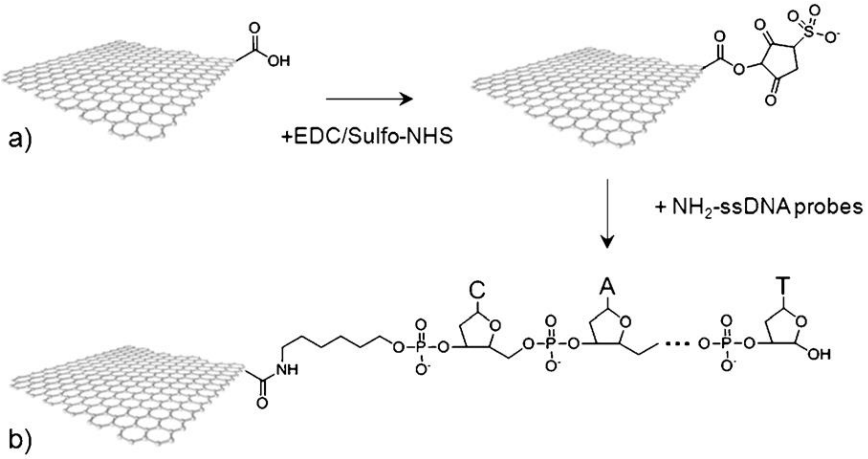

Fig. 30. *Covalent functionalization of graphene by ssDNA. a) Sufo- NHS esters formed on carboxylated graphene react with amino-modified ssDNA probes to form an amide bond; this results in, b) covalently func- tionalized graphene by ssDNA.*

3.1.3 Through materials like nanoparticles and polymers

The graphene–nanoparticle hybrid structures are particularly interesting because

not only do they display the individual properties of the nanoparticles and of graphene, but they can also exhibit additional synergistic properties thereby enhancing the achievable sensitivity and selectivity using a variety of sensing mechanisms.

3.1.4 Through aromatics compounds

Aromatic molecules have large aromatic plane and can anchor onto the reduced graphene oxide nanosheets surface without disturbing its electronic conjugation, providing stability for reduced graphene oxide. The most popular are perylene tetracarboxylic acid[120] and pyrenebutyric acid [121] (Fig. 31).

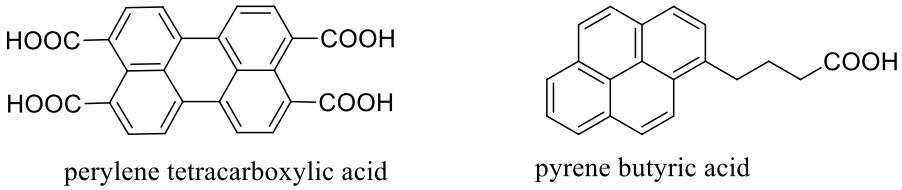

perylene tetracarboxylic acid pyrene butyric acid

Fig 31. *The structure of the aromatic molecules*

The aromatic molecules act as wedges and penetrate slowly between the planar graphene layers usually by the assistant of sonication. Meanwhile, the aromatic molecules functionalization with RGO lead to a variety of terminated groups, which can not only remarkably improve the dispersibility and further functionalization and modification, but also offer opportunities for sensing performance.

For each approach of immobilization, some examples of DNA sensor based on RGO are presented as followed.

3.2 DNA sensors based on RGO with nanoparticles

The graphene–nanoparticle hybrid structures as well as their application in electronic, electrochemical sensors will be shown in detail.

Silver nanoparticles (AgNPs), as a typical noble metal nanoparticles, are extensively used in DNA hybridization sensing for amplification of hybridization event owing to their catalytic properties and also exhibit the high electrical and thermal conductivities[122]. The scheme was shown in Fig. 32.

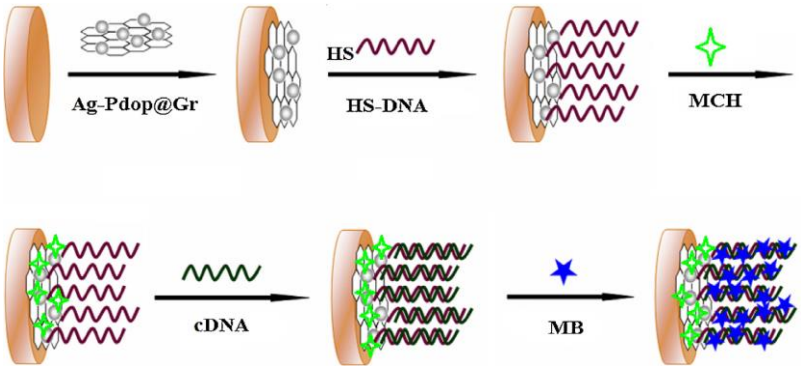

Fig. 32. *Schematic diagram of the electrochemical DNA biosensor.*

Extensive research has been carried out on RGO-based non-covalent functionalized electrochemical biosensors, the development of highly sensitivity and selectivity using self-assembled nanomaterial platform was imperative.

3.3 DNA sensors based on RGO with conductive polymers (CPs)

Fabrication of electrochemical sensors based on RGO-CPs becomes a popular approach in many electroanalytical investigations and shows good potential for constructing the sensors with high sensitivity and selectivity to detect target molecules based on different analytical strategies.

Various polymers, such as poly(methyl-meta acrylate) (PMMA),[123,124] poly(dimethylsiloxan) (PDMS),[125] polypropylene (PP)[126] are used in biosensing and mirco-array technologies.

3.4 DNA sensors based on RGO with aromatic molecules

Lee et al.[127] used a tetrapyrene derivative functionalized by an oligoetherdendron to exfoliate graphite and stabilize graphenic layers. The tetrapyrene aromatic rings interacted with RGO, while oligoether chains induce a high hydrophilic character to the nanomaterial. The authors elucidated that the same tetrapyrene derivative is unable to disperse SWNTs, indicating that the planarity of the carbon nanostructure is a crucial factor for the formation of an effective π stacking.

Bose et al.[121] employed the organic 9-anthracene carboxylic acid (9-ACA) to

improve the dispersibility in aqueous solution, which penetrates deeper inside the graphite flakes and finally exfoliates to form individual layers. The out-of-plane –COOH group helps in achieving stable dispersion in water and strong π–π interaction prevents the exfoliated sheets from restacking. The proposed mechanism for the formation of stable aqueous dispersion was shown in Fig. 33.

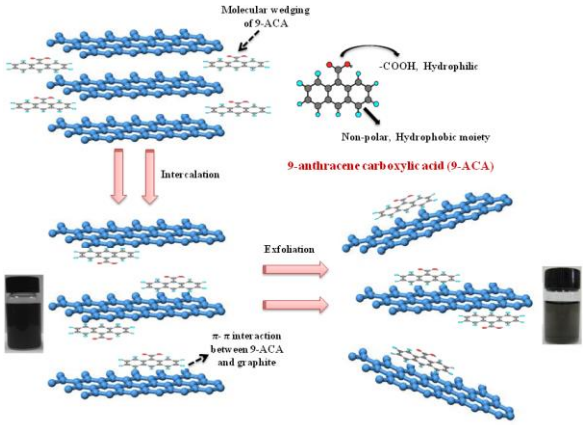

Fig. 33. *Proposed mechanism for the formation of stable aqueous dispersion of graphene.*

Extensive researches have been carried out on RGO with the conjugated polymers and aromatic compounds include poly(sodium 4-styrenesulfonate) (PSS), sulfonated polyaniline[128], poly(3-hexylthiophene) (P3HT)[129], conjugated polyelectrolyte[130], 7,7,8,8-tetracyanoquinodimethane anion[131], tetrasulfonate salt of copper phthalocyanine (TSCuPc)[132], porphyrin derivatives[133],[134,135], pyridine and fluorinated benzene derivatives[136,137], quinoline[138], pyrene[139–144], triphenylene[145], polymer ionic liquids[146], and cellulose derivatives [147] through noncovalent interaction, and the π–π interactions can cause the stabilization of the afforded graphene nanosheets in organic solvents.

For example, Chunder et al. disclosed that a sulfonate groups on TSCuPc introduced negative charges on the reduced graphene oxide sheets and facilitated the dispersion of RGO, providing single sheet of TSCuPc functionalized RGO. Compared to the RGO without TSCuPs, irreversible aggregation and precipitation of graphitic

sheets occurred.

3,4,9,10-Perylene tetracarboxylic acid (PTCA), bearing π-conjugated perylene ring and carboxylic acid groups, was used to decorate graphene (Fig. 34). Based on the π–π stacking and hydrophobic interactions between the perylene ring and the basal plane of graphene, PTCA molecules separated graphene sheets efficiently and decorated them with plenty of –COOH. This method resolved the graphene aggregation problem, and the resulting hybrids dispersed well in aqueous solution. After activation, NH_2–ssDNA was covalently immobilized on the hybrid, which presented as lying structure. Hybridization to cDNA induced the lying ssDNA to standing dsDNA, which caused the graphene interfacial property changes, such as negative charge and conformation.

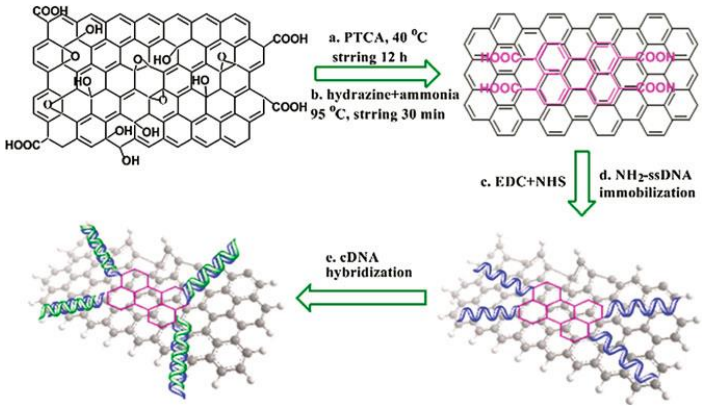

Fig. 34. *Schematic representation of graphene functionalization with PTCA, ssDNA immobilization, and hybridization*

CHAPTER III: Chemistry of Porphyrin in Biosensor Application

Porphyrins are a class of molecules widely present in nature and function in a large variety of roles ranging from oxygen transport, electron transfer, and oxidation catalysts to photosynthesis. They are among the most widely distributed and important cofactors found in nature and a crucial regulatory effectors in many biochemical mechanisms. Thus, porphyrins play an important role in numerous areas such as bioorganic and bioinorganic chemistry, biomedical sciences, photodynamic therapy and solar energy conversion. In this context, porphyrin chemistry has known and gained special attention over the years. In this chapter, we will focus on briefly presenting the structure/properties and synthesis of the porphyrins, followed by some examples of their applications in biosensors chemistry to help

1. Structure and properties of porphyrins

1.1. Structure

The porphyrins are aromatic tetrapyrrolic macrocycles with 22 π electrons, 18 of which are involved in aromaticity. Three main types of carbon atoms can be distinguished in these molecules, which are noted respectively α, β and *meso*. We have depicted (Fig. 35) the simplest porphyrins (called porphine) and the carbon atoms were numbered according to the IUPAC nomenclature.

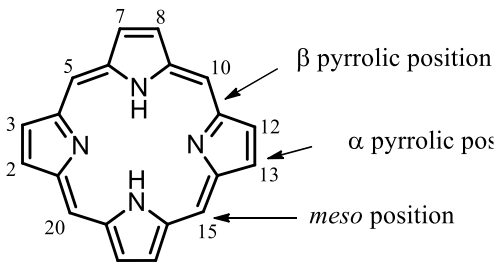

Fig. 35. *Structure of porphine*

The porphyrins can be classified according to the substituents carried by the β or *meso* carbon atoms and by the nature of the metal complexed by the macrocycle. The term free base is used in the absence of metal and metalloporphyrin in the opposite case. We show below two conventional examples of meso-substituted porphyrins free (tetraphenylporphyrin) and metaled with zinc.(Fig. 36)

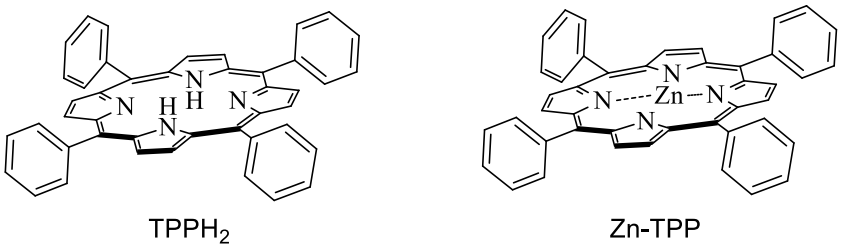

Fig. 36. *two examples of structure of free and metaled porphyrin*

1.2 Optical and electrochemical Properties

Because of their particular electronic structure, porphyrins are highly colored molecules. They present two types of absorption bands in the ultraviolet and visible domains, attributed to transitions π-π *:

- a very intense band ($\varepsilon > 10^5$ $mol^{-1}.L.cm^{-1}$) located between 380 and 450 nm, called band Soret. It is characteristic of the aromaticity of the molecule.

- a series of bands in the visible called Q bands, less intense ($\varepsilon \sim 10^4$ $mol^{-1}.L.cm^{-1}$) but nevertheless responsible for the color of the porphyrins. The number of Q bands generally makes it possible to distinguish the free-base porphyrins and the metalloporphyrins. The free bases have four bands Q whereas the metalloporphyrins, which have a larger symmetry, have only two (or even one) in general. The energy and intensity of these bands depend on the substituents of the porphyrin, the metal, the additional ligands on the metal, the macrocycle deformations, the solvent and the interactions between chromophores in the multi-porphyrinic buildings.

2. Synthesis of meso substituted porphyrin

These last fifteen years, the synthesis chemistry of *meso*-substituted porphyrin has considerably been developed and improved, decreasing the purifications step, the number of regioisomers synthesized [148]. Today, there are three ways to access such molecules (scheme. 37). The first approach consists in a mixed condensation using pyrrole and various aldehydes[149](path A). In this case, the number of regioisomers formed is very large and the purification and separation workup are cumbersome. The latter one is the combination of pyrrole building blocks with aldehydes that can be used in a [2+2] or [3+1] condensation reaction[150] (path B). All these reactions involve acid-catalyzed condition reactions, often resulting in by product formations and limiting the types of substituents used. At least, the last strategy, developed by Senge et al. is to introduce different substituents directly at the *meso*-positions from trisubstituted porphyrines, for example[151]. The path A and B will be particularly focus on in the next parts.

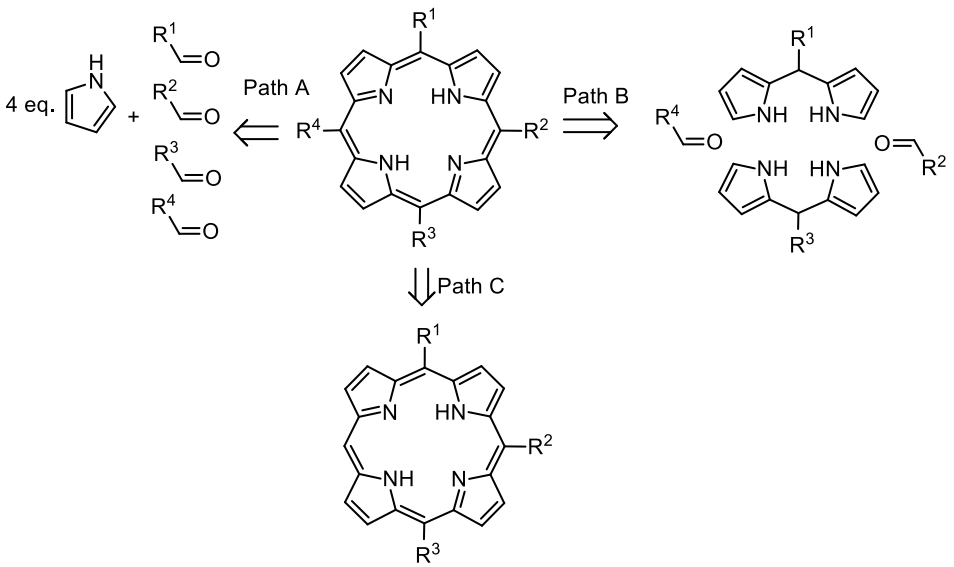

Fig 37. *General approach for the synthesis of porphyrin*

2.1 Direct method (path A)

Tetraphenylporphyrin (TPP) was first synthesized in 1936 by Rothmund[152] and

improved in 1967 by Adler and Longo mixing benzaldehyde and pyrrole in refluxing propionic acid for 30 min and then opening to air [153]. Under these conditions, a greater variety of substituted benzaldehydes were converted into the corresponding 5,10,15,20-tetraphenylporphyrins, and in some cases, the yield could up to 20%. Differentially functionalized porphyrins can also be prepared by using two different aldehydes under essentially the same conditions. The Adler–Longo method is often used to obtain unsymmetrically substituted tetraphenylporphyrins with groups suitable for further modification.

While the above methods show the utility of the propionic acid method, there are several drawbacks. The formation of the reduced porphyrin (chlorin) invariably contaminates the product and a high percentage of by-products are also formed. Another problem is the failure of the reaction with aldehydes containing acid sensitive functional groups. These drawbacks associated with the rather harsh conditions could be overcome using method developed by Lindsey et al[154]. The Lindsey method relies on the existence of the formation of porphyrinogen as an intermediate in porphyrin synthesis. After the equilibrium has been established, an oxidant is added which converts the porphyrinogen to the corresponding porphyrin irreversibly (Fig. 38). The advantage of this method is that it allows the formation of porphyrins from acid sensitive aldehydes, in higher yields, with more facile purification.

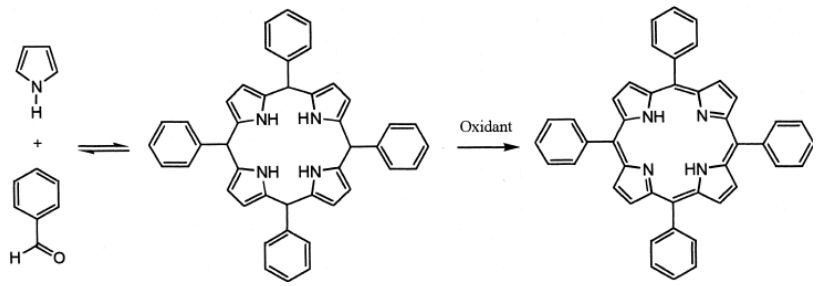

Fig. 38. *Formation of tetraphenylporphyrin (TPP) by Lindsey*

2.2 [2+2] Porphyrin synthesis (path B)

Meso-substituted porphyrins can be prepared from two dipyrromethanes and appropriated benzaldehyde under lewis acidic conditions using method what are

commonly called [2+2] synthesis. Early work was pioneered by MacDonald[155] and considerably improved by Lindsey's works. The basic synthetic route is shown in Fig. 39. The method involves use of one dipyrromethane bearing two formyl groups α-pyrrolic nitrogen and another dipyrromethane with no α-substitution.

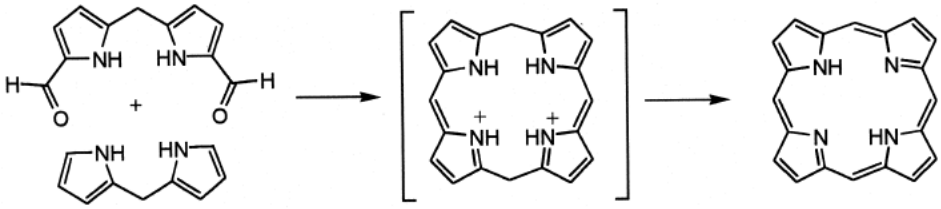

Fig. 39. *2+2 Porphyrin synthesis by MacDonald*

There is obvious scope for the preparation of a large number of functionalized porphyrins using [2+2] route, and a great of regioselectivity can be attained compared to the Adler and Lindsey methods. The 2+2 route has become very popular in recent years due to its flexibility, and there are many reports of porphyrin synthesis based on this method. It is, however, very dependent on the availability of suitable dipyrromethane building blocks, and the preparation of dipyrromethanes has also been the subject of several recent studies.

3. Interaction between porphyrins and graphene

The great similarity of structure (planarity, conjugated network..) and the ability for both to introduce different substituants on the aromatic system, as previously showed, promote the association of graphene and poprhyrins.

For example, the presence of carboxylic groups on the edge of RGO structure allowed the covalent attachment of the protoporphyrin IX on the sheets of RGO in presence of coupling agent[156].

Diazonium chemistry has aslo been used recently by Wang et al. for the preparation of nanohybrids based on RGO and porphyrin. Upon heating of a diazonium salt, a highly reactive free radical is produced, which attacks the double bonds sp^2 carbon atoms on the surface of RGO, forming a covalent sp^3 bond[157–159],

The porphyrin molecules were thereby covalently attached to the surface of RGO via a benzene ring. The preparations are shown in Fig. 40.

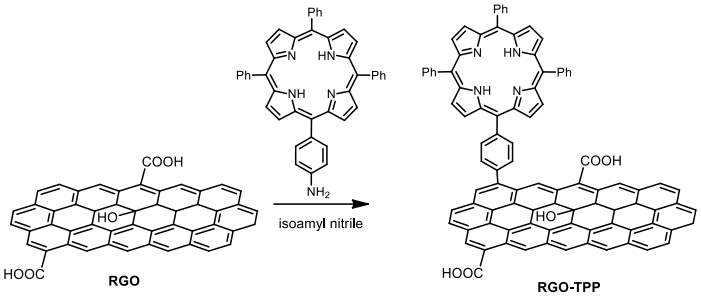

Fig. 40. *Preparation of RGO-TPP using diazonium reaction*

Authors demonstrated that attachment of the porphyrin units to the surface of the RGO by diazotization significantly improves the solubility and ease of processing of these RGO-based nanocomposites.

Another approach consisted to use some nanoparticles of gold previously deposited on RGO to fix a sulfhydryl-porphyrin through S–Au bond[160] (Fig. 41).

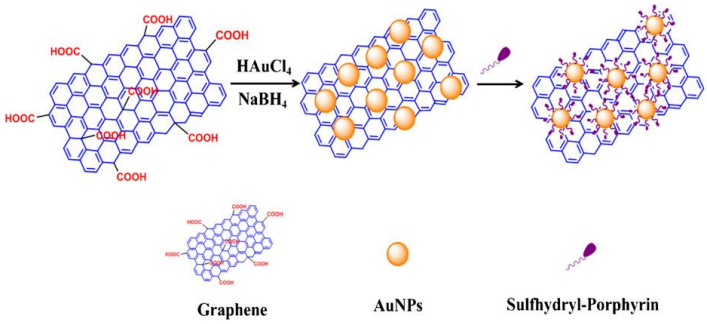

Fig. 41. *The preparation process of porphyrin/AuNPs/graphene nanocomposites*

Finally, the most common approach is to associate porphyrins and graphene through non-covalent interactions including π–π stacking interactions. In this case, this mode of associations don't disturb the intrinsic physical and chemical properties of graphene. The introduction of charged on porphyrins can promote the dispersion of graphene in aqueous solution and avoid thus its agglomeration. Thus, a *meso*-tetra(4-carboxyphenyl) cobalt porphyrin (CoTCPP) [161] can be strongly adsorbed on graphene through π–π stacking and hydrophobic interactions to avoid graphene aggregation and introduce more negatively charged –COOH groups and functionalities on graphene

surface, without destroying the conjugated π–system of graphene. Another example of charged tetraphenylporphyrines[133], a positively (TPP-ammonium) and a negatively (TPP-SO_3Na) molecules have also been used as dispersant for preparation of chemical reduced graphene oxide nanohybrides (Fig. 42).

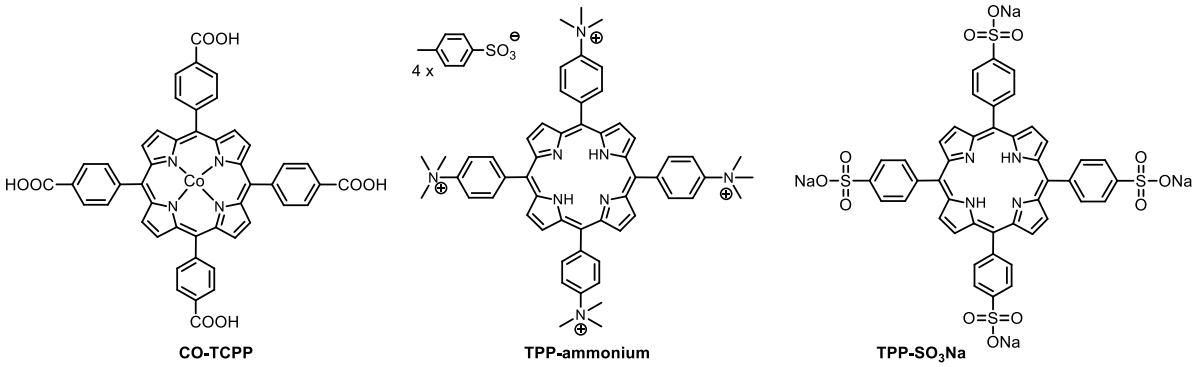

Fig. 42. *Molecular structures of CO-TCPP, TPP-SO_3Na and TPP-ammonium*

They have found that the π-π interactions taking place between porphyrins and RGO, as well as the porphyrin molecular architecture, play an important role in producing highly dispersible RGO sheets in water. Somes applications for employing porphyrin-graphene nanocomposites.

3.1 Oxygen Reduction Reaction

Jahan et al.[162] employed reduced graphene oxide sheets functionalized on either side of the basal plane with pyridine ligands, which was considered as struts to link metalloporphyrin nodes to form the hybrid graphene-MOF framework. At the same time, the oxygenated functional groups on RGO can facilitate ORR by acting as an electron transfer mediator. They found that the addition of pyridine functionalized graphene changes the crystallization process of iron−porphyrin in the MOF, increases its porosity, and enhances the electrochemical charge transfer rate of iron−porphyrin. The graphene−metalloporphyrin hybrid shows facile 4-electron ORR and can be used as a promising Pt-free cathode in alkaline direct methanol fuel cell. The schematic representation was shown in Fig. 43.

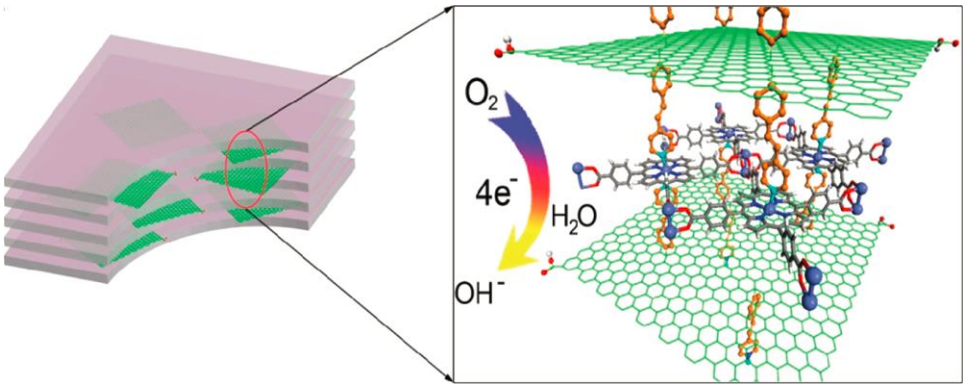

Fig. 43. *Schematic representation of graphene−metalloporphyrin hybrid*

3.2 Photoelectochemical detection of hydroquinone (HQ)

Hu et al. [160] developped a photoelectrochemical sensor based on the porphyrin-functionalized gold nanoparticles on graphene for the detection of hydroxyquinone (HQ) under white light illumination. The proposed photoelectrochemical method could detect hydroquinone with a wide linear response ranging from 20 to 240 nM. The detection limit was 4.6 nM for HQ (Fig. 44). In this case, the porphyrin exhibits its catalytic properties for the oxidation of hydroquinone into quinone.

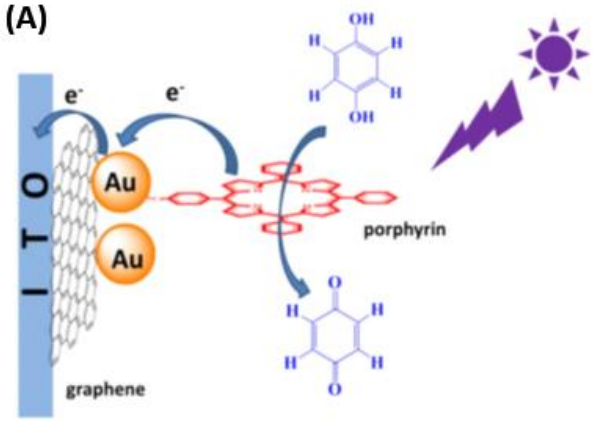

Fig. 44. *Schematic diagram of photoelectrochemical sensor*

3.3 Porphyrin Functionalized Graphene for Sensitive Electrochemical Detection of Uric Acid

Yang et al.[163] developed an amperometric biosensor based on porphyrin and graphene oxide for the detection of uric acid (Fig. 45). A *tetrakis*(aminophenyl)porphyrin (TCPP) of cobalt was strongly adsorbed on graphene oxide through π-stacking and hydrophobic interactions. The nanocomposite combing electronic properties of RGO and special electrocatalytic behavior of porphyrin with good biocompatible was applied for detecting uric acid (UA). The biosensor showed a wide linear range, (0.02 to 5 mM), a quick response, a low level of detecting limitation (1 μM) with excellent repeatability and stability. The large surface area of RGO made great contribution to biosensor performance, including high conductivity and quick electron transfer between porphyrin and RGO.

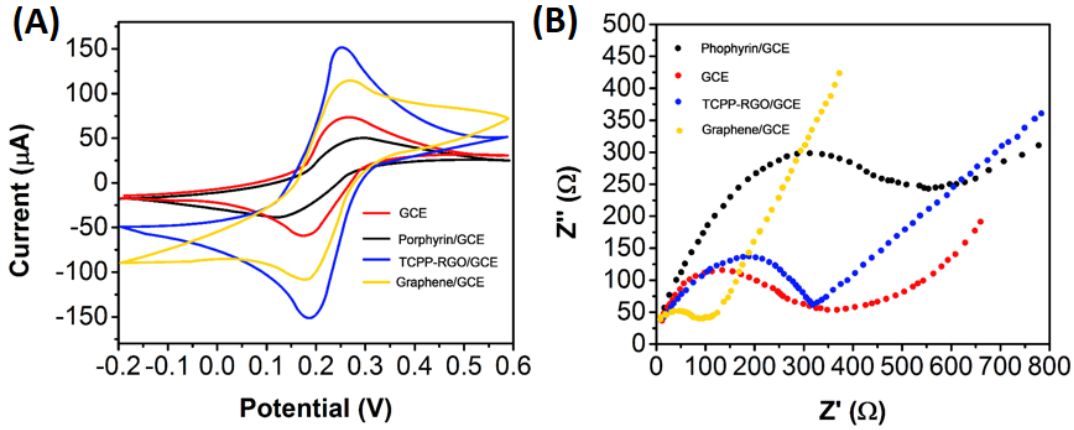

Fig. 45. *(A) Cyclic voltammograms (CVs) and (B) Electrochemical impedance spectroscopy (EIS) spectra of 10 mM $Fe(CN)_6^{3-/4-}$ in 1.0 M KCl at bare GCE, TCPP and TCPP-RGO modified GC electrode. Scan rate: 50 mV/s.*

REFERENCES:

1. Clark Jr., *et al.,* Electrode systems for continuous monitoring in cardiovascular surgery. *Ann. N. Y. Acad. Sci.* **102,** 29–45 (1962).
2. Daniels, P. B., *et al.,* Surface plasmon resonance applied to immunosensing. *Sensors and Actuators* **15,** 11–18 (1988).
3. Zhang, Y. and Tadigadapa, S. Calorimetric biosensors with integrated microfluidic channels. *Biosens. Bioelectron.* **19,** 1733–1743 (2004).
4. Guilbault, G. G., *et al.,* A piezoelectric immunobiosensor for atrazine in drinking water. *Biosens. Bioelectron.* **7,** 411–419 (1992).
5. Heller, A. Amperometric biosensors. *Current Opinion in Biotechnology* **7,** 50–54 (1996).
6. GS, S., *et al.,* Biosensors: A Modern Day Achievement. *J. Instrum. Technol.* **2,** 26–39 (2014).
7. Palecek, E. and Fojta, M. Electrochemical DNA Sensors. *Bioelectron. From Theory to Appl.* **21,** 127–192 (2005).
8. Chaubey, A. and Malhotra, B. D. Mediated biosensors. *Biosens. Bioelectron.* **17,** 441–456 (2002).
9. Millan, K. M. and Mikkelsen, S. R. Sequence-selective biosensor for DNA based on electroactive hybridization indicators. *Anal. Chem.* **65,** 2317–2323 (1993).
10. Gooding, J. J., *et al.,* Self-assembled monolayers into the 21st century: Recent advances and applications. *Electroanalysis* **15,** 81–96 (2003).
11. Shao, Y. *et al.* Graphene based electrochemical sensors and biosensors: A review. *Electroanalysis* **22,** 1027–1036 (2010).
12. Gooding, J. J. *et al.* Protein electrochemistry using aligned carbon nanotube arrays. *J. Am. Chem. Soc.* **125,** 9006–9007 (2003).
13. Heller, A. Electrical wiring of redox enzymes. *Acc. Chem. Res.* **23,** 128–134 (1990).
14. Bernhardt, P. V. Enzyme electrochemistry-Biocatalysis on an electrode. *Aust. J. Chem.* **59,** 233–256 (2006).
15. Wang, J. Nanoparticle-based electrochemical bioassays of proteins. *Electroanalysis* **19,** 769–776 (2007).
16. Patolsky, F., *et al.,* Nanowire-based biosensors. *Analytical Chemistry* **78,** 4260–4269 (2006).
17. Patolsky, F. Detection, Stimulation, and Inhibitionof Neuronal Signals with High-DensityNanowire Transistor Arrays. *Science* **313,** 1–5 (2006).
18. Patolsky, F., *et al.,* Nanowire-Based Nanoelectronic Devices in the Life Sciences. *MRS Bull.* **32,** 142–149 (2007).
19. Wang, J. Electrochemical glucose biosensors in *Electrochemical Sensors, Biosensors and their Biomedical Applications* 57–69 (2008).
20. Gooding, J. J. Electrochemical DNA Hybridization Biosensors. *Electroanalysis* **14,** 1149–1156 (2002).
21. Wang, J. Electrochemical nucleic acid biosensors. *Anal. Chim. Acta* **469,** 63–71 (2002).
22. Wan, Y. *et al.,* Ligase-based multiple DNA analysis by using an electrochemical sensor array. *Biosens. Bioelectron.* **24,** 1209–1212 (2009).
23. Zeng, G. *et al.,* Gold nanoparticles/water-soluble carbon nanotubes/aromatic diamine polymer composite films for highly sensitive detection of cellobiose dehydrogenase gene. *Electrochim. Acta* **56,** 4775–4782 (2011).

24. Carpini, G., *et al.,* Oligonucleotide-modified screen-printed gold electrodes for enzyme-amplified sensing of nucleic acids. *Biosens. Bioelectron.* **20,** 167–175 (2004).
25. Hajdukiewicz, J., *et al.,* An enzyme-amplified amperometric DNA hybridisation assay using DNA immobilised in a carboxymethylated dextran film anchored to a graphite surface. *Biosens. Bioelectron.* **25,** 1037–1042 (2010).
26. Spain, E. *et al.,* High sensitivity DNA detection using gold nanoparticle functionalised polyaniline nanofibres. *Biosens. Bioelectron.* **26,** 2613–2618 (2011).
27. Kang, D. *et al.,* Comparing the properties of electrochemical-based DNA sensors employing different redox tags. *Anal. Chem.* **81,** 9109–9113 (2009).
28. Ricci, F. *et al.,* Surface chemistry effects on the performance of an electrochemical DNA sensor. *Bioelectrochemistry* **76,** 208–213 (2009).
29. Xiao, Y., *et al.,* Label-free electrochemical detection of DNA in blood serum via target-induced resolution of an electrode-bound DNA pseudoknot. *J. Am. Chem. Soc.* **129,** 11896–11897 (2007).
30. Anne, A., *et al.,* J. 3′-ferrocene-labeled oligonucleotide chains end-tethered to gold electrode surfaces: Novel model systems for exploring flexibility of short DNA using cyclic voltammetry. *J. Am. Chem. Soc.* **125,** 1112–1113 (2003).
31. Moiroux, J., *et al.,* 3 ′ -Ferrocene-Labeled Oligonucleotide Chains End-Tethered to Gold Electrode Surfaces : Novel Model Systems for Exploring Flexibility of Short DNA Using Cyclic Voltammetry. *JACS Commun.* **125,** 1112–1113 (2003).
32. Gao, C., *et al.,* The new age of carbon nanotubes: an updated review of functionalized carbon nanotubes in electrochemical sensors. *Nanoscale* **4,** 1948–63 (2012).
33. Rasheed, P. A. and Sandhyarani, N. A highly sensitive DNA sensor for attomolar detection of the BRCA1 gene : signal amplification with gold nanoparticle clusters. *Analyst* **140,** 2713–2718 (2015).
34. PALEČEK, E. Oscillographic Polarography of Highly Polymerized Deoxyribonucleic Acid. *Nature* **188,** 656–657 (1960).
35. Paleček, E. Adsorptive transfer stripping voltammetry: Determination of nanogram quantities of DNA immobilized at the electrode surface. *Anal. Biochem.* **170,** 421–431 (1988).
36. Bollo, S., *et al.,* Electrooxidation of DNA at glassy carbon electrodes modified with multiwall carbon nanotubes dispersed in chitosan. *Electroanalysis* **19,** 833–840 (2007).
37. Cui, M., *et al.,* A label-free electrochemical DNA biosensor for breast cancer marker BRCA1 based on self-assembled antifouling peptide monolayer. *Sensors Actuators, B Chem.* **244,** 742–749 (2017).
38. Zhu, L., *et al.,* DNA electrochemical biosensor based on thionine-graphene nanocomposite. *Biosens. Bioelectron.* **35,** 507–511 (2012).
39. Li, C. *et al.,* An ultrasensitive and label-free electrochemical DNA biosensor for detection of DNase I activity. *RSC Adv.* **7,** 21666–21670 (2017).
40. Bo, Y., *et al.,* A novel electrochemical DNA biosensor based on graphene and polyaniline nanowires. *Electrochim. Acta* **56,** 2676–2681 (2011).
41. Radhakrishnan, S. *et al.* Polypyrrole-poly(3,4-ethylenedioxythiophene)-Ag (PPy-PEDOT-Ag) nanocomposite films for label-free electrochemical DNA sensing. *Biosens. Bioelectron.* **47,** 133–140 (2013).
42. Huang, K. J., *et al.,* A sensitive electrochemical DNA biosensor based on silver nanoparticles-

polydopamine@graphene composite. *Electrochim. Acta* **118,** 130–137 (2014).

43. Wang, J., *et al.,* A sensitive DNA biosensor fabricated from gold nanoparticles, carbon nanotubes, and zinc oxide nanowires on a glassy carbon electrode. *Electrochim. Acta* **55,** 4436–4440 (2010).
44. Yan, F. *et al.,* Electrochemical DNA biosensor for the detection of specific gene related to Microcystis species. *Electrochem. commun.* **3,** 224–228 (2001).
45. Liu, X. G., *et al.,* Electrochemical detection of avian influenza virus H5N1 gene sequence using a DNA aptamer immobilized onto a hybrid nanomaterial-modified electrode. *Electrochim. Acta* **56,** 6266–6270 (2011).
46. Nambiar, S. and Yeow, J. T. W. Conductive polymer-based sensors for biomedical applications. *Biosensors and Bioelectronics* **26,** 1825–1832 (2011).
47. Li, X., *et al.,* Label-free detection of DNA hybridization based on poly (indole-5-carboxylic acid) conducting polymer. **2,** 104–110 (2008).
48. Bangar, M. A., *et al.,* Single Conducting Polymer Nanowire Based Sequence-Specific , Base-Pair-Length Dependant Label-free DNA Sensor. *Electroanalysis* **23**, 371–379 (2011).
49. Peng, H., *et al.,* Label-free detection of DNA hybridization based on a novel functionalized conducting polymer. *Biosens. Bioelectron.* **22,** 1868–1873 (2007).
50. Davis, F., *et al.,*Single gene differentiation by DNA-modified carbon electrodes using an AC impedimetric approach. *Anal. Chem.* **79,** 1153–1157 (2007).
51. Weng, J. *et al.,* Label-Free DNA Sensor by Boron-Doped Diamond Electrode Using an ac Impedimetric Approach. *Anal Chem.* **80,** 7075–7083 (2008).
52. Mohan, S., *et al.,* A label-free genosensor for BRCA1 related sequence based on impedance spectroscopy. *Analyst* **135,** 2887 (2010).
53. Gu, H., *et al.,* Electrochemical impedance sensing of DNA hybridization on conducting polymer film-modified diamond. *J. Phys. Chem. B* **109,** 13611–13618 (2005).
54. Wang, M. *et al.* Electrochemical detection of DNA immobilized on gold colloid particles modified self-assembled monolayer electrode with silver nanoparticle label. *Journal of Pharmaceutical and Biomedical Analysis*, **33,** 1117–1125 (2003).
55. Ozsoz, M. *et al.,* Electrochemical genosensor based on colloidal gold nanoparticles for the detection of Factor V Leiden mutation using disposable pencil graphite electrodes. *Anal. Chem.* **75,** 2181–2187 (2003).
56. Kerman, K., *et al.,* Modification of Escherichia coli single-stranded DNA binding protein with gold nanoparticles for electrochemical detection of DNA hybridization. *Analy. Chimica Acta,* **510,** 169–174 (2004).
57. Feng, K. J. *et al.,* A nano-porous CeO_2/Chitosan composite film as the immobilization matrix for colorectal cancer DNA sequence-selective electrochemical biosensor. *Talanta* **70,** 561–565 (2006).
58. Tang, L. *et al.,* Preparation, structure, and electrochemical properties of reduced graphene sheet films. *Adv. Funct. Mater.* **19,** 2782–2789 (2009).
59. Spain, E., *et al.,* DNA sensor based on vapour polymerised pedot films functionalised with gold nanoparticles. *Biosens. Bioelectron.* **41,** 65–70 (2013).
60. Wilson, J., *et al.,* Polypyrrole-polyaniline-Au (PPy-PANi-Au) nano composite films for label-free electrochemical DNA sensing. *Sensors Actuators, B Chem.* **171–172,** 216–222 (2012).
61. Nowicka, A. M., *et al.,* Polypyrrole-Au Nanoparticles Composite as Suitable Platform for DNA

Biosensor with Electrochemical Impedance Spectroscopy Detection. *Electrochim. Acta* **140,** 65–71 (2014).

62. Phiri, J., *et al.,* General overview of graphene: Production, properties and application in polymer composites. *Mater. Sci. Eng. B* **215,** 9–28 (2017).
63. Nada F. Atta, A. G. and E. H. E.-A. *Graphene-A Platform for Sensor and Biosensor Applications*. *Biomedical Engineering, trends in Materials Science*
64. Hang, L., *et al.,* A high-performance DNA biosensor using polyhydroxylated fullerenol as 3D matrix for probe immobilization. *Electrochem. commun.* **47,** 84–87 (2014).
65. Li, J., *et al.,* DNA biosensor based on chitosan film doped with carbon nanotubes. *Anal Biochem.,* **346,** 107–114 (2005).
66. Cai, H., *et al.,* Carbon nanotube-enhanced electrochemical DNA biosensor for DNA hybridization detection. *Analytical and Bioanalytical Chemistry*, **375**, 287–293 (2003).
67. Singh, R. *et al.,* Nanobiocomposite platform based on polyaniline-iron oxide-carbon nanotubes for bacterial detection. *Bioelectrochemistry* **86,** 30–37 (2012).
68. Miodek, A., *et al.,* E-DNA Sensor of Mycobacterium tuberculosis Based on Electrochemical Assembly of Nanomaterials (MWCNTs/PPy/PAMAM). *Anal. Chem.* **87,** 9257–9264 (2015).
69. Yang, S. T., *et al.,* Pharmacokinetics, metabolism and toxicity of carbon nanotubes for bio-medical purposes. *Theranostics* **2,** 271–282 (2012).
70. Lam, C. W., *et al.,* A review of carbon nanotube toxicity and assessment of potential occupational and environmental health risks. *Crit Rev Toxicol* **36,** 189–217 (2006).
71. Firme, C. P. and Bandaru, P. R. Toxicity issues in the application of carbon nanotubes to biological systems. *Nanomedicine: Nanotechnology, Biology, and Medicine* **6,** 245–256 (2010).
72. Pumera, M., *et al.,* Graphene for electrochemical sensing and biosensing. *TrAC - Trends in Analytical Chemistry* **29,** 954–965 (2010)..
73. Novoselov, K. S. *et al.,* Electric field effect in atomically thin carbon films. *Science* **306,** 666–669 (2004).
74. Chen, P. Y., *et al.,* Progress in Materials Science. *Biol. Mater. Funct. Adapt. bioinspired Des.* **57,** 1492–1704 (2012).
75. Chen, W. and Yan, L. Preparation of graphene by a low-temperature thermal reduction at atmosphere pressure. *Nanoscale* **2,** 559 (2010).
76. Kuila, T. *et al.,* Recent advances in graphene-based biosensors. *Biosens. Bioelectron.* **26,** 4637–4648 (2011).
77. Du, M., *et al.,* Ionic liquid-functionalized graphene as modifier for electrochemical and electrocatalytic improvement: Comparison of different carbon electrodes. *Anal. Chim. Acta* **690,** 169–174 (2011).
78. Pumera, M. Graphene-based nanomaterials for energy storage. *Energy & Environmental Science* **4**, 668–674 (2011).
79. Craciun, M. F., *et al.,* Tuneable electronic properties in graphene. *Nano Today* **6,** 42–60 (2011).
80. Lonkar, S. P., *et al.,* Recent advances in chemical modifications of graphene *Nano Research* 1–36 (2014).
81. Kotov, N. A. and Kelly, J. W. Carbon sheet solutions Proteins downhill all the way. *Nature* **442,**
82. Liang, X., *et al.,* Graphene transistors fabricated via transfer-printing in device active-areas on large wafer. *Nano Lett.* **7,** 3840–3844 (2007).
83. Nai, B. *et al.,* Catalyst-Free Efficient Growth , Orientation and Biosensing Properties of

Multilayer Graphene Nanoflake Films with Sharp Edge Planes. *Advanced Functional materials* **18,** 3506–3514 (2008).

84. Sutter, P. W., *et al.,* Epitaxial graphene on ruthenium. *Nat Mater* **7,** 406–411 (2008).
85. Berger, C. *et al.,* Science. **312,** 1191–1196 (2006).
86. Ouerghi, A. *et al.,* Epitaxial graphene on 3C-SiC (111) pseudosubstrate : Structural and electronic properties. *Physical Review B* **82**, 1–6 (2010).
87. Miyamoto, Y., *et al.,* Regular of epitaxial graphene layers on 3C SiC/Si (111) as function of annealing temperature in UHV. **7,** 107–109 (2009).
88. Gupta, B. *et al.,* Evolution of epitaxial graphene layers on 3C SiC / Si (1 1 1) as a function of annealing temperature in UHV. *Carbon* **68,** 563–572 (2014).
89. Suemitsu, M., *et al.,* Graphene Formation on a 3C-SiC(111) Thin Film Grown on Si(110) Substrate. *Journal of Surface Science and Nanotechnology* **7,** 311–313 (2009).
90. Novoselov, K. S. *et al.,* Electric field effect in atomically thin carbon films. *Science* **306,** 666–669 (2004).
91. Dan, Y., *et al.,* Intrinsic response of graphene vapor sensors. *Nano Lett.* **9,** 1472–1475 (2009).
92. Blake, P. *et al.,* Graphene-Based Liquid Crystal Device *Nano Lett.* **8,** 1704–1708 (2008).
93. Lotya, M. *et al.,* Liquid Phase Production of Graphene by Exfoliation of Graphite in Surfactant / Water Solutions. *J. Am. Chem. Soc.,* **131**, 3611–3620 (2009).
94. Liu, B. N. *et al.,* One-Step Ionic-Liquid-Assisted Electrochemical Synthesis of Ionic-Liquid-Functionalized Graphene Sheets Directly from Graphite . *Adv. Funct. Mater.* **18,** 1518–1525 (2008).
95. Murat Alanyalioglu *et al.,* The synthesis of graphene sheets with controlled thickness and order using surfactant-assisted electrochemical processes. *Carbon* **50,** 142–152 (2012).
96. Marcano, D. C. *et al.,* Improved synthesis of graphene oxide. *ACS Nano* **4,** 4806–4814 (2010).
97. Dikin, D. A. *et al.,* Preparation and characterization of graphene oxide paper. *Nature* **448,** 457–460 (2007).
98. Pham, T. A., *et al.,* One-step reduction of graphene oxide with l-glutathione. *Colloids Surfaces A Physicochem. Eng. Asp.* **384,** 543–548 (2011).
99. Sheng, K. X., *et al.,* High-performance self-assembled graphene hydrogels prepared by chemical reduction of graphene oxide. *Xinxing Tan Cailiao/New Carbon Mater.* **26,** 9–15 (2011).
100. Stankovich, S. *et al.,* Synthesis of graphene-based nanosheets via chemical reduction of exfoliated graphite oxide. *Carbon.* **45,** 1558–1565 (2007).
101. Ramesha, G. K. and Sampath, S. Electrochemical Reduction of Oriented Graphene Oxide Films: An in Situ Raman Spectroelectrochemical Study. *J. Phys. Chem. C* **113,** 7985–7989 (2009).
102. Xiong, Z., *et al.,* Electrochemical reduction of graphene oxide films : Preparation , characterization and their electrochemical properties. *Chinese Sci. Bull.* **57,** 3000–3009 (2012).
103. Gilje, S. *et al.,* Processable aqueous dispersions of graphene nanosheets. *Nat. Nanotechnol.* **3,** 101–105 (2008).
104. Eda, G., *et al,*. Large-area ultrathin films of reduced graphene oxide as a transparent and flexible electronic material. **3,** 1–5 (2008).
105. Gilje, S., *et al.,* A Chemical Route to Graphene for Device Applications. *Nano Lett.* **7,** 3394–3398 (2007).
106. Neto, A. H. C. and Novoselov, K. New directions in science and technology : two-dimensional

crystals. **82501,** (2011).

107. Pumera, M. Graphene in biosensing. *Materials Today* **14,** 308–315 (2011).
108. Bolen, M. L., *et al.*, Graphene formation mechanisms on 4 H-SiC (0001). *Phys. Rev. B* **80**, 1–9 (2009).
109. Telieps, W., *et al.*, An analytical reflection and emission UHV surface electron microscope. *Ultramicroscope* **17,** 57–66 (1985).
110. Irving, S. M., and Walker, P. L., Interaction of evaporated carbon with heated metal substrates. *Carbon* **5,** 399–402 (1967).
111. Balandin, A. A. Thermal properties of graphene and nanostructured carbon materials. *Nat. Mater.* **10,** 569–581 (2011).
112. Search, H. *et al.*, Morphology of graphene thin film growth on SiC(0001). *New Journal of Physics* **10**, 023034 (2008)**.**
113. Niyogi, S. *et al.* Solution properties of graphite and graphene. *J. Am. Chem. Soc.* **128,** 7720–7721 (2006).
114. Lu, L. M. *et al.*, Supramolecular assembly of enzyme on functionalized graphene for electrochemical biosensing. *Biosens. Bioelectron.* **45,** 102–107 (2013).
115. Georgakilas, V. *et al.*, Noncovalent Functionalization of Graphene and Graphene Oxide for Energy Materials, Biosensing, Catalytic, and Biomedical Applications. *Chemical Reviews* **116,** 5464–5519 (2016).
116. Kabeláč, M., *et al.*, Influence of a charged graphene surface on the orientation and conformation of covalently attached oligonucleotides: a molecular dynamics study. *Phys. Chem. Chem. Phys.* **14,** 4217 (2012).
117. Hu, Y., *et al.*, Biocompatible Graphene for Bioanalytical Applications. *Mol. Sci.* **2,** 11–34 (2015).
118. Song, B. *et al.*, Graphene on Au (111): A Highly Conductive Material with Excellent Adsorption Properties for High-Resolution Bio/Nanodetection and Identification. **19,** 585–589 (2010).
119. Bonanni, A., *et al.*, Nucleic Acid Functionalized Graphene for Biosensing. *Chem. - A Eur. J.* **18,** 1668–1673 (2012).
120. Hu, Y. *et al.*, Label-free electrochemical impedance sensing of DNA hybridization based on functionalized graphene sheets. *Chem. Commun.* **47,** 1743–1745 (2011).
121. Bose, S., *et al.*, Preparation of non-covalently functionalized graphene using 9-anthracene carboxylic acid. *Nanotechnology* **22,** 405603 (2011).
122. Azizi, S. N., *et al.*, Preparation of Ag/NaA zeolite modified carbon paste electrode as a DNA biosensor. *Sensors Actuators, B Chem.* **181,** 319–325 (2013).
123. Fixe, F. Functionalization of poly(methyl methacrylate) (PMMA) as a substrate for DNA microarrays. *Nucleic Acids Res.* **32,** e9 1–8 (2004).
124. Kimura, N. One-step immobilization of poly(dT)-modified DNA onto non-modified plastic substrates by UV irradiation for microarrays. *Biochem. Biophys. Res. Commun.* **347,** 477–484 (2006).
125. Liu, D., *et al.*, Immobilization of DNA onto Poly (dimethylsiloxane) Surfaces and Application to a Microelectrochemical Enzyme-Amplified DNA Hybridization Assay. *Society* 5905–5910 (2004).
126. Shchepinov, M. S., *et al.*, Steric factors influencing hybridisation of nucleic acids to

oligonucleotide arrays. *Nucleic Acids Res.* **25,** 1155–1161 (1997).

127. Su, Q. *et al.*, Composites of Graphene with Large Aromatic Molecules. *Adv. Mater.* **21,** 3191–3195 (2009).
128. Gamo, Y., *et al.*, Atomic structure of monolayer graphite formed on Ni (111). **374,** 61–64 (1997).
129. Moritz, W. *et al.* Structure Determination of the Coincidence Phase of Graphene on Ru (0001). *Pysical Review Letters*. **104**, **136102,** 13–16 (2010).
130. Boneschanscher, M. P. *et al.*, Structure and local variations of the graphene moire on Ir(111). *Pysical Review B***, 88,** 201406, 1–6 (2013).
131. Loginova, E., *et al.*, Defects of graphene on Ir(111): Rotational domains and ridges. *Phys. Rev. B* 85430-1–8 (2009).
132. Moreau, E. *et al.*, Graphene growth by molecular beam epitaxy on the carbon-face of SiC Graphene growth by molecular beam epitaxy on the carbon-face of SiC. *Applied Physics Letters*, **97**, 241907, 1–4 (2013).
133. Geng, J. and Jung, H. T. Porphyrin functionalized graphene sheets in aqueous suspensions: From the preparation of graphene sheets to highly conductive graphene films. *J. Phys. Chem. C* **114,** 8227–8234 (2010).
134. Elektronen-rastermikroskop, D., *et al.*, Das. Das Elektronen-Rastermikroskop. Theoretische Grundlagen. 553–572 (1938).
135. Search, H. *et al.* Ultrathin epitaxial cobalt films on graphene for spintronic investigations and applications. **103040,**
136. Chen, I.-W. P., *et al.*, Exfoliation and Performance Properties of Non-Oxidized Graphene in Water. *Sci. Rep.* **4,** 3928 (2015).
137. Bourlinos, A. B., *et al.*, Liquid-Phase Exfoliation of Graphite Towards Solubilized Graphenes. *Small* **5,** 1841–1845 (2009).
138. Kim, J. *et al.*, Moisture Barrier Composites Made of Non-Oxidized Graphene Flakes. *Small* **11,** 3124–3129 (2015).
139. Song, S. H. *et al.*, Enhanced thermal conductivity of epoxy-graphene composites by using non-oxidized graphene flakes with non-covalent functionalization. *Adv. Mater.* **25,** 732–737 (2013).
140. Manuscript, A. Nanoscale. (2010).
141. Zhang, M. *et al.*, Production of graphene sheets by direct dispersion with aromatic healing agents. *Small* **6,** 1100–1107 (2010).
142. An, X. *et al.*, Stable aqueous dispersions of noncovalently functionalized graphene from graphite and their multifunctional high-performance applications. *Nano Lett.* **10,** 4295–4301 (2010).
143. Jang, J.-H., *et al.*, Direct preparation of 1-PSA modified graphenenanosheets by supercritical fluidic exfoliation and its electrochemical properties. *J. Mater. Chem.* **21,** 3462–3466 (2011).
144. Yang, H. *et al.*, A simple method for graphene production based on exfoliation of graphite in water using 1-pyrenesulfonic acid sodium salt. *Carbon* **53,** 357–365 (2013).
145. Das, S. *et al.*, Non-covalent functionalization of pristine few-layer graphene using triphenylene derivatives for conductive poly (vinyl alcohol) composites. *Polymer.* **53,** 2485–2494 (2012).
146. Kim, T., *et al.*, Synthesis of phase transferable graphene sheets using ionic liquid polymers. *ACS Nano* **4,** 1612–1618 (2010).
147. Erhart, H., *et al.*, In Situ SEM Study of the High-Temperature Oxidation of an Fe--Mn-AI-Si

Alloy. **21,** 81–88 (1983).

148. Shanmugathasan, S., *et al.,* Advances in Modern Synthetic Porphyrin Chemistry. **56,** 1025–1046 (2000).
149. Adler, A. D., *et al.,* On the preparation of metalloporphyrins. *J. Inorg. Nucl. Chem.* **32,** 2443–2445 (1970).
150. Rao, P. D., *et al.,* Rational Syntheses of Porphyrins Bearing up to Four Different Meso Substituents. 7323–7344 (2000).
151. Senge, M. O. Nucleophilic Substitution as a Tool for the Synthesis of Unsymmetrical Porphyrins. **38,** 733–743 (2005).
152. Rothemund, P. A New Porphyrin Synthesis. The Synthesis of Porphin. *J. Am. Chem. Soc.* **58,** 625–627 (1936).
153. Adler, A. D. *et al.,* A simplified synthesis for meso-tetraphenylporphine. *J. Org. Chem.* **32,** 476–476 (1967).
154. Lindsey, J. S., *et al.,* Rothemund and Adler-Longo reactions revisited: synthesis of tetraphenylporphyrins under equilibrium conditions. *J. Org. Chem.* **52,** 827–836 (1987).
155. Arsenault, G. P., *et al.,* Pyrromethanes and Porphyrins Therefrom. *J. Am. Chem. Soc.* **82,** 4384–4389 (1960).
156. Lv, M., *et al.,* Selective and sensitive electrochemical detection of dopamine based on water-soluble porphyrin functionalized graphene nanocomposites. *RSC Adv.* **4,** 9261–9270 (2014).
157. Georgakilas, V. *et al.,* Functionalization of graphene: Covalent and non-covalent approaches, derivatives and applications. *Chemical Reviews* **112,** 6156–6214 (2012).
158. Paulus, G. L. C., *et al.,* Covalent electron transfer chemistry of graphene with diazonium salts. *Acc. Chem. Res.* **46,** 160–170 (2013).
159. Jiang, D. E., *et al.,* How do aryl groups attach to a graphene sheet? *J. Phys. Chem. B* **110,** 23628–23632 (2006).
160. Hu, Y. *et al.,* Photoelectrochemical sensing for hydroquinone based on porphyrin-functionalized Au nanoparticles on graphene. *Biosens. Bioelectron.* **47,** 45–49 (2013).
161. Liu, F., *et al.,* A selective and sensitive sensor based on highly dispersed cobalt for the detection of methyl parathion. *J Solid State Electrochem.*, **20**, 599–607 (2015).
162. Jahan, M., *et al.,* Electrocatalytically Active Graphene–Porphyrin MOF Composite for Oxygen Reduction Reaction. *J. Am. Chem. Soc.* **134,** 6707–6713 (2012).
163. Yang, Y. *et al.,* Porphyrin Functionalized Graphene for Sensitive Electrochemical Detection of Uric Acid. *Int. J. Electrochem. Sci.* **11,** 7370–7379 (2016).

PART B:

RESULTS AND DISCUSSION

CHAPTER I: Synthesis and properties of nanomaterials

Abstract

The hybrid nanomaterials which combined the features of both graphene (high conductivity and large specific surface area) and porphyrins (physical and chemical properties and electron transfer ability) were successfully synthesized. To investigate the characteristic properties of as-prepared nanomaterials, scanning electron microscopy (SEM), atomic force microscopy (AFM), UV-visible spectra, Fourier Transform infrared spectra (FT-IR), X-ray photoelectron spectra (XPS) and Raman spectroscopy were utilized. We confirm that the porphyrins interacted with CRGO and enhance the dispersion of graphene nano-sheet. The formation of hybrid nanomaterials through non-covalent interaction have no effect on electronic properties of chemically reduced graphene oxide (CRGO) and simultaneously introduce effectively functionalized groups on the surface of CRGO. Observed by AFM, the H_2TPP-4CP with more negative charge is anchored at the plane-like edges of CRGO which is considered as the electrochemical active centers through π-π stacking and hydrogen bond favoring the electron transfer process through hybrid nanomaterials. The electrochemical properties was explored by electrochemical impedance spectroscopy (EIS) and cyclic voltammetry (CV), which both confirm that the tight interaction exists between H_2TPP and CRGO, and the hybrid nanomaterial H_2TPP-4CP/CRGO possesses more negative charge due to the carboxylic groups on the surface introduced by attached porphyrins. The superior conductivity of the hybrid nanomaterial is proven through charge transfer resistance measured by EIS. Also, the value of n which reflects the charge distribution of the surface decreases from 1 to 0.5 obtained by the fitting data of EIS illustrating the increase of plane-like edge after modification process. The electrochemical process and reversibility monitored in redox marker p-benzoquinone/hydroquinone, the neutral redox marker without charge ligands demonstrates that the hybrid nanomaterials possess high electroactivity with enhanced k_s calculated by Nicolson model, compared to CRGO. The incorporation of manganese (III) is favor to further investigate properties of the nanomaterial through its electrochemical signal variation of the Mn^{3+}/Mn^{2+} redox complex. The ability of CRGO facilitates to immobilize a large amount of porphyrin. The advantages of such hybrid nanomaterial explore a high scope to their application in electrochemical biosensor.

Materials and Methods

1. Reagents

Graphene oxide was purchased from Aldrich. High purity graphite rods (99.995%, 6 mm diameter, 150 mm length) were purchased from Sigma-Aldrich. Sodium hydroxide (NaOH) was provided by Alfa Aesar. Hydrogen peroxide (H_2O_2) was purchased by Acros Organics. Aqueous solutions were purified with Milli-Q water (18.2 MΩ cm). Pyrrole and dichloromethane (DCM) were distilled under argon prior to use. All other solvents were used without purification. Reactions were monitored by thin layer chromatography (TLC) performed on silica gel sheets containing UV fluorescent indicator (60 F254 Merck). Yields refer to chromatographically pure compounds.

N, N-Dimethylformamide (DMF) was provided by Sigma-Aldrich. Phosphate buffers saline (PBS) pH=7.4, contained 10 mM Na_2HPO_4, 1.8 mM KH_2PO_4, 2.7 mM KCl and 137 mM NaCl was prepared with double distilled water, filtered by 0.22 μm membrane filter and stored at 4 ℃ until use.

2. Instruments and measurements

^1H and ^{13}C NMR spectra were recorded on Bruker *AC 250 and Bruker AV 360* spectrometers (63 and 90 MHz for ^{13}C, respectively). Chemical shifts δ, are reported in ppm taking residual $CDCl_3$ as the internal reference.

Mass spectra were recorded on a *Finningan-MAT-95-S*, using MeOH/CH_2Cl_2/H_2O (45/40/15, v/v) as solvent.

Scanning Electron Microscopy (SEM) images were acquired using a ZEISS SUPRA™ 55VP GEMINI®.

Atomic Force Microscopy. A commercial dimension 3100 (Vecco Instruments, USA)

atomic force microscope was used for topographical characterization of the samples. All measurements were performed in the tapping mode using rectangular silicon AFM tip.

UV-visible spectra were recorded with *uvikon xl* spectrometer.

Fourier Transform infrared spectra (FT-IR) were measured using a Bruker IFS66 FT-IR spectrometer equipped with a MCT detector and an attenuated total reflectance (ATR) crystal of germanium.

X-ray photoelectron spectroscopy (XPS) were conducted with a VG ESCALAB MKII spectrometer. The XPSPEAK software (Version 4.1) was used to deconvolute the narrow-scan XPS spectra of the C1s of the samples, using adventitious carbon to calibrate the C1s binding energy (284.5 eV).

Electrochemical measurements were performed using an AUTOLAB PGSTAT 100 electrochemical analysis system controlled by NOVA software (Methrom). The three-electrode cell was purchased from BASI and consisted of glassy carbon electrode (GCE) (surface 0.071 cm^2) as working electrode, a platinum as counter-electrode and Ag/AgCl as reference electrode. The analysis were performed by electrochemical impedance spectroscopy (EIS) and cyclic voltammetry (CV).

EIS analysis were performed in $[Fe(CN)_6]^{3-/4-}$ at 0.15 V vs. Ag/AgCl at DC potential of 10 mV with the frequency ranging from 100 KHz to 0.1 Hz. The impedance measurements in PBS solution were obtained at -0.3 V vs. Ag/AgCl at DC potential of 10 mV with the frequency ranging from 100 KHz to 0.01 Hz.

CV analysis were realized in 0.1 M KCl with 5 mM $[Fe(CN)_6]^{3-/4-}$ species in the range of potential from -0.2 to 0.6 V at various scan rates in the range 0.005–1 V s^{-1} and also analyzed in 0.1 M KCl with 1 mM benzoquinone in the range of potential from -0.4 to 0.2 V at various scan rates in the range 0.05–1 V s^{-1}.

3. Synthesis and preparation of nanomaterials

3.1 Synthesis of porphyrins

3.1.1 Synthesis of porphyrin functionalized with one carboxylic group

The synthesis of porphyrins is known to be tedious, long and complex[1]. Herein, we propose, a simple and effective way to prepare the tetraphenylporphyrin bearing one carboxylic group (H_2TPP-1CP) from the 5-(*p*-methoxyphenyl)triphenylporphyrin in three steps (Scheme 1.1). 5-(*p*-methoxyphenyl)triphenylporphyrin was first obtained in one step via a [2+2] condensation reaction from dipyrromethane and benzaldehyde with a good yield (20%).[2] The synthesis process is shown in scheme 1.1. After deprotection in acidic conditions, porphyrin bearing the hydroxy group was then condensed with 5–bromopentanenitrile by Willamson's condition to afford compound modified with nitrile. To obtain carboxylic porphyrin (H_2TPP-1CP), nitrile was hydrolyzed by 12M HCl and afforded the modified porphyrin with carboxylic group with good yields 32% (Scheme 1.2). The experimental section is shown in details in Supporting Informations.

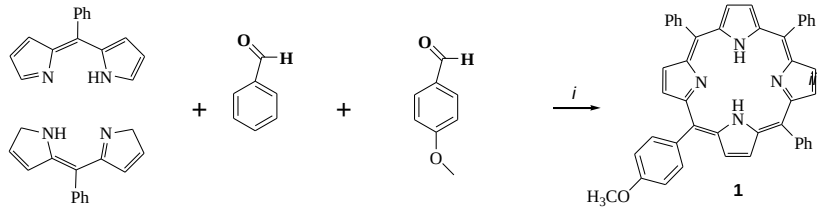

Scheme 1. 1. *Synthesis of 5-(p-methoxyphenyl)triphenylporphyrin (i) 1) TFA and 2) DDQ, air*

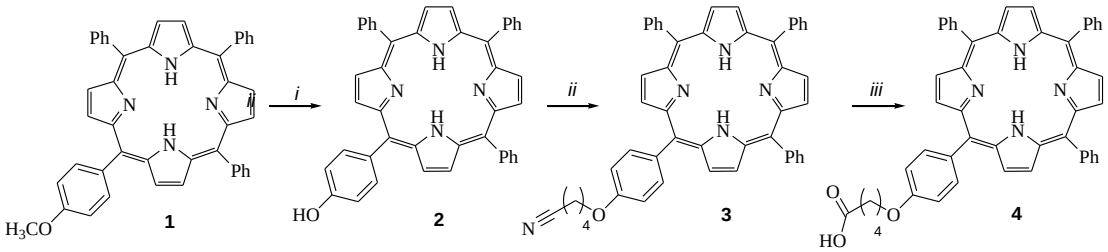

Scheme 1. 2. *Synthesis of H_2TPP-1CP (i) BBr_3, DCM, rt, 12h, 85%; (ii) $CsCO_3$, 5-Bromovaleronitrile DMF, 60 ℃, 12h, 60%; (iii) Dioxane, HCl 12M, 80 ℃, 24h, 62%*

3.1.2 Synthesis of metalated porphyrin functionalized with one carboxylic group

In order to study the electrochemical behavior of metallotetraphenylporphyrin both in the nanomaterial and biosensor, electroactive metal ion was incorporated into the macrocycle. The tetrapyrrolic macrocycle was quantitatively converted to metalated porphyrins inserted manganese (III) using $Mn(OAc)_2$ in dimethylformamide (Scheme 1.3). UV-visible spectrum demonstrated the insertion of manganese (III) into tetraphenylporphyrin macrocycle.

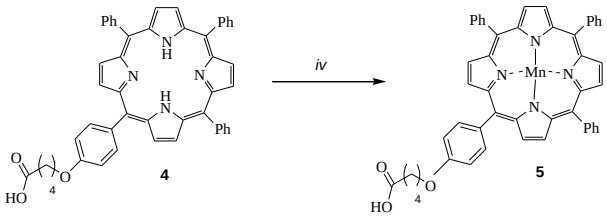

Scheme 1. 3. *Synthesis of metalated H_2TPP-1CP (MnTPP-1CP) (iv) $Mn(OAc)_2$, DMF, 80 ℃, 2 days.*

3.1.3 Synthesis of porphyrin functionalized with four carboxylic groups

The symmetrical tetraphenylporphyrin bearing four carboxylic groups (H_2TPP-4CP, **9**) is prepared from the 5, 10, 15, 20-*tetrakis* (*p*-methoxyphenyl)triphenylporphyrin (**6**) in three steps (Scheme 1.4) following the same procedure as H_2TPP-1CP. Due to the symmetry of the porphyrin (**6**), the strategy applied for the synthesis is Adler and Longo, in one step via a condensation reaction from four equivalents of pyrrole units and four equivalent of p-methoxybenzaldehyde in propionic acid (Scheme 1.5). After simple purification, porphyrin (**6**) is obtained with a good yield (30%).

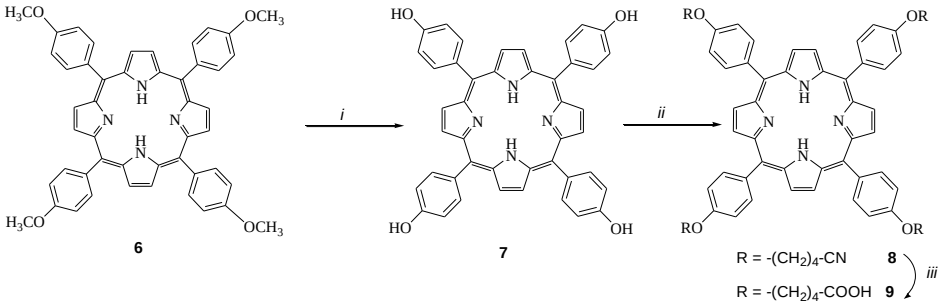

Scheme 1. 4*. Synthesis of H_2TPP-4CP* (**9**) *(i) BBr_3, DCM, rt, 18h, 86%; (ii) $CsCO_3$, 5-Bromovaleronitrile DMF, 60 ℃, 24h, 34%; (iii) Dioxane, HCl 12M, 80 ℃, 12h, 32%*

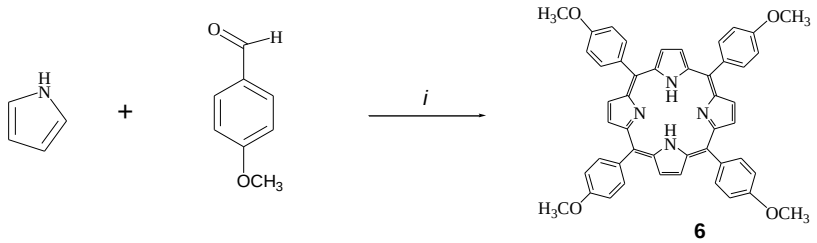

***Scheme** 1. 5. Synthesis of 5, 10, 15, 20-(p-methoxyphenyl)triphenylporphyrin (i) Propionic acid, 140 ℃, reflux 1.5*

3.2 Synthesis of Different types of graphene nano-sheets

Three different types of graphene nano-sheets were synthesized and compared. The first approach was explored by the electrochemical exfoliation of graphite and the others are reductive conversions from graphene oxide (GO) via either an electrochemical method to form ERGO nanomaterial or chemical reduced graphene oxide, denoted as CRGO. The electrochemical performance was optimized by cyclic voltammetry test in $[Fe(CN)_6]^{3-/4-}$. The characteristics and electrochemical properties were analyzed by XPS, Raman, and CV.

3.2.1 Synthesis of graphene via electrochemical exfoliation of graphite (EEG)

The electrochemical reduction of graphite rods was performed following the procedure described by Rao et *al*[3]. Graphite rod as working electrode was inserted into electrochemical cell with solution of 3 M NaOH and 130 mM H_2O_2. Platinum sheet as used as counter-electrode with 5 cm separation and 10V were applied between two electrodes during 15min. This reaction was conducted 4 times. Corrosion of the graphite anode were observed and subsequent black precipitate in solution was gradually obtained. The precipitate was collected by centrifugation at 10000 rpm, and then washed by distilled water, diluted HCl, and distilled water until pH=7.0. Then the solid was washed by ethanol and dried in oven overnight at 60 degree under vacuum. The exfoliated graphite solution was prepared by dispersing 1 mg of exfoliated graphite into 1 mL DMF, and then ultrasonicated during 1h for further test. The exfoliated process was shown in Fig. 1.1.

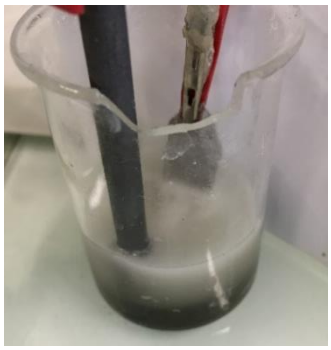

***Fig. 1.1**. The electrochemical exfoliation process*

3.2.2 Synthesis of RGO by using GO via electrochemical methods (ERGO)

The reduction of GO by electrochemical methods to obtain ERGO was carried out following the method described by Zhang et al[4]. It was performed after the immobilization of GO on the surface of GCE. The modified electrode was introduced in a 6 M NaOH and the reduction was performed by scanning the potential from -1.6 to 0 V vs. Ag/AgCl for 8 cycles at 50 $mV.s^{-1}$. The modified electrode was then washed with distilled water.

3.2.3 Synthesis of RGO by using GO via chemical methods (CRGO)

The commercial GO was firstly dispersed in DMF (0.5 mg mL^{-1}) under ultrasonically treatment for 30 min, and then heated in an oil bath (153 ℃) for 1 h to obtain CRGO. As seen in Fig. 1.2, the color of the dispersion changed from brown to black, initially signaling the conversion of GO into CRGO. Afterwards, CRGO was obtained after centrifugation under the rate of 10000 rpm and separated from the DMF solution. Successive centrifugations in water and in ethanol were done to wash CRGO sheets and then dried in oven overnight[5].

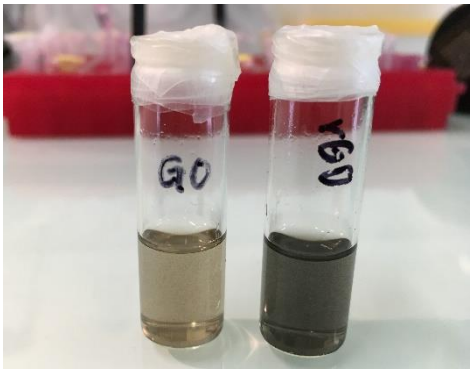

***Fig. 1.2**. The photograph of GO in DMF before (left) and after (right) reduction.*

3.3 Preparation of H_2TPP/CRGO hybrid nanomaterial suspensions

The designated CRGO solution was prepared by dispersing 1 mg of CRGO in 1 mL DMF, and ultrasonicated for 1h. The H_2TPP-1CP and H_2TPP-4CP solutions were prepared by dispersing 0.1 mg of porphyrins in 1 mL DMF, separately, and ultrasonicated for 30 min. The two kinds of porphyrin/CRGO nanomaterial suspensions, named H_2TPP-1CP/CRGO and H_2TPP-4CP/CRGO, were prepared by mixing 10 µL of CRGO suspension (1 mg mL^{-1}) and 10 µL volume of H_2TPP-1CP and H_2TPP-4CP solutions (0.1 mg mL^{-1}) separately to obtain 10:1 weight ratio of CRGO to porphyrin, followed by sonication for 30 min.

Results and Discussion

1. Properties of the materials

1.1 Porphyrin and metalloporphyrin

The UV-visible spectra of H_2TPP-1CP and H_2TPP-4CP display characteristic bands of porphyrin, including an intense Soret band at 419 nm and four characteristic visible absorption bands (Q-bands) at 514, 551, 591, and 645 nm as is shown in Fig. 1.3. Incorporation of manganese (III) into tetraphenylporphyrin macrocycle to form metallotetraphenylporphyrin (MnTPP-1CP) leads to the reduction of the Q bands from four to two in the UV−visible spectra and a red shift in Soret band. This result confirms the introduction of metal ions into the marcocycle.

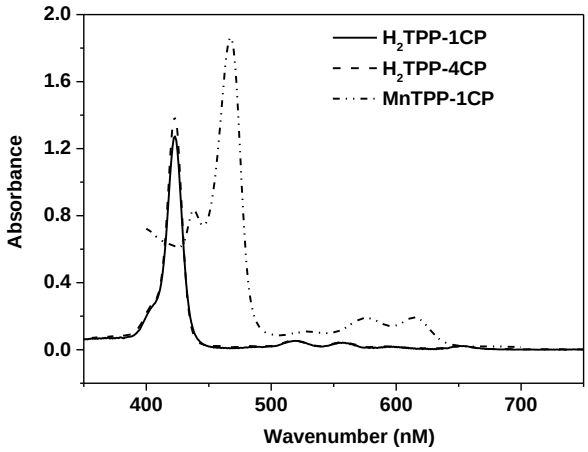

***Fig. 1.3**. UV-Visible spectra of H_2TPP-1CP, H_2TPP-4CP and MnTPP-1CP measured in DMF*

1.2 Characteristics of reduced graphene

GO is generally highly oxygenated, bearing hydroxyl, epoxide, diol, ketone and carboxyl functional groups that disturb the van der waals interactions and significantly improve solubility in water and solvents. Chemical reduction of GO removes the oxygen functional group from the surface. The reduction of GO also favors the formation of hetero-structure with plane-like edge and nano band which is electrochemical active compared to basal plane electrochemically inert[6]. Thus depending on the methods of reduction the electrochemical properties and the rate of homogenous electron transfer should be improved.

To intuitively evaluate the reduction level and determine the composition of the obtained CRGO sheets, X-ray photoelectron spectroscopy (XPS) was utilized. As shown in Fig. 1-4, the C/O ratio in the exfoliated commercial GO increases remarkably after chemical reduction. The specific peaks at between 286 and 289 eV, which are assigned to epoxide, hydroxyl, and carboxyl groups remarkably decrease, revealing that the oxygen-containing groups were eliminated. Meanwhile, the intensity of the peak located at a binding energy of 284 eV, which is corresponding to sp^2 carbon, is much enhanced compared to that of peak centered at 285.5 eV (sp^3 carbon)[7], demonstrating that the obtained CRGO has a high reductive level. The ratio of carbon content in GO and CRGO is estimated to be 45% and 86% respectively. In the same way the ratio of oxygen content decreases from 55 % for GO to 14% for CRGO (Table 1.1).

The result of XPS shown in Fig. 4D appears a new peak at 290.1 eV corresponding to the π-π^* conjugation, indicating that the CRGO is compact with multi-layer stacks.

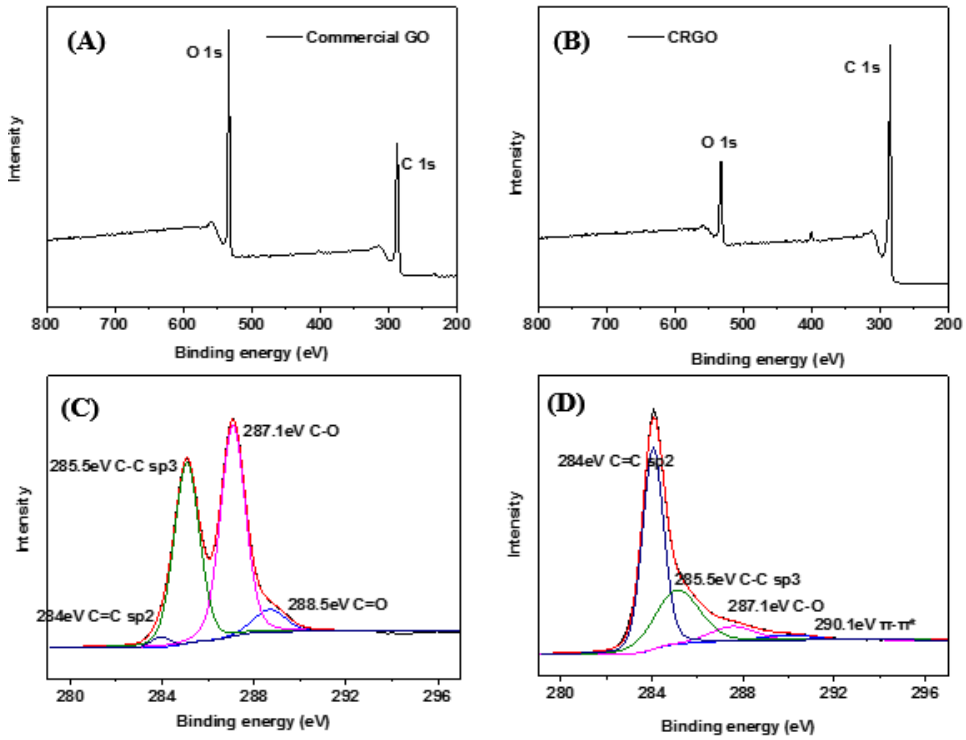

***Fig. 1.4**. X-ray photoelectron spectra of the GO before (A) and after (B) reductive reaction. , and (C), (D) the corresponding C1s XPS spectra.*

***Table 1.1**. Physical parameters extracted from XPS spectra.*

Peak Table : GO					
Name	Peak BE	FWHM eV	Area (P) CPS.eV	Area (N)	Atomic %
O1s	533.13	2.96	1180555.15	1180555.15	55
C1s	286.66	4.27	980100.11	980100.11	45

Peak Table : CRGO					
Name	Peak BE	FWHM eV	Area (P) CPS.eV	Area (N)	Atomic %
O1s	532.27	3.86	406502.21	2261.28	14
C1s	285	3.07	1004332.75	14256.22	86

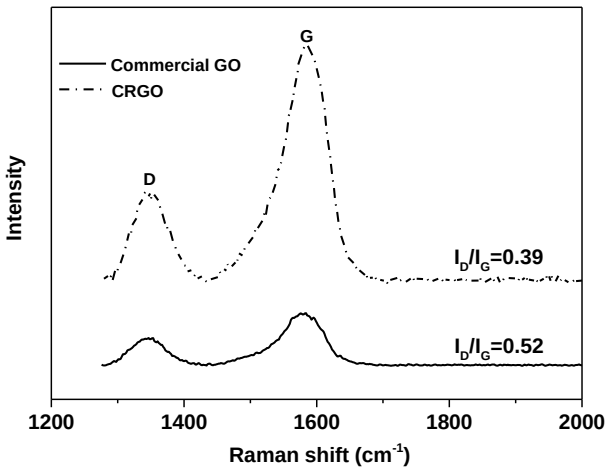

Fig. 1.5. *Raman spectra of GO and CRGO*

Complementary to XPS data, Raman spectroscopy, which is powerful and most widely used technique to characterize properties of graphene such as defect and disordered structures, has been performed before and after reduction of graphene (Fig. 1.5). Raman spectra of graphene give two characteristic bands, the D band at 1360 cm^{-1} related to the vibration of carbon atoms with sp^3 configuration of disordered graphene, while the G bond at 1585 cm^{-1} is associated to in-plane vibration of sp^2-bonded of carbon atoms. The I_D/I_G ratio gives information on the defect of graphene or the graphene sheet domains. Fig. 1-5 shows the spectra of GO and CRGO. After chemical reduction of graphene the band D and G remain at the same position. However small variation in I_D/I_G ratio, is observed where the ratio decrease after reduction of graphene. This indicates an increase of the sp^2-bond and less disorder in structure. Thus CRGO possess less defect than GO, which could favor the conductivity and electron transfer ability. Same behavior was observed concerning the chemical reduction of GO[8].

To check the electron transfer properties of CRGO compared to GO, the electron transfer were analysis through redox properties of redox couple $[Fe(CN)_6]^{3-/4-}$. Thus layers of both materials GO and CRGO were deposited on the surface of GCE through drop casting and electron transfer were analyzed by cyclic voltammetry (CV) in solution containing the redox couple. Fig. 1.6A shows the CV obtained on GCE

(curve a), GCE modified with GO (curve b) and with CRGO (curve c). GO underlines lower current density and decreased reversibility compared to GCE. In the case of electrode modified with CRGO, an increase of redox current as well as the reversibility of the redox process were obtained. This could be explained by both the decrease of oxidative species such as epoxide and hydroxyl groups and increase of sp^2 domains after graphene reduction which leads to more conductive carbon nanomaterials. In the same way the increase of electrochemical properties of graphene could be related to the increase of edge surface compared where reduction could increase the exfoliation and formation of graphene sheet domains. This result is in agreement with the data in literature where electrochemical activity of edge plane is improved compared to basal plane[9].

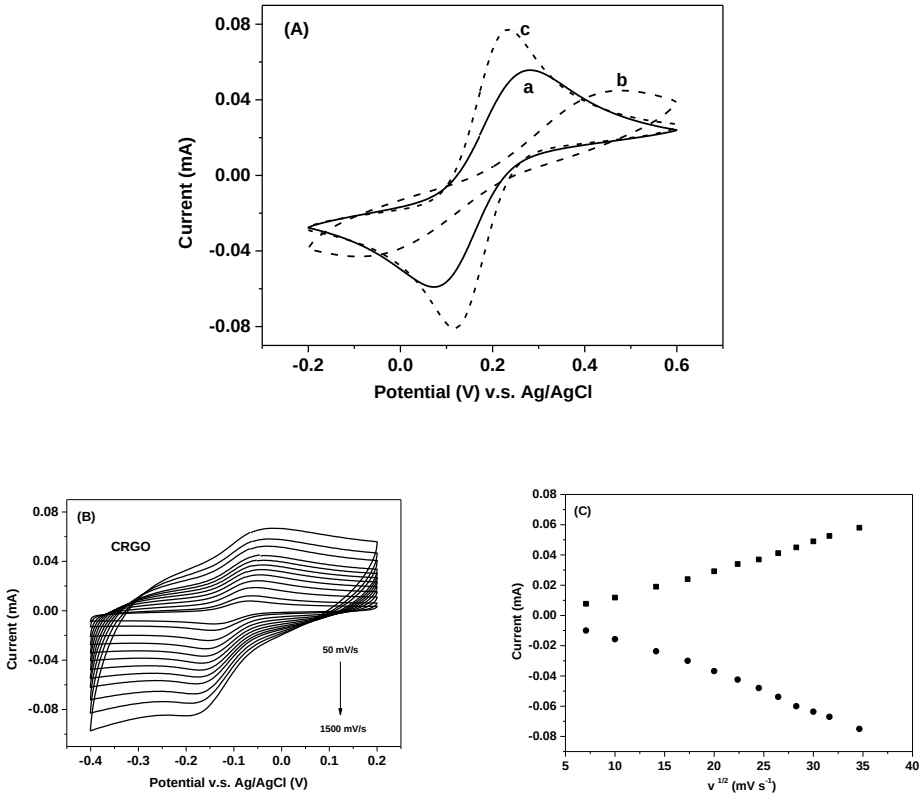

Fig. 1.6 *(A) CV measurements of GCE electrode modified with GCE (a), commercial GO (b), CRGO (c). The analysis were performed in solution 5 mM* $[Fe(CN)_6]^{3-/4-}$ *with scan rate 50mVs*$^{-1}$*, (B) CRGO obtained in 0.1 M KCl with 1 mM benzoquinone in the range of potential from -0.4 to 0.2 V at various scan rates in the range 0.05-1 V s*$^{-1}$*, and (C) shows the variation of anodic and cathodic current peaks vs.* $v^{1/2}$

Both these results are in agreement with Raman results and confirm that chemical reduction of graphene oxide leads to increase of conductivity due to decrease of oxide on the surface and increase of graphene sheet layers. For quasi-reversible electrode, of which peak potential separation is larger than 59.5/*n* mV, where *n* is the number of electron transferred of benzoquinone, although the cathodic peak current equals to its corresponding anodic one, the Nicholson method was used to calculate the rate constant[10]. Following the Nicholson's working curve, the ΔE_p can be converted into a dimensionless kinetic parameter ψ for the coefficient of electron transfer $\alpha = 0.5$, which is directly proportional to the reciprocal of the square root of scan rate $v^{-1/2}$ (Fig. S1-3). The rate constant can thus be calculated by equation (1):

$$k_s = \frac{slope}{\sqrt{RT/nFAD}} \quad (1)$$

where k_s is given in cm s^{-1}, the slope is obtained from a linear fit of $\psi \sim v^{-1/2}$ relationship, *n* is the number of electron transfer (*n*=2), *F* is the Faraday constant and *D* the diffusion coefficient of the redox marker benzo/hydroquinone in aqueous media which is obtained by the Randles–Sevcik equation[11], $i_p = 2.99\times10^5\, nACD^{1/2}v^{1/2}$ (*D*= 1.17×10^{-6} cm^2 s^{-1}). The k_s value is calculated to be 0.011 cm s^{-1} for CRGO, which is close to that of carbon pyrolysed at 800 °C (0.018 cm s^{-1}) in the same order of magnitude[10].

2. Interaction between porphyrins and CRGO

2.1 The association and dispersion

The hybrid nanomaterial suspensions were prepared by adding H_2TPP into 1 mg mL^{-1} as-obtained CRGO, followed by ultrasonication for 30 min, the as-prepared H_2TPP-1CP and H_2TPP-4CP suspensions were kept in the fridge over one week. As observed in Fig. 1.7, the CRGO is aggregated and the precipitate is observed, in

contrast, the addition of porphyrin into CRGO suspension results in the formation of more stable and homogeneous hybrid nanomaterial suspensions, thus illustrates that the porphyrin functionalized with carboxylic group improves the solubility and dispersion of CRGO.

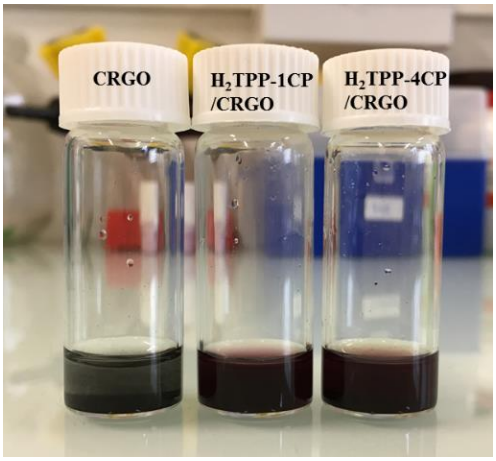

Fig.1.7. *Images of DMF dispersions (1 mg mL^{-1}) of CRGO, H_2TPP-1CP/CRGO and H_2TPP-4CP/CRGO.*

To characterize such hybrid nanomaterials and their properties, various physical and chemical methods were investigated. SEM and AFM images were performed for the characterization of morphologies. Spectroscopic characterization by UV-Visible, FT-IR and Raman were realized for molecular characterization and EIS, CV for electrochemical analysis to investigate electron transfer properties.

2.2 Morphologies characterization

Morphologies of the as-prepared hybrid nanomaterials were characterized by SEM image of deposit layer on GCE electrode and the results were shown in Fig. 1.8. The images show the CRGO (image a), the nanomaterials with H_2TPP-1C/CRGO (image b), and H_2TPP-4C/CRGO (image c). Fig. 1.8a shows that CRGO exhibits compact sheet with irregular layer structure with folding. Nano sheets with many wrinkles and corrugation are also observed. In the case of hybrid nanomaterial H_2TPP-1CP/CRGO associated with functionalized porphyrin bearing one carboxylic group, a dispersed nano-sheet layer is observed with formation of high edge surface. This behavior is improved in the case of association of modified porphyrin bearing 4 carboxylic groups. H_2TPP-4CP/CRGO displays a dispersion into monolayer of

graphene sheet or few-layered stacks. The flakes appear thin and semitransparent with less wrinkled textures compared to CRGO. This demonstrates that the anchoring of porphyrin moieties weakens the interaction between the CRGO sheets, which further improves the dispersion of CRGO and formation of nano-sheets of graphene and edge surface. The flakes of H_2TPP-1CP/CRGO fold together with ordered flakes of 20-30 μm range and present crinkly sheets with more aggregation, compared to that of H_2TPP-4CP/CRGO with 5-10 μm range. The more extensive dispersion of H_2TPP-4CP/CRGO is due to the larger size of the H_2TPP-4CP macromolecules and also the negative charge provided by carboxylic group which could lead to more electrostatic interaction with graphene compared to that of H_2TPP-1CP bearing one carboxylic group.

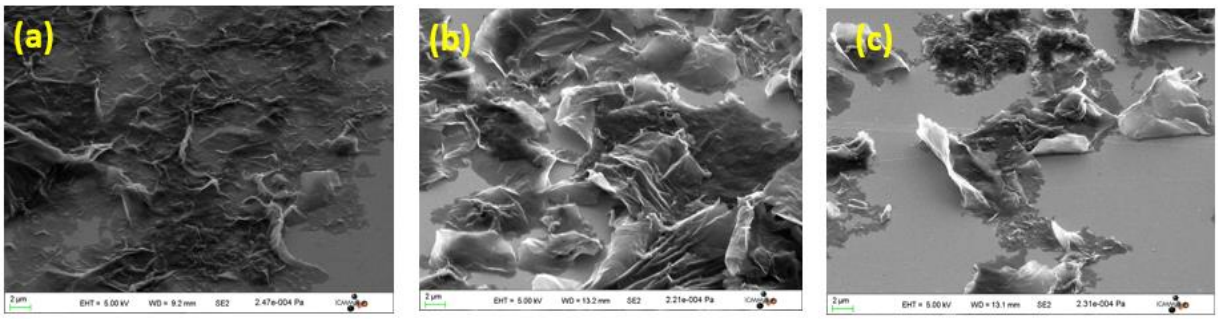

Fig. 1.8. *SEM images of (a) CRGO and, (b) H_2TPP-1CP/CRGO, and (c). H_2TPP-4CP/CRGO*

The surface topologies of CRGO and hybrid nanomaterials H_2TPP-1CP/CRGO and H_2TPP-4CP/CRGO have been also studied by atomic force microscopic (AFM). Fig. 1.9a displays an image of CRGO sheets exhibiting flat surface and compact structure with roughness of 6nm. which is greater than the theoretical value for graphene nanosheets of 0.34 nm owing to the multi-layer of graphene sheets on the surface[12,13] and π-conjugated compact surface of CRGO. In the case of hybrid nanomaterials H_2TPPs/CRGO, as we can see in Fig. 1.9b and c, nanosheets of graphene were formed, due to the association of porphyrins, which lead to the dispersion of CRGO. The roughness factor of hybrid nanomaterial H_2TPP-1CP/CRGO is up to 250 nm, also due to the formation of small nano-sheet domains

and edge plane which are upward. From the result of Fig. 1.9c, it is noteworthy that the comparison of the images at the edges of the CRGO sheets is higher than that of interior regions (black circle in Fig. 1.9c). This phenomenon is likely caused by the presence of a higher density of functional groups where the association of porphyrins could be favored at the edge as observed also previously in the case of association of modified porphyrin with CRGO[14].

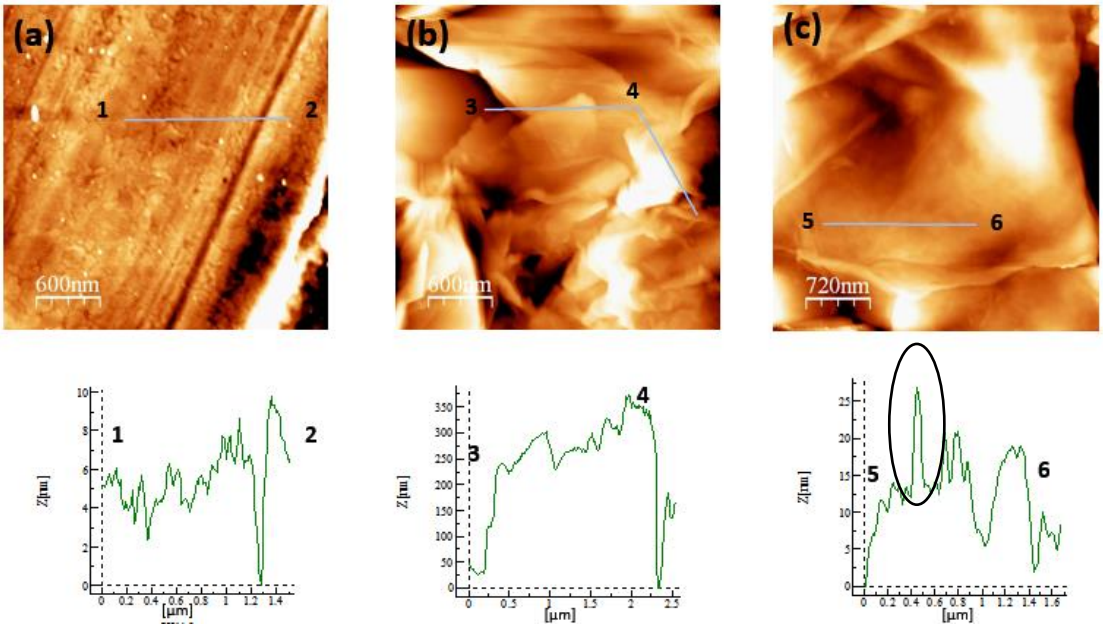

Fig. 1.9. *AFM images of (a) CRGO and, (b) H_2TPP-1CP/CRGO, and (c). H_2TPP-4CP/CRGO*

2.3 Molecular characteristics and electronic properties of nanomaterials

The comprehensive exploration including the molecular characteristics and electronic properties of the interaction between H_2TPP with different carboxylic groups and CRGO were performed through spectroscopic studies.

2.3.1 Molecular characteristics

Association between H_2TPP and CRGO of hybrid nanomaterials was evaluated by UV-visible and FT-IR spectroscopies. The UV-visible absorption of complex H_2TPP-1CP/CRGO (Fig. 1.10A) and H_2TPP-4CP/CRGO (Fig. 1.10B) in DMF exhibits an intense Soret band at 417 nm characteristics of the electronic transition of complex from deeper π levels to LUMO and the four characteristic Q bands between

500 and 700 nm corresponding to π - π* electronic transition from the HOMO to the LUMO[15]. After the association of CRGO there is no shift on the Soret band of porphyrin, indicating that the association of porphyrin and CRGO has no effect on the electronic properties of the macrocycle of porphyrin. However, a decrease in the intensity of the absorbance has been observed with the successive addition of CRGO with constant concentration of porphyrin, which confirmed the intimate interaction between H_2TPP and CRGO. The spectra in Fig. 1.10A and B were further analyzed using the Benesi-Hildebrand expression by equation (2):

$$\frac{1}{\Delta D} = \frac{1}{1 * \varepsilon_{417} * K_a * C_{H_2TPP} * C_{CRGO}} + \frac{1}{\varepsilon_{417} * C_{H_2TPP}} \quad (2)$$

where K_a denotes the apparent association constant, ε is the molar absorption coefficient of porphyrin adsorbed on CRGO. Inverse of the difference absorbance at 417 nm (1/D417) was plotted versus inverse of the CRGO concentration ($1/C_{CRGO}$). Using the slope and the intercept of the linear fit we obtained the apparent association constant of H_2TPP-1CP/CRGO and H_2TPP-4CP/CRGO calculated to be 85.1 g^{-1} L and 64.4 g^{-1} L, respectively, which exhibit in the same order of magnitude of previous 56.6 g^{-1}.[16] However, the large apparent value of K_a shows that the interaction between H_2TPP and CRGO sheets is rather strong and that it can be achieved in relatively dilute solutions.

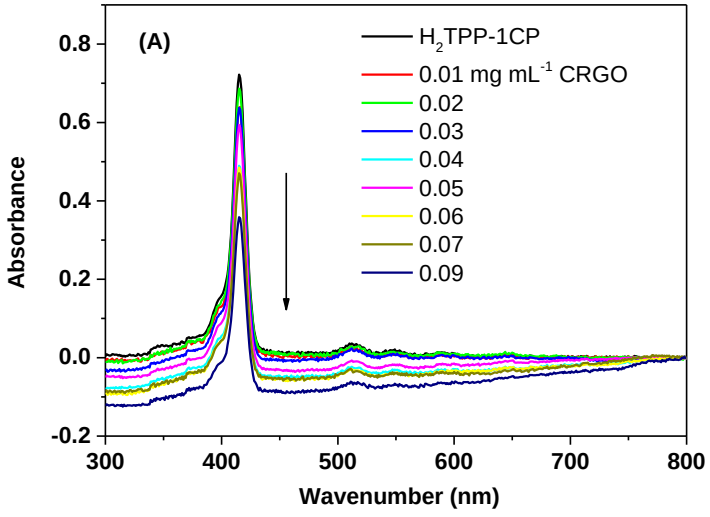

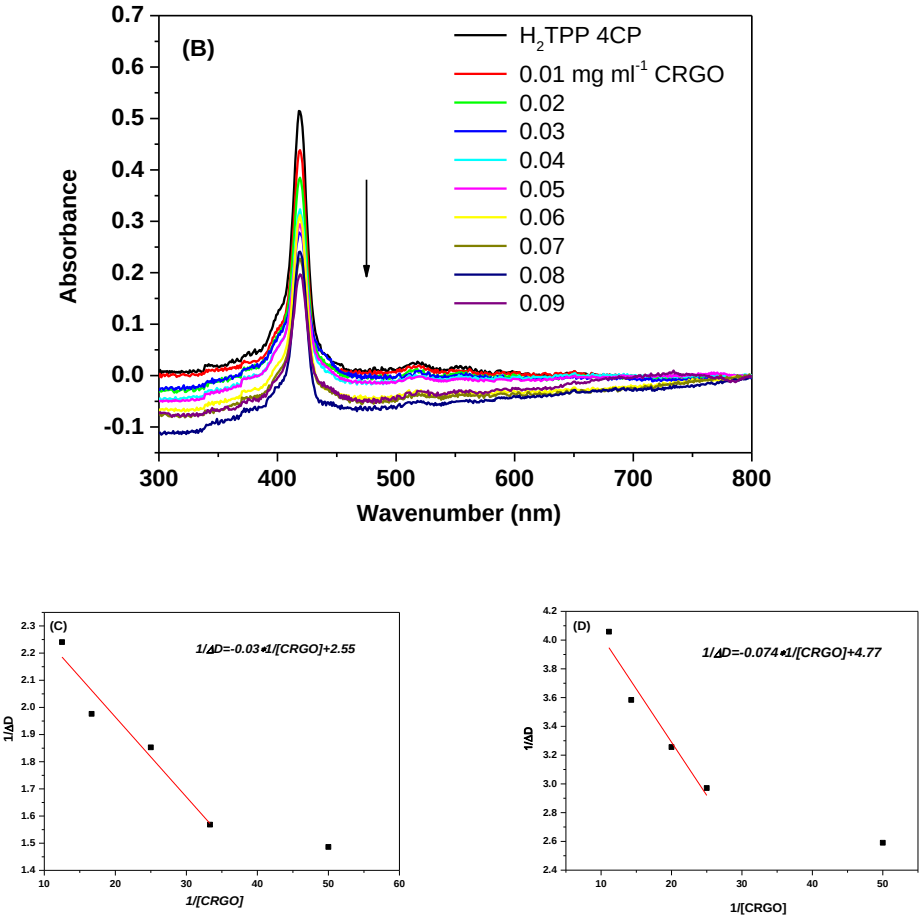

Fig. 1.10. *UV-Visible spectrum of (A) H_2TPP-1CP and H_2TPP-1CP/CRGO; (B) H_2TPP-4CP and H_2TPP-4CP/CRGO with successive increased comcentration of CRGO measured in DMF. The affinity constant calculation of H_2TPP-1CP/CRGO (C) and H_2TPP-4CP/CRGO (D)*

The as-prepared hybrid nanomaterial suspensions were dropped casting on GCE plates. The obtained samples were characterized by FT-IR spectroscopy. For H_2TPP-1CP/CRGO, the FT-IR spectra (Fig. 1.11A) exhibits a band at 3256 cm^{-1} which is assigned to OH vibrations of carboxylic group of modified porphyrin and two stretching vibration bands in the double band region, at 1727 cm^{-1} corresponding to the C=O vibration and at 1577 cm^{-1} that can be attributed to C=C vibration. In comparison with H_2TPP-1CP, the value of C=C shifts from 1611 to 1577 (33 cm^{-1} shift) due to π-π interaction between phenyl substituted porphyrin and π-conjugated CRGO. For H_2TPP-4CP/CRGO (Fig. 1.11B), the analogous result is observed,

however, the red shift is merely 15 cm^{-1}, which is much lower than that of H_2TPP-1CP/CRGO. The phenomenon is attributed to the less π-conjugation, probably due to the anchoring of H_2TPP-4CP is more on the edges of CRGO instead of the basal plane. The 21 cm^{-1} red shift of C=O value due to the formation of hydrogen bond between H_2TPP-4CP and CRGO, however, scarcely shift for H_2TPP-1CP/CRGO further demonstrate that the H_2TPP-4CP is anchored at the edge of CRGO which is expected to enhance the electron transfer. The data of functional groups in details are shown in Table S1.1.

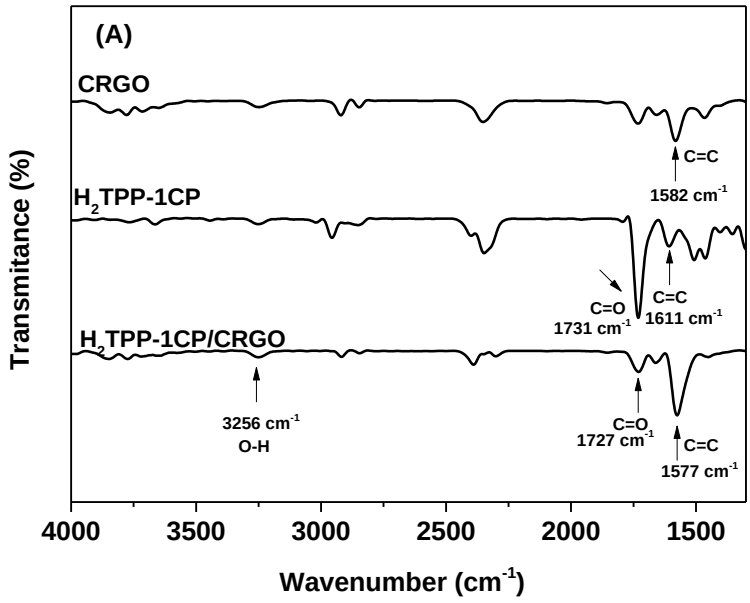

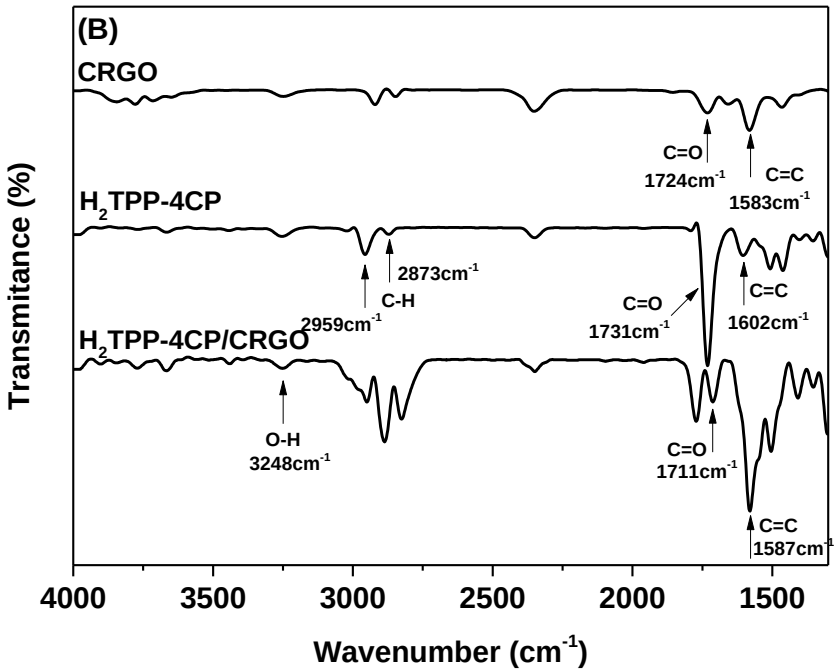

Fig. 1.11. *(A) FT-IR spectroscopy and (B) FT-IR of (a) CRGO, (b) H_2TPP-4CP, and (c) H_2TPP-4CP/CRGO*

The interaction between the CRGO and H_2TPP were also characterized by using Raman spectroscopy (Fig. 1.12). The Raman spectra of CRGO show two broad peaks at 1352 and 1602 cm^{-1}, which correspond to the D- and G-bands of CRGO. After interacted with H_2TPP-1CP and H_2TPP-4CP, the intensity ratio of D/G was increased compared to that observed in CRGO. The increase of the I_D/I_G intensity ratio suggests that the average size of the sp^2 domain is decreased and the sp^3 domain is increased upon association of the H_2TPP and also the formation of various graphene domains. The formation of the various graphene domains could be related to the high dispersion process as observed previously in SEM and AFM images. The low shift of the G-band could be contributed to electron doping as a consequence of π-π interaction between porphyrin and CRGO[17,18], which demonstrates that the porphyrin has little effect on the electronic properties of CRGO. The higher I_D/I_G ratio of H_2TPP-4CP/CRGO, compared to the H_2TPP-1CP/CRGO, confirming more defect of H_2TPP-4CP/CRGO, which is coincide to the result of FT-IR.

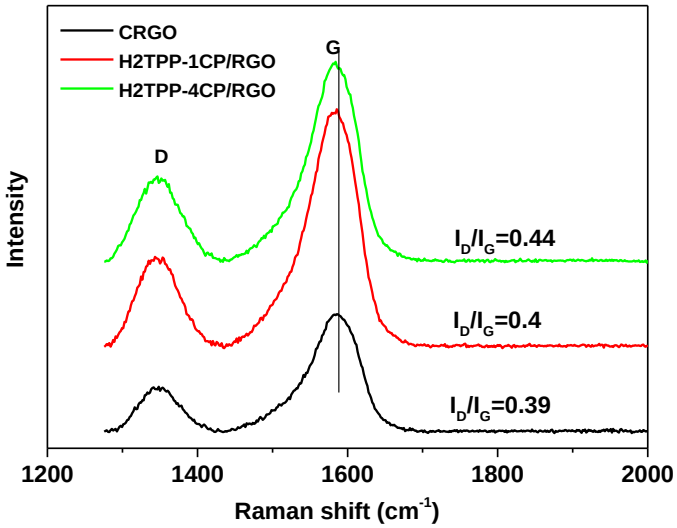

Fig. 1.12. *Raman spectra of CRGO, H_2TPP-1CP/CRGO and H_2TPP-4CP/CRGO*

2.3.2 Electrochemical characteristics

Electrochemical impedance measurement (EIS) was used to characterize electrochemical properties of the modified layer especially the interface between the electrode and solution, including the impedance of the layer, capacitance of the electric double layer and the electron transfer resistance (R_{ct}). Thus the analysis has been performed in PBS free of redox marker and the results were shown in Fig. 1.13. The Nyquist plot of the nanomaterials H_2TPP/CRGO deposit on GCE exhibit a semicircle portion and any diffusion process is observed at low frequency range compared to GCE demonstrating the electron transfer-limited process. After the addition of H_2TPP, a second circle has been observed presumably due to the exfoliation and dispersion of CRGO. The EIS data are fitted by Randles equivalent circuit model, where R_s is the electrolyte resistance, R_{ct} is the electron transfer resistance, while the double layer capacitance (C_{dl}) is replaced by constant phase element (CPE). The impedance of CPE could be written as $Z_{CPE} = 1/Q(j\omega)^n$, where Q and n are independent of the frequency, ω is the radial frequency and n is a dimensional parameter reflecting the surface charge distribution, where the value is $-1 < n < 1$. When n=1 a pure capacitance is obtained, for $n = 0.5$ the impedance is corresponding to Warburg, when $0 < n < 1$ the impedance is CPE. The analytical

treatment of impedance data allows discrimination between CPE behavior or capacitance. The value of *n* can be determined by fitting the EIS data. The diameter of semi-circle related to the value of R_{ct} decreases from 92.4 kΩ to 72.4 kΩ and 59.4 kΩ with respectively GCE H_2TPP-4CP/CRGO and H_2TPP-1C/CRGO which indicates that the formation of hybrid nano-materials and the association of H_2TPP enhances the charge transfer process. Compared to H_2TPP-1CP/CRGO, the less decrease of R_{ct} value of H_2TPP-4CP/CRGO with four carboxylic groups is probably attributed to the more negatively charge of porphyrin which results in the separation and no connection of dispersed nanosheets. The EIS data were satisfactory fitted by modified equivalent circuit model, and allows determining electrical parameters for each layer formation. The capacitance is directly related to the thickness of the layers. From the capacitance value obtained by the CPE_2 for H_2TPP-1CP/CRGO and H_2TPP-4CP/CRGO, the thickness of H_2TPPs layers could be estimated following the equation 3:

$$C = \frac{A\varepsilon_0\varepsilon_1}{d} \qquad (3);$$

where ε_0 is the vacuum dielectric constant, ε_1 is the double layer dielectric constant, *A* is the surface area and *d* is the thickness of the layer. The thickness of the H_2TPP layers could be calculated from the capacitance value obtained from the second film of H_2TPP layers. The value calculated to be 72 ± 9.3 nm and 20.4 ± 1.2 nm, respectively for H_2TPP-1CP/CRGO and H_2TPP-4CP/CRGO, further confirming that for H_2TPP-1CP/CRGO, the nano-sheet is formed and the higher value, compared to H_2TPP-4CP/CRGO, exhibits some aggregated domains upwards, and for H_2TPP-4CP/CRGO, the porphyrin is anchored at the edge of CRGO, which is in agreement with the results of AFM.

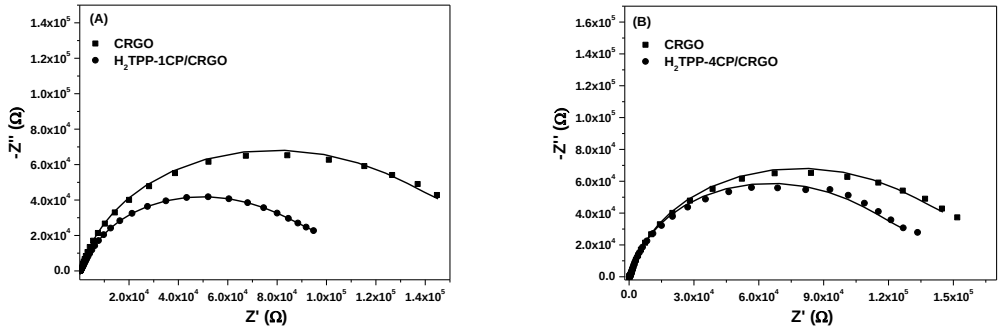

Fig. 1.13. *Nyquists plots measured in PBS solution at applied potentiel -0.3V with Dc potential of 10mV at frequency range of 100 KHz to 0.01Hz with various modified electrode H_2TPP-1CP/CRGO (A) and H_2TPP-4CP/CRGO (B)*

For further comprehensive investigation of the effect of negative charge on the charge transfer in the complex, the negatively charge redox marker $[Fe(CN)_6]^{3-/4-}$ was utilized for EIS measurement. The Nyquists plots are shown in Fig. 1.14. The diameter of semicircle corresponding to the R_{ct} increases from 3.32 kΩ to 3.49 kΩ after interaction between H_2TPP-1CP and CRGO, for the nanomaterial H_2TPP-4CP/CRGO, the R_{ct} increases much higher from 3.32 kΩ to 8.43 kΩ, which is attributed to the more negatively charge induced on the surface, which blocks the diffusion of ion to the electrode surface. The nanomaterial was also characterized by cyclic voltammetry (CV) in the presence of negative redox marker $[Fe(CN)_6]^{4-/3-}$ (Fig. 1.15). The diffusion coefficient value was calculated to be 6×10^{-6} cm^2 s^{-1} and 2.4×10^{-6} cm^2 s^{-1}, respectively for H_2TPP-1CP/CRGO and H_2TPP-4CP/CRGO. Meanwhile, the calculated electron transfer constant k_s of redox marker with negative ligants is affected by hybrid nanomaterials with negative charge. In the case of CV with negative redox marker, with the increase of carboxylic group, the reversibility becomes worse, which can be attributed to the strong electrostatic repulsion blocking the diffusion of negative ions to the electrode surface.

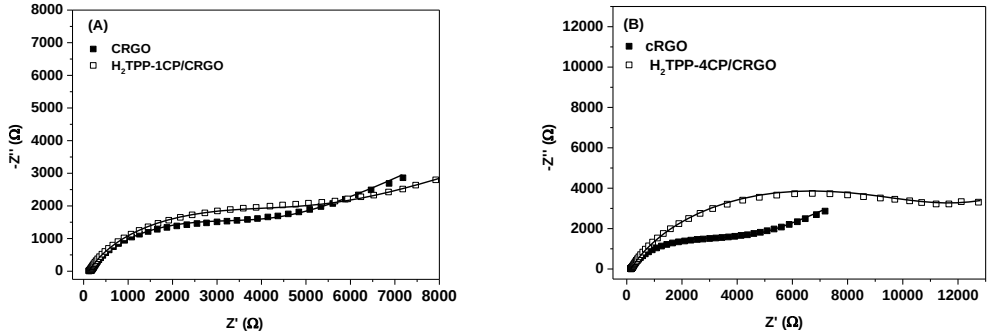

Fig. 1.14. *Nyquists plots measured in $[Fe(CN)_6]^{3-/4-}$ solution at applied potentiel 0.15 V with various modified electrode (A)CRGO, H_2TPP-1CP/CRGO and (B) H_2TPP-4CP/CRGO.*

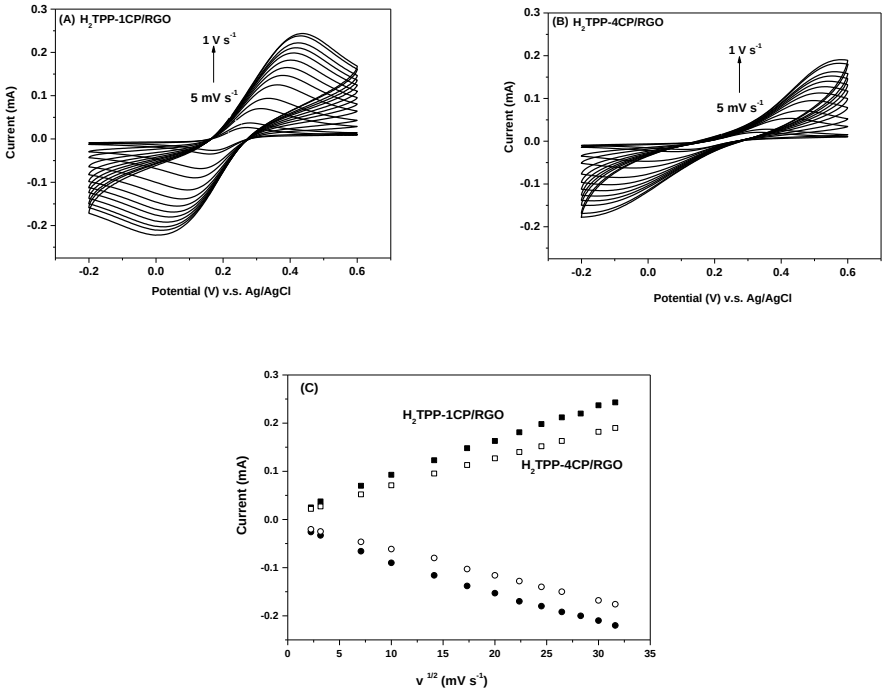

Fig. 1.15. *Cyclic voltamograms for glassy carbon electrode covered by (A) H_2TPP-1CP/CRGO, (B) H_2TPP-4CP/CRGO obtained in 0.1 M KCl with 5 mM $[Fe(CN)_6]^{3-/4-}$ species in the range of potential from -0.2 to 0.6 V at various scan rates in the range 0.005-1 V s, and* (C) *shows the variation of anodic and cathodic current peaks vs. $v^{1/2}$*

When the neutral redox marker p-benzoquinone/hydroquinone was employed for electrochemical characterization, the remarkably higher electrochemical process and high reversibility is observed for both hybrid nanomaterials (Fig. 1.16). The rates of

homogenous electron transfer (k_s) followed by Nickolson model (Fig. S1.3) for H_2TPP-1CP/CRGO and H_2TPP-4CP/CRGO are calculated to be 0.028cm s^{-1} and 0.01 cm s^{-1} respectively, which is the same magnitude order of the value 0.01cm s^{-1} for CRGO and to a great extent increase the electron transfer of benzoquinone compared to bare GCE (0.0013 cm s^{-1})[10], further elucidating that the addition of H_2TPP-1CP/CRGO enhance the electron transfer and the addition of H_2TPP-4CP/CRGO has no effect on the rate of electron transfer. The kinetic data is summarized in Table 1.1.

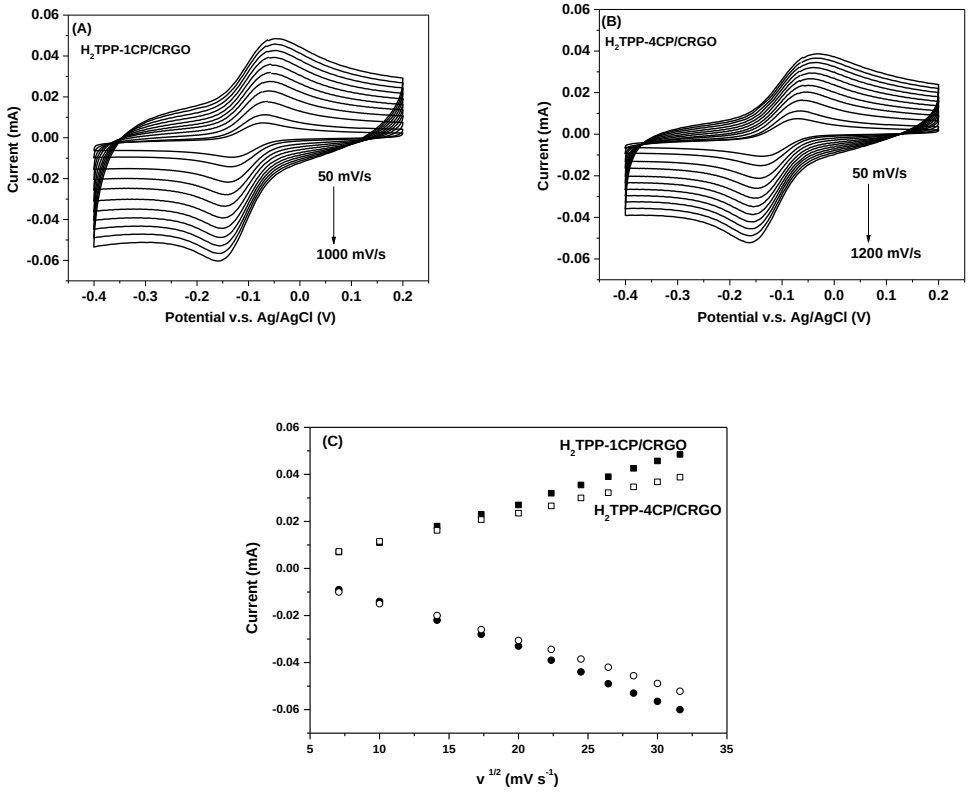

Fig. 1.16. *Cyclic voltamograms for glassy carbon electrode covered by (A) H_2TPP-1CP/CRGO, (B) H_2TPP-4CP/CRGO obtained in 0.1 M KCl with 1 mM benzoquinone in the range of potential from -0.4 to 0.2 V at various scan rates in the range 0.05-1 V s^{-1}, and The (C) show the variation of anodic and cathodic current peaks vs. $v^{1/2}$*

Table 1.1*. Electrochemical parameters obtained for electrodes of various modifications*

	In PBS			In benzoquinone		In $Fe(CN)_6^{3-/4-}$	
	R_{ct} (KΩ)	**N**	**Thickness (nm)**	**Do (10^{-6} cm^2 s^{-1})**	**k_s ($cm.s^{-1}$)**	**Do (10^{-6} cm^2 s^{-1})**	**k_s ($cm.s^{-1}$)**
CRGO	135 ±2.43	0.941 ±0.006	4.42± 0.91	1.17	0.01		
H_2TPP-1CP/CRGO	59.4± 1.34	0.532±0.01	72.1 ± 9.3	0.99	0.02	6.11	0.0057
H_2TPP-4CP/CRGO	72.4± 1.59	0.562±0.01	20.4 ± 1.2	0.56	0.01	2.47	0.0006

From these results, we can conclude that after the addition of porphyrin, the electron transfer is enhanced and the rugosity factor is increased, compared to CRGO. The thickness of H_2TPP-1CP/CRGO is much higher than that of H_2TPP-4CP/CRGO, even which is much larger, indicating that H_2TPP-1CP and CRGO were associated through π-π interaction between phenyl group and π-conjugated CRGO, which presumably induce the carboxylic group with carbon chain upwards. However, for H_2TPP-4CP/CRGO, due to the formation of hydrogen bond, the thickness is less than the value of H_2TPP-1CP/CRGO, which has no effect on the electron transfer of redox marker p-benzoquinone/hydroquinone. We can propose a mechanism of the H_2TPP/CRGO association where the H_2TPP-1CP and H_2PTT-4CP were associated through π-π interaction of phenyl group with the graphene sheet specialy in the plane-like edge. This could be presented in scheme 1.6.

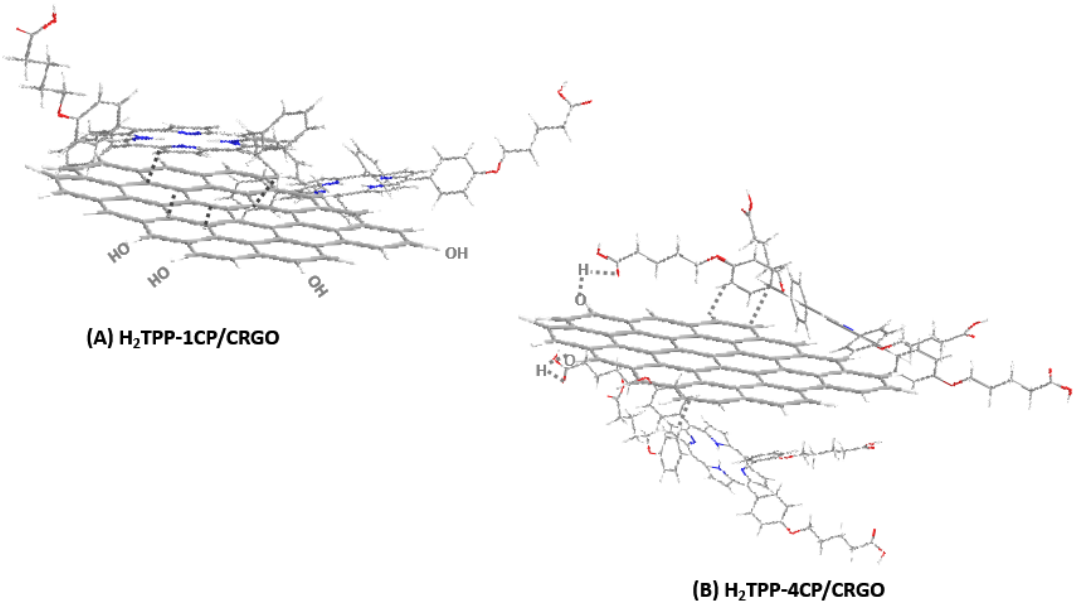

Scheme 1.6. *Schematic representation of interaction between H_2TPP and CRGO*

3. Interaction between metallporphyrins and CRGO

In order to further investgate the coverage of porphyrin, the metallporphyrin where manganese was chosen as metallic cation due to its reversible was monitored through electrochemical signal response of the Mn^{3+}/Mn^{2+} redox complex.

3.1 Molecular characteristics

Association of MnTPP-1CP/CRGO composite was evaluated by various methods, including UV-visible and FT-IR, as previously tested for H_2TPPs/CRGO. The UV-visible absorption of the MnTPP-1CP/CRGO composite in DMF exhibits a Soret band at 470 nm characteristic of the π–π electronic transition of metal complex and the two Q bands (569 and 607 nm) (Fig. S1.1). This result underlines that the association of the metalloporphyrin with graphene remains unmodified conformation of the porphyrin once adsorbed onto graphene surface. Fourier transform infrared spectroscopy (FT-IR) was also used to characterize the MnTPP-1CP/CRGO nanomaterial (Fig. S1.2). The FT-IR spectra of MnTPP-1CP/CRGO exhibit a large band at 3250 cm^{-1} which is assigned to OH vibrations of carboxylic group of modified

porphyrin and two stretching vibration bands in the double band region, at 1679 cm^{-1} corresponding to the C=O vibration and at 1592 cm^{-1} that can be attributed to C=C vibration. In comparison with the FT-IR spectrum of MnTPP-1CP, these two latter bands shift to lower wavenumber values. These results indicate that MnTPP-1CP interacts tightly with the conjugated aromatic structure of CRGO through π-π stacking and consequently this decreases the distance between CRGO and MnTPP-1CP.

3.2 Electrochemical characteristics

Beside the aromatic properties of MnTPP-1CP which enable strong interaction with CRGO, the presence of manganese complex exhibits interesting redox properties that could be used for the characterization of intrinsically properties of hybrid nanomaterial MnTPP-1CP/CRGO in phosphate buffer. Thus, a modified electrode was prepared by drop-coating a solution of MnTPP-1CP in DMF (0.1 mg/mL) onto CRGO-glassy carbon electrode surface. After drying, the modified surface was analyzed by square wave voltammetry (SWV), cyclic voltammetry (CV), and electrochemical Impedance (EIS) in PBS solution (Fig. 1.17).

As shown by the square wave voltammogram (Fig. 1.17A), CRGO-based electrode covered with MnTPP-1CP exhibits in PBS, a pair of apparent peaks at -0.56 and -0.44 V vs Ag/AgCl (Fig. 1.17A.c) compared to CRGO electrode (Fig. 1.17A.a). These two peaks correspond respectively to the reduction of Mn^{3+} to Mn^{2+} at -0.56 V and the reverse reaction at -0.44 V. Surface coverage (Γ) of the manganese (III) tetraphenylporphyrin attached to CRGO can be measured from CV measurements (Fig. 1.17B), following the equation 4 [19]:

$$\Gamma = \frac{Q}{nFA} \quad (4)$$

Where Q is the charge under the cathodic or anodic wave, n is number of electrons involved in the redox process, F is the Faraday constant, and A is the area of the electrode. On the basis of equation 4, we calculated that the average surface coverage of MnTPP-1CP is 3.34 ± 0.13 nmol cm^{-2}. These results agree with those obtained for a monolayer formation on an electrode surface[20]. Fig. 1.17B.b displays

the electrochemical signal of the manganese porphyrin after simple adsorption on the electrode surface. In this case, the average surface coverage was estimated to be 0.78 ± 0.07 nmol cm^{-2}, which was almost 4-times lower than the result obtained from hybrid nano-material MnTPP-1CP/CRGO electrode.

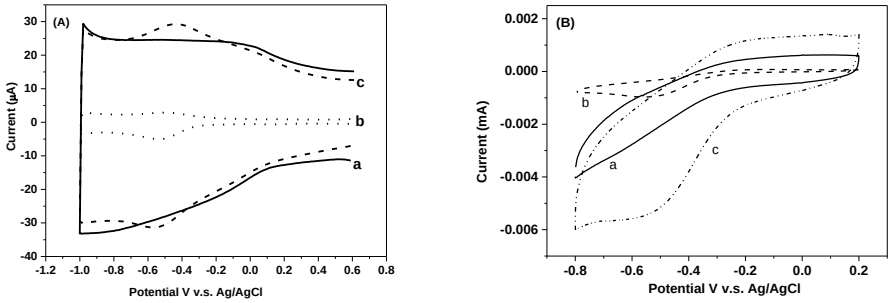

Fig 1.17. *(A) SWV measured with scan rate 12.5 mV.s^{-1} and (B) CV measurements in PBS at the scan rate of 20 mV/s for various modified GCE with CRGO (a), MnTPP-1CP (b), and MnTPP-1CP/CRGO (c)*

Electrochemical impedance measurement (EIS) was also used to characterize electrochemical properties of the modified layer especially the interface between the electrode and solution, including the impedance of the layer, capacitance of the electric double layer and the electron transfer resistance (R_{ct}). The analogous results as H_2TPPs/CRGO are shown in Fig. 1.18 and data in Table S1.3. From the diameter of the semi-circle, after modification with MnTPP-1CP; the value of R_{ct} decreases slightly from 158 kΩ (curve a of Fig. 1.18) to 132 kΩ (curve c of Fig. 1.18) indicating that the metalloporphyrin affects the conductivity of the layer and then the efficiency of electron transfer. Indeed, when MnTPP-1CP is adsorbed directly onto GCE, the diameter of the semi-circle increases obviously (894 kΩ) indicating a low electron transfer (curve b of Fig. 1.18). These results are in good accordance with those obtained from the SWV experiments.

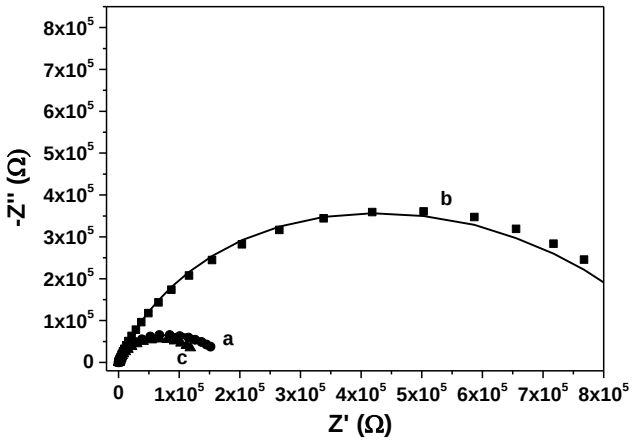

Fig 1.18. *Nyquists plots measured in PBS solution with Dc potential of 10mV at frequency range of 100 KHz to 0.1 Hz with various modified electrode CRGO (a), MnTPP-1CP (b), MnTPP-1CP/CRGO (c)*

All these results demonstrate i) the strong π–π stacking interactions between CRGO and the manganese porphyrin and ii) the ability of CRGO to immobilize a large amount of MnTPP-1CP. Furthermore, the combined porphyrin-graphene framework exhibits an excellent conductivity and a good electron transfer that both contribute to amplify the redox signal of metalloporphyrin.

Thanks to the properties of metalloporphyrin, the conditions of biosensor construction will be optimized and detected in detail next chapter.

Conclusion

In conclusion, tetraphenylporphyrins functionalized with one and four carboxylic groups were successfully synthesized by a simple and effective way in our work. Meanwhile, the synthesized different types of graphene has been performed. The chemically reduced graphene oxide (CRGO) was characterized by XPS and Raman spectroscopy. The CRGO nanomaterial demonstrates high level of reduction. The electrochemical performance exhibits high electrochemical activity monitored by high reversibility of redox marker $[Fe(CN)_6]^{3-/4-}$ and high intensity compared to other carbon materials GO and GCE. The homogenous electron transfer k_s calculated from CV data following Nicolson model shows a value of as 0.01 cm s^{-1} which is in the same order of magnitude of carbon pyrolysed at 800 °C (0.018 cm s^{-1}) electrode. The associations of H_2TPPs bearing one and 4 carboxylic groups were also investigated. We demonstrate that the association between H_2TPP-1CP and CRGO is performed through π-π interaction between phenyl groups and graphene nanosheet with higher thickness, compared to the H_2TPP-4CP with more negative charge of carboxylic group which is favored to anchoring at the edge of the graphene and forms hydrogen bond with hydroxyl group. The dispersion of CRGO is efficiently enhanced with the association process. Meanwhile, the addition of porphyrin has no effect on the k_s compared to CRGO, which is up to 0.02 cm s^{-1} and 0.01 cm s^{-1}, respectively for H_2TPP-1CP/CRGO and H_2TPP-4CP/CRGO. Thus we demonstrate that the non-covalent interaction between H_2TPP and CRGO leads to not only introduce the functionalization of CRGO and introduction of carboxylic group onto CRGO surface, but also retain their structural and electrochemical properties of CRGO. The incorporation of manganese (III) is favor to further investigate properties of the nanomaterials through its electrochemical signal variation of the Mn^{3+}/Mn^{2+} redox complex. The ability of CRGO facilitated to immobilize a large amount of porphyrin.

Supporting Informations

1. Synthesis of 5-[4-(carboxylbutyloxy)phenyl]-10,15,20-triphenylporphyrin (H_2TPP-1CP)

5-(4-methoxyphenyl)-10,15,20-triphenylporphyrin. (1)

This compound was synthesized in one step from the diphenylporphyrin according to the literature as described in a previous paper. [21]

5-(4-hydroxyphenyl)-10,15,20-triphenylporphyrin (2)

Boron tribromide (0.15mL, 7.6 eq.) was added at 0 ℃ onto 5-(4-methoxyphenyl)-10,15,20-triphenylporphyrin (**1**) (137 mg, 0.2 mmol) dissolved in 23 mL CH_2Cl_2 under argon. The crude solution was mixed during 12 hours at room temperature. The solution was then basified with a saturated Na_2CO_3 solution and washed with water until the neutrality. The organic phase was then dried over Na_2SO_4 and concentrated to give 110 mg (85%) of the crude product (**2**). Compound **2** was directly used in the next step without any purification. ^{1}H NMR (250MHz, $CDCl_3$): δ 8.88 (m, 8 H, pyrrol-H_{meso}), 8.24 (m, 6 H, Ar-*H*), 8.07 (d, $^3J_{H,H}$ = 8.5 Hz, 2H, Ar-H), 7.80 (m, 9H, Ar-*H*), 7.12 (d, $^3J_{H,H}$ = 8.25 Hz, 2H, Ar-*H*), -2.06 (ls, 2H, NH).

5-[4-(valeronitrile)phenyl]-10,15,20-triphenylporphyrin (3)

On a solution of porphyrin (2) (50 mg, 0.073 mmol, 1eq) in DMF (25 mL) was added 0.48g Cs_2CO_3 (1.46 mmol, 20eq) under argon for stirring 2h at room temperature. And then 0.17 ml 5- bromopentanenitrile was added (1.46 mmol, 20eq) into the solution and the mixture was heated at 60 ℃ during 2 days. The solution was concentrated under vacuum and extracted with CH_2Cl_2 and washed with H_2O. The organic phase was then dried over Na_2SO_4 and concentrated to give 44 mg (60%) of the crude product (3) and was directly used for the next step. ^{1}H NMR (300MHz, $CDCl_3$): δ 8.87 [8H, d, J=7.8 Hz], 8.24 [6H, d, J=6.9 Hz], 8.14 [2H, d, J=8.4 Hz], 7.77 [9H, t, J=6.6 Hz, Ha], 7.28 [2H, d, J=6 Hz], 4.3 [2H, t, J=5.55Hz], 2.6 [2H, t, J=6.75Hz], 2.19 [4H, m],-2.74 [2H, s];. FT-IR (ATR) 2093 cm^{-1} ($\nu_{C\equiv N}$). HRMS (APCI

MS) *m/z* calcd. for $C_{48}H_{37}N_7O$, $(M+H)^+$ 728.3132, found 728.3084.

5-[4-(carboxylbutyloxy)phenyl]-10,15,20-triphenylporphyrin (4)

On a solution of porphyrin (**3**) (200 mg, 0.28 mmol) in 8 mL dioxanne, was added 1.17 mL of a concentrated HCl solution. The reaction was running vigorously at 80 ℃ during 12 hours. Dichloromethane was added and the crude mixture was washed with water, dried over Na_2SO_4. Crude product was obtained with 76.5% of yield (156 mg) as a pure violet powder. ^{1}H NMR (300MHz, $CDCl_3$): δ: 8.9 [8H, m]; 8.3 [6H, m]; 8.2 [2H, d, J= 8.1 Hz]; 7.8 [9H, m]; 7.2 [2H, d, J= 7.5Hz]; 4.2 [2H, t, J=4.8 Hz]; 2.6 [2H, t, J= 6.9Hz]; 2.0 [4H, m]; -2.7 [2H, s, NH]. UV-vis spectrum in DMF: λ_{max}, 419 nm; 515 nm; 551 nm; 592 nm; 647 nm.

2. Synthesis of MnTPP-1CP (Metalated H_2TPP-1CP)

Porphyrine (**4**) (30 mg, 0.04 mmol) was dissolved in 10 mL of DMF in presence of a large excess of the corresponding ionic metal salts, $Mn(OAc)_2$. The reaction was then running two days under argon at 80 ℃. The DMF was removed and CH_2Cl_2 was added. Then organic phase was washed many times with water and after evaporation of the solvent.

3. Synthesis of 5,10,15,20-[4-(carboxylbutyloxy)phenyl] tetraphenylporphyrin (H_2TPP-4CP)

5,10,15,20--(4-methoxyphenyl) triphenylporphyrin. (5)

The distilled pyrrol (5.6 mL, 1 eq.) dissolved in 20 mL propionic acid was added into p-methoxybenzaldehyde (9.75 mL, 1 eq) dissolved in 300 mL propionic acid under argon. The crude solution was reflux during 1.5 h at 140 ℃. DDQ was added to oxidize the crude sample. The solution was then evaporated and purificated.

5,10,15,20-(4- hydroxyphenyl) tetraphenylporphyrin (6)

Boron tribromide (1.16mL, 22 eq.) was added at 0 ℃ onto *5,10,15,20-(4-*

methoxyphenyl) tetraphenylporphyrin **(6)** (400 mg, 54 mmol) dissolved in 80 mL CH_2Cl_2 under argon. The crude solution was mixed during 18 hours at room temperature. The solution was then basified with a saturated Na_2CO_3 solution and washed with water until the neutrality. The organic phase was then dried over Na_2SO_4 and concentrated to give 319 mg (86%) of the crude product **(7)**. Compound **7** was directly used in the next step without any purification. ^{1}H NMR (250MHz, $CDCl_3$): δ 8.88 (m, 8 H, pyrrol-*H*$_{meso}$), 8.24 (m, 6 H, Ar-*H*), 8.07 (d, $^3J_{H,H}$ = 8.5 Hz, 2H, Ar-*H*), 7.80 (m, 9H, Ar-*H*), 7.12 (d, $^3J_{H,H}$ = 8.25 Hz, 2H, Ar-*H*), -2.06 (ls, 2H, NH).

5,10,15,20-[4-(valeronitrile)phenyl] tetraphenylporphyrin (8)

On a solution of porphyrin **(7)** (50 mg, 0.073 mmol, 1eq) in DMF (25 mL) was added 0.48g Cs_2CO_3 (1.46 mmol, 20eq) under argon for stirring 2h at room temperature. And then 0.17 ml 5- bromopentanenitrile was added (1.46 mmol, 20eq) into the solution and the mixture was heated at 60 ℃ during 2 days. The solution was concentrated under vacuum and extracted with CH_2Cl_2 and washed with H_2O. The organic phase was then dried over Na_2SO_4 and concentrated to give 25 mg (34%) of the crude product **(8)** and was directly used for the next step. ^{1}H NMR (300MHz, $CDCl_3$): δ 8.87 [8H, d, J=7.8 Hz], 8.24 [6H, d, J=6.9 Hz], 8.14 [2H, d, J=8.4 Hz], 7.77 [9H, t, J=6.6 Hz, Ha], 7.28 [2H, d, J=6 Hz], 4.3 [2H, t, J=5.55Hz], 2.6 [2H, t, J=6.75Hz], 2.19 [4H, m],-2.74 [2H, s];. FT-IR (ATR) 2093 cm^{-1} ($\nu_{C\equiv N}$).

5,10,15,20-[4-(carboxylbutyloxy)phenyl] tetraphenylporphyrin (9)

Nitrile was hydrolyzed by HCl 12M and afforded carboxylic porphyrin **9**. On a solution of porphyrin **(8)** (100 mg, 0.1 mmol) in 4 mL dioxanne, was added 1.8 mL of a concentrated HCl solution. The reaction was running vigorously at 80 ℃ during 12 hours. Dichloromethane was added and the crude mixture was washed with water, dried over Na_2SO_4. Crude product was obtained with 32% of yield (35 mg) as a pure powder. ^{1}H NMR (300MHz, $CDCl_3$): δ 8.9 [8H, m]; 8.3 [6H, m]; 8.2 [2H, d, J= 8.1 Hz]; 7.8 [9H, m]; 7.2 [2H, d, J= 7.5Hz]; 4.2 [2H, t, J=4.8 Hz]; 2.6 [2H, t, J= 6.9Hz];

2.0 [4H, m]; -2.7 [2H, s, NH]. HRMS (APCI MS) *m/z* calcd. for $C_{64}H_{62}N_4O_{12}$, $(M+H)^+$ 1079.22, found 1079.22. UV-vis spectrum in DMF: λ_{max}, 419 nm; 515 nm; 551 nm; 592 nm; 647 nm.

Table S1.1. *Peak assignment for CRGO, H_2TPP-1CP, H_2TPP-4CP, H_2TPP-1CP/CRGO, and H_2TPP-4CP/CRGO obtained from FTIR spectra*

CRGO	Bond	Wavenumber	**H_2TPP-1CP**	Bond	Wavenumber	**H_2TPP-1CP/CRGO**	Bond	Wavenumber
	ν O-H	3248		ν O-H	3259		ν O-H	3256
	ν C=O	1724		ν C=O	1729		ν C=O	1727
	ν C=C	1583		ν C=C	1611		ν C=C	1572
		1466			1462			1456
	ν C-OH	1224		ν C-OH	1252			
	ν C-O-C	1074						
	ν_{as} CH_2	2921		ν_{as} CH_2	2955		ν_{as} CH_2	2927
	ν_s CH_2	2854		ν_s CH_2	2844		ν_s CH_2	2844
		2352			2341			2385
				ν C=C in pyridyl aromatic ring	1511			1661
					1152			1213
				δ N-H	964		δ N-H	960
CRGO	Bond	Wavenumber	**H_2TPP-4CP**	Bond	Wavenumber	**H_2TPP-4CP/CRGO**	Bond	Wavenumber
	ν O-H	3248		ν O-H	3259		ν O-H	3253
	ν	1724		ν C=O	1733		ν C=O	1711

	C=O							
	ν C=C	1583		νC=C	1605		νC=C	1578
		1466			1462			1406
	νC-OH	1224		νC-OH	1246		νC-OH	1257
	νC-O-C	1074						
	ν_{as} CH_2	2921		ν_{as} CH_2	2955		ν_{as} CH_2	2955
	ν_s CH_2	2854		ν_s CH_2	2880		ν_s CH_2	2888
								2822
		2352			2352			2348
								1771
				νC=C in pyridyl aromatic ring	1506		νC=C in pyridyl aromatic ring	1501
					1412			
				νC=N	1356		νC=N	1354
					1168			1138
					1064			
				δ N-H	953		δ N-H	975

Table S1.2*. Summary of estimated EIS parameters obtained in PBS buffer, pH 7.4. Results are mean ±S.D. obtained from 3 independent measurements in each series*

	R_s (Ω)	**R_{ct1} (KΩ)**	**CPE1 (µMho)**	**N1**	**W1 (µMho)**	**R_{ct2} (KΩ)**	**CPE2 (µMho)**	**N2**	
CRGO	92.4 ±1.2	135 ±1.8	18.7 ±1.2	0.94 ±0.6	166 ±2.57				0.07
H_2TPP-1CP/RGO	82.8± 1.5	72.6 ±5.2	28.0± 2.9	0.96 ±1.5		59.4 ±2.3	99.3± 9.5	0.53 ±2.1	0.06
H_2TPP-4CP/RGO	91.6 ±1.1	102± 3.9	20.3± 2.2	0.98 ±1.1		72.4 ±2.2	98.9± 10.2	0.56 ±2.1	0.05

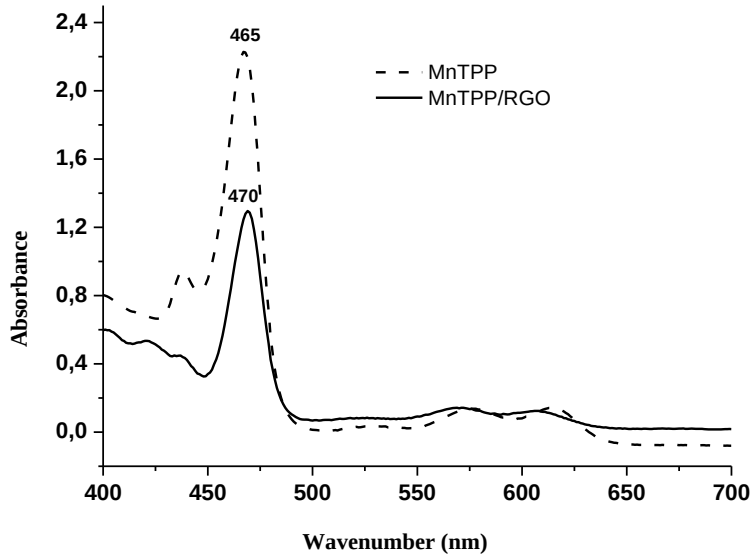

Fig. S1.1. *UV-Visible spectra of MnTPP-1CP and MnTPP-1CP/ CRGO measured in DMF.*

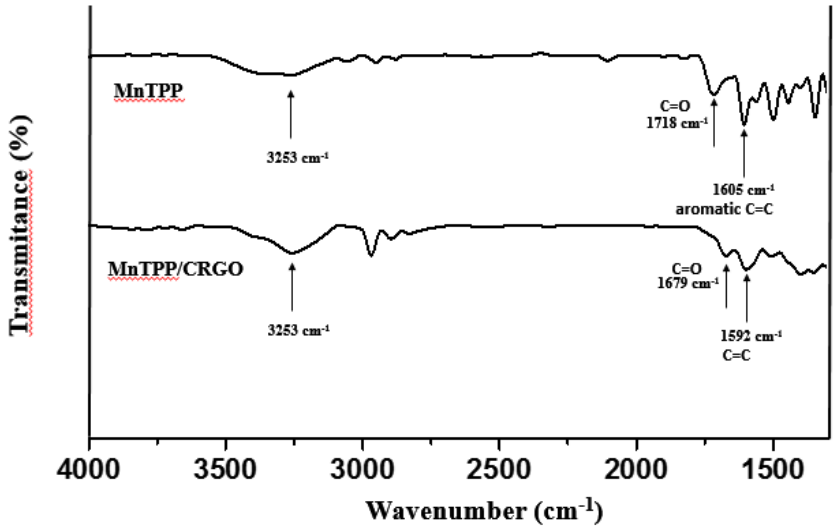

Fig. S1.2. *FT-IR of (a) MnTPP-1CP and (b) MnTPP-1CP/C`RGO*

Table S1.3*. Electricals parameters measured from the fitting data of the Nyquist plot*

	Rs (Ω)	**R_{et1} (KΩ)**	**CPE_1 (µMho)**	**N_1**	**W_1 (µMho)**	**R_{et2} (KΩ)**	**CPE_2 (µMho)**	**N_1**	**χ^2**
CRGO	92.4 ±1.2	135 ±1.8	18.7 ±1.2	0.94 ±0.6	166 ±2.57				0.07

MnTPP-1CP	89.9 ±1.4	894 ±1.5	1.48 ±1.2	0.86 ±0.24					0.09
MnTPP-1CP/CRGO	64.2 ±2.9	132 ±3.0	22.8 ±1.7	0.86 ±1.1		144 ±5.9	11.3 ±1 1.4	0.68 ±2.0	0.16

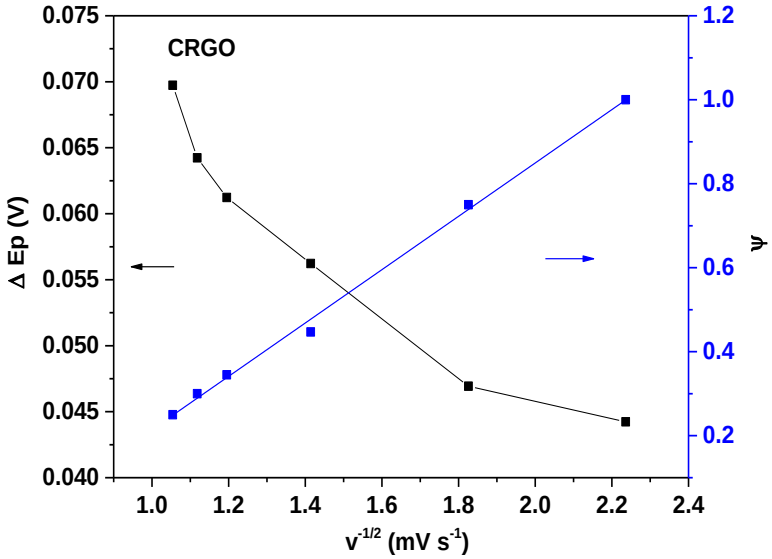

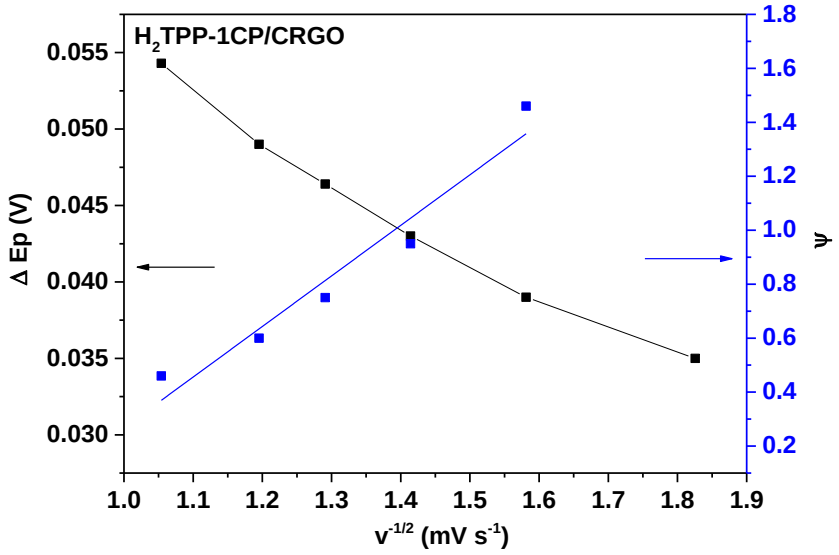

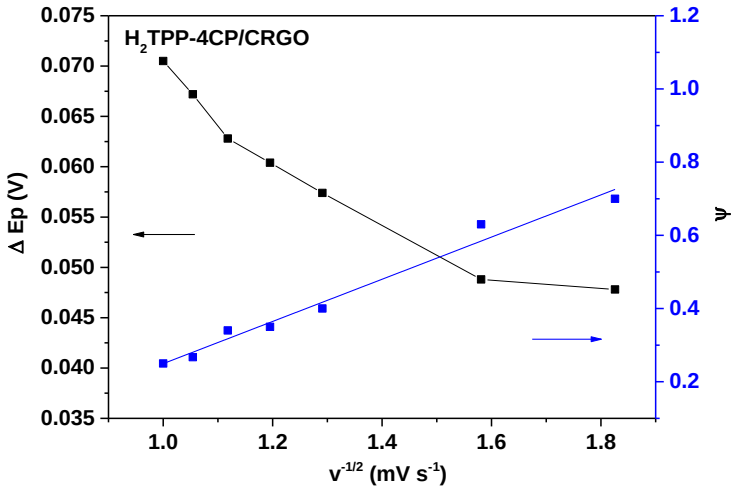
H2TPP-4CP/CRGO
Δ Ep (V)
ψ
v-1/2 (mV s-1)
0.075
0.070
0.065
0.060
0.055
0.050
0.045
0.040
0.035
1.2
1.0
0.8
0.6
0.4
0.2
1.0
1.2
1.4
1.6
1.8

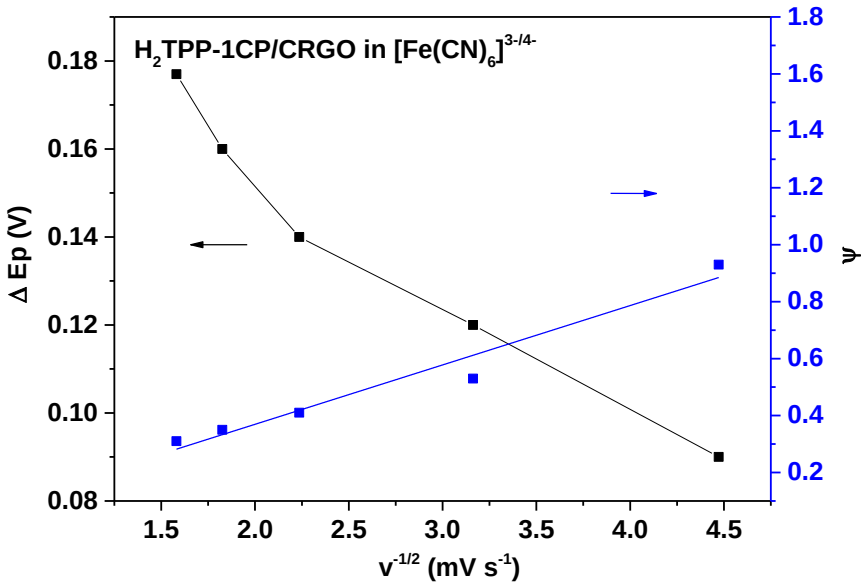
H2TPP-1CP/CRGO in [Fe(CN)6]3-/4-
Δ Ep (V)
ψ
v-1/2 (mV s-1)
0.18
0.16
0.14
0.12
0.10
0.08
1.8
1.6
1.4
1.2
1.0
0.8
0.6
0.4
0.2
1.5
2.0
2.5
3.0
3.5
4.0
4.5

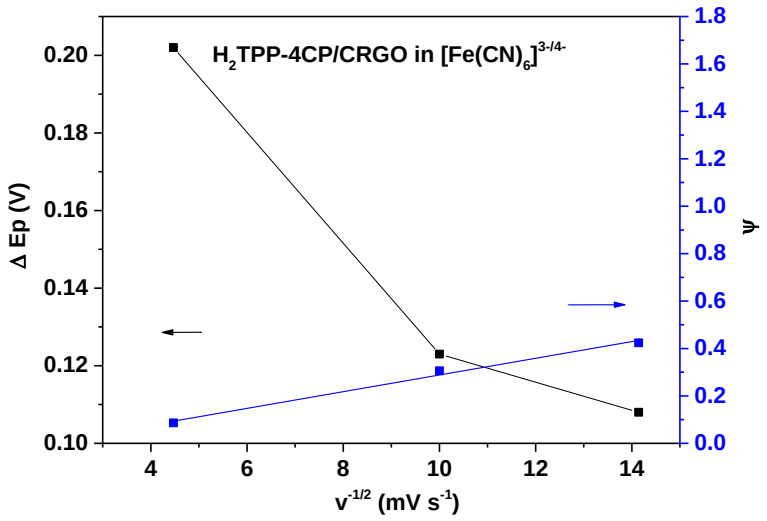

Fig. S1.3. *Relationship of ΔE_p and ψ versus $v^{-1/2}$ in benzoquinone and $Fe(CN)_6^{3-/4-}$, from which the k_s of CRGO, H_2TPP-1CP/CRGO, and H_2TPP-4CP/CRGO were calculated.*

REFERENCES:

1. Shanmugathasan, S., Edwards, C. and Boyle, R. W. Advances in modern synthetic porphyrin chemistry. *Tetrahedron* **56,** 1025–1046 (2000).
2. Varamo, M., Loock, B., Maillard, P. and Grierson, D. S. Development of strategies for the regiocontrolled synthesis of meso-5,10,20-triaryl-2,3-chlorins. *Org. Lett.* **9,** 4689–4692 (2007).
3. Rao, K. S., *et al.* Role of Peroxide Ions in Formation of Graphene Nanosheets by Electrochemical Exfoliation of Graphite. *Sci. Rep.* **4,** 1–6 (2014).
4. Xiong, Z., *et al.* Electrochemical reduction of graphene oxide films : Preparation, characterization and their electrochemical properties. *Chinese Science Bulletin,* **57,** 3045–3050 (2012).
5. Ai, K., *et al.* A novel strategy for making soluble reduced graphene oxide sheets cheaply by adopting an endogenous reducing agent. *J. Mater. Chem.,* 21, 3365–3370 (2011).
6. Shen, A. *et al.* Oxygen reduction reaction in a droplet on graphite: Direct evidence that the edge is more active than the basal plane. *Angew. Chemie Int. Ed.* **53,** 10804–10808 (2014).
7. Li, X. *et al.* Highly conducting graphene sheets and Langmuir-Blodgett films. *Natue Nanotechnol.* **3,** 1–5 (2008).
8. Guo, H., *et al.* A Green Approach to the Synthesis of. *ACS Nano* **3,** 2653–2659 (2009).
9. Shao, Y. *et al.* Graphene based electrochemical sensors and biosensors: A review. *Electroanalysis* **22,** 1027–1036 (2010).
10. Sun, T. *et al.* Rapid electron transfer by the carbon matrix in natural pyrogenic carbon. *Nat. Commun.* **8,** 14873 (2017).
11. Wang, A. *et al.* Covalent functionalization of reduced graphene oxide with porphyrin by means of diazonium chemistry for nonlinear optical performance. *Sci. Rep.* **6,** 23325 (2016).
12. Stankovich, S. *et al.* Synthesis of graphene-based nanosheets via chemical reduction of exfoliated graphite oxide. *Carbon N. Y.* **45,** 1558–1565 (2007).
13. Mcallister, M. J. *et al.* Single Sheet Functionalized Graphene by Oxidation and Thermal Expansion of Graphite. *Chem. Mater* **19,** 4396–4404 (2007).
14. He, Y. *et al.* Fusing tetrapyrroles to graphene edges by surface-assisted covalent coupling. *Nat. Chem.* **9,** 1–6 (2016).
15. Zhou, W. *et al.,* Metallo-deuteroporphyrin complexes derived from heme: A homogeneous catalyst for cyclohexane oxidation. *Appl. Catal. A Gen.* **358,** 136–140 (2009).
16. Wojcik, A. and K. P. V. Reduced Graphene Oxide and Porphyrin.An Interactive Affair in 2-D\r. *ACS Nano* **4,** 6697–6706 (2010).
17. Das, B., *et al.,* Changes in the electronic structure and properties of graphene induced by molecular charge-transfer. *Chem. Commun.* **2008,** 5155–5157 (2008).
18. Das, A. *et al.,* Monitoring dopants by Raman scattering in an electrochemically top-gated graphene transistor. *Nat. Nanotechnol.* **3,** 210–215 (2008).
19. R., A. J. B. and L. *Electrochemical Methods: Fundamentals and Applications, 2nd ed. Annual Review of Materials Science* **30,** (2001).
20. Cabrita, J. F., *et al.,* Mixed self-assembled monolayers of Co-porphyrin and n-alkane phosphonates on gold. *Surf. Sci.* **605,** 1409–1416 (2011).
21. Gryko, D. T. and Tasior, M. Simple route to meso-substituted trans-A2B2-porphyrins bearing pyridyl units. *Tetrahedron Lett.* **44,** 3317–3321 (2003).

PART B:

RESULTS AND DISCUSSION

CHAPTER II:

DNA sensor based on MnTPP-1CP/CRGO

Abstract

A novel electrochemical DNA sensor based on self-assembled hybrid nanomaterial of a π-conjugated structure of reduced graphene oxide (CRGO) and a manganese (III) tetraphenylporphyrin bearing a carboxylic group at the para position of a phenyl group modified manganese tetraphenylporphyrin (MnTPP-1CP) is described. In chapter I, the MnTPP-1CP/CRGO platform has been characterized by various methods. We have demonstrated that the two-dimensional structure and conjugated system of CRGO allowed strong interactions of metalloporphyrins and the interaction between MnTPP-1CP and CRGO had no effect on the structural and conductive properties of the CRGO. The purpose in this chapter is to exploit a DNA sensor based on the hybrid nanomaterial MnTPP-1CP/CRGO which could improve the electrical properties and lead to a sensing layer for electrochemical DNA detection. The functionalization of phenyl ring with a carboxylic group allows the attachment of single-stranded amino DNA (ssDNA) on the complex through a covalent bond. The manganese (Mn) has been chosen as metallic cation, due to its reversible and electrochemical signal response that will allow the electrochemical characterization. The strategy followed for the DNA sensor construction was a step by step method (scheme 2.1) where each step has been characterized through different analytical techniques such as FT-IR, UV and electrochemical measurements. The immobilization of ssDNA and hybridization with complementary sequences lead to the change of electrochemical properties for MnTPP-1CP/CRGO. The condition for the process of DNA sensor construction and hybridization, of which the concentration ratio of MnTPP-1CP and CRGO, the concentration of activated reactants (EDC and NHS), and the hybridization time have been optimized by various electrochemical tests. EIS experiments demonstrate an increase of impedance after DNA probe grafting and hybridization. A detection limit of 6×10^{-14} M has been calculated and a dynamic range of 1×10^{-16} M to 1×10^{-11} M has been shown. Selectivity of the DNA sensor has been investigated in presence of non-complementary and one-mismatched

DNA sequence.

Materials and Methods

1. Reagents

Phosphate buffers saline (PBS) pH=7.4, contained 10 mM Na_2HPO_4, 1.8 mM KH_2PO_4, 2.7 mM KCl and 137 mM NaCl was prepared with double distilled water, filtered by 0.22 µm membrane filter and stored at 4 ℃ until use.

All DNA sequences were provided by Eurogentec company. The DNA probe was a 25-bases sequence with six carbon chains as spacer and with amine group on 5' phosphoryl terminus: NH_2-C6 -5'-TCA-ATC-TCG-GGA-ATC-TCA-ATG-TTA-G-3'. The sequence of 25-bases target specific for DNA probe was 5'-CTA-ACA-TTG-AGA-TTC-CCG-AGA-TTG-A-3'. The non-complementary and the one-mismatched 25-bases oligonucleotide was 5'-CTA-ACA-TTG-AGA-TTC-CGA-GAT-TGA-GAT-CTT-C-3' and 5'-CTA-ACA-TTG-ACA-TTC-CCG-AGA-TTG-A-3' respectively.

2. Instruments and measurements

Scanning Electron Microscopy (SEM) images were acquired using a ZEISS SUPRA^{TM} 55VP GEMINI®.

Atomic Force Microscopy (AFM). A commercial dimension 3100 (Vecco Instruments, USA) atomic force microscope was used for topographical characterization of the samples. All measurements were performed at the tapping mode using rectangular silicon AFM tip.

UV-visible spectra were recorded with *uvikon xl* spectrometer.

Fourier Transform infrared spectra (FT-IR) were measured using a Bruker IFS66 FT-IR spectrometer equipped with a MCT detector and an attenuated total

reflectance (ATR) crystal of germanium.

Electrochemical measurements were performed using an AUTOLAB PGSTAT 100 electrochemical analysis system controlled by NOVA software (Methrom). The three-electrode cell was purchased from BASI and consisted of glassy carbon electron (GCE) (surface 0.071 cm^2) as working electrode, a platinum as counter-electrode and Ag/AgCl as reference electrode. The analyses were performed by cyclic voltammetry (CV), square wave voltammetry (SWV) and electrochemical impedance spectroscopy (EIS).

CV analysis were realized in 0.1 M KCl with 5 mM $[Fe(CN)_6]^{3-/4-}$ species in the range of potential from -0.2 to - 0.6 V with scan rate 50 $mV.s^{-1}$.

SWV measurements were performed in PBS in the range of potential of 0.6 to -1.0 V with potential amplitude of 50 mV and step height of 10 mV frequency of 1.25 Hz, the measurement is corresponding to scan rate of 12.5mV/s.

EIS analysis were performed in $[Fe(CN)_6]^{3-/4-}$ at 0.15 V vs. Ag/AgCl at DC potential of 10 mV with the frequency ranging from 100 KHz to 0.1 Hz. The impedance measurements in PBS solution were obtained at -0.3 V vs. Ag/AgCl at DC potential of 10 mV with the frequency ranging from 100 KHz to 0.01 Hz.

3. Construction of DNA sensor

The CRGO solution was prepared by dispersing 1 mg of CRGO in 1 mL DMF, and ultrasonicated for 1h. The 1 µL of the prepared CRGO solution was drop-coated onto the electrode surface followed by drying step under the lamp. A drop of 1 µL of a various concentration 0.01, 0.05, 0.1, 0.5, 1 mg/mL MnTPP solution in DMF was deposited onto the CRGO/GCE and the modified surface was then dried and rinsed with distilled water to remove non-specific adsorptions. Finally, the MnTPP-1CP/CRGO was activated in a freshly prepared 10 mM PBS solution (pH=7.4) of 20 mM EDC and 32 mM NHS. The activation step was running 1h at room temperature followed by immersing the electrode into a solution of 1 µM ssDNA for 1h at room

temperature. Subsequently, the obtained DNA sensor was thoroughly rinsed with distilled water and stored in PBS at 4 ℃ before use.

4. Target detection

The DNA hybridization reaction was conducted by immersing the DNA sensor into a 5 µL solution of different concentration of DNA target of hepatite C gene for reaction at 47 ℃. The hybridization time was firstly optimized by EIS measurement in the presence of fixed concentration of DNA target at various time from 20 min to 60 min. The optimized time was evaluated to be 40 minutes (Fig. 2.2). The target concentrations are added successively from 100 aM, 1 fM, 10 fM, 100 fM, 1 pM, 10 pM, 1 nM to 10 nM. After each incubation, the modified electrode was washed with distilled water for three times to eliminate no hybridized ssDNA.

To check the reproducibility, the experiment was repeated four times with freshly prepared DNA sensors individually. The whole preparation process was outlined in Scheme 2.1.

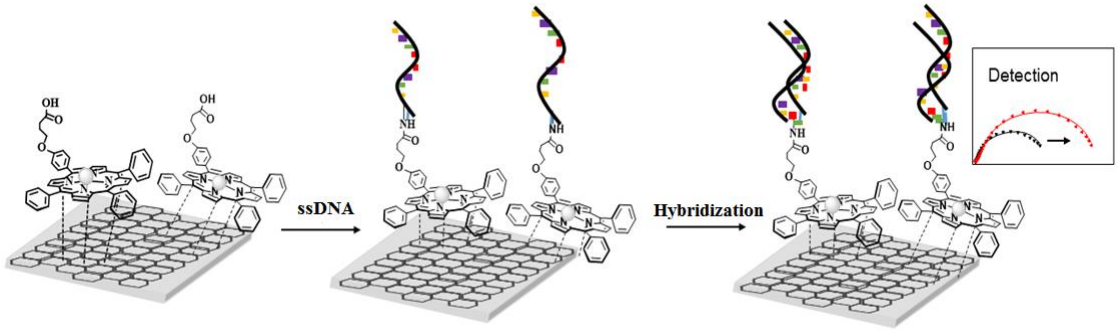

Scheme 2.1. *Schematic representation of DNA sensor*

Results and Discussion

1. Optimization of the construction of DNA sensor

In order to optimize the condition for the construction of DNA sensor, the condition for the process of DNA sensor construction and hybridization, of which the concentration ratio of MnTPP-1CP and CRGO, the concentration of activated reactants (EDC and NHS), and the hybridization time have been optimized by various electrochemical tests.

a) The concentration of MnTPP-1CP

Various concentration of MnTPP-1CP (1, 0.5, 0.1, 0.05, and 0.01 mg mL^{-1}) solutions were prepared in 1 mL DMF. And the concentration of the CRGO was fixed to 1 mg mL^{-1}. The preliminary measurements for the construction and hybridization of DNA senor were monitored by detecting the reversible redox electrochemical signal response of Mn via SWVs (Fig. 2.1A). The histogram presents the relative variation of current peak after the detection of 1 µM of target for different concentration of MnTPP-1CP. It shows that the best concentration of metalloporphyrin in DMF that leads to the highest variation of relative current is 0.1 mg mL^{-1} (Fig. 2.1B). This concentration will be used for the next step.

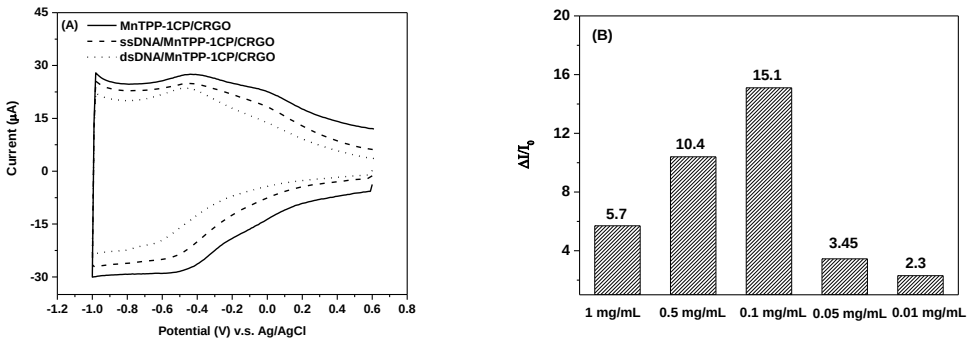

Fig. 2.1. *(A) The SWV measurements in PBS, scan rate 12.5 mV.s^{-1} for 0.1 mg ml^{-1} MnTPP-1CP and 1 mg ml^{-1}CRGO modified electrode (line), after ssDNA*

immobilization (dashed line), and after hybridization of 1μM target (dotted line); (B) Histogram of the relative variation of current peak of SWVs for DNA sensors after detection of 1 μM target.

b) The addition of NHS in coupling

The activated conditions in coupling reaction have also been optimized. The DNA sensors were activated by immersing the MnTPP-1CP/CRGO electrode in PBS solution including 20 mM EDC in presence of 35 mM NHS or without NHS. The electrochemical detection was monitored by SWV. The estimated relative current ($\Delta I/I_0$) was shown in Fig. 2.2A. The addition of the NHS has positive effect on the performance of the DNA sensor. Indeed, the presence of NHS as activated reactant increases considerably the relative variation of current peak of the porphyrin complex. The effect of EDC concentration has also been investigated in the condition of the fixed ratio of EDC and NHS (1:1.75). The result exhibits that the higher concentration of EDC has negative effect on the performance of DNA senor. The optimized activated condition for activating carboxylic group should to be 20 mM EDC and 35 mM NHS.

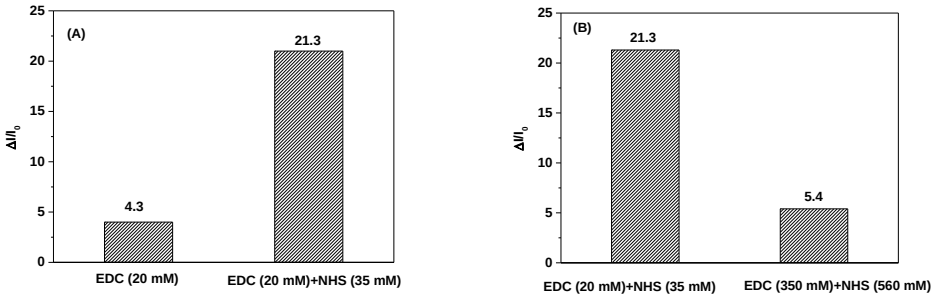

Fig. 2.2. *(A) The effect of the addition of NHS, and (B) the concentration of EDC*

c) Hybridization time

The hybridization time was optimized by EIS measurement in the presence of fixed concentration DNA target (1 fM) at various time from 20 min to 60 min (Fig. 2.3). The electron transfer resistance of $[Fe(CN)_6]^{3-/4-}$ complex increases with the hybridization time to reach to a plateau after 40 minutes (Fig 2.3. Insert). The

hybridization time used for the next step will be then 40 minutes.

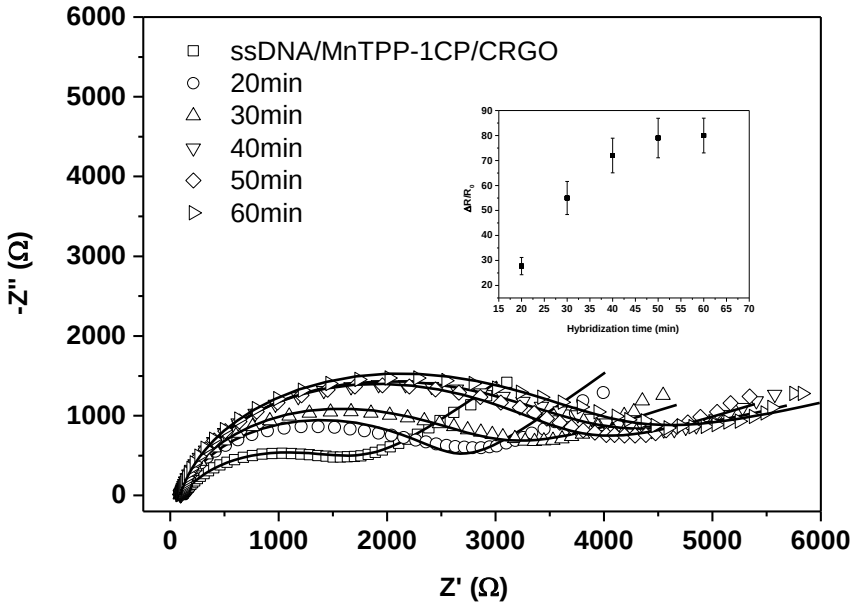

Fig. 2.3. *EIS obtained after DNA detection of 1fM of target after different hybridization times (20, 30, 40, 50 and 60 min.) in 5 mM $[Fe(CN)_6]^{3-/4-}$; Insert: calibration curve.*

2. Construction of the DNA sensor

Single-stranded DNA (ssDNA) was covalently interacted with metalloporphyrin through an amide link. The ssDNA labelled with an amine group with 6 carbonyl spacer (C6 amino link) are able to react with carboxylic groups present in metalloporphyrin immobilized on the CRGO surface. The reaction was performed in presence of EDC and NHS, as activating agents for one hour. After washing the modified electrode with distilled water to remove any reactants left, the surface was analyzed in buffer solution.

The coupling reaction was confirmed by FT-IR measurements and the FT-IR spectra of the ssDNA/MnTPP-1CP/CRGO surface (Fig. S2.1) exhibits the appearance of some new peaks at 3000 cm^{-1}, 1757 cm^{-1} , 1584 cm^{-1} and at 956 cm^{-1} which correspond to C-H, C=O, C-N and phosphates stretching, respectively confirming the presence of acids nucleic on the surface. These results suggest the covalent interaction

between ssDNA with MnTPP-1CP/CRGO on the electrode surface.

The formation of the electrochemical DNA sensor was then monitored by square wave voltammetry in PBS buffer thanks to the electrochemical signal response of Mn (Fig. 2.4A). SWV shows a decrease of the current, at -0.56 V corresponding to the reduction of Mn(III) to Mn (II) complex, after the immobilization of ssDNA. As it has been previously observed[1], this phenomenon is explained by the slow diffusion of ions to the surface during the redox process due to the attachment of large ssDNA molecules on the electrode surface.

Fig. 2.4B shows the EIS measurements performed in 5 mM $[Fe(CN)_6]^{3-/4-}$ species after the modification of GCE surface. Results demonstrate an obvious decrease of electron transfer resistance (R_{ct}) after the interaction of ssDNA and MnTPP-1CP (Fig. 2.4B, b). The increased R_{ct} verifies the successful covalently interaction between ssDNA and MnTPP-1CP. The reason for this variation can be ascribed to the blocking of ions diffusion to the electrode surface. The stability over the time of the electrochemical signal of the metalloporphyrin was evaluated by SWV experiments in PBS (Fig. S2.2). Scarce significant variation of both oxidation and reduction of the current and potential is observed, demonstrating for the first time the excellent stability of the biolayer due to strong interactions between MnTPP-1CP and CRGO through π-π stacking.

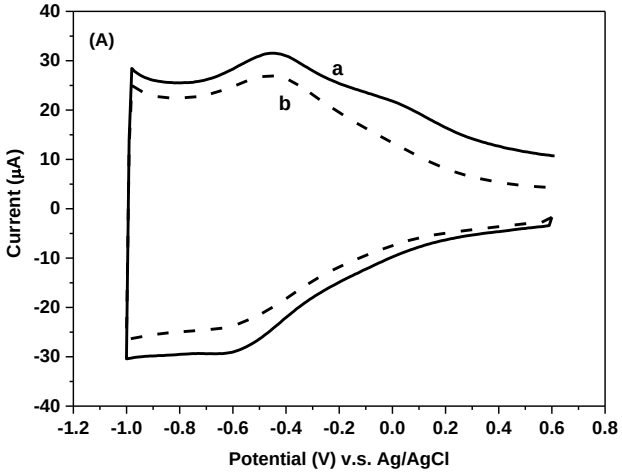

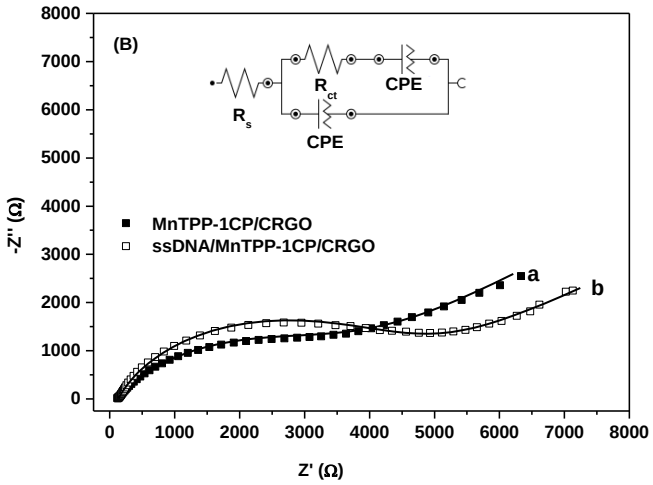

Fig. 2.4. *(A) SWV measurements in PBS, scan rate 12.5 mV.s^{-1}, and (B) Nquist diagram obtained in 5 mM $[Fe(CN)_6]^{3-/4-}$ for MnTPP-1CP/CRGO modified electrode (a) and after ssDNA immobilization. Inset: equivalent circuit used to model impedance data in the presence of redox couples. R_s electrolyte solution resistance, R_{ct} element of interfacial electron transfer resistance, CPE constant phase element*

3. Detection of DNA target

Hybridization reaction was performed with complementary targets (cDNA) containing complementary sequence to the DNA probe by successive addition of various concentrations ranging from 100 aM to 10 nM (Fig. 2.5A, b-i). Electrochemical detection of DNA targets was monitored by EIS measurements in 5 mM $[Fe(CN)_6]^{3-/4-}$, as redox indicator. EIS is known to be a sensitive and reliable electrochemical technique to monitor the detection of biorecognition events at the electrode interface[2].

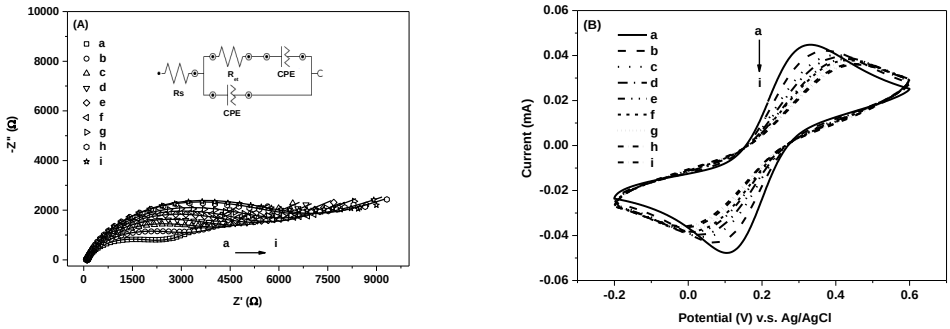

Fig 2.5. *Detection of complementary target of different concentrations: 100 aM; 1 fM; 10 fM; 100 fM; 1 pM; 10 pM; 1 nM; 10 nM (b-i). Measurements realized in 5 mM $[Fe(CN)_6]^{3-/4-}$(A) Nyquist diagrams obtained after hybridization. Inset: equivalent circuit used to model impedance data in the presence of redox couples. (B) CV obtained after hybridization*

After hybridization, EIS measurements show an increase of the charge transfer resistance with the increasing concentration of cDNA target. As mentioned before, ssDNA bases block the diffusion of $[Fe(CN)_6]^{3-/4-}$ species to the electrode surface. When ssDNA hybridized with cDNA, double-helix structure was formed and electronegative phosphate groups are introduced on the surface. It is more difficult for $[Fe(CN)_6]^{3-/4-}$ to reach the electrode due to the electrostatic repulsion. Hence, the R_{ct} value increases with the formation of double-stranded DNA (Fig 2.5A)[3]. Hybridization reaction was also performed by CV measurements in $[Fe(CN)_6]^{3-/4-}$ solution (Fig. 2.5B). The current of $[Fe(CN)_6]^{3-/4-}$ and the reversibility of redox process decrease with the increasing concentration of cDNA. These results are in good agreement with those obtained in EIS experiments. The logarithmic relationship between $\Delta R_{ct}/ R_{ct\ ssDNA}$ and the concentration of the cDNA target was shown in Fig. 2.6.

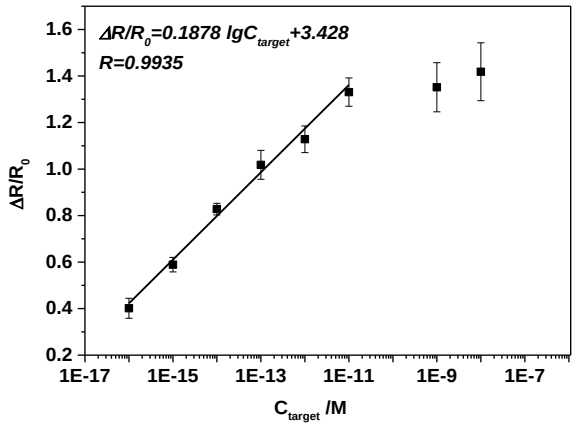

Fig 2.6. *Plot of the relative changes of the electron transfer resistance $\Delta R_{ct}/ R_{ct\ ss\ DNA}$ versus concentration. Data points are the mean values ± RSD obtained with four independent experiments.*

The ΔR_{ct} corresponds to the difference between R_{ct} value of the ssDNA immobilized on the electrode surface and that after hybridization with cDNA ($\Delta R_{ct} = R_{ct,dsDNA} - R_{ct,ssDNA}$). The regression equation is $\Delta R_{ct}/ R_{ct,ssDNA}$ = 0.188 lg C_{target} +3.428 with regression coefficient of 0.993. The detection limit is estimated to be 2×10^{-16} M (signal-to-noise ratio of 4 independent measurements, taking into accord the standard deviation of 0.043). The DNA sensor based on MnTPP-1CP/CRGO nanomaterial exhibits a high sensitivity probably for all previous ascribed reasons such as the high specific surface of CRGO and the short distance between MnTPP-1CP and CRGO which increases the electron transfer. Comparing with other nano-materials based on CRGO reported in literature for the DNA detection, our work presents an excellent sensing platform (Table 2.1).

Table 2.1. *Comparison of the proposed method with some reported DNA sensors*

Detection technique	Detection limit (M)	indicator	Ref
EIS	1.0×10^{-13}	Label-free ERGO-modified electrode	[4]
EIS	1.1×10^{-13}	GO anchored on a diazonium-functionalized electrode	[5]
SERS[a]	1.0×10^{-11}	Graphene CVD associated with gold nanoparticles	[6]

Fluorescence	4.0×10^{-11}	FAM-labelled GO/polymer complex	[7]
EIS	5.0×10^{-13}	3,4,9,10-Perylene tetracarboxylic acid functionalized graphene-modified electrode	[8]
EIS	4.2×10^{-15}	Poly(xanthurenic acid) associated with ERGO	[9]
EIS	6×10^{-14}	MnTPP-1CP/CRGO	Our work

[a] SERS- Surface-Enhanced Raman Scattering

4. Selectivity and reproducibility

To test the selectivity of the DNA sensor based on MnTPP/RGO platform during the hybridization, different DNA sequences were tested for a low concentration (1 nM) in 5 mM $[Fe(CN)_6]^{3-/4-}$. The $\Delta R_{ct}/ R_{ct,ssDNA}$ values were recorded and compared with that obtained after hybridization with cDNA (Fig. 2.7).

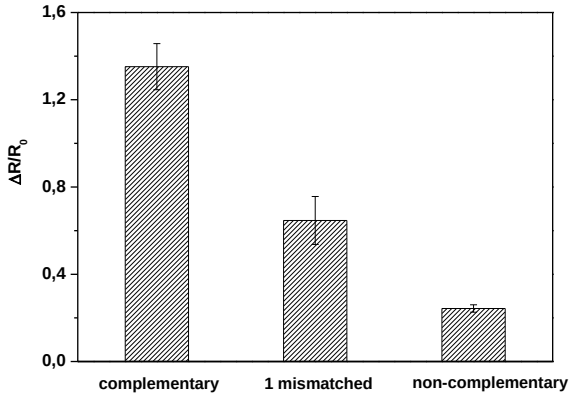

Fig 2.7. *Histogram of $\Delta R_{ct}/ R_{ct,ssDNA}$ for DNA sensor after detection of 1nM of cDNA, cDNA with one-base mismatched, and non-complementary sequence, respectively.*

The $\Delta R_{ct}/ R_{ct,ssDNA}$ values were calculated to be 64%, 27% and 9% after hybridization with cDNA, cDNA with one-base mismatched and non-complementary sequences, respectively. This indicates that the DNA sensor has a good hybridization selectivity to discriminate the complementary from the non-complementary sequences. Nethertheless, this selectivity might be improved by adding more negative charges on

the electrode surface. Indeed, the low variation observed for the non-complementary DNA could be attributed to the non-specific adsorptions of the DNA onto electrode surface. Increasing the number of negative charges on the surface might limit the interaction of the negatively charged ssDNA sequences by electrostatic repulsion. For example, the introduction of more carboxylic functions on phenyl groups of the metalloporphyrin might improve the selectivity to the target sequences detection.

The reproducibility of the DNA hybridization platform was tested by four impedance measurements with four independent biosensors. Each sensing layer was freshly prepared. A relative standard deviation (RSD) of less than 3% for the $\Delta R_{ct}/R_{ct,ssDNA}$ value was estimated, which showed the high reproducibility of the biosensor layer.

Conclusion

In conclusion, based on a π-conjugated framework composed of a manganese (III) tetraphenylporphyrin and graphene, we design the first example of electrochemical DNA sensor for highly sensitive and selective detection of DNA target. We have demonstrated the different advantages of using the manganese tetraphenylporphyrin in such material. The manganese tetraphenylporphyrin was functionalized with one carboxylic group for covalently interaction with ssDNA on the GC electrode surface which offers a stable sensing layer. The incorporation of a redox metal inside the macrocycle ring of porphyrin allows the electrochemical characterization of the film. EIS measurement demonstrates that the R_{ct} value of the MnTPP-1CP/CRGO hybrid nanomaterial increases after ssDNA immobilization and hybridization to its complementary sequences, which is used as a sensing signal. A detection limit of 2×10^{-16} M is estimated with a moderate selectivity that could be improved by introducing more negative charge function on the porphyrins, thanks to their chemical modification ability. These results demonstrate that MnTPP-1CP/CRGO platform provided a very good candidate for direct DNA sensor and are very promising in DNA sensors applications.

Supporting Informations

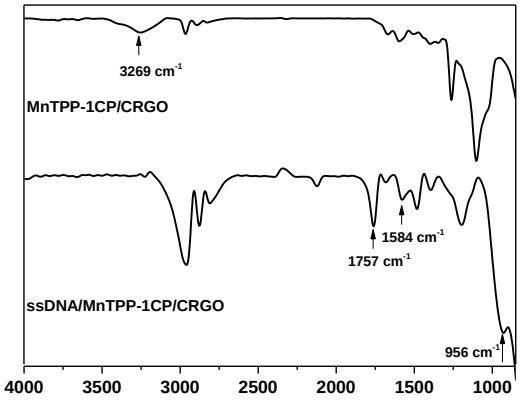

Fig. S2.1. *FT-IR spectra of MnTPP-1CP/CRGO and after covalently interacted with ssDNA through amide link.*

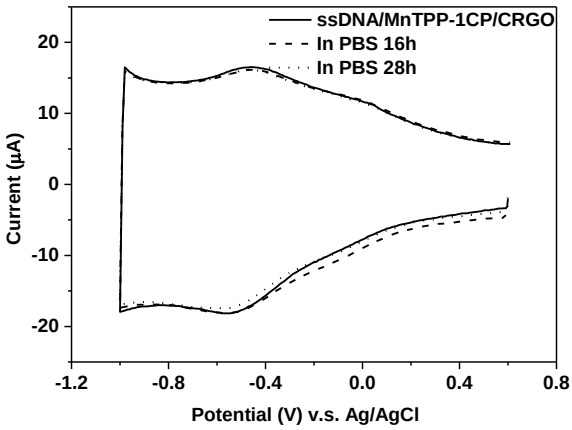

Fig. S2.2. *SWV measurements in PBS with scan rate 12.5 mV.s^{-1} for ssDNA/MnTPP-1CP/CRGO (a) and after immersed in PBS after 16h (b) and 28h (c).*

REFERENCES:

1. Miodek, A., *et al.*, E-DNA Sensor of Mycobacterium tuberculosis Based on Electrochemical Assembly of Nanomaterials (MWCNTs/PPy/PAMAM). *Anal. Chem.* **87,** 9257–9264 (2015).
2. Lisdat, F. and Sch äfer, D. The use of electrochemical impedance spectroscopy for biosensing. *Anal. Bioanal. Chem.* **391,** 1555–1567 (2008).
3. Hu, Y. *et al.* Decorated graphene sheets for label-free DNA impedance biosensing. *Biomaterials* **33,** 1097–1106 (2012).
4. Q.J. Gong, *et al.* A sensitive impedimetric DNA biosensor for the determination of the HIV gene based on electrochemically reduced graphene oxide. *Anal. Methods* **7,** 2554–2562 (2015).
5. Hu, Y. *et al.* Analytica Chimica Acta Simple and label-free electrochemical assay for signal-on DNA hybridization directly at undecorated graphene oxide. *Anal. Chim. Acta* **753,** 82–89 (2012).
6. He, S. *et al.* Graphene-based high-efficiency surface-enhanced Raman scattering-active platform for sensitive and multiplex DNA detection. *Anal. Chem.* **84,** 4622–4627 (2012).
7. Xing, X. *et al.* Ampli fi ed Fluorescent Sensing of DNA Using Graphene Oxide and a Conjugated Cationic Polymer. *Biomacromolecules* **14,** 117–123 (2013).
8. Hu, Y. *et al.* Label-free electrochemical impedance sensing of DNA hybridization based on functionalized graphene sheets. *Chem. Commun.* **47,** 1743–1745 (2011).
9. Yang, T. *et al.* Synchronous electrosynthesis of poly(xanthurenic acid)-reduced graphene oxide nanocomposite for highly sensitive impedimetric detection of DNA. *ACS Appl. Mater. Interfaces* **5,** 3495–3499 (2013).

PART B:

RESULTS AND DISCUSSION

CHAPTER III:

DNA sensor based on H_2TPP-nCP/CRGO

Abstract

We present a novel electrochemical DNA sensor based on self-assembled nanomaterial of a π-electron-rich conjugated structure of chemically reduced graphene oxide (CRGO) associated with two types of π-conjugated tetraphenylporphyrin functionalized with one or four carboxylic groups (H_2TPP-1CP and H_2TPP-4CP respectively). Porphyrin molecules are versatile compounds that are easily functionalized with numerous designed carboxylic groups that could covalently interact with a 5'-amino single-strand DNA (ssDNA) through stable amide link. The H_2TPP-nCP/CRGO hybrid nanomaterials (with n=1 or 4) covalently attached with single-strand DNA (ssDNA/H_2TPP-nCP/CRGO) were characterized by Atomic Force Microscopy (AFM) and electrochemical methods. The electronic properties of such nanomaterials were studied through square wave voltammetry (SWV), electrochemical impendence spectra (EIS), and cyclic voltammetry (CV). On respectively employing a negatively charged redox marker, $[Fe(CN)_6]^{3-/4-}$ and a neutral couple one, *p*-benzoquinone, the pattern of interaction between H_2TPP-nCP/CRGO and ssDNA could be envisaged by means of the calculated relative change of diffusion coefficient (D_0) and homogenous electron constant (k_s). The DNA immobilization and hybridization with complementary sequences were monitoring by following the variation of the reduced current of redox couple *p*-benzoquinone. On the basis of previously developed and optimized conditions, the electrochemical DNA sensor based on H_2TPP-4CP/CRGO was prepared and exhibited a linear range from 10^{-18} to 10^{-11} M with a detection limit as low as 7×10^{-19} M. Moreover, compared to ssDNA/H_2TPP-1CP/CRGO platform, we demonstrated that the increase of carboxylic groups on the porphyrin macrocycle, are able to diminish non-specific absorption on the electrode surface. Indeed, a highest selectivity of DNA sensor based on H_2TPP-4CP/CRGO has been investigated in presence of non-complementary DNA target. Furthermore, the DNA sensor demonstrated the ability for sensing DNA of rpoB gene

of *Mycobacterium tuberculosis* in real PCR samples. The elaborated DNA sensor was suitable for detection of sequences with wild-type samples, discriminating them from a single nucleotide polymorphism (SNP) T (TCG/TTG) with mutation. This shows enormous potential on this platform for further application in pathogens diagnostic and therapeutic purpose.

Materials and Methods

1. Reagents

All DNA sequences were provided by Eurogentec company. The DNA probe was a 25-bases sequence with six carbon chains as spacer and with amine group on 5' phosphoryl terminus: NH_2-C_6 -5'-TCA-ATC-TCG-GGA-ATC-TCA-ATG-TTA-G-3'. The sequence of 25-bases target specific for DNA probe was 5'-CTA-ACA-TTG-AGA-TTC-CCG-AGA-TTG-A-3'. The non-complementary 25-bases oligonucleotide was 5'-CTA-ACA-TTG-AGA-TTC-CGA-GAT-TGA-GAT-CTT-C-3'.

DNA probe specific for PCR samples contained 18-bases and was also modified with six carbonyl chain bearing amine group at terminal position: NH_2-C_6-5'-CCG-ACT-CTC-GGC-GCT-GGG-3'. PCR samples with (c PCR) or without (nc PCR) specific sequence were composed of bases and come from rpoB gene of *M. tuberculosis*. c PCR samples were wild type stems and the nc PCR samples were from five different *M. tuberculosis* stems: 2-09, 7-09, 8-09, 10-09 and 11-09, and had the same sequence. The results for nc PCR samples are presented as average response obtained from these five different *M. tuberculosis* stems.

Phosphate buffers saline (PBS) pH=7.4, contained 10 mM Na_2HPO_4, 1.8 mM KH_2PO_4, 2.7 mM KCl and 137 mM NaCl was prepared with double distilled water, filtered by 0.22 µm membrane filter and stored at 4 ºC until use.

2. Instruments and measurements

Atomic Force Microscopy. A commercial dimension 3100 (Vecco Instruments, USA) atomic force microscope was used for topographical characterization of the samples. All measurements were performed at the tapping mode using rectangular silicon AFM tip.

Electrochemical measurements were performed using an AUTOLAB PGSTAT 100 electrochemical analysis system controlled by NOVA software (Metrohm). The three-electrode cell was purchased from BASI and consisted of glassy carbon electron (GCE) (surface 0.071 cm^2) as working electrode, a platinum as counter-electrode and Ag/AgCl as reference electrode. The analyses were performed by cyclic voltammetry (CV), square wave voltammetry (SWV) and electrochemical impedance spectroscopy (EIS).

CV analysis were realized in 0.1 M KCl with 5 mM $[Fe(CN)_6]^{3-/4-}$ species in the range of potential from -0.2 to 0.6 V at various scan rates in the range 0.005-1 V s^{-1} and also analyzed in 0.1 M KCl with 1 mM benzoquinone in the range of potential from -0.4 to 0.2 V at various scan rates in the range 0.05-1 V s^{-1}.

SWV measurements were performed in 0.1 M KCl with 1 mM benzoquinone in the range of potential from -0.4 to 0.6 V with potential amplitude of 50 mV and step height of 10 mV frequency of 1.25 Hz, the measurement is corresponding to scan rate of 12.5 mV/s.

EIS analysis were performed in $[Fe(CN)_6]^{3-/4-}$ at 0.15 V vs. Ag/AgCl at DC potential of 10 mV with the frequency ranging from 100 KHz to 0.1 Hz. The impedance measurements in PBS solution were obtained at -0.3 V vs. Ag/AgCl at DC potential of 10 mV with the frequency ranging from 100 KHz to 0.01 Hz.

3. Construction of DNA sensor

A drop of 2 µL of the prepared H_2TPP-1CP/CRGO suspension were deposited onto a glassy carbon electrode surface (GCE) followed by drying step under the lamp. The modified surface was then dried and rinsed with distilled water to remove no specific adsorptions. Finally, the H_2TPP-1CP/CRGO surface was activated with a freshly prepared 10 mM PBS solution (pH=7.4) containing 20 mM EDC, 32 mM NHS. The activation step was running for 1h at room temperature. Then the electrode was immersed in 1 µM solution of ssDNA probe prepared in PBS buffer for 1h at

room temperature. Subsequently, the obtained DNA sensor based on H_2TPP-1CP/CRGO was thoroughly rinsed with distilled water and stored in PBS at 4 ℃ before use. After each step of construction of the DNA sensor, the modifications of the electrode surface were controlled by SWV method. The DNA sensor based on H_2TPP-4CP/CRGO was constructed according to the same procedure as that based on H_2TPP-1CP/CRGO.

4. DNA Target detection

The DNA hybridization of complementary 25-bases targets with ssDNA probe associated to the modified GCE surface was performed by immersing the modified electrode in solution of various concentration of DNA target of hepatite C gene for 40 min at 47 ℃. The target concentrations are increased successively from 1 aM, 10 aM, 100 aM, 1 fM, 10 fM, 100 fM, 1 pM, 10 pM to 1 nM. After each incubation, the modified electrode was washed with distilled water for three times to eliminate no hybridized single strand DNA and then analyzed by SWV method. The detection of non-specific interactions was conducted according to the same procedure described previously, by immersing the modified electrode in a PBS buffer solution containing different concentration of non-complementary DNA target in from 1 aM, 10 aM, 100 aM, 1 fM, 10 fM, 100 fM, 1 pM, 10 pM to 1 nM. To check the reproducibility, the experiment was repeated four times with freshly prepared DNA sensors individually.

5. PCR sample detection

The DNA from PCR samples was denaturized by heating at 95 ℃ for 5 min, and then immersed in an ice bath for 1 min[1]. The hybridization of c PCR samples was performed by immersing the electrode modified DNA probe specific for PCR samples in solution of 1 fM c PCR for 40 min at 47 ℃. The same conditions were applied for the detection of the same concentration of nc PCR.

Results and Discussion

1. DNA sensor based on H_2TPP-1CP/CRGO

1.1 Construction of DNA sensor

DNA sensor construction involves covalent attachment of single stranded DNA probes (ssDNA) labelled with an amine group with 6 carbon atoms as spacer (C6 amino link). The ssDNA probe was covalently bonded to the carboxylic groups present in H_2TPP-1CP/CRGO hybrid complex through an amide link. The reaction was performed in presence of EDC and NHS, as activating agents for one hour. After washing the modified electrode with distilled water to remove any reactants left. The formation of DNA sensor was monitoring by electrochemical impedance measurement (EIS) and cyclic voltammetry (CV) in both $[Fe(CN)_6]^{3-/4-}$ and *p*-benzoquinone solution and by square wave voltammetry (SWV) in *p*-benzoquinone solution only.

Impedance measurement (EIS) was used to characterize electrochemical properties of the modified layer, especially the interface between the modified electrode and the solution, including the impedance of the layer, capacitance of the electric double layer and the electron transfer resistance (R_{ct}). The results performed in PBS before (Fig 3.1, curve a) and after the reaction of ssDNA probe with H_2TPP-1CP (Fig. 3.1, curve b) are shown in Fig. 3.1 and data in supplementary information (Table S3.1). After ssDNA interaction, an obvious increase of the electron transfer resistance (R_{ct2}, Table S3.1) from 59 to 166 kΩ is observed and confirms that the successful covalently attachment of ssDNA onto H_2TPP-1CP/CRGO layer. This variation can be explained by a blocking of diffusion ions process to the electrode surface. The thickness of the layer is sharply deceased from 72 to 31 nm (Table S3.1) and the N_2 value (Table S3.1) which reflects the roughness of the surface remains

constant (from 0.53 to 0.57). These results presumably indicate that the covalently immobilized ssDNA lies on the hybrid nanomaterial surface, which leads to the H_2TPP-1CP is flattened and thus decreases the thickness of the nanomaterial layer.

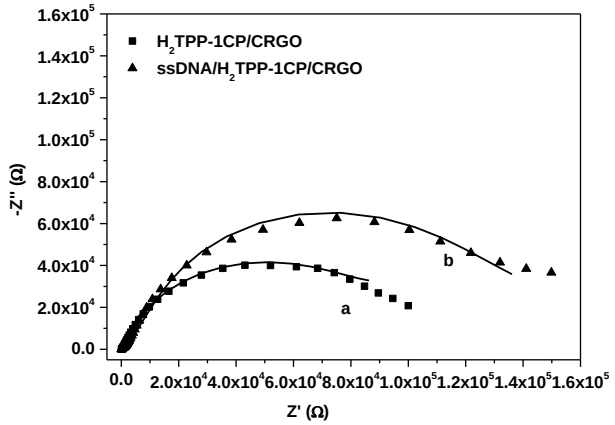

Fig. 3.1. *Nyquists plots measured in PBS solution with modified electrode H_2TPP-1CP/CRGO (a) and ssDNA/H_2TPP-1CP/CRGO (b).*

In order to further evaluate the electronic properties and construction of the ssDNA/H_2TPP-1CP/CRGO surface, CV and EIS measurements were performed in 5 mM $[Fe(CN)_6]^{3-/4-}$ species (Fig. 3.2). Fig. 3.2A shows that after the immobilization of ssDNA, the redox peaks of $[Fe(CN)_6]^{3-/4-}$ couple have separately shift to the irreversible trend, meanwhile the R_{ct} estimated remains constant (from 3.49 to 3.56 kΩ, Table S3.2). This result can also suggest that the immobilization of ssDNA tends to lie on the hybrid surface through layer by layer, which has a little influence on the electric properties of the surface.

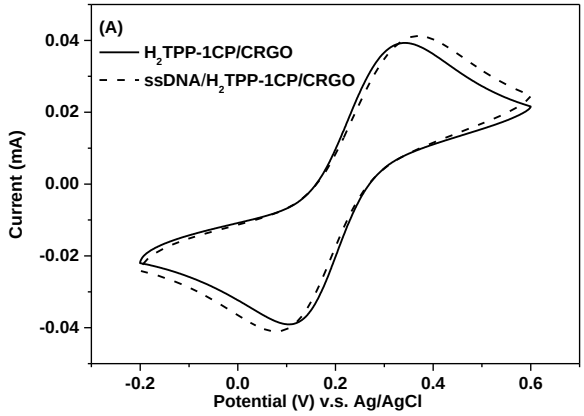

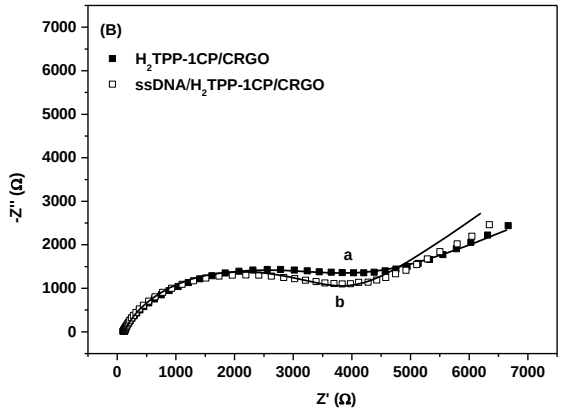

Fig.3.2. *(A) Cyclic voltammograms and (B) Nyquists plots of H_2TPP-1CP/CRGO before (solid black line or a) and after (dashed black line or b) immobilization of ssDNA. Recorded in 0.1 M KCl with 5 mM $[Fe(CN)_6]^{3-/4-}$ species*

A schematic scheme can be proposed as shown in Schema 3.1.

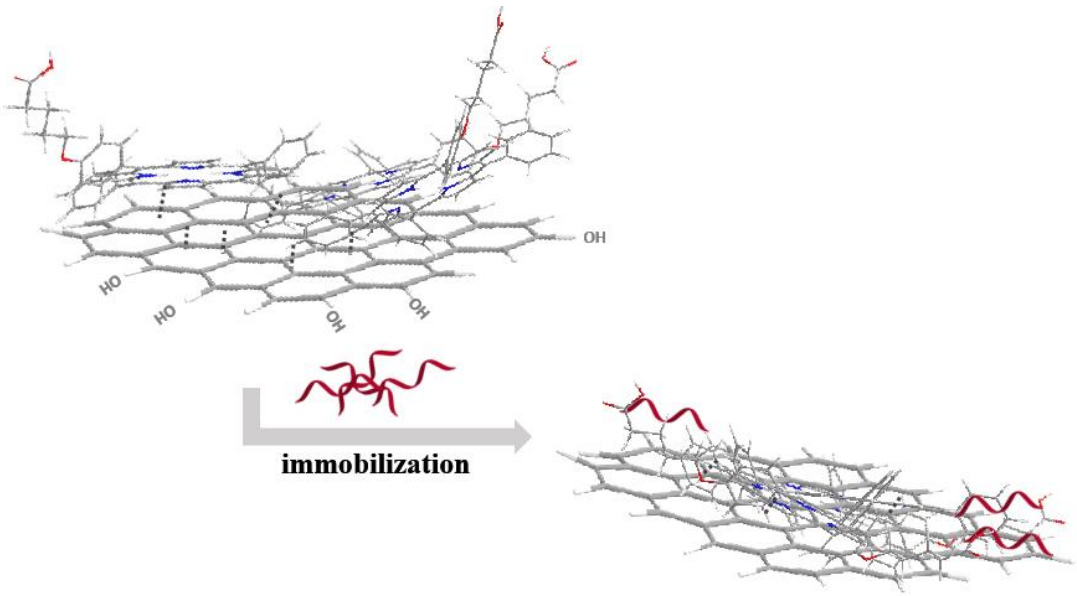

Schema 3.1. *The immobilization of ssDNA on the H_2TPP-1CP/CRGO hybrid nanomaterial*

The diffusion coefficient (D_0) and kinetic constant (k_s) of redox species in solution can be evaluated by CV measurements recorded at different scan rates. D_0 can be calculated according to the Randles–Sevcik equation ($i_p = 2.99\times10^5 nACD_0^{1/2}v^{1/2}$) where D_0 is the slope of the curve i_p versus $v^{1/2}$, n is electron number transferred, *C* concentration of species and *A* electrode area in cm^2 . k_s is determined

by the slope of the curve ΔEp versus $v^{-1/2}$ (Fig. S3.1). These parameters have been calculated for both $[Fe(CN)_6]^{3-/4-}$ and benzoquinone/hydroquinone redox couples before and after ssDNA immobilization. All the results are presented in Table 3.1.

For both redox couples, D_0 decreases sensibly after ssDNA immobilization, from 6×10^{-6} to 4.6×10^{-6} cm^2 s^{-1} in $[Fe(CN)_6]^{3-/4-}$ solution and from 1×10^{-6} to 0.5×10^{-6} cm^2 s^{-1} in the neutral redox marker *p*-benzoquinone. This confirms that the successful interaction between ssDNA and hybrid nanomaterial which is in agreement with the result of EIS in PBS. The diffusion process of redox molecules in solution to the electrode surface becomes more difficult due to the presence of the ssDNA layer on the modified electrode.

Table 3.1. *Summary of the diffusion coefficient (D_0) and k_s of the redox marker $[Fe(CN)_6]^{3-/4-}$ and p-benzoquinone for H_2TPP-1CP/CRGO and ssDNA/H_2TPP-1CP/CRGO*

	In $[Fe(CN)_6]^{3-/4-}$		**In benzoquinone**	
	D_0 (10^{-6} cm^2 s^{-1})	**k_s(cm s^{-1})**	**D_0 (10^{-6} cm^2 s^{-1})**	**k_s(cm s^{-1})**
H_2TPP-1CP/CRGO	6.0	0.0057	1.0	0.0279
ssDNA/H_2TPP-1CP/CRGO	4.6	0.0014	0.5	0.012

Fig. 3.3 shows the SWVs of the modified electrode surface performed in benzoquinone solution before and after ssDNA immobilization. The voltammograms exhibit a decrease of reductive current of benzoquinone to hydroquinone after ssDNA covalently interacted with H_2TPP-1CP/CRGO platform. This can be explained by either to the low electron transfer or to the slow diffusion of ions to the electrode surface during redox process, due to the attachment of ssDNA molecules, as observed in previous work[2,3]. The electrochemically reduced signal current decreases in proportional to the amount of the ssDNA immobilized on the H_2TPP-1CP/CRGO layer. On the basis of the variation of the charge Q obtained under the cathodic wave

by SWV experiments at E_{red} = -0.1 V, a variation (ΔQ) is calculated to be 0.029 mC. A variation of the surface coverage (ΔΓ) can be calculated according to the equation: ΔΓ = ΔQ / nFA (Eq.2), where n is the number of electrons involved in the redox process, F the Faraday constant, and A the area of the electrode. The decrease of the surface coverage of benzoquinone (2.2 ± 0.65 nmol cm^{-2}) reflects the immobilization of ssDNA on the H_2TPP-1CP/CRGO layer.

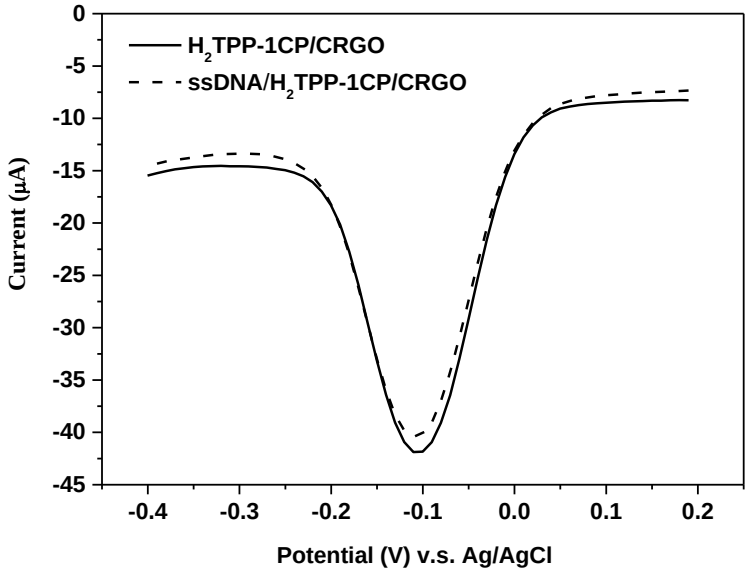

Fig. 3.3. *SWVs of H_2TPP-1CP/CRGO before (solid line) and after (dashed line) immobilization of ssDNA, recorded in 0.1 M KCl with 1 mM , scan rate of 12.5mV s^{-1}.*

1.2 Detection of DNA sensor

Hybridization reaction was performed by successive addition of complementary targets (cDNA) containing complementary sequence to the DNA probe. The evaluated concentrations of targets are ranging from 10 aM to 10 nM. Electrochemical detection of DNA targets was monitored by EIS measurements in 5 mM $[Fe(CN)_6]^{3-/4-}$ (Fig. 3.4A). After hybridization, EIS measurements show an increase of the charge transfer resistance with the increasing concentration of cDNA target. As mentioned before, ssDNA bases block the diffusion of $[Fe(CN)_6]^{3-/4-}$ species to the electrode surface. When ssDNA hybridized with cDNA target, double-helix structure is formed and electronegative phosphate groups are introduced on the

surface. It is more difficult for $[Fe(CN)_6]^{3-/4-}$ to reach the electrode due to the electrostatic repulsion. Hence, the R_{ct} value increases with the formation of double-stranded DNA (Fig 3.4A). Hybridization reaction was also performed by CV measurements in $[Fe(CN)_6]^{3-/4-}$ solution (Fig. 3.4B). The current of $[Fe(CN)_6]^{3-/4-}$ is decreased and the reversibility of redox process is lost with the increasing of the target concentration. These results are in good agreement with those obtained in EIS experiments. The evaluated logarithmic relationship between $\Delta R_{ct}/R_{ct\ ssDNA}$ and the concentration of the cDNA target was shown in the inset of Fig. 3.4A. The ΔR_{ct} corresponds to the difference between R_{ct} value of the ssDNA linked to the electrode surface and that after hybridization with cDNA ($\Delta R_{ct} = R_{ct,dsDNA} - R_{ct,ssDNA}$). The regression equation was $\Delta R_{ct}/R_{ct,ssDNA} = 0.1642 \lg C_{target} + 2.77$ with regression coefficient of 0.98. The detection limit was estimated to be 7×10^{-14} M (signal-to-noise ratio of 3 independent measurements, taking into accord the standard deviation of 0.2136).

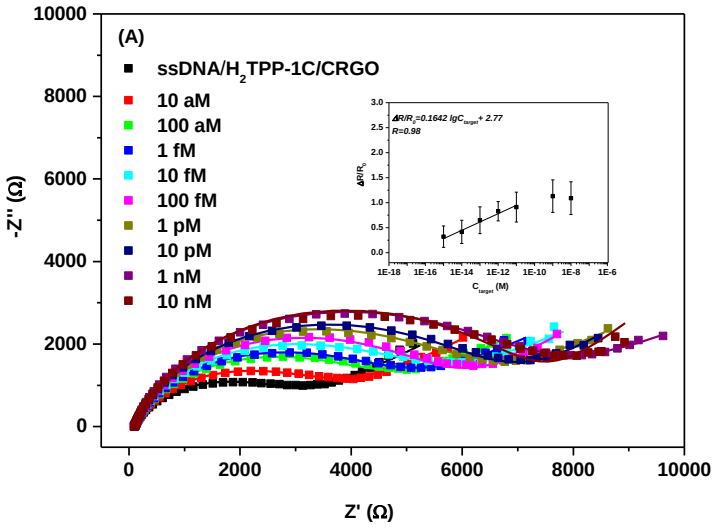

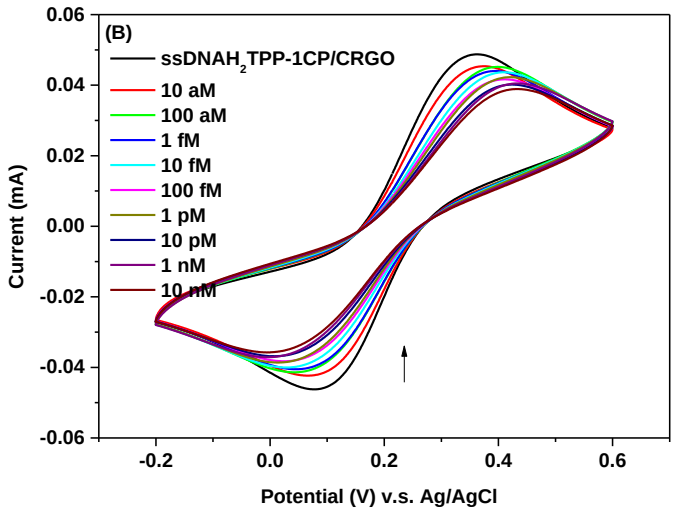

Fig. 3.4. *Detection of complementary target of different concentrations: 10 aM; 1 fM; 10 fM; 100 fM; 1 pM; 10 pM; 1 nM; 10 nM. in 5 mM* $[Fe(CN)_6]^{3-/4-}$*, (A) EIS measurments, the inset is the relative changes of the electron transfer resistance* $\Delta R_{ct}/R_{ct\ ssDNA}$ *vs. concentration (B) CV.*

To eliminate the effect of electrostatic repulsions between the negatively charged DNA skeleton and negative redox ions in solution, the electrochemical detection of DNA targets was monitored in 1 mM benzoquinone by SWV measurements. Fig. 3.5 exhibits the SWV plots of DNA sensor based on H_2TPP-1CP/CRGO after hybridization with DNA target in concentrations range from 1 aM to 1 nM. The reduction current of benzoquinone species into hydroquinone decreases with the increasing concentration of cDNA targets. As previously observed, this phenomenon is merely due to the formation of double-helix structure, which further block the diffusion of p-benzoquinone species to the electrode.

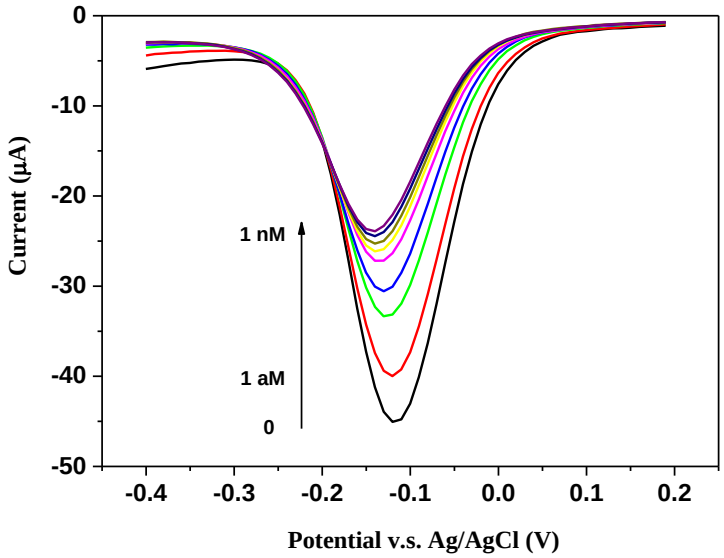

Fig. 3.5. *SWV experiments during detection of biosensors based on H_2TPP-1CP/CRGO at various concentration of targets (1 aM to 1 nM).*

The relative changes of current peak versus the concentration of complementary ssDNA targets were shown in Fig. 3.6. The detection limit was estimated to be 2×10^{-18} M for DNA sensor based on H_2TPP-1CP/CRGO, (signal-to-noise ratio of 3 independent measurements, taking into accord the standard deviation of 0.0101), which is lower by four orders of magnitude compared to that estimated in $[Fe(CN)_6]^{3-/4-}$ solution for the same DNA sensor.

1.3 Selectivity of DNA sensor

To test the selectivity of the DNA sensor based on H_2TPP-1CP/CRGO, non-specific interactions were studied by incubating the DNA sensor with non-complementary DNA targets (nc DNA) in the same conditions as for the detection of complementary target. SWV analyses were performed in 1 mM benzoquinone solution after incubating the sensor in various concentrations of nc DNA targets ranging from 1 aM to 1 nM. Fig. 3.6A presents the superposition of the calibration curves obtained for detection of c DNA and nc DNA. Although the calibration curve is below that obtained during the detection of c DNA, this biosensor gives a positive

response in the presence of non-complementary DNA strands. The histogram in the Fig. 3.6B shows a 30% variation of the current in presence only of 1 fM of nc DNA. This positive signal of the sensor can be explained by undesired interactions of nc DNA with the modified electrode surface, such as Van der Waals interactions, π-stacking interactions with aromatic DNA bases. Similar results were also observed during the detection of nc DNA of the DNA sensor based on MnTPP/CRGO materials (Part B. chapter II). To eliminate this phenomenon, we proposed to increase the number of negative charges of the nanomaterials on the electrode surface. Indeed, with an electrode surface charged more negatively, we expected that the DNA strands, also charged negatively, less interact. A solution is to increase the number of carboxylic functions on the porphyrins skeleton that becomes negatives at pH 7. Thus we proposed to synthesize a new porphyrin bearing four carboxylic groups on phenyl groups (H_2TPP-4CP) and to integrate in the DNA sensor

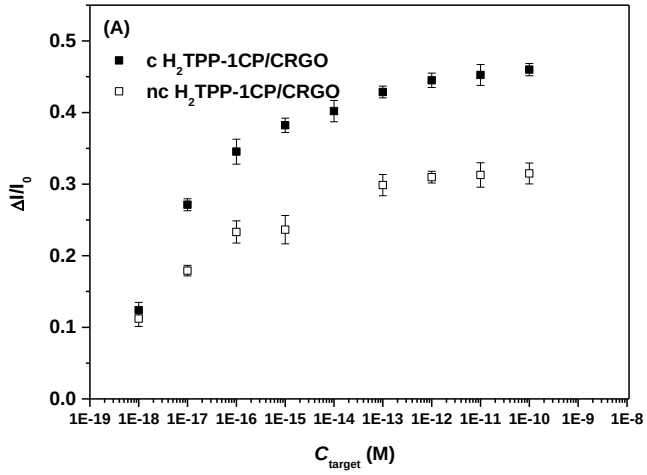

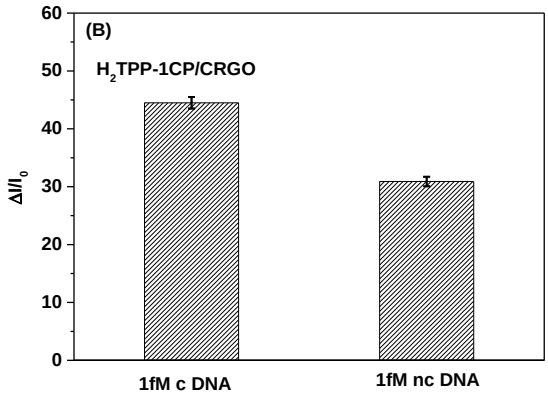

Fig. 3.6. *(A) Plot of the relative changes of the current peak versus concentration of DNA targets on the H_2TPP-1CP/CRGO.. (B) Histogram comparing hybridization signal after detection of 1 pM of c DNA and nc DNA sample. Data points are the mean values ± RSD obtained with three.*

2 DNA sensor based on H_2TPP-4CP/CRGO

2.1 Construction of DNA sensor

The sDNA strands were immobilized in the same conditions than those used for the construction of the sensor based on H_2TPP-1CP/CRGO (paragraph 1.1). The modified layer was characterized by electrochemical experiments. EIS measurement results performed in PBS before (curve a) and after the reaction of ssDNA probe with H_2TPP-4CP (curve b) are shown in Fig. 3.7 and data in supplementary information (Table S3.4). An obvious increase from 72 to 154 kΩ of the electron transfer resistance after immobilization confirms as well the successfully covalently attachment of ssDNA to H_2TPP-4CP/CRGO composite. This variation can still be explained by a blocking of diffusion ions process to the electrode surface. The thickness is deceased from 20 to 6 nm (Table S3.4) and the N_2 (that reflects the roughness of the layer) varies from 0.56 to 0.64. These results indicate that the covalently attachment of ssDNA on the hybrid nanomaterial surface affects the molecular organization on the surface. This can explain the decrease of the thickness of the nanomaterial layer as it was also observed with the previous DNA sensor

(paragraph 1.1)

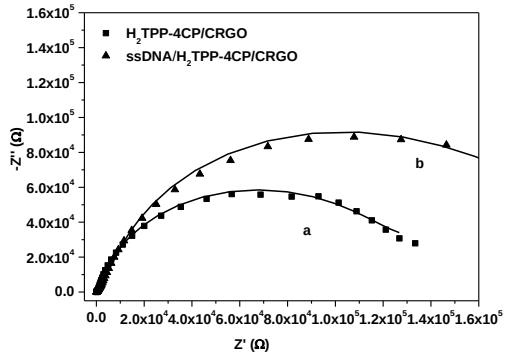

Fig. 3.7. *Nyquists plots measured in PBS solution (a) H_2TPP-4CP/CRGO and (b) ssDNA/H_2TPP-4CP/CRGO.*

A study of the ssDNA/H_2TPP-4CP/CRGO surface, was performed by the CV and EIS in 5 mM negatively $[Fe(CN)_6]^{3-/4-}$ species after the immobilization of ssDNA (Fig. 3.8). CV experiments (Fig. 3.8A) show that after the immobilization of ssDNA, redox signal of $[Fe(CN)_6]^{3-/4-}$ species becomes more reversible (increase of the current intensity and ΔE closed to 60 mV). The estimated electron resistance transfer (R_{ct}) sharply decreases from 8.4 to 2.3 kΩ (the data is shown in Table. S3.5) (Fig. 3.8B). The interaction between H_2TPP-4CP/CRGO and ssDNA has an apparent effect on the electronic properties of the modified surface, presumably due to a rearrangement of the orientation of the biomaterial to the electrode surface induced by the charge repulsions that lead to modifications of the electronic charges on the surface.

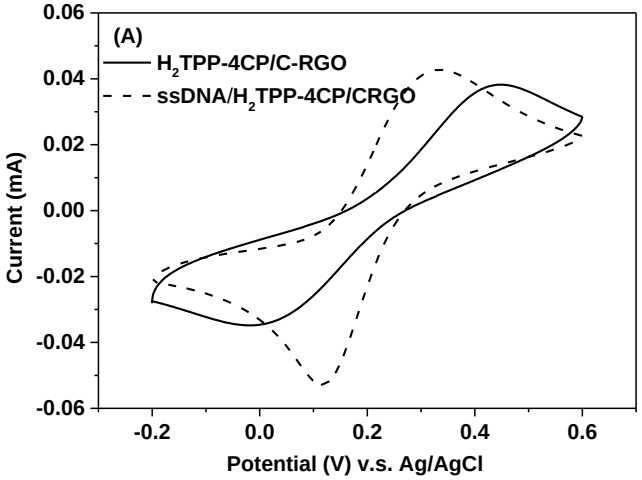

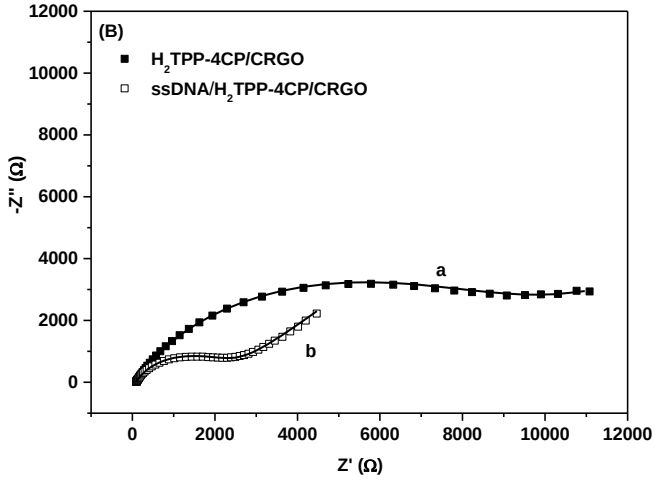

Fig. 3.8. *(A) Cyclic voltammograms of immobilization of ssDNA and (B) Nyquists plots recorded in 0.1 M KCl with 5 mM $[Fe(CN)_6]^{3-/4-}$ of H_2TPP-4CP/CRGO before (solid black line or a) and after (dashed black line or b).*

Fig. 3.9 shows the SWVs performed after the construction of DNA sensor exhibiting a decreasing of current after ssDNA covalently interacted with H_2TPP-4CP/CRGO surface. The variation of ΔQ is calculated to be 0.06 mC and the calculated surface coverage of reduced benzoquinone is evaluated as 4.6 ± 0.43 nmol cm^{-2} which is around 2 times higher compared to that of the H_2TPP-1CP/CRGO modified electrode. This demonstrates that with the same initial concentration of porphyrin, a largest amount of ssDNA is immobilized on the surface of the H_2TPP-4CP/CRGO. This result is not surprising since the number of reactive carboxylic functions has also increased on the surface.

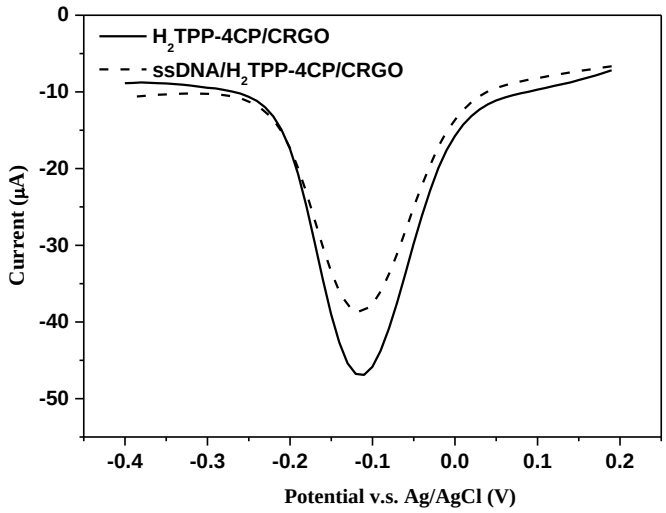

Fig. 3.9. *SWVs of H_2TPP-4CP/CRGO before (solid line) and after (dashed line) immobilization of ssDNA, recorded in 1 mM benzoquinone scan rate of 12.5mV s^{-1}.*

The diffusion coeffcient (D_0) of the redox marker $[Fe(CN)_6]^{3-/4-}$ in aqueous media was calculated by the Randles-Sevcik equation (Table 3.2) following the same procedure as H_2TPP-1CP/CRGO used. It was estimated to be 2.5×10^{-6} cm^2 s^{-1} before and 4×10^{-6} cm^2 s^{-1} after the attachment of ssDNA on the nanomaterial. The D_0 increases sensibly which is in good agreement with CV and EIS observations (better reversibility of the redox system and better conductivity of the nanolayer). In *p*-benzoquinone solution, the neutral redox marker, D_0 was also calculated and was found to be 5.6×10^{-6} cm^2 s^{-1} before and after the immobilization of ssDNA, the value decreases to 3.8×10^{-6} cm^2 s^{-1} (Table 3.2). In this case, the diminution of D_0 can only be explained by steric effects due to the presence of the ssDNA anchored on the surface, that blocks the diffusion of ions to the electrode, instead of charge repulsions because the redox marker is neutral.

Table 3.2. *Summary of the diffusion coefficient (D_0) of the redox marker $[Fe(CN)_6]^{3-/4-}$ and p-benzoquinone for H_2TPP-4CP/CRGO and ssDNA/H_2TPP-4CP/CRGO*

	In $[Fe(CN)_6]^{3-/4-}$		In benzoquinone		
	D_0 (10^{-6} cm^2 s^{-1})	**k_s(cm s^{-1})**	**D_0 (10^{-6} cm^2 s^{-1})**	**k_s(cm s^{-1})**	**Q (mC)**
H_2TPP-4CP/CRGO	2.5	0.0006	5.6	0.008	0.58 ±0.12
ssDNA/H_2TPP-4CP/CRGO	4	0.0003	3.8	0.005	0.52 ±0.11

A larger amount of ssDNA immobilized on the modified surface, presumably due to the covalently interaction between hybrid complex and ssDNA tends to overwhelm the carboxylic group on the edge of the CRGO which induce the symmetrical side of carboxylic group erected slightly enhancing the diffusion of the benzoquinone. The schematic graph is shown in scheme 3.2.

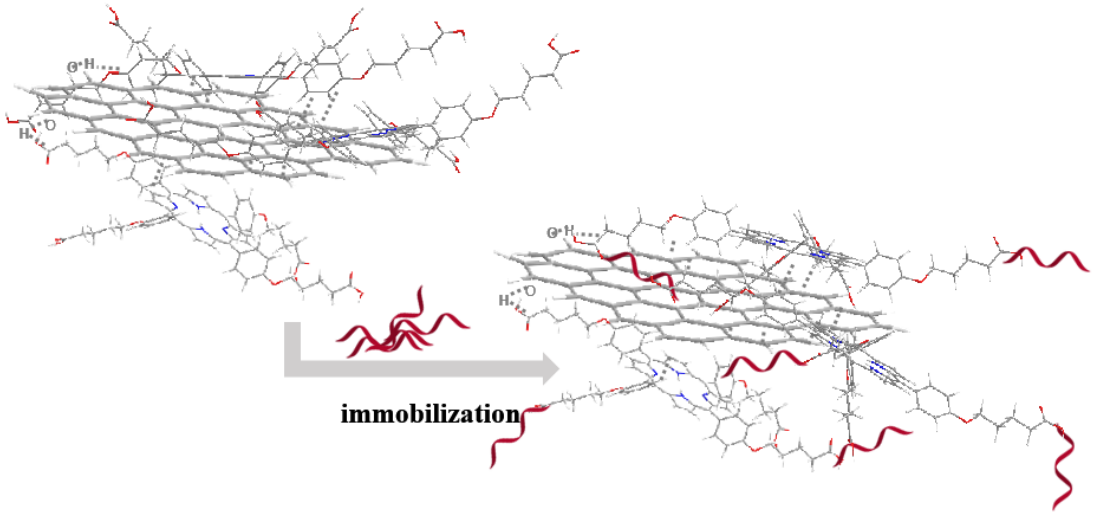

Schema 3.2. *The immobilization of ssDNA on the H_2TPP-4CP/CRGO hybrid nanomaterial*

2.2 Detection of DNA sensor

Hybridization reaction was performed with complementary targets (cDNA) by successive additions of various concentrations ranging from 10 aM to 100 nM. Electrochemical detection of DNA targets was monitored by EIS and CV measurements in 5 mM $[Fe(CN)_6]^{3-/4-}$, as redox indicator (Fig. 3.10). After hybridization, an increase of the charge transfer resistance (Fig. 3.10A) was observed

with the increasing concentration of cDNA target and a decrease of the reversibility of the redox process of $[Fe(CN)_6]^{3-/4-}$ species (Fig. 3.10B) was noticed. These results indicate the formation of double-stranded DNA (dsDNA) as previously observed in the case of the DNA sensor based on H_2TPP-1C/CRGO. Relationship between ΔR_{ct}/ $R_{ct\ ss\ DNA}$ and the log of the concentration of the cDNA target was evaluated (inset of Fig. 10A). The regression equation is $\Delta R_{ct}/ R_{ct,ssDNA}$ = 0.1425 lgC_{target} +2.55 with regression coefficient of 0.99. The detection limit was estimated to be 6 × 10^{-17} M (signal-to-noise ratio of 3 independent measurements, taking into accord the standard deviation of 0.2617).

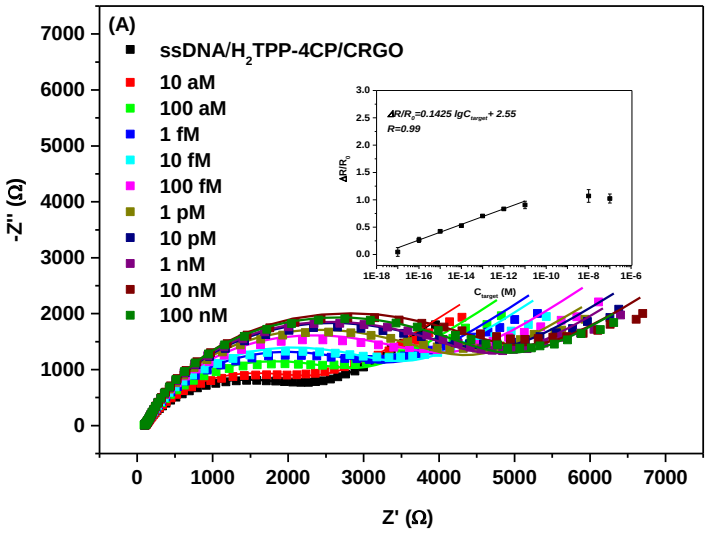

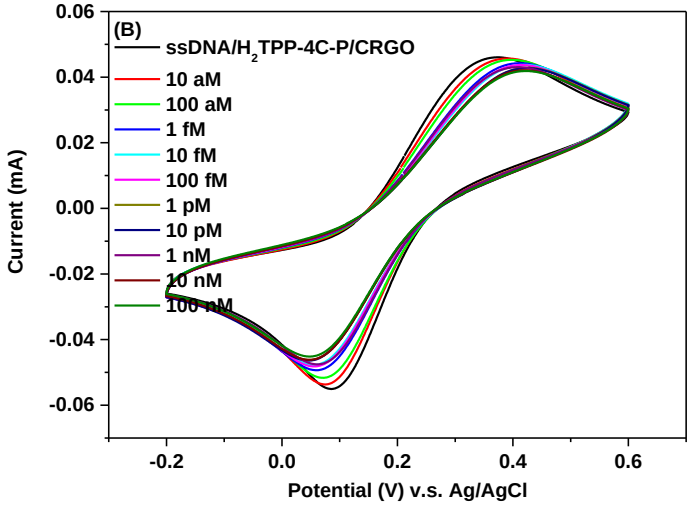

Fig. 3.10. *Detection of complementary target of different concentrations: 10 aM; 1 fM; 10 fM; 100 fM; 1 pM; 10 pM; 1 nM; 10 nM; 100 nM in 5 mM $[Fe(CN)_6]^{3-/4-}$ (A) Nyquist diagrams (B) CV.*

To eliminate the effect of electronic repulsions, the electrochemical detection of DNA targets was monitored by SWV measurements in 1 mM benzoquinone. Fig. 3. 11 exhibits the SWV plots for DNA sensor response after hybridization of various concentrations of DNA target range from 1 aM to 1 nM. The reduction current of benzoquinone to hydroquinone decreases with the increasing concentration of cDNA targets, merely due to the formation of double-strand structure, which further block the diffusion of p-benzoquinone species to the electrode.

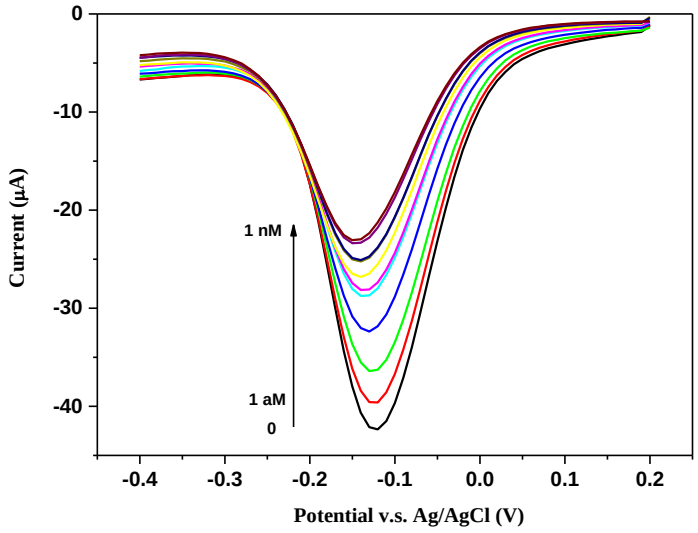

Fig. 3.11. *SWVs experiments for detection in benzoquinone solution with the scan rate 12.5 mV.s^{-1}*

2.3 Selectivity of the DNA sensor

Fig. 3.12 A presents the superposition of the calibration curves obtained after incubation of the sensor in various concentrations of c DNA and nc DNA targets at the concentrations ranging from 1 aM to 1 nM in 1 mM benzoquinone solution. The two calibration curves indicate clearly that the DNA sensor based on H_2TPP-4CP/CRGO has a good hybridization selectivity to discriminate the non-complementary from the complementary sequences. Compared to the previously

prepared sensor (paragraph 1.1), the improved selectivity might be attributed to the increase of some residual carboxylate groups on the electrode surface. The large amount of carboxylate functions introduced on phenyl groups of the porphyrin leads to a surface more negatively charged preventing then the undesired interactions of the DNA by charge repulsions. This improves the selectivity to the target sequences detection

However, the calibration curve for nc DNA detection increases for lower concentrations to reach to a plateau. This increase can be attributed to non-specific adsorptions of the nc DNA onto the GC electrode surface. Indeed, Fig. S3.2 (supporting information) shows that after the immersion of the bare GC electrode in 1 nM target for 40 min. in 47 ℃, a relative change of the current (ΔI/I) is up to 15%. This result is in the same order of magnitude than the variation observed during the detection of 1 fM of nc DNA taget presented in the histogram (Fig. 3.12 B).

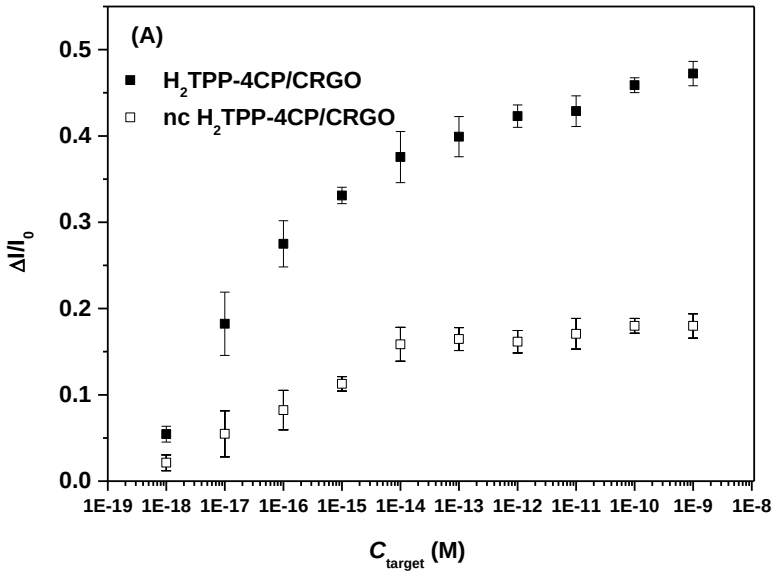

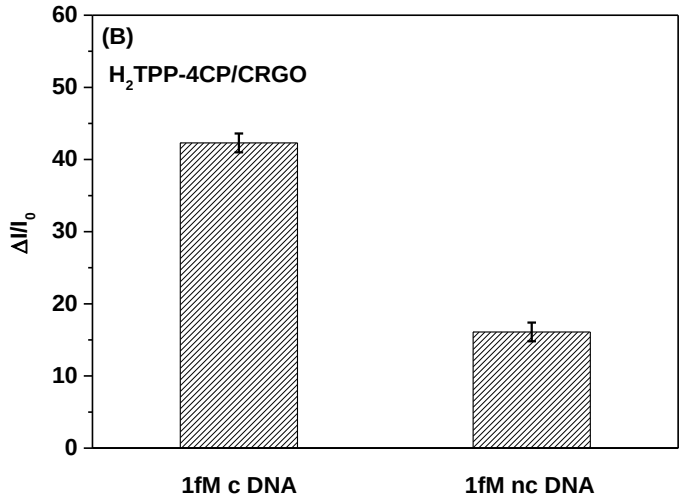

Fig. 3.12. *(A) Plot of the relative changes of the peak current versus concentration of DNA targets on the H_2TPP-4CP/CRGO in benzoquinone. (B) Histogram comparing hybridization signal intensities. Data points are the mean values ±RSD obtained with three measurements.*

3 Comparison of properties for H_2TPP-nCP bearing different carboxylic groups

3.1 Summary and Comparison of ssDNA/H_2TPP-nCP/CRGO nanomaterial

Comparing to the electronic properties recorded in two different redox markers, a negatively charged [$Fe(CN)_6^{3-/4-}$] and a neutral one (benzoquinone), we noticed some real difference of the two bio-nanomaterials, in term of thickness, configuration of ssDNA on H_2TPP-nCP/CRGO layer and the repartition of charges on the surface. The measurement data were summaried in Table 3.3.

The decreased of coverage of benzoquinone which is reduced on the ssDNA/H_2TPP-4CP/CRGO modified electrode is 2 times higher compared to that of ssDNA/H_2TPP-1CP/CRGO, demonstrating that a larger amount of ssDNA is immobilizated on the surface of the H_2TPP-4CP/CRGO.

In solution of [$Fe(CN)_6^{3-/4-}$], compared to slightly increase relative R_{ct} of H_2TPP-1CP/CRGO (+ 5%) after the immobilization of ssDNA, the $\Delta R_{ct}/R_{ct}$ decreased

obviously with a relative value of -73 % for H_2TPP-4CP/CRGO. This indicates that the H_2TPP-4CP/CRGO nanomaterial become more conductive after grafting ssDNA on it that can be explained by a repartition of charges differently with such material. This observation is supported by the increase of the relative diffusion value [$\Delta D_0/D_0$ = 60%] of $Fe(CN)_6^{3-/4-}$ ions and the reversibility of the redox marker signal (Fig. 3.8). Although a larger amount of ssDNA is immobilized on the surface, the D_0 increases, suggesting that the ssDNA is covalently interacted with hybrid complex on the edge of the CRGO instead of on the stacking basal plane. Indeed, we proposed in the chapter I, that the H_2TPP-4CP interacted with CRGO on its edge. Furthermore, the thinner thickness of 6 nm could also support the hypothesis. In contrast, the decreased of $\Delta D_0/D_0$ after ssDNA immobilization of H_2TPP-1CP/CRGO nanomaterial indicates that the ssDNA lie on the surface of hybrid nanomaterial, layer by layer, which block the diffusion of the $Fe(CN)_6^{3-/4-}$ ions to the surface. A higher thickness of 30 nm also confirms this result.

In *p*-benzoquinone solution, eliminating the effect of the charge, difference are also noticed and are in good agreement with the organisation of ssDNA we proposed. Compared to H_2TPP-1CP/CRGO, a lower decrease of relative value of $\Delta D_0/D_0$ and $\Delta k_s/k_s$ are observed for H_2TPP-4CP/CRGO nanomaterial after reaction, in spite of a larger amount of ssDNA immobilized on the modified surface. As we think, it is presumably due to the covalently interaction of ssDNA with hybrid nanomaterial on the edge of the CRGO, and thus leads to release the surface and facilitates the diffusion of the ions to the electrode surface.

Table 3.3. *Summary of data for ssDNA/H_2TPP-1CP/CRGO and ssDNA/H_2TPP-4CP/CRGO*

			In $[Fe(CN)_6]^{3-/4-}$			**In benzoquinone**	
	Γ (nmol cm^{-2})	**Thickness (nm)**	**$\Delta R_{ct}/R_{ct}$**	**$\Delta D_0/D_0$**	**$\Delta k_s/k_s$**	**$\Delta D_0/D_0$**	**$\Delta k_s/k_s$**
ssDNA/H_2TPP-1CP/CRGO	**2.2 ±0.65**	**30**	**5%**	**-23%**	**-75%**	**-50%**	**-57%**
ssDNA/H_2TPP-4CP/CRGO	**4.6 ±0.43**	**6**	**-72.6%**	**60%**	**-50%**	**-32.1%**	**-37.5%**

3.2 AFM morphologies of ssDNA/H_2TPP-nCP/CRGO layer

To further characterize hybrid nanomaterials and their morphology, AFM images were performed for ssDNA/H_2TPP-1CP/CRGO layer (a) and ssDNA/H_2TPP-4CP/CRGO (b) after ssDNA immobilization (Fig. 3.13). As it is shown, the morphology is completely different compared to the two DNA sensors: a surface more dense and compact for picture a) and a surface with helical elements for picture b). In the latter case, the helical structures could be attributed to the single-strand structure of ssDNA, grafted certainly on the edge of the hybrid complex. In contrast for ssDNA/H_2TPP-1CP/CRGO, the surface is more compact due to probably an immobilization of ssDNA layer by layer, homogeneously, on the plane hybrid surface layer.

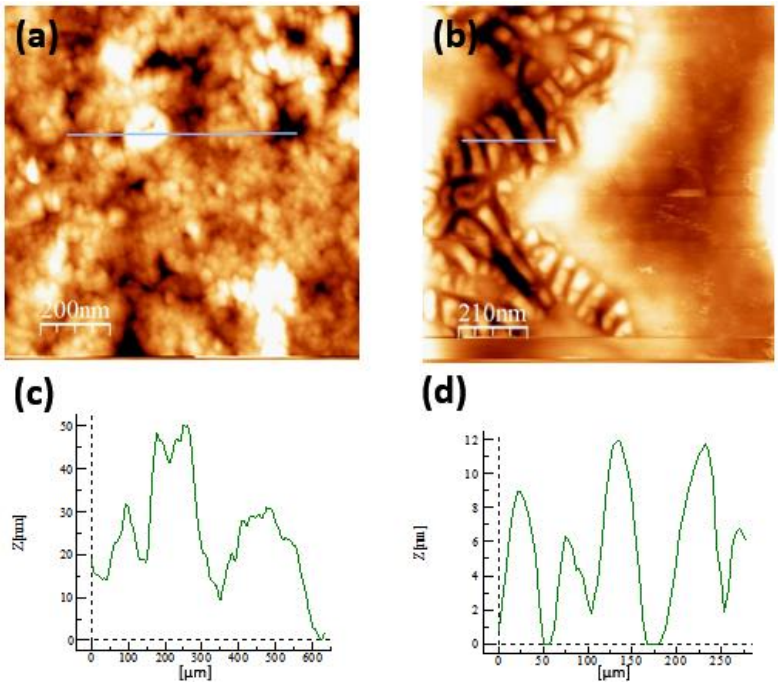

Fig. 3.13. *AFM images of (a) ssDNA/H_2TPP-1CP/CRGO and (b) ssDNA/H_2TPP-4CP/CRGO; and (c), (d) line cross-section analysis of the AFM images respectively.*

3.3 Summary and Comparison of Detection of ssDNA/H_2TPP/CRGO

The performance of the two DNA sensors, monitored by different electrochemical techniques (EIS and SWV) in presence of the two redox markers

($Fe(CN)_6^{3-/4-}$ and benzoquinone) are summarized in the Table 3.4, for better view.

In benzoquinone solution by SWVs analysis, DNA sensor based on H_2TPP-4C/CRGO exhibits a higher LOD than the other but the linear range is sensibly in the same order of magnitude for the two sensors even if the amount of ssDNA immobilized on the surface of the H_2TPP-4C/CRGO is larger. Thus, the selectivity, tested in neutral redox marker for the detection of 1 fM of non-complementary target (Fig. 3.14, deduced from the results of Fig. 3.6 and 3.12), exhibits a better response for the DNA sensor based on H_2TPP-4CP/CRGO, with only 15% of variation for the relative change of peak current compared to 30% for the DNA sensor based on H_2TPP-1CP/CRGO. This difference can be explained by the presence of more negative charges on the surface, due to larger amount of carboxylic functions on porphyrins, preventing so the non-specific interactions with DNA sequences to the surface. However, this result was improved but not completely satisfactory.

The DNA sensor based on the H_2TPP-4CP/CRGO hybrid nano-material demonstrated better performance and was used to further explore in detecting PCR samples.

Table 3.4. *Summary of detection data*

	EIS in $[Fe(CN)_6]^{3-/4-}$		**SWV in benzoquinone**		
	LOD (M)	**Linear range (M)**	**LOD (M)**	**Linear range (M)**	**nc 1fM ($\Delta I/I_0$)**
H_2TPP-1CP/CRGO dsDNA	7×10^{-14}	10^{-11}~10^{-9}	2×10^{-18}	10^{-18}~10^{-12}	30%
H_2TPP-4CP/CRGO dsDNA	6×10^{-17}	10^{-17}~10^{-9}	7×10^{-19}	10^{-18}~10^{-11}	15%

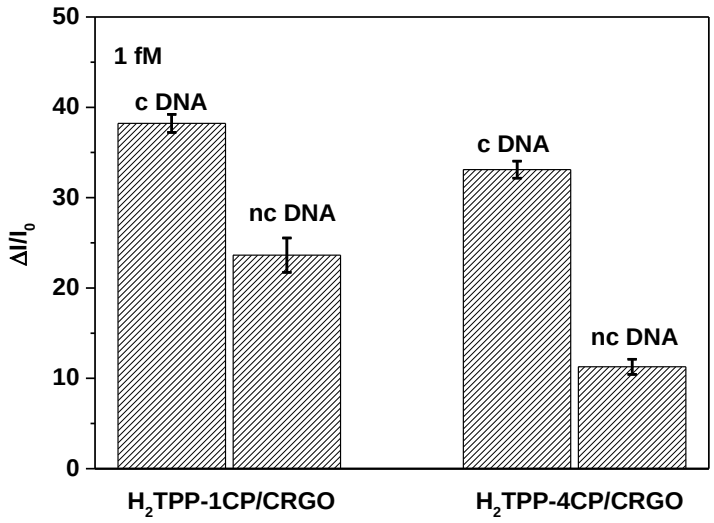

Fig. 3.15. *Histogram comparing hybridization signal intensities for DNA sensor after detection of 1 fM of c DNA and nc DNA sample. Data points are the mean values ± RSD obtained with three independent experiments.*

3.4 DNA Detection from Clinical Samples of Drug Resistant Mycobacterium tuberculosis

The PCR samples (c PCR) were composed of DNA fragment of 411 bases length from *ropB* with the wild-type sequence. As a negative control, DNA sequence containing punctual TTG mutation (nc PCR) was used. The hybridization reactions with the sample with wild-type sequence (c PCR) and the sample with TCG/TTG mutation (nc PCR) were performed. The PCR sample detection by DNA sensor based on H_2TPP-4CP/CRGO was analyzed using SWV techniques and the results are illustrated in Fig. 3.15A. Hybridization with the wild-type c PCR sample, leads to a decrease in reduction current of benzoquinone. The average variation of current was calculated as 23 ± 2.5% (shown in Fig. 3.15B, a). This result was obtained after 3 independent measurements from different M. tuberculosis DNA clinical isolates. Hybridization with nc PCR sample, resulted in a small variation in current calculated as 4 ± 1.9% (Fig. 3.15B, b).

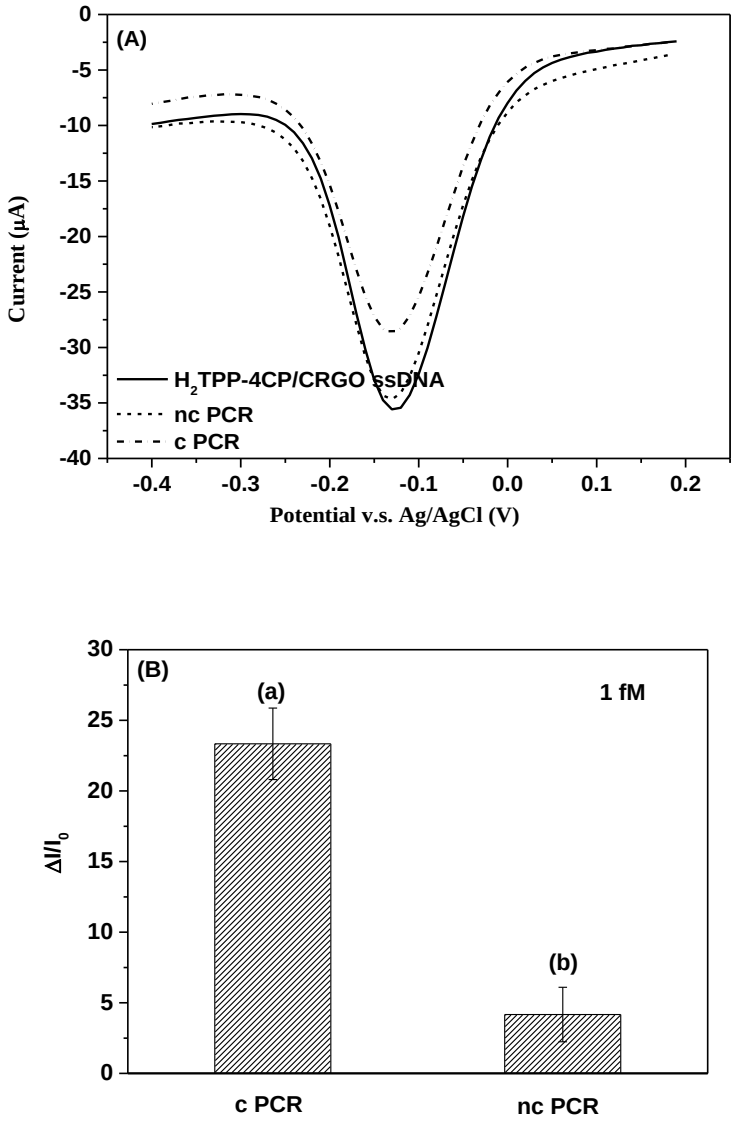

Fig. 3.15. *Detection of c PCR and nc PCR sequence in benzoquinone (A) SWVs measurements scan rate 12.5 mV.s^{-1} (B) Histogram comparing hybridization signal intensities for detection of 1 fM of c PCR and nc PCR sample. Data points are the mean values ±RSD obtained with three independent experiments.*

Conclusion

In conclusion, we successfully design electrochemical DNA sensor for highly sensitive and selective detection of DNA target based on a π-conjugated nanomaterial composed of chemically reduced graphene oxide (CRGO) and tetraphenylporphyrin functionalized with numerous carboxylic groups (H_2TPP-nCP$_{n=1,\ 4}$). Through electrochemical analysis and AFM measurements of the modified surface, we proposed two different modes of DNA immobilizing on the nanomaterial surface depending on its nature: a) the immobilized ssDNA lies on the plane hybrid surface homogeneously layer by layer for H_2TPP-1CP/CRGO material, and b) for H_2TPP-4CP/CRGO, the ssDNA sequences graft on the edge of the hybrid complex and tend to overwhelm the construction of carboxylic group on the edge of the CRGO. However, increasing the number of carboxylic functions on porphyrin afforded a largest amount of immobilized ssDNA on the complex surface and offered a stable and highly sensitive sensing layer. The hybridization reaction on the modified electrode was monitored by SWV analysis using p-benzoquinone, demonstrated that the electrochemically reduced signal current decreases in proportional to the amount of the complementary DNA target. The proposed DNA sensor showed high sensitivity for detecting complementary DNA in a wide linear range [10^{-18}-10^{-12} M] and [10^{-18} M-10^{-11} M] for DNA sensor based on H_2TPP-1CP/CRGO and H_2TPP-4CP/CRGO, respectively with a detection limit as low as 2×10^{-18} and 7×10^{-19} M (S/N = 3). Most importantly, we demonstrated that the selectivity was enhanced by introducing numerous negative charged functional groups on the porphyrins. Indeed, only 15% of variation for the relative change of peak current were observed during the detection of non-complementary DNA sequence at low concentration compared to 30% for the sensor based on H_2TPP-1CP/CRGO. However this value is still high and should be improved such as blocking the glassy carbon electrode with aromatic compounds to avoid any self-assembled adsorptions on the electrode. The Chapter IV will discuss

about that.

Furthermore, the versatile elaborated DNA sensor based on H_2TPP-4CP/CRGO endows property for sensing DNA of rpoB gene of *Mycobacterium tuberculosis* in real PCR samples. This shows enormous potential on H_2TPP-4CP/CRGO platform with electrical conductivity and dispersibility for further applications in pathogens diagnostic and therapeutic purpose.

Supporting Information

***Table S3.1**. Summary of estimated EIS parameters of H_2TPP-1CP/RGO and ssDNA/H_2TPP-1CP/CRGO obtained in PBS buffer, pH 7.4. Results are mean ±S.D. obtained from 3 independent measurements in each series*

	R_s (Ω)	R_{ct1} (KΩ)	CPE 1 (µMho)	N1	R_{ct2} (KΩ)	CPE 2 (µMho)	N2	Thickness (nm)	Capacitance (µF)	χ^2
H_2TPP-1CP/CRGO	82.8 ±1.5	72.6 ±5.2	28.0 ±2.9	0.96 ±1.5	59.4 ±2.3	99.3 ±9.5	0.53 ± 2.1	72 ±9.3	0.0027	0.06
ssDNA/H_2TPP-1CP/CRGO	87.0 ±2.5	66.9 ±1.5	48.2 ±2.6	1.1 ± 1.7	166 ± 1.5	41.7 ±3.4	0.575 ±2.2	31 ±3.5	0.0064	0.03

***Table S3.2**. Summary of estimated EIS parameters of H_2TPP-1CP/RGO and ssDNA/H_2TPP-1CP/CRGO obtained in 0.1 M KCl containing 5 mM $[Fe(CN)_6]^{3-/4-}$ solution.*

	R_s (Ω)	R_{ct} (KΩ)	CPE1 (µMho)	N1	CPE2 (µMho)	N2	χ^2
H_2TPP-1CP/CRGO	100 ±0.5	3.49 ±3.2	10.8 ±2.6	0.742 ±0.4	249 ±2.7	0.392 ±4.1	0.04
ssDNA/H_2TPP-1CP/CRGO	117 ±0.8	3.56 ±1.2	5.09 ±3.3	0.795 ±0.5	335 ±2.6	0.5	0.04

***Table S3.3**. Summary of estimated EIS parameters of ssDNA/H_2TPP-1CP/CRGO and dsDNA/H_2TPP-1CP/CRGO obtained in 0.1 M KCl containing 5 mM $[Fe(CN)_6]^{3-/4-}$ solution.*

	R_s (Ω)	R_{ct1} (KΩ)	CPE1 (µMho)	N1	CPE2 (µMho)	N2	χ^2
ssDNA/H_2TPP-1CP/CRGO	95.6 ±0.6	2.65 ±2.9	7.24 ±3.3	0.778 ±0.53	370 ±2.6	0.396 ±4.0	0.02
10aM	100 ±0.55	3.29 ±2.9	7.5 ±2.8	0.784 ±0.5	356 ±3.0	0.399 ±4.6	0.018
1fM	99.9 ±0.5	4.35 ±3	6.46 ±2.6	0.798 ±0.43	340 ±4.0	0.386 ±5.9	0.019
100fM	94.5 ±0.6	5.49 ±2.	5.86 ±2.	0.808 ±0.4	408 ±4.	0.461 ±7	0.02

		3	6	3	8		
1nM	104 ±0.6	6.52 ±3.9	4.45 ±2.8	0.83 ±0.4	320 ±7.4	0.36 ±10.6	0.03

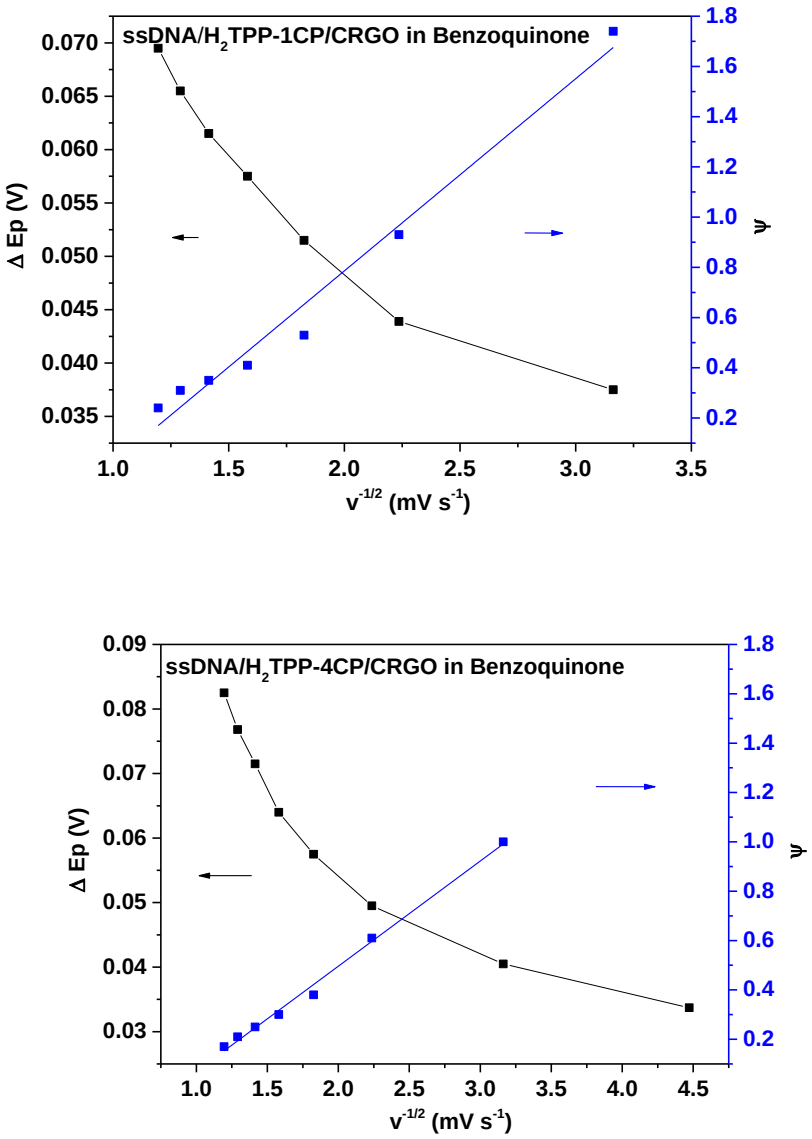

Fig. S3.1. *Relationship of ΔE_p and ψ versus $v^{-1/2}$ in benzoquinone, from which the k_s of ssDNA/H_2TPP-1CP/CRGO, and ssDNA/H_2TPP-4CP/CRGO were calculated.*

***Table S3.4**. Summary of estimated EIS parameters of H_2TPP-4CP/RGO and ssDNA/H_2TPP-4CP/CRGO obtained in PBS buffer, pH 7.4.*

	R_s (Ω)	R_{ct1} (KΩ)	CPE 1 (µMho)	N1	W1 (µMho)	R_{ct2} (KΩ)	CPE2 (µMho)	N 2	χ^2	Thickness (nm)	Capacitance (µF)
H_2TPP-4CP/CRGO	91.6 ±1.1	102 ± 3.9	20.3 ± 2.2	0.98 ±0.01		72.4 ±2.2	98.9 ± 10.2	0.56 ±0.01	0.05	20.4 ±1.2	0.009
ssDNA/H_2TPP-4CP/CRGO	102 ±4.1	116 ± 3.1	20.5 ± 2.1	1.03 ±0.01		154 ±3.2	28.8 ± 4.2	0.64 ±0.01	0.04	6.5 ±0.5	0.029

***Table S3.5**. Summary of estimated EIS parameters of H_2TPP-4CP/RGO and ssDNA/H_2TPP-4CP/CRGO obtained in $[Fe(CN)_6]^{3-/4-}$ at 0.15 V vs. Ag/AgCl.*

	R_s (Ω)	R_{ct1} (KΩ)	CPE1 (µMho)	N1	CPE2 (µMho)	N2	χ^2
H_2TPP-4CP/CRGO	91.7 ±3.5	8.43 ±5.1	13.3 ±2.0	0.731 ±0.04	294 ±10	0.355 ±0.013	0.01
ssDNA/H_2TPP-4CP/CRGO	95 ±0.5	2.28 ±0.86	9.74 ±2.2	0.74 ±0.03	395 ±1.3	0.502 ±0.01	0.015

***Table S3.6**. Summary of estimated EIS parameters of ssDNA/H_2TPP-4CP/CRGO and dsDNA/H_2TPP-4CP/CRGO obtained in 0.1 M KCl containing 5 mM $[Fe(CN)_6]^{3-/4-}$ solution at applied potentiel 0.15 V vs. Ag/AgCl.*

	R_s (Ω)	R_{ct1} (KΩ)	CPE1 (µMho)	N1	CPE2 (µMho)	N2	χ^2
ssDNA/H_2TPP-4CP/CRGO	96.8 ±0.7	1.92 ±2.2	16.2 ±2.9	0.753 ±0.05	465 ±1.8	0.481 ±0.04	0.009
10aM	101 ±0.9	1.82 ±2.	18.5 ±4.	0.809 ±0.0	390 ±2.	0.465 ±0.0	0.02

		7	3	8	1	4	
100aM	89.1 ±1.2	2.32 ±2.7	15.1 ±4.5	0.823 ±0.01	386 ±2.8	0.475 ±0.03	0.03
1fM	96.8 ±1.2	2.67 ±2.5	13.1 ±4.3	0.838 ±0.08	374 ±2.9	0.476 ±0.02	0.03
100fM	94.2 ±1.1	3.31 ±2.2	11.4 ±3.9	0.849 ±0.08	361 ±3.2	0.482 ±0.03	0.04
1nM	96.7 ±0.8	3.87 ±1.4	9.85 ±2.6	0.868 ±0.05	415 ±2.8	0.466 ±0.04	0.02

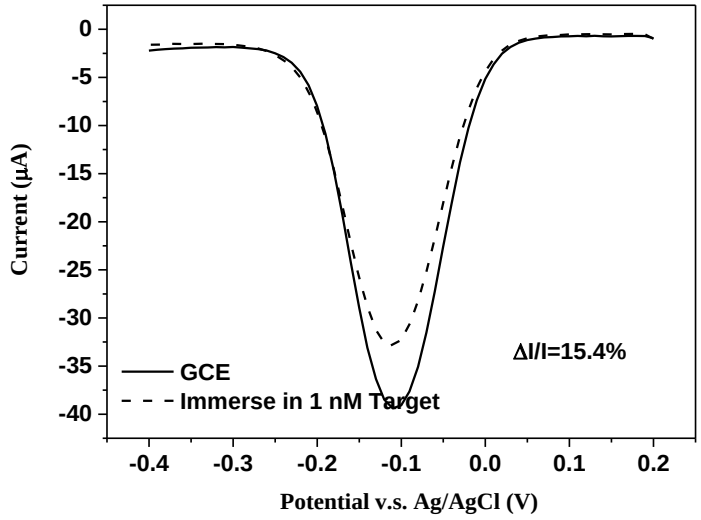

Fig. S3.2. *SWVs of GCE (solid line) and after immersion in 1 nM DNA target (dashed line), recorded in 0.1 M KCl with 1 mM benzoquinone in the range of potential from -0.4 to 0.2 V with the scan rate of 12.5mV s^{-1}.*

REFERENCES:

1. Park, Y. J., *et al.*, A novel thermostable arylesterase from the archaeon Sulfolobus solfataricus P1: Purification, characterization, and expression. *J. Bacteriol.* **190,** 8086–8095 (2008).
2. L ệ H. Q., *et al.* A. Investigation of SPR and electrochemical detection of antigen with polypyrrole functionalized by biotinylated single-chain antibody : A review. *Anal. Chim. Acta* **674,** 1–8 (2010).
3. Chebil, S. *et al.* Biosensors and Bioelectronics Electrochemical detection of d -dimer as deep vein thrombosis marker using single-chain d -dimer antibody immobilized on functionalized polypyrrole. *Biosens. Bioelectron.* **26,** 736–742 (2010).

PART B:

RESULTS AND DISCUSSION

CHAPTER IV:
Self-assembled selective DNA sensor

Abstract

A novel "signal-on" electrochemical DNA sensor with excellently sensitivity and selectivity was explored after pre-functionalization of GC electrode surface with a thin layer of β-phenylethylamine (β-PEA). The purpose of incorporating β-PEA layer in such DNA sensor was to underlines homogenous surface coverage of composite H_2TPP-4CP/CRGO with preformed self-assembled-monolayers (SAM) with phenyl in end position. Such function could improve the immobilization of composite as followed, thus can be obtained by π-π staking interaction of composite formed with graphene and the end-functional groups of SAM layer. In addition, such modification demonstrates its ability to prevent non-specific adsorptions of DNA on electrode surface during the hybridization reaction. The formation of β-PEA layer was optimized by electrodeposition of monomer in different concentrations, followed by the immobilization of hybrid complex moieties H_2TPP-4CP/CRGO and the grafting of ssDNA. All the steps of construction were studied and characterized by SWV, EIS measurements and AFM experiments. We demonstrated that the electrodeposition of β-PEA onto the glassy carbon leads to a homogeneous surface and allows to obtain a uniform covering of H_2TPP-4CP/CRGO on the electrode. It also increases the conductivity of the H2TPP-4CP/CRGO/β-PEA platform that thus promotes the reduction process of the benzoquinone. Detection of cDNA was investigated for sensing layer formed with various thickness of the β-PEA layer obtained by various concentration of the β-PEA for their electrodeposition. The sensing response obtained for DNA detection varied depending of the thickness of the layer. The superior performance for DNA sensing was obtained for H_2TPP-4CP/CRGO/2 β-PEA platform formed with high concentration of β-PEA which exhibits excellently sensitivity with limit detection low to 1.3×10^{-19} M and broad linear range from 10^{-18} to 10^{-9} M. In this case a "signal-on" was observed instead of signal off detection obtained in the previous surface. Moreover, the selectivity was investigated and the

H_2TPP-4CP/CRGO/2 β-PEA platform afford less non-specific ssDNA adsorption with only 2.5% of current variation

Materials and Methods

1. Reagents

N, *N*-Dimethylformaldehyde (DMF), acetonitrile (ACN), and β-phenylethylamine (β-PEA) were provided by Sigma- Aldrich, *N*-hydroxysuccinimide (NHS) from Fluka (Switzerland) and *N*-(3-dimethylaminopropyl)-*N'*-ethylcarbodiimide hydrochloride (EDC) from Sigma-Aldrich. Phosphate buffers saline (PBS) pH=7.4, contained 10 mM Na_2HPO_4, 1.8 mM KH_2PO_4, 2.7 mM KCl and 137 mM NaCl was prepared with double distilled water, filtered by 0.22 µm membrane filter and stored at 4 ºC until use.

All DNA sequences were provided by Eurogentec company. The DNA probe was a 25-bases sequence with six carbon chains as spacer and with amine group on 5' phosphoryl terminus: NH_2-C6 -5'-TCA-ATC-TCG-GGA-ATC-TCA-ATG-TTA-G-3'. The sequence of 25-bases target specific for DNA probe was 5'-CTA-ACA-TTG-AGA-TTC-CCG-AGA-TTG-A-3'. The non-complementary and the one-mismatched 25-bases oligonucleotide was 5'-CTA-ACA-TTG-AGA-TTC-CGA-GAT-TGA-GAT-CTT-C-3' and 5'-CTA-ACA-TTG-ACA-TTC-CCG-AGA-TTG-A-3' respectively.

2. Instruments and measurements

Atomic Force Microscopy (AFM). A commercial dimension 3100 (Vecco Instruments, USA) atomic force microscope was used for topographical characterization of the samples. All measurements were performed at the tapping mode using rectangular silicon AFM tip.

Fourier Transform infrared spectra (FT-IR) were measured using a Bruker IFS66 FT-IR spectrometer equipped with a MCT detector and an attenuated total reflectance (ATR) crystal of germanium.

Electrochemical measurements were performed using an AUTOLAB PGSTAT

100 electrochemical analysis system controlled by NOVA software (Methrom). The three-electrode cell was purchased from BASI and consisted of glassy carbon electron (GCE) (surface 0.071 cm^2) as working electrode, platinum as counter-electrode and Ag/AgCl as reference electrode. The analyses were performed by electrochemical impedance spectroscopy (EIS) and square wave voltammetry (SWV).

The impedance measurements performed in PBS solution were obtained at -0.3 V vs. Ag/AgCl at DC potential of 10 mV with the frequency ranging from 100 KHz to 0.01 Hz.

SWV measurements were performed in 0.1 M KCl with 1 mM benzoquinone in the range of potential from -0.4 to 0.6 V with potential amplitude of 50 mV and step height of 10 mV frequency of 1.25 Hz, the measurement is corresponding to scan rate of 12.5mV/s.

3. Electrodeposition of β-phenylethylamine (β-PEA)

Various concentrations of 1 mM, 2 mM, and 4 mM of β-phenylethylamine were prepared in a mixture of acetonitrile and H_2O with volume ratio of 1:1 containing 0.1 M $LiClO_4$. Covalently graft of β-phenylethylamine (β-PEA) onto the glassy carbon electrode (GCE) was performed by electrochemical oxidation by immersing the electrode in the solution of phenylethylamine. Cyclic voltammetry method was performed with the range of potential from 0 to 1.5 V *vs.* Ag/AgCl during 10 cycles at a scan rate of 50 mV $s^{-1.}$ This is corresponding to a saturation of the surface as any variation of current was observed. After molecules attachment onto the electrode surface, the electrode was carefully washed with double-distilled water. The electrode are named 1 β-PEA/GCE, 2 β-PEA/GCE and 4 β-PEA/GCE respectively for 1 mM, 2 mM, and 4 mM of β-PEA concentration.

4. Construction of DNA sensor

A drop of 2 µL of the prepared 0.1 mg mL^{-1} H_2TPP-4CP/CRGO suspension was deposited onto the β-PEA modified glassy carbon electrode surface followed by drying step under the lamp, and rinsing with distilled water. Finally, the H_2TPP-4CP/CRGO was activated in a freshly prepared 10 mM solution (pH=7.4) PBS of 20 mM EDC, 32 mM NHS. The activation step was running for 1h at room temperature. Then the electrode was immersed in 1 µM solution of ssDNA probe prepared in PBS buffer for 1h at room temperature. Subsequently, the obtained DNA sensor based on H_2TPP-4CP/CRGO/PEA was thoroughly rinsed with distilled water and stored in PBS at 4 ℃ before use. After each step of construction of the DNA sensor, the surface modifications were controlled by SWV method in benzoquinone.

5. Target detection

The DNA hybridization of complementary 25-bases targets was performed by immersing each DNA sensor in solution of various concentration of DNA target of hepatite C gene for 40 min at 47 ℃. The target concentrations were added successively from 1 aM, 10 aM, 100 aM, 1 fM, 10 fM, 100 fM, 1 pM, 10 pM to 1 nM. After each incubation, the modified electrode was washed with distilled water for three times to eliminate no hybridized single strand DNA and then analyzed by SWV method in benzoquinone. The detection of non-specific interaction was conducted by immersing the electrode in solution of different concentration of non-complementary DNA target in PBS buffer from 1 aM, 10 aM, 100 aM, 1 fM, 10 fM, 100 fM, 1 pM, 10 pM to 1 nM and incubated in the same conditions as for complementary target. To check the reproducibility, the experiment was repeated four times with freshly prepared biosensors individually.

Results and Discussion

1. Electrodeposition of β-PEA

Fig. 4.1 exhibits the CV of electrodeposition process after each cycles in presence of the three different concentrations of β-PEA. In the three cases, the shape of voltammograms is similar. During the first cycle, a single broad and chemically oxidative irreversible peak at around +1.25V with a maximal intensity current (10 µA, 20 µA and 40 µA respectively) is observed and after each cycle the current decrease more or less rapidly.

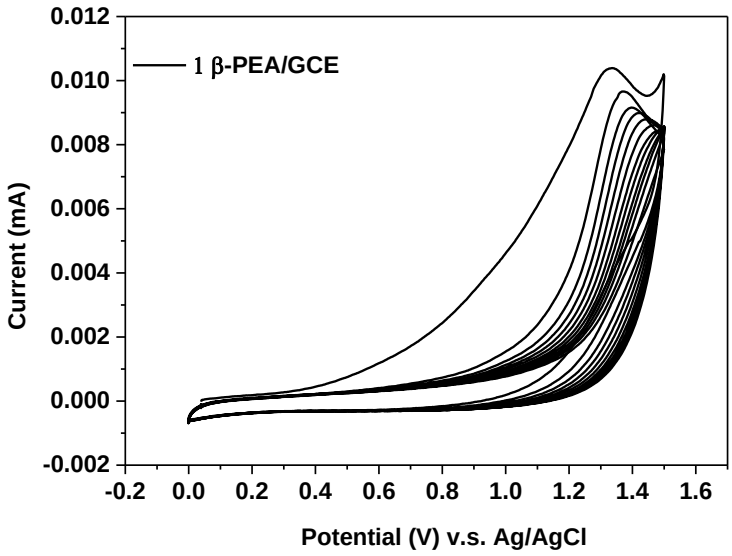

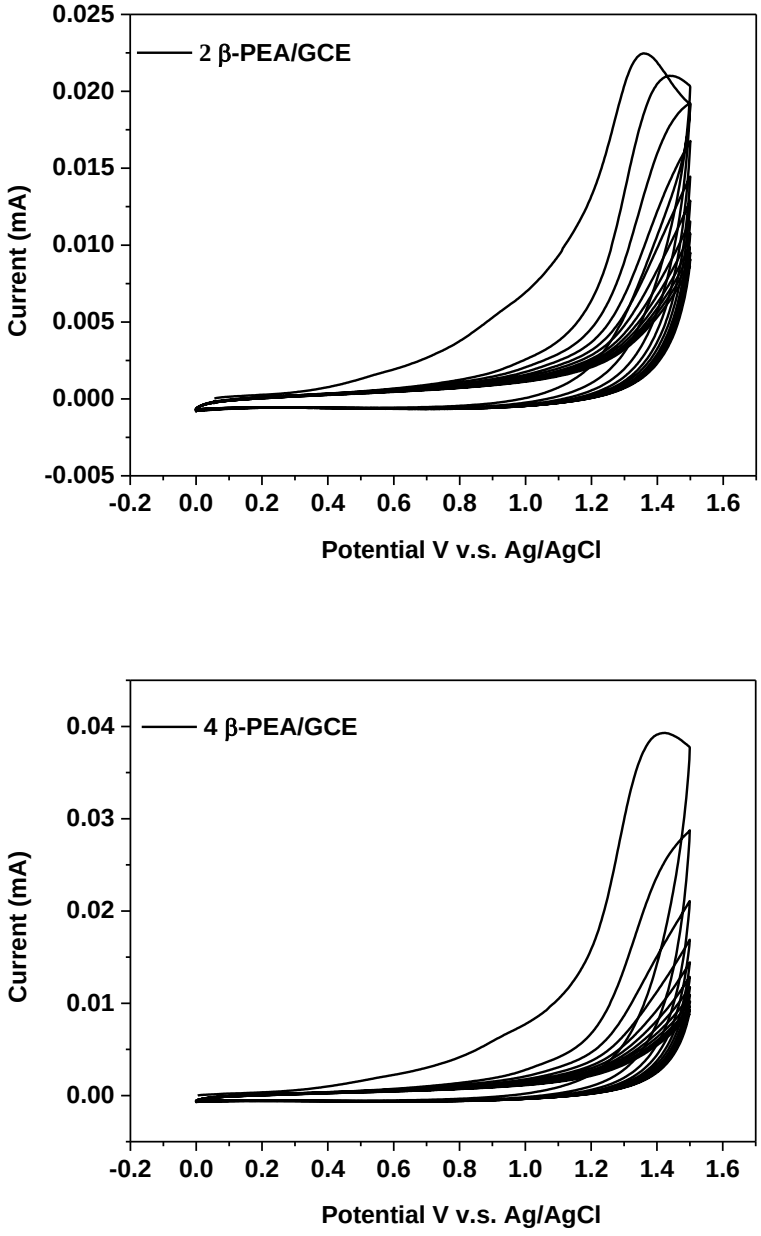

***Fig.4.1**. Cyclic voltammograms of 1mM, 2 mM, 4 mM β-PEA on GC electrode in ACN:H_2O (volume ratio of 1:1) containing 0.1 M $LiClO_4$, scan rate 50 mV.s^{-1}*

As previously demonstrated by Bartlett group[1, 2], the electrodeposition process proceeds initially via the one-electron oxidation of an amine functionality to its corresponding cation radical ($–NH^{\bullet+}$) observed during the first scan, which subsequently reacts with carbon surface to forms a carbon-nitrogen linkage (Scheme 4.1). The absence of the corresponding cathodic peak on the reverse scan indicates that the amine radical cation undergoes fast interaction to the GCE. In subsequent

scans, complete disappearance of the oxidation peak demonstrates that the electrode was completely saturated by grafting β-PEA layer onto the surface.

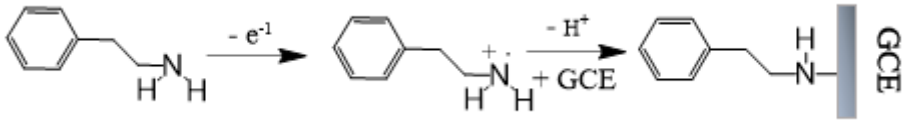

Scheme 4.1. *The schematic formation of reactive radical amine group*

2. Characterisation of self-assembled H_2TPP-4CP/CRGO/β-PEA

The electrochemical properties were analysed by SWVs in 1 mM benzoquinone of modified GCE with the various β-PEA layer before and after the interaction of each electrode with H_2TPP-4CP/CRGO hybrid complex (Fig. 4.2). Square wave voltammograms exhibit for 1 β-PEA/GCE, 2 β-PEA/GCE, and 4 β-PEA/GCE electrode, a reduction peak at -0.15 V, -0.16 V, and -0.28 V respectively corresponding to the reduction of benzoquinone to hydroquinone. We noticed an important shift of the potential reduction peak to negative values for the 4 β-PEA/GCE electrode surface indicating that the reduction of benzoquinone on this surface undergoes more difficult certainly due to a higher density of PEA layer. The charge measured (Q) under the benzoquinone reduction wave of the 4 β-PEA/GCE electrode is evaluated to be as 0.106 mC compared to 0.215 and 0.240 mC for 1 β-PEA/GCE and 2 β-PEA/GCE, respectively, confirming that less benzoquinone species are reduced with such layer (Table 4.2).

After the interaction of H_2TPP-4CP/CRGO nanomaterial, the reduction potential of benzoquinone shifts positively to -0.12 V for the three modified electrodes H_2TPP-4CP/CRGO/1 β-PEA, CRGO/2 β-PEA, and H_2TPP-4CP/CRGO/4 β-PEA electrode surface.

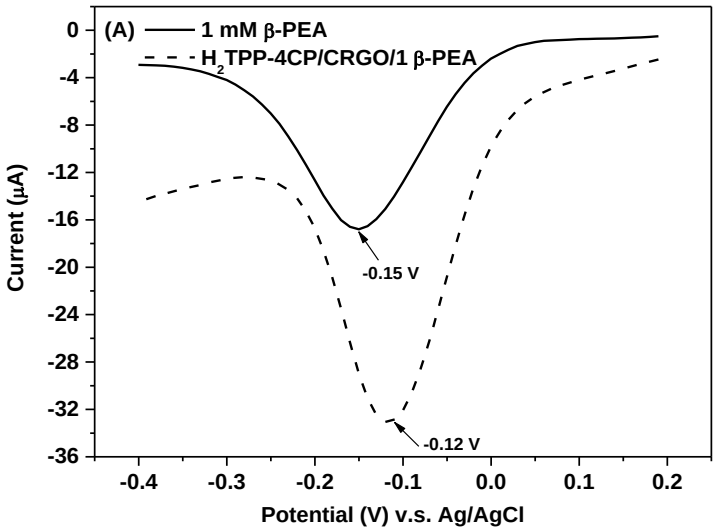
(A)
1 mM β-PEA
H2TPP-4CP/CRGO/1 β-PEA
-0.15 V
-0.12 V
Current (μA)
Potential (V) v.s. Ag/AgCl
0
-4
-8
-12
-16
-20
-24
-28
-32
-36
-0.4
-0.3
-0.2
-0.1
0.0
0.1
0.2

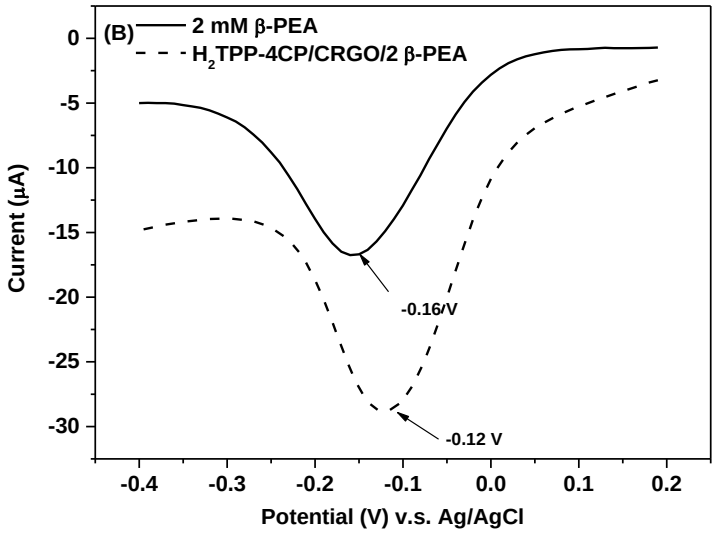
(B)
2 mM β-PEA
H2TPP-4CP/CRGO/2 β-PEA
-0.16V
-0.12 V
Current (μA)
Potential (V) v.s. Ag/AgCl
0
-5
-10
-15
-20
-25
-30
-0.4
-0.3
-0.2
-0.1
0.0
0.1
0.2

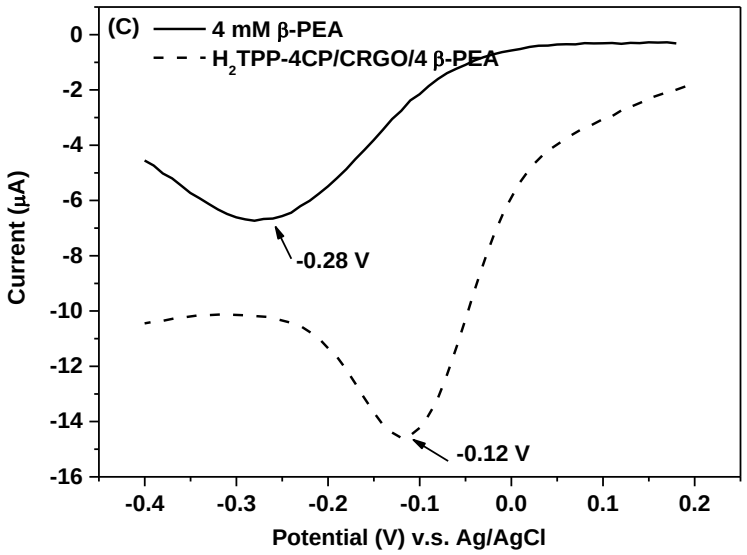

Fig. 4.2. *SWVs of 1 β-PEA/GCE (A), 2 β-PEA/GCE (B), and 4 β-PEA/GCE (C) respectively before (solid line) and after (dashed line) immobilization of H_2TPP-4CP, in 1 mM benzoquinone in the scan rate of 12.5mV s^{-1}.*

Moreover, in comparing to the three types of layer, the amount of charge (Q) evaluated from the reduction wave increases of a factor of 2 after composite immobilization (Table 4.1). These results demonstrated that the introduction of graphene on the β-PEA improves the conductivity of the electrode surface, facilitating both the reduction reaction and increasing the amount of reduced benzoquinone species.

Table 4.1. *Summary data before and after the immobilization of H_2TPP-4CP for various β-PEA/GCE respectively*

	Q (mC)	**ΔQ**	**ΔE red (V)**
1β-PEA	0.215±0.003	0.201±0.003	0.04
H_2TPP-4CP/CRGO/1 β-PEA	0.416±0.006		
2 β-PEA	0.240±0.007	0.254±0.001	0.06
H_2TPP-4CP/CRGO/2 β-PEA	0.494±0.009		
4 β-PEA	0.106±0.008	0.167±0.001	0.16
H_2TPP-4CP/CRGO/4 β-PEA	0.273±0.009		

In order to demonstrate the effects of PEA on the electrical properties of nanomaterial, impedance measurement (EIS) was also used to characterize electrochemical properties of the modified layer especially the interface between the electrode and solution, including the impedance of the layer, capacitance of the electric double layer and the electron transfer resistance (R_{ct}). EIS measurements were investigated in PBS for H_2TPP-4CP/CRGO/1β-PEA and H_2TPP-4CP/CRGO/2β-PEA electrodes and compared to H_2TPP-4CP/CRGO electrode.

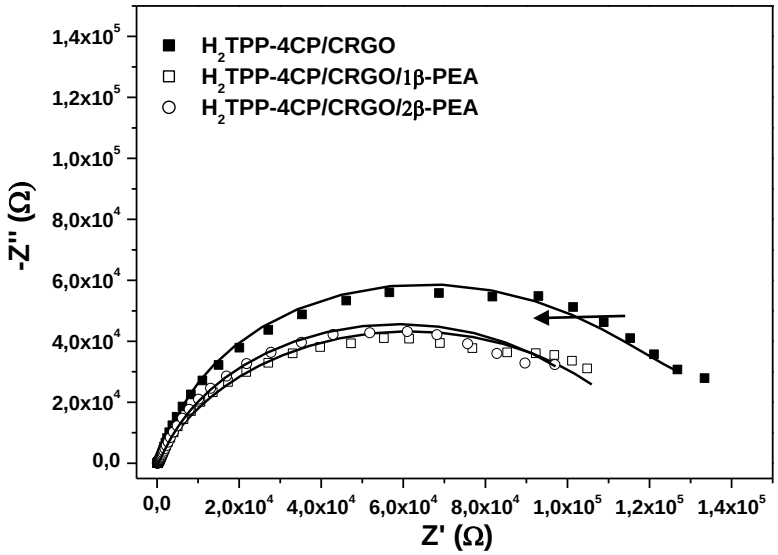

Fig. 4.3. *Nyquists plots measured in PBS solution with Dc potential of 10mV at frequency range of 100 KHz to 0.1 Hz with various modified electrode H_2TPP-4CP/CRGO, H_2TPP-4CP/CRGO/1β-PEA, and H_2TPP-4CP/CRGO/2β-PEA*

Results are shown in Fig. 4.3 and the curves show a decrease of the diameter of the semi-circle for electrodes after modification of β-PEA layer indicating that the nanocomplex has been well interacted with phenyl group in the end position of β-PEA layer through π-π stacking tightly and enhances the efficiency of electron transfer and further the conductivity of the nanomaterial compared to a free-PEA one. This supplementary layer allows a better organisation of modified reduced graphene like a homogeneous and a uniform distribution of H_2TPP-4CP/CRGO composites over the electrode.

AFM measurements were performed of β-PEA modified electrode (a, c) and

H_2TPP-4CP/CRGO/β-PEA (b, d) for two concentrations of β-PEA 1mM and 2 mM. The images are displayed in Fig. 4.4. Compared to the AFM result of H_2TPP-4CP/CRGO/the free β-PEA with the thickness of around 25nm (Fig. 1.9c), the thickness of H_2TPP-4CP/CRGO/β-PEA (Fig. 4.4b, d) pre-functionalized with β-PEA was decreased to 10nm and 15nm, respectively, which was due to the intense interaction between the conjugated-electron-rich ring of nanocomposite H_2TPP-4CP/CRGO and aromatic phenyl ring of β-PEA, which is in good accordance with the results of EIS.

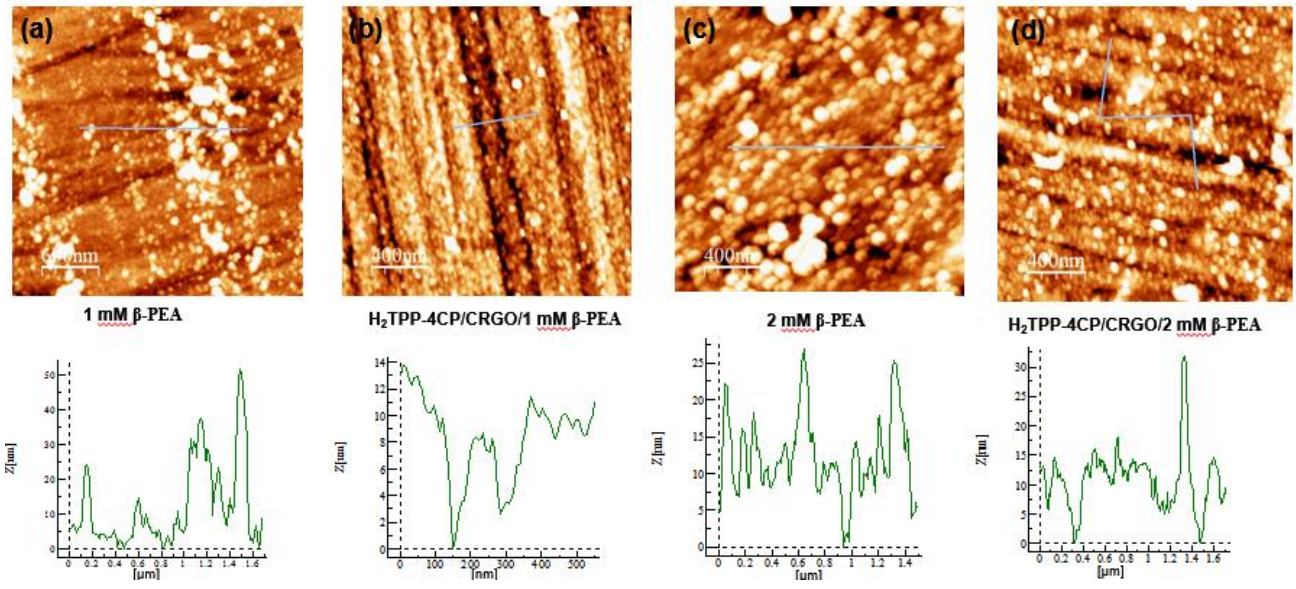

Fig. 4.4*. AFM images of 1 β-PEA /GCE (a) and 2 β-PEA/GCE (c), and of H_2TPP-4CP/CRGO/1 β-PEA (b) and H_2TPP-4CP/CRGO/2 β-PEA (d), respectively.*

As it can be seen in Fig. 4.4a, the 1 β-PEA /GCE surface exhibits a disordered topography surface where PEA is electrodeposited irregularly on the electrode surface with some free-space of glassy carbon. The nanomaterial H_2TPP-4CP/CRGO (Fig. 4.4b) was immobilized following the morphology surface of 1 β-PEA /GCE same through π-π stacking interactions both on the electrode and with aromatic ring of β-PEA. In the case of 2 β-PEA /GCE surface, where the initial concentration of β-PEA was two times higher, AFM image (Fig. 4.4c) exhibits an obviously homogeneous film surface, which demonstrating that the β-PEA molecular are deposited uniformly

and oriented well on the GCE surface. It is noteworthy that after the immobilization of the hybrid nanomaterial, the obtained roughness has no significant variation, which means that H_2TPP-4CP/CRGO was uniformly covered on the β-PEA surface (Fig. 4.4d). The schematic graph was shown in Scheme 2 and we can conclude that the concentration of the β-PEA alters the interfacial architecture of the GCE surface, and from the layer formed with 1 mM to 2mM, the architecture of the β-PEA varies from disordered to self-assembled layer with high ordered construction, and the orientation from perpendicular to parallel to the GCE surface.

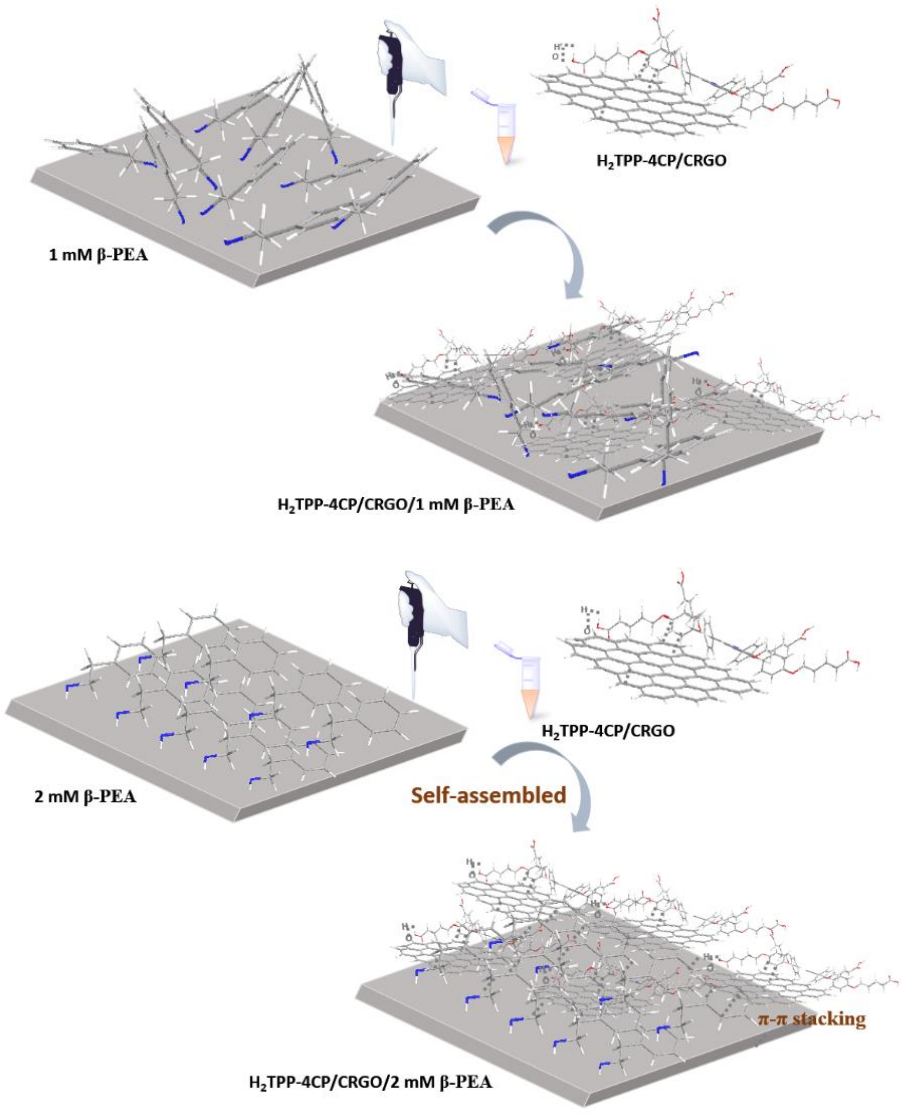

Scheme 4.2. *The schematic graph for the orientation transform from perpendicular to parallel to the GCE surface.*

3. Construction of the DNA sensor

DNA sensor construction involves covalent attachment of single stranded DNA probes (ssDNA) for DNA target detection. The ssDNA probe was covalently bonded to the carboxylic groups present in H_2TPP-4CP/CRGO/β-PEA hybrid complex through an amide link. The reaction was performed in presence of EDC and NHS, as activating agents for one hour and the modified electrode was washed with distilled water to remove any reactants left. The construction of DNA sensor was monitored by square wave voltammetry (SWV) in 1mM *p*-benzoquinone solution (Fig. 4.5).

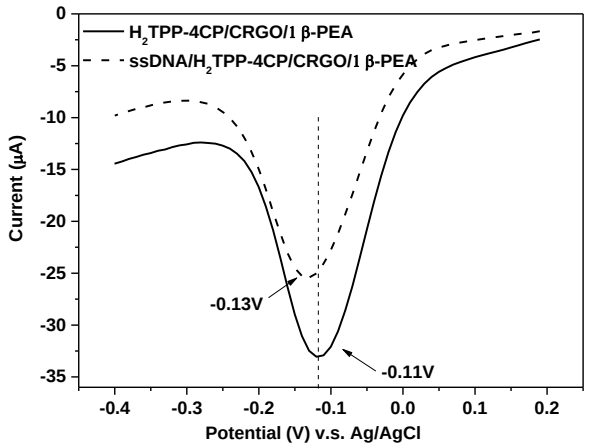

Fig. 4.5. *SWVs of H_2TPP-4CP/CRGO/1 β-PEA before (solid line) and after (dashed line) immobilization of ssDNA, scan rate of 12.5mV s^{-1}.*

The grafting of ssDNA on the H_2TPP-4CP/CRGO/1β-PEA modified electrode undergoes a decrease of intensity current and a negatively shift of the reduction potential peak of around 20 mV. A similar variation was also observed for both H_2TPP-4CP/CRGO/2 β-PEA and H_2TPP-4CP/CRGO/4 β-PEA surface with a potential shift of 13 and 15 mV, respectively (Fig. S4.1). No potential variation was noticed during the attachment of ssDNA onto the H_2TPP-4CP/CRGO electrode free β-PEA. These results demonstrate that the anchored ssDNA on the H_2TPP-4CP/CRGO/β-PEA modified electrode with such materials disturbed the redox reaction of benzoquinone according to an ampero- and potentiometry process due

probably the presence of high negatively charged surface provided by oriented H_2TPP-4CP/CRGO.

The variation of surface coverage (ΔΓ), reflecting the amount of ssDNA fixed on the modified surface, was calculated from SWV experiments (Table 4.2). Compared to value previously obtained for the free β-PEA nanomaterial (line 1), the amount of ssDNA anchored onto the modified surface is sensitively highest with β-PEA layer (4.6 nmol.cm^{-2} compared to 8.6; 11.3 and 6 nmol.cm^{-2}). The quantity of fixed biomolecules is depending on H_2TPP-4CP present on electrode. Result suggests that the amount of immobilized H_2TPP-4CP/CRGO composite is highest on the surface due to two-dimensional π-stacking interactions with aromatic rings of β-PEA molecules or carboxylic groups of porphyrins are more accessible for DNA attachment. Furthermore, values of ΔQ and so ΔΓ are in the same order for the three materials: H_2TPP-4CP/CRGO/1 β-PEA, H_2TPP-4CP/CRGO/2 β-PEA and H_2TPP-4CP/CRGO/4 β-PEA that demonstrate a significant effect of the β-PEA concentration for layer where optimum is obtained with layer formed with 2mM.

Table 4.2. *Summary of calculated parameters after the immobilization of ssDNA for each nanomaterials*

	ΔQ (mC)	**ΔΓ (nmol cm^{-2})**
ssDNA/H_2TPP-4CP/CRGO	0.06	4.6
ssDNA/H_2TPP-4CP/CRGO/1 β-PEA	0.114	8.6
ssDNA/H_2TPP-4CP/CRGO/2 β-PEA	0.15	11.3
ssDNA/H_2TPP-4CP/CRGO/4 β-PEA	0.08	6.0

4. Detection of DNA target

Hybridization reaction was performed with complementary targets (cDNA) by

successive addition of various concentrations ranging from 1 aM to 1 nM for various DNA sensors based on H_2TPP-4CP/CRGO/1 β-PEA, H_2TPP-4CP/CRGO/2 β-PEA, and H_2TPP-4CP/CRGO/4 β-PEA, respectively. The electrochemical detection of DNA targets was monitored by SWV measurements in 1 mM benzoquinone. (Fig. 4.6)

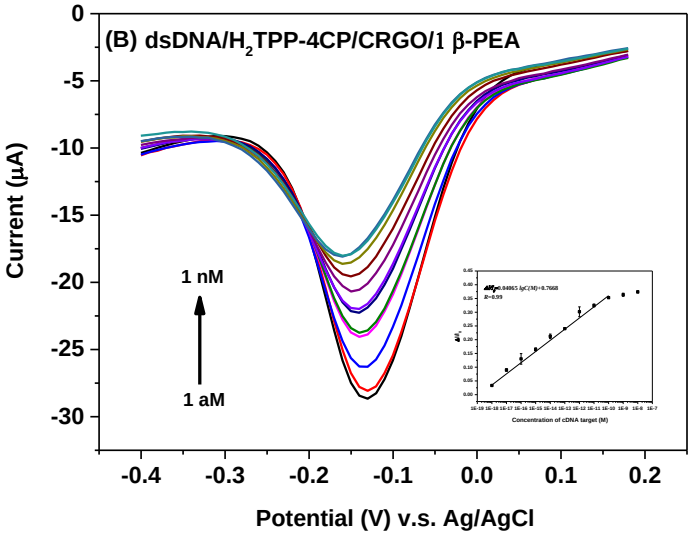

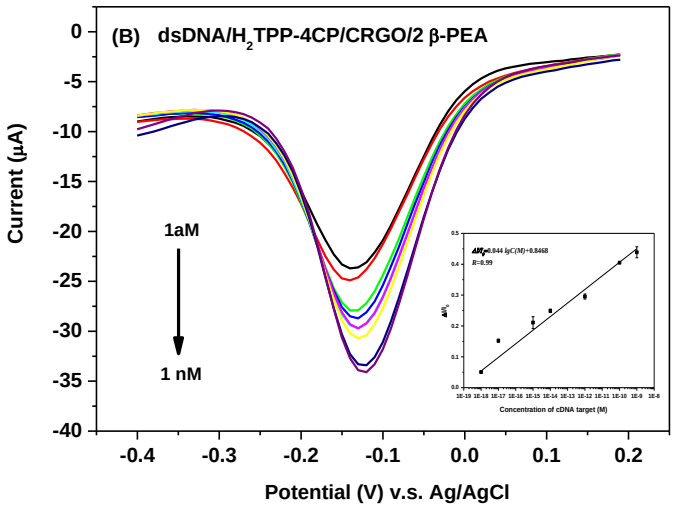

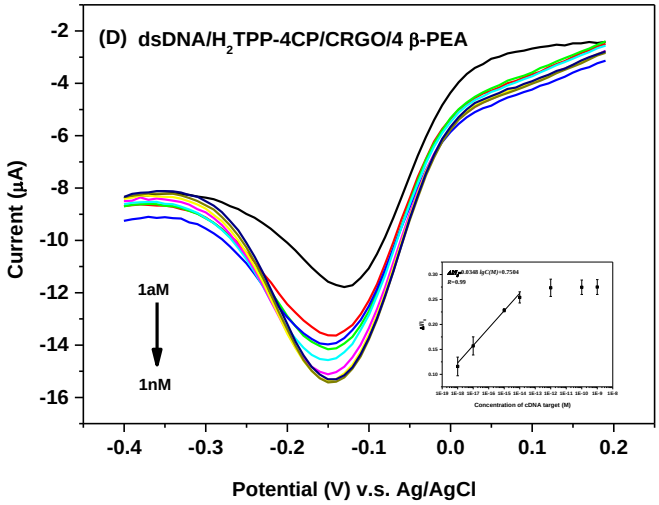

Fig. 4.6. *SWVs experiments for detection of cDNA targets (1 aM to 1 nM). scan rate 12.5 mV.s^{-1} 1 mM benzoquinone. H_2TPP-4CP/CRGO/1 β-PEA (A), H_2TPP-4CP/CRGO/2 β-PEA (B), and H_2TPP-4CP/CRGO/4 β-PEA (C). The insets: logarithmic relationship Data points are the mean values ±RSD obtained with three independent experiments.*

SWV results exhibit different behavior of DNA sensing depending on the concentration of immobilized PEA. Indeed, the current intensity of benzoquinone decreases with the increasing concentration of cDNA targets for sensor based on H_2TPP-4CP/CRGO/1β-PEA (Fig. 4.6 b) which presents the same behavior of the surface free of PEA. The formation of double-strand DNA structure blocks the surface and prevents diffusion process of p-benzoquinone species to it. However, sensors formed with with more concentrated β-PEA layer on the electrode (Fig. 4.6 b and c), show response totally inversed where current intensity of benzoquinone increases with the increasing concentration of cDNA targets. The formation of the double-strand DNA structure during the hybridization releases the conductive surface that means the surface is less blocked favoring the reduction process of benzoquinone. The ssDNA lies certainly on the modified surface through interactions and in presence of complementary ssDNA the double-strand DNA structure goes up, releasing the surface. The ordered organization of the sensor layer afforded a “signal on” during the detection, that is, could be explained by high organization of the composite H_2TPP-

4CP/CRGO and high density of SS DNA on the surface which cover the graphene surface. When hybridization is performed double strand DNA are formed which is pick up from the surface leading to higher diffusion of redox probe and increase in current density. This interpretation should be confirmed in future by AFM image and other measurement such as EIS.

From calibrations curves, the sensor exhibiting the best performance appears to be the sensor based on H_2TPP-4CP/CRGO/ 2 β-PEA material in term of LOD (1.2 10^{-16} M) and linear range [10^{-18}-10^{-9} M] (Table 4.3, Fig. S4.2). We also noticed that the linear range is higher with a material based on β-PEA layer and it increases with the increasing of its concentration to then, decreases.

In view of all these results, the most ordered and uniformed self-assembled surface (H_2TPP-4CP/CRGO/ 2 β-PEA) leads to the sensor with the best performance.

Table 4.3. *Summary of performance of DNA sensors*

	LOD (M)	**Linear range (M)**
ssDNA/H_2TPP-4CP/CRGO previously	7×10^{-19}	10^{-18}~10^{-11}
ssDNA/H_2TPP-4CP/CRGO/1β-PEA	1×10^{-19}	10^{-18}~10^{-10}
ssDNA/H_2TPP-4CP/CRGO/2β-PEA	1.3×10^{-19}	10^{-18}~10^{-9}
ssDNA/H_2TPP-4CP/CRGO/4 β-PEA	1.2×10^{-18}	10^{-18}~10^{-14}

5. Selectivity and reproducibility

Fig. 4.7 shows the results of SWV analysis obtained after incubation of the DNA sensors based on H_2TPP-4CP/CRGO/1 β-PEA, H_2TPP-4CP/CRGO/2 β-PEA, and H_2TPP-4CP/CRGO/4 β-PEA, respectively in successive concentrations of nc DNA targets ranging from 1 aM to 1 nM. These results clearly indicate that reduction current of benzoquinone is sensitively no affected for sensor based on high amount of β-PEA immobilized on the GCE surface (Fig. 4.7.b and c). For 1 fM nc DNA targets

detection, the relative current variation ($\Delta I/I_0$) was also evaluated to be 10 %, 2.5 % and 2.8 % for H_2TPP-4CP/CRGO/1 β-PEA, H_2TPP-4CP/CRGO/2 β-PEA, and H_2TPP-4CP/CRGO/4 β-PEA surface respectively. This variation has to be compared with the 15% of variation for response of sensor based with H_2TPP-4CP/CRGO. The electrodeposition of β-PEA onto the electrode surface improved considerably the selectivity of the sensor. For a layers formed with concentration of 2mM and 4mM phenylethylamine molecules organize themselves on the surface of the electrode, offering a two-dimensional and organized surface. The composite interact in greater quantity according to π-π interactions allowing fixing higher amount of ssDNA on it. High density of ssDNA which is interacted with the nanocomposite surface prevent the non-specific interaction of the non-complementary DNA with carbon surface. In the other way the variation after high concentration undergoes a decrease of the current density contrary to target DNA which leads to increases in the current activity of redox marker.

The calibration curve obtained with non-complementary target were plotted for the various biosensors with phenylethylamine layer and with free layer Fig. 4.8. The curve demonstrate advantageous surface with the high density which prevent totally non-specific adsorptions even for high concentration of non-complementary DNA up to nanomolar range. This gives a great advantage of this biosensor to be used in real application for the detection of genomic DNA.

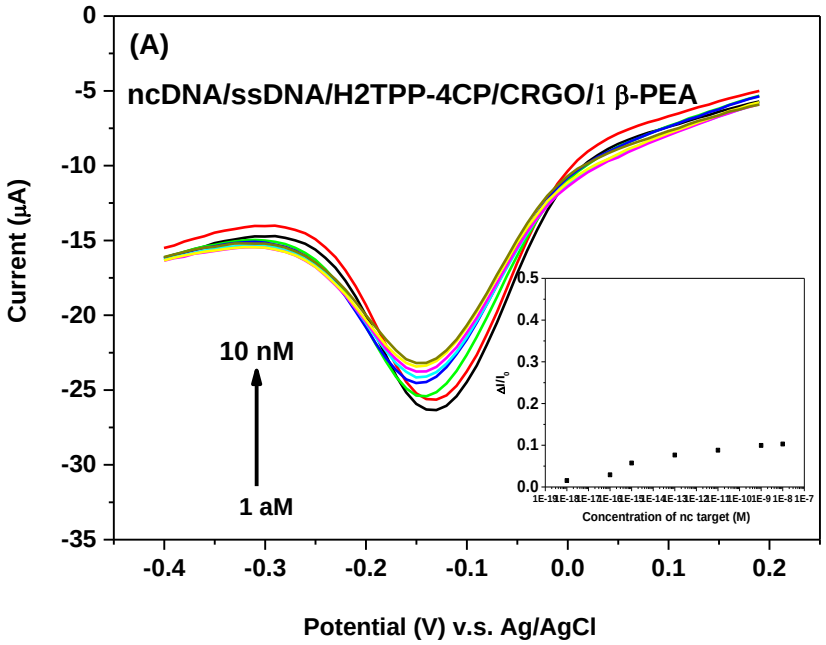
(A)
ncDNA/ssDNA/H2TPP-4CP/CRGO/1 β-PEA
10 nM
1 aM
Current (μA)
Potential (V) v.s. Ag/AgCl
ΔI/I0
Concentration of nc target (M)

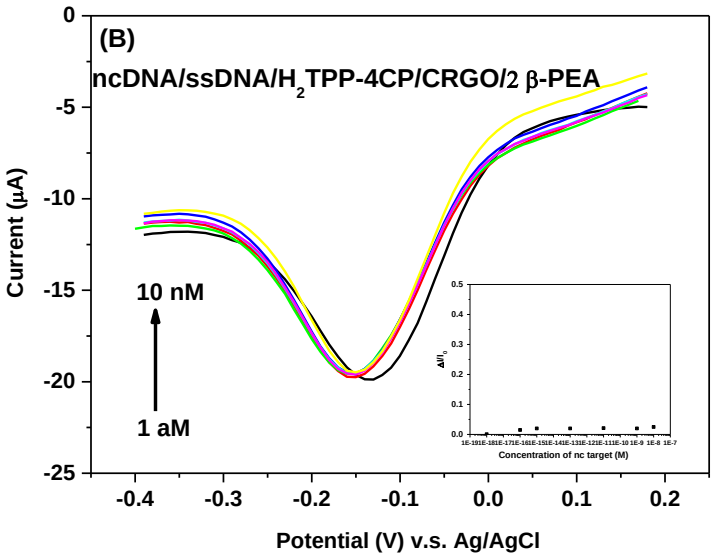
(B)
ncDNA/ssDNA/H2TPP-4CP/CRGO/2 β-PEA
10 nM
1 aM
Current (μA)
Potential (V) v.s. Ag/AgCl
ΔI/I0
Concentration of nc target (M)

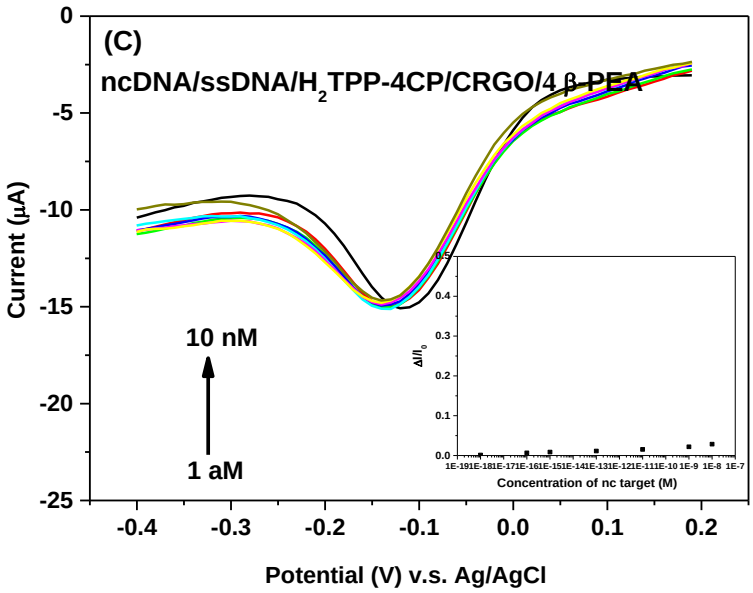

Fig. 4.7. *SWVs experiments for ncDNA targets detection (1 aM to 1 nM), in benzoquinone, DNA sensors based on H_2TPP-4CP/CRGO/1 β-PEA (B), H_2TPP-4CP/CRGO/2 β-PEA (C), and H_2TPP-4CP/CRGO/4 β-PEA (D) The insets are the plot of logarithmic relationship Data points are the mean values ± RSD obtained with three independent experiments.*

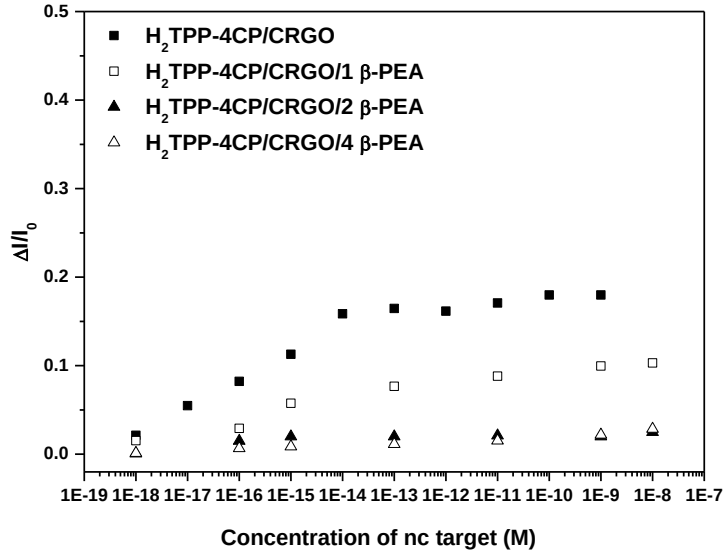

Fig. 4.8. *The summary plot of logarithmic relationship between $\Delta I/ I_0$ and the concentration of the ncDNA targets.*

Conclusion

In this work, a novel "signal-on" electrochemical DNA with high sensitive and selectivity was developed based on nanocomposite H_2TPP-4CP/CRGO deposit on GCE modified with dense self-assembled layer of phenylethylamine formed by electrodeposition on GCE. Optimisation of such layers were realised through electro-oxidation of various concentration of PEA from 1, 2, 4 mM with cyclic voltammetry with 10 cycles. The electrochemical properties and morphology studies of such layers demonstrated that covering the electrode with β-PEA film offers a homogeneous and uniform repartition of the nanocomposite H_2TPP-4CP/CRGO onto the surface. The optimum density is obtained with layers, formed with 2 mM of β-PEA. This film increases the interaction of the nanocomposite H_2TPP-4CP/CRGO due to the presence of phenyl in end position favoring π-π interactions. The conductivity of the surface after the addition of the composite enhances the reduction process of benzoquinone as redox marker. The immobilization of ssDNA onto H_2TPP-4CP/CRGO/β-PEA involves a decrease of current intensity and a negatively shift of reduction peak of benzoquinone, demonstrating that the ssDNA blocks the surface and prevents the diffusion process of benzoquinone species on it. Detection of complementary ssDNA with sensor based on H_2TPP-4CP/CRGO/ β-PEA with dense and ordered architecture surface of β-PEA involved a "signal-on" of sensing response with an increase of current intensity by the increase of the target concentration. We demonstrate also that, the incorporation of β-PEA layer between GC electrode and the nanocomposite overcame the problem of the non-specific adsorptions of ssDNA on the graphene surface. Indeed, the electrodeposition of β-PEA with concentration of 2mM leads totally to avoid the variation of signal with non-complementary target in large concentration until nanomolar range compared the non-specific adsorption with sensor based with H_2TPP-4CP/CRGO free of PEA where the variation lead 15% for high concentration of DNA..

The DNA sensor based on H_2TPP-4CP/CRGO/2β-PEA platform demonstrated to

be a performing tool and could be expected to be successfully applied for real samples detection demonstrating a potential application in DNA sensing.

Supporting Information

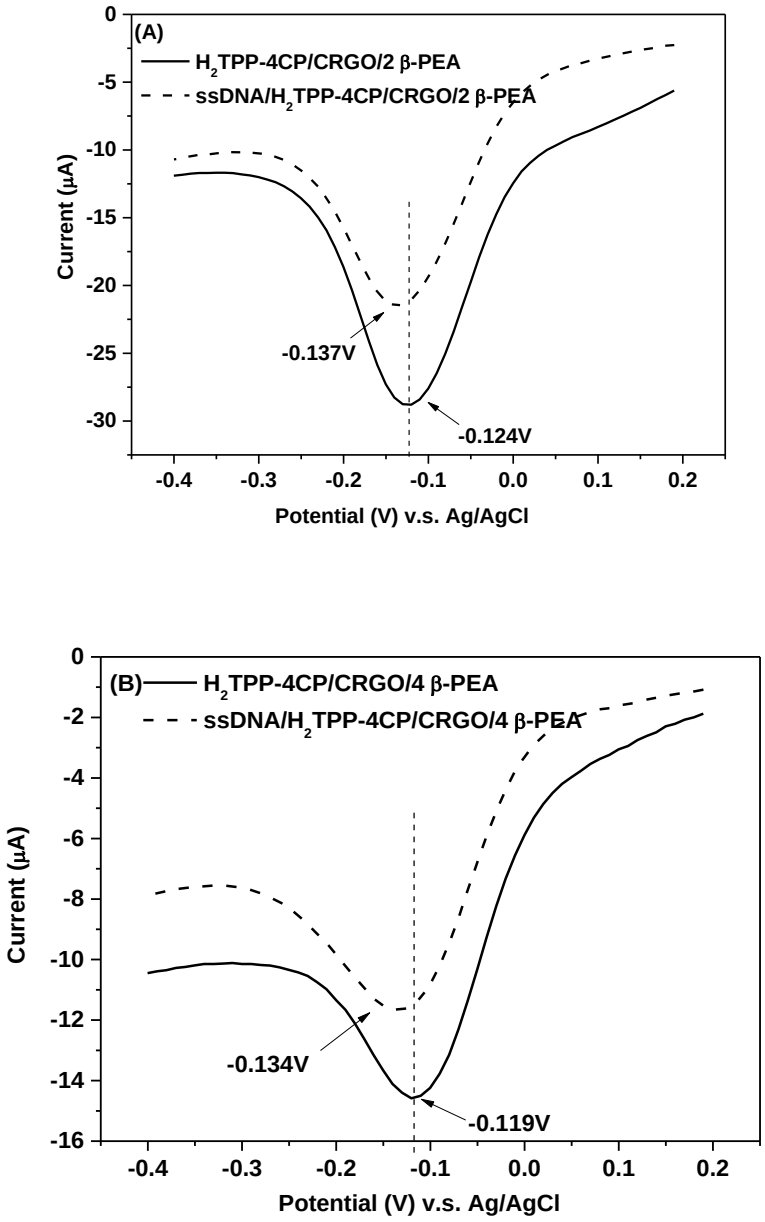

Fig. S4.1. *SWVs of H_2TPP-4CP/CRGO/2 β-PEA (A), and H_2TPP-4CP/CRGO/4 β-PEA (B), respectively before (solid line) and after (dashed line) immobilization of ssDNA, scan rate of 12.5mV s^{-1}*

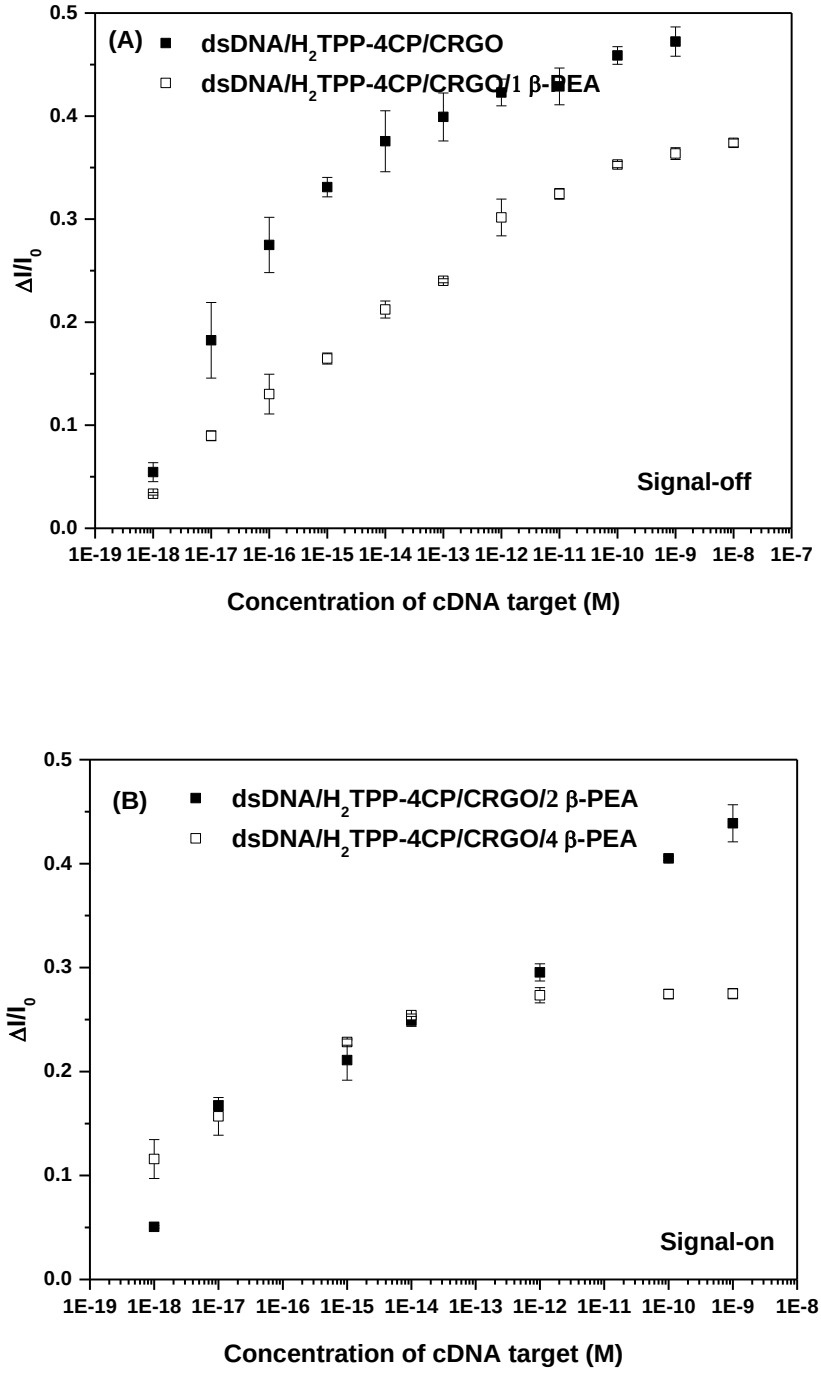

Fig. S4.2. *The summary plots of logarithmic relationship between ΔI/ I_0 and the concentration of the cDNA targets.*

REFERENCES:

1. Ghanem, M. A., Chrétien, J.-M., Pinczewska, A., Kilburn, J. D. & Bartlett, P. N. Covalent modification of glassy carbon surface with organic redox probes through diamine linkers using electrochemical and solid-phase synthesis methodologies. *J. Mater. Chem.* **18,** 4917–4927 (2008).
2. Chrétien, J. M., Ghanem, M. A., Bartlett, P. N. & Kilburn, J. D. Covalent tethering of organic functionality to the surface of glassy carbon electrodes by using electrochemical and solid-phase synthesis. *Chem. - A Eur. J.* **14,** 2548–2556 (2008).

GENERAL

CONCLUSIONS

GENERAL CONCLUSIONS

The project of my thesis consisted in the development of biomaterials able to act as molecular transducers for the construction of DNA sensors. For this purpose, I focused my research on the hybrid nanomaterials which combined the features of both graphene (high conductivity and large specific surface area) and porphyrins (physical and chemical properties and electron transfer ability) to obtain the excellent electronchemical response and analytical performance of DNA sensors. These DNA sensors were used for detection of DNA from various infectious diseases like hepatitis C and tuberculosis.

The tetraphenylporphyrins bearing one (H_2TPP-1CP) and four carboxylic group (H_2TPP-4CP) at the para position of a phenyl group were successfully synthesized by a simple and effective way. The tetraphenylporphyrin bearing one carboxylic group incorperated manganese (III) (MnTPP-1CP) was also prepared. Meanwhile, the various types of graphene were synthesized by different methods, such as exfoliation of graphite and reduction of graphene oxide via electrochemical (ERGO) and chemical reductive methods (CRGO), respectively. The chemically nanomaterial reduced graphene oxide (CRGO) was characterized by XPS and Raman spectroscopy and demonstrates high level of reduction and best electrochemical properties.

The comprehensive exploration including the molecular characteristics and electronic properties of the interaction between H_2TPP with different carboxylic groups and CRGO were performed through SEM, AFM, UV-visible, FT-IR spectroscopic studies, and EIS measurements. The anchoring of porphyrin moieties weakens the interaction between the CRGO sheets, which further improves the dispersion of CRGO and formation of nano-sheets of graphene and edge surface. The obtained apparent association constant between the H_2TPPs and CRGO was calculated using the Benesi-Hildebrand expression to be 85.1 g^{-1} L and 64.4 g^{-1} L, respectively for H_2TPP-1CP/CRGO and H_2TPP-4CP/CRGO confirming the strong

interaction between H_2TPP and CRGO sheets. The thickness of porphyrin obtained from EIS was calculated to be 72 ± 9.3 nm and 20.4 ± 1.2 nm, respectively for H_2TPP-1CP/CRGO and H_2TPP-4CP/CRGO, confirming that for H_2TPP-1CP/CRGO, the nano-sheet is formed and the higher value, compared to H_2TPP-4CP/CRGO, exhibits some aggregated domains upwards, and for H_2TPP-4CP/CRGO, the porphyrin is anchored at the edge of CRGO and meanwhile, forms hydrogen bond with carboxylic group of porphyrins.

In order to further investigate the charactristics and electrochemical properties of coverage of hybrid nanomaterial H_2TPP-nCP/CRGO, a porphyrin of manganese was synthezised. The manganese (Mn) was chosen as metallic cation due to its redox properties and reversible signal. Charactersitics of the layer (average surface coverage, electron transfert resistance,) was investigated thanks the electrochemical signal response of the Mn^{3+}/Mn^{2+} redox complex. All the results demonstrate strong π–π stacking interactions between the manganese porphyrin (MnTPP-1CP) and CRGO and the ability of CRGO to immobilize a large amount of MnTPP-1CP offering a stable sensing layer.

For the first time, DNA sensors based on MnTPP-1CP was elaborated, where one carboxylic group was covalently functionalized with ssDNA on the GC electrode surface. The incorporation of a redox metal inside the macrocycle ring of porphyrin allows the electrochemical characterization of the film. Optimized conditions for the process of construction of DNA sensor and hybridization were performed including the concentration ratio of MnTPP-1CP and CRGO, the concentration of activated reactants (EDC and NHS), and the hybridization time. A detection limit of 2×10^{-16} M was estimated with a moderate selectivity demonstrating that the combined porphyrin-graphene framework exhibits an excellent conductivity and a good electron transfer which contributes to amplify the redox signal of metalloporphyrin. Furthermore, it demonstrate to be a very good candidate for direct DNA sensor and are very promising in DNA sensors applications. Nethertheless, after hybridization with cDNA with one-base mismatched and non-complementary sequences, the ΔR_{ct}/

$R_{ct,ssDNA}$ values were calculated to be 27% and 9% respectively. This undesired variation observed after the non-complementary DNA interaction could be attributed to some non-specific adsorptions of the DNA onto the electrode surface. Increasing the number of negative charges on the surface should limit this kind of interactions by charge repulsions and so should improve the DNA sensor performance.

Thus, a designed electrochemical DNA sensor based on π-conjugated nanomaterial composed of chemically reduced graphene oxide (CRGO) and tetraphenylporphyrin functionalized with numerous carboxylic groups (H_2TPP-n$CP_{n=1,4}$) was constructed and compared through electrochemical analysis in different types of redox indicators, negatively charged $[Fe(CN)_6]^{3-/4-}$ and a neutral couple one, *p*-benzoquinone/hydroquinone. The morphology of modified surface was also studied thanks AFM measurements. In conclusion, we proposed two different modes of ssDNA immobilizing on the nanomaterial surface depending on its nature: a) immobilized ssDNA lies on the plane hybrid surface homogeneously layer by layer for H_2TPP-1CP/CRGO nanomaterial, and b) for H_2TPP-4CP/CRGO, ssDNA sequences graft on the edge of the hybrid complex and tend to overwhelm the construction of carboxylic group on the edge of the CRGO. Therefore, increasing the number of carboxylic functions on porphyrin afforded a largest amount of immobilized ssDNA on the complex surface and offered a stable and highly sensitive sensing layer. The proposed DNA sensor showed high sensitivity for detecting complementary DNA in a wide linear range [10^{-18}-10^{-12} M] and [10^{-18} M-10^{-11} M] for DNA sensor based on H_2TPP-1CP/CRGO and H_2TPP-4CP/CRGO, respectively with a detection limit as low as 2×10^{-18} and 7×10^{-19} M (S/N = 3). Most importantly, we demonstrated that the selectivity was enhanced by introducing numerous negative charged functional groups on the porphyrins. Indeed, only 15% of variation for the relative change of peak current were observed during the detection of non-complementary DNA sequence at low concentration compared to 30% for the sensor based on H_2TPP-1CP/CRGO. However this value is still high and should be improved such as blocking the glassy carbon electrode with aromatic compounds to avoid any

self-assembled adsorptions on the electrode. Furthermore, the versatile elaborated DNA sensor based on H_2TPP-4CP/CRGO endows property for sensing DNA of rpoB gene of *Mycobacterium tuberculosis* in real PCR samples. This shows enormous potential on H_2TPP-4CP/CRGO platform with electrical conductivity and dispersibility for further applications in pathogens diagnostic and therapeutic purpose.

In order to further eliminate the non-specific absorption, the modification of the glassy carbon electrode surface is imperative and neccessary. In this work, a mono layer of β-phenylethylamine (β-PEA) was electrodeposited and formed on the GCE. The modified electrodes employing in various concentration of β-PEA (1, 2, and 4 mM), followed by the immobilization of hybrid complex moieties H_2TPP-4CP/CRGO were studied and characterized by SWV and the morphology by AFM experiments. The results demonstrated that concentration of the β-PEA alters the interfacial architecture of the GCE surface, and from the layer formed with 1 mM to 2mM, the architecture of the β-PEA varies from disordered to self-assembled layer with high ordered and uniform construction. An optimum density was obtained with layers, formed with 2 mM of β-PEA. This film increases the interaction of the nanocomposite H_2TPP-4CP/CRGO due to the presence of phenyl favoring π–π interactions and increase the conductivity of the surface after the addition of the composite, that enhances the oxydo-reduction process of benzoquinone as redox marker. Detection of complementary ssDNA with sensor based on H_2TPP-4CP/CRGO/ 2 β-PEA involved a "signal-on" of sensing response with an increase of current intensity by the increase of the target concentration and exhibited an excellently sensitivity with a limit detection low to 1.3×10^{-19} M and broad linear range from 10^{-18} to 10^{-9} M. Moreever, the electrodeposition of of β-PEA with concentration of 2 mM, prevented totally non-specific adsorptions with the surface during the detection of non-complementary target in large concentration compared to sensor based with H_2TPP-4CP/CRGO free of PEA where the variation lead 15% for high concentration of DNA.

In my work, a novel and optimized "signal-on" electrochemical DNA with

excellently high sensitive and selective was employed based on the H_2TPP-4CP/CRGO/2 β-PEA/GCE surface, which will be expected to be successfully applied for PCR samples detection demonstrating a potential healthy applicate.

ABBERVIATIONS

ABBREVIATIONS

PANI-NF	polyaniline nanofibers
MB	methylene blue
AuNP	gold nanoparticles
Th-G	thionine-graphene
PPy-PEDOT	poly(3,4-ethylenedioxythiophene)
FLN	polyhydroxylated fullerenol
TGA	thioglycolic acid
CNTs	carbon nanotubes
SiC	silicon carbide
SDBS	sodium dodecylbenzene sulfonate
AgNPs	silver nanoparticles
UA	uric acid
TCPP	tetrakis(aminophenyl)porphyrin
NaOH	sodium hydroxide
PDMS	poly(dimethylsiloxan)
PTCA	3,4,9,10-Perylene tetracarboxylic acid
PP	polypropylene
TPP	tetraphenylporphyrin
PMMA	poly(methyl-meta acrylate)
$NaBH_4$	sodium borohydrate
H_2O_2	hydrogen peroxide
DCM	dichloromethane
DMF	*N, N*-Dimethylformamide
GO	graphene oxide
CRGO	chemically reduced graphene oxide
EEG	electrochemical exfoliation of graphite
ERGO	electrochemical reduced graphene oxide
CRGO	chemical reduced graphene oxide
MnTPP-1CP	metallotetraphenylporphyrin

H_2TPP-1CP	tetraphenylporphyrin bearing one carboxylic group
H_2TPP-4CP	tetraphenylporphyrin bearing 4 carboxylic groups
ssDNA	single strand oligonucleotide
cDNA	complementary single strand DNA
GCE	glassy carbon electrode
TFA	tetrahydrofuran
DDQ	2,3-Dichloro-5,6-dicyano-p-benzoquinone
EDA	ethylendiamine
NHS	N-Hydroxysuccinimide
LOD	limit of detection
CVD	chemical vapor deposition
EIS	electrochemical impedance measurement
CV	cyclic voltammetry
SWV	square wave voltammetry
FT-IR	Fourier Transform infrared spectra
XPS	X-ray photoelectron spectroscopy
AFM	Atomic Force Microscopy
TLC	thin layer chromatography
CPE	carbon paste electrode
Rs	resistance of electron transfer

Titre : Synthèse de nouveaux nanomatériaux basés sur des porphyrines et du graphène pour l'élaboration de biocapteurs d'ADN sensibles et sélectifs.

Mots clés : nanomatériaux; porphyrines; graphène; sensible; sélectif; biocapteur

Résumé: La conception et le développement de biocapteurs pour la détection directe de biomarqueurs dans un échantillon de fluide biologique constituent un véritable défi dans la recherche pour leur application dans le système de point de soins en diagnostic. Mon projet est axé sur l'élaboration d'une nouvelle plateforme de décomposition biologique composée de graphène qui présente une surface électroactive et spécifique élevée permettant de greffer de nombreux biomolécules avec des métalloporphyrines en tant que nouveau marqueur redox pour suivre le processus de reconnaissance biologique obtenu dans le cas d'un capteur d'ADN. Le concept sera de démontrer que les métalloporphyrines où le potentiel d'oxydo-réduction pourrait être contrôlé par la nature des ions métalliques pourraient être appliquées dans une plate-forme de biocapteurs électrochimique multidétection. L'association de la métalloporphyrine avec le graphène offrira de nombreux avantages, comme la promotion de la réaction de transfert d'électrons et ayant une grande surface pour l'immobilisation des protéines. La détection de la cible présente sera réalisée suite à l'activité redox des métalloporphyrines greffées à la surface.

Nous avons déjà synthétisé différentes métalloporphyrines modifiées et caractérisées par des techniques habituelles de spectrométrie telles que la RMN, les UV et la MS. Le biocapteur d'ADN a été construit par le composite de graphène et métalloporphyrine et sonde d'ADN comme biorécepteur suivant l'approche d'attachement covalent et l'optimisation de la construction de biocapteur pour améliorer la stabilité et la reproductibilité.

Et nous avons déjà fait une détection de l'ADN cible par diverses méthodes électrochimiques, y compris la voltamétrie cyclique, la voltampérométrie à onde carrée et la spectroscopie d'impédance. Cette stratégie a été réalisée d'abord avec la porphyrine Mn insérée puis généralisée à divers complexes métalliques pour une approche multidétection.

Parallèlement, les nanomatériaux hybrides combinant les caractéristiques du graphène (haute conductivité et grande surface spécifique) et des porphyrines (propriétés physiques et chimiques et capacité de transfert d'électrons), tels que la tétraphénylporphyrine portant un et quatre groupes carboxyliques nommés H_2TPP-nCP (n = 1, 4) et la tétraphénylporphyrine incorporant du manganèse (III) (MnTPP-1CP) ont été synthétisés avec succès. L'interaction entre H_2TPP-nCP (n = 1, 4) et l'oxyde de graphène chimiquement réduit (CRGO) a été étudiée dans mon travail de thèse. Pour étudier les propriétés caractéristiques des nanomatériaux préparés, la microscopie électronique à balayage (MEB), la microscopie à force atomique (AFM), les spectres UV-visible, les spectres infrarouges à transformée de Fourier (FT-IR) et les spectres de photoélectrons X.

Afin d'éliminer l'absorption non spécifique, la modification de l'électrode par le PEA a également été appliquée et obtenir une excellente application pour la détection de la cible d'ADN

Title : Synthesis of new nanomaterials based on porphyrins and graphene for elaboration of sensitive and selective DNA biosensors.

Keywords : nanomaterials; porphyrins; graphene; sensitive; selective; biosensor

Abstract : The design and development of biosensors for direct detection of biomarkers in biological fluid sample is real challenge in research for their application in point of care system in diagnostic. My project is focus on the elaboration of a new platform for biological detaction composed of graphene which exhibits a high electroactive and specific surface suitable for grafting numerous biomoleculer with metalloporphyrins as a novel redox marker for following biological recognition process obtained in the case of DNA sensor. The concept will be to demonstrate that the metaloporphyrines where there redox potential could be controlled by the nature of metal ions could be applied in multidetection electrochemical biosensor platform. The association of metalloporphyrin with graphene will offer numerous advantages, as promoting electron transfer reaction and having a large surface for protein immobilization. The detection of target present will be performed following redox activity of the metalloporphyrins grafted on the surface.

We have already synthesized various modified metalloporphyrins and characterizatized by usual spectrometry techniques such as NMR, UV and MS. The DNA biosensor has been constructed by the composite of graphene and metalloporphyrin and DNA probe as bioreceptor following covalent attachment approach and optimization of the biosensor construction for improving stability and reproducibility.

And we have already done some detection of DNA Target by various electrochemical methods including cyclic voltammetry, square wave voltammetry and impedance spectroscopy. This strategy was performed firstly with on Mn inserted porphyrin and then generalized to various metal complex for multidetection approach.

Meanwhile, the hybrid nanomaterials which combined the features of both graphene (high conductivity and large specific surface area) and porphyrins (physical and chemical properties and electron transfer ability), such as tetraphenylporphyrin bearing one and four carboxylic group named H_2TPP-nCP(n=1, 4) and tetraphenylporphyrin incorporating manganese (III) (MnTPP-1CP) were successfully synthesized. The interaction modes between H_2TPP-nCP(n=1, 4) and chemically reduced graphene oxide (CRGO) was studied in my thesis work. To investigate the characteristic properties of as-prepared nanomaterials, scanning electron microscopy (SEM), atomic force microscopy (AFM), UV-visible spectra, Fourier Transform infrared spectra (FT-IR), X-ray photoelectron spectra (XPS). In order to eliminate the non-specific absorption, the modification of the electrode by monolayer PEA was also applied and obtain excellent application for the detection of DNA target

Université Paris-Saclay
Espace Technologique / Immeuble Discovery
Route de l'Orme aux Merisiers RD 128 / 91190 Saint-Aubin, France